Injectable formulations forming an implant in situ as vehicle of silica microparticles embedding superparamagnetic iron oxide nanoparticles for the local, magnetically mediated hyperthermia treatment of solid tumors

Pol-Edern Le Renard

Thesis

Injectable formulations forming an implant in situ as vehicle of silica microparticles embedding superparamagnetic iron oxide nanoparticles for the local, magnetically mediated hyperthermia treatment of solid tumors

LE RENARD, Pol-Edern

Abstract

Cette thèse présente les travaux de développement de formulations injectables capables de se solidifier in situ, formant ainsi un implant piégeant des microparticules magnétiques en vue du traitement de tumeurs par induction magnétique d'une hyperthermie locale modérée. Nous exposons tout d'abord le contexte physique, biologique et clinique de l'hyperthermie comme traitement anticancéreux, particulièrement des modalités électromagnétiques. Les performances in vitro et in vivo des matériaux et formulations sont alors présentées. L'objet du chapitre suivant est la caractérisation des propriétés physicochimiques, magnétiques, et chauffantes, dans un champ magnétique alternatif (115 kHz, 9 - 12 mT), des microparticules de silice renfermant des nanoparticules d'oxyde de fer superparamagnétiques (SPIONs) et de deux de leurs formulations: un hydrogel d'alginate de sodium et un organogel de poly(éthylène-co-alcool vinylique) dans le diméthylsulfoxide. Finalement, nous présentons le potentiel thérapeutique de 20 minutes d'hyperthermie locale induite après injection de l'organogel superparamagnétique dans un modèle murin sous-cutané de tumeurs nécrosantes de colocarcinome humain.

Reference

LE RENARD, Pol-Edern. *Injectable formulations forming an implant in situ as vehicle of silica microparticles embedding superparamagnetic iron oxide nanoparticles for the local, magnetically mediated hyperthermia treatment of solid tumors*. Thèse de doctorat : Univ. Genève, 2011, no. Sc. 4346

Université de genève
Section des Sciences Pharmaceutiques
Laboratoire de pharmacie galénique

FACULTÉ DES SCIENCES
Professeur Eric Doelker
Docteur Olivier Jordan

Injectable formulations forming an implant in situ as vehicle of silica microparticles embedding superparamagnetic iron oxide nanoparticles for the local, magnetically mediated hyperthermia treatment of solid tumors

THÈSE

présentée à la Faculté des sciences de l'Université de Genève

pour obtenir le grade de Docteur ès sciences, mention sciences pharmaceutiques

par

Pol-Edern Le Renard

de

Thionville (France)

THÈSE N°4346

GENÈVE

Atelier d'impression numérique - Repromail

2011

UNIVERSITÉ
DE GENÈVE

FACULTÉ DES SCIENCES

Doctorat ès sciences
Mention sciences pharmaceutiques

Thèse de *Monsieur Pol-Edern LE RENARD*

intitulée :

" Injectable Formulations Forming an Implant *in situ* as Vehicle of Silica Microparticles Embedding Superparamagnetic Iron Oxide Nanoparticles for the Local, Magnetically Mediated Hyperthermia Treatment of Solid Tumors "

La Faculté des sciences, sur le préavis de Messieurs E. DOELKER, professeur honoraire et directeur de thèse (Section des sciences pharmaceutiques), O. JORDAN, docteur et codirecteur de thèse (Section des sciences pharmaceutiques), P. VAUPEL, professeur (Département de radio-oncologie et radiothérapie, Université Johannes Gutenberg de Mayence, Allemagne), J.-Ch. LEROUX, professeur (Institut für Pharmazeutische Wissenschaften, Eidgenössische Technische Hochschule, Zurich, Suisse) et Madame C. WILLHEM, docteure (Laboratoire de matière et systèmes complexes, Université Paris-Diderot, France), autorise l'impression de la présente thèse, sans exprimer d'opinion sur les propositions qui y sont énoncées.

Genève, le 7 septembre 2011

Thèse - 4346 -

Le Doyen, Jean-Marc TRISCONE

Acknowlegement/Remerciements

Je tiens à remercier par dessous tout Nadja, à qui je dédie cette thèse.

Mes remerciements vont au Professeur Eric Doelker pour avoir dirigé cette thèse et mes activités d'assistant. Je remercie bien sûr Olivier Jordan, scientifique de génie dont je souhaite saluer la profonde implication.
Je souhaite ici remercier l'aide et l'implication si importantes de Franz Buchegger, auquel ce travail doit sa qualité et sa pertinence en particulier pour son pendant *in vivo*. Je remercie tout les membres du service de médecine nucléaire de Lausanne.
Je remercie le Professeur Daniel Rüfenacht pour avoir suggéré et supervisé nombre d'aspects fondamentaux de ce projet.
Je remercie le docteur Xavier Montet du Service de Radiologie de l'hôpital HUG à Genève.
Je remercie le Professeur Hofmann et le docteur Alke Petri-Fink pour leurs contributions fondamentales à cette thèse.
Je remercie le Professeur Bosman, avec lequel j'ai eu tant de plaisir à critiquer les résultats de ce travail aux vues implacables de l'histologie. Je remercie par la même le Docteur Susanne Leuba pour son accueil et tous les membres du l'institut de pathologie du CHUV à Lausanne.
Je remercie les collaborateurs aussi nombreux que chaleureux: Antonin Faes, Rolf Lortz, Carmine Senator, Jean-Philippe Rapin.
Je remercie mes collègues. Je remercie Myrtha Copin pour son aide et me joins à l'opinion générale pour saluer son engagement auprès des doctorants. Je remercie Nathalie Boulens qui a su me supporter au quotidien, et avec qui j'ai tant de plaisir à partager le bureau et la paillasse tout comme les repas. Je remercie Claudia Di Tomaso et Emilie Patois pour les agréables moments partagés. Aussi, chère Adriana Hapca, je voudrais te remercier du fond du coeur pour tout ce que tu m'as appris de la science et de la vie.

Je n'oublie pas non plus de remercier ma famille qui est l'origine de ma profonde curiosité, que je n'ai pas manqué de solliciter lors de ce travail.
Au delà, je remercie les Professeurs, pharmaciens, médecins et scientifiques qui ont compté dans mon parcours scientifique: Professeur Marie Christine Béné et Professeur Gilbert Faure, Docteur Fréderic Massin, Docteur Sébastien Gibot et le Docteur Cédryck Vaquette.

Pour finir, je remercie infiniment les membres du jury de cette thèse dont j'admire les travaux:

le Professeur Peter Vaupel, à qui je marque mon admiration pour le travail de référence international si précieux pour les pharmaciens et médecins, de l'étudiant au chercheur.
Sehr geehrter Herr Professor Vaupel. Ich möchte Ihnen herzlich danken für all Ihre wissenschaftlichen Arbeiten sowie für Ihr Interesse an der Unsrigen.

le Professeur Jean-Christophe Leroux qui, en tant que spécialiste des questions de pharmacie galénique, m'a fait l'extrême honneur de juger ce travail.

le docteur Claire Wilhem, dont les travaux au carrefour du magnétisme et de la biologie ont été source non seulement d'admiration mais surtout d'émulation.

General Table of Contents

Foreword.....1

Chapter 1.....7

Chapter 2.....132

Chapter 3.....175

Chapter 4.....209

Summary and conclusions.....235

Résumé.....241

Abbreviations.....245

Detailed Table of Contents

Foreword....1

Chapter 1....7

1 Introduction: understanding the complexity of hyperthermia....10
1.1 Biological and clinical rationale for induced hyperthermia....11
1.1.1 Heat effects and toxicity at the cellular level....11
1.1.1.1 Morphostructural changes induced by heat....13
1.1.1.2 Metabolic effects of heat....22
1.1.1.3 Heat cytotoxicity and thermal dosimetry....25
1.1.1.4 Molecular biology of stress responses: heat shock, hypoxia and connections....34
1.1.2 Hyperthermia in oncology....39
1.1.2.1 Hyperthermia treatment modalities....39
1.1.2.2 Hyperthermia and solid tumor pathophysiology....41
1.1.2.3 Hyperthermic therapy combinations, emphasis on embolization procedures....48
1.1.2.4 Hyperthermia and immunological considerations....50
1.2 Current technical status of induced hyperthermia....52
1.2.1 Physical modalities for induced hyperthermia....52
1.2.2 Inductive modalities....54
1.2.3 Magnetic losses....55
1.2.3.1 Hysteresis losses....55
1.2.3.2 Losses by magnetic relaxations....56
2 Formulations for local hyperthermia treatment of hard tissue tumors....58
2.1 Magnetic ceramic, glass and glass-ceramic materials....63
2.2 Glass/ceramic particles and microspheres....70
2.3 Magnetic materials for cementoplasty....75
3 Formulations and minimally invasive procedures for magnetically mediated local hyperthermia treatment of soft tissue tumors....77
3.1 Arterial injections and arterial embolization hyperthermia (AEH)....77
3.1.1 Microparticles....80
3.1.2 Formulation forming-depot....81
3.2 Direct intratumoral injection (DIH: direct injection hyperthermia)....83
3.2.1 Formulation forming depot....83
3.2.2 Formulations forming implants in situ....84
4 Magnetic liposomes and local hyperthermia treatment of tumors....91
4.1 General characteristics of liposomes....91
4.2 Magnetoliposomes and magnetically induced local hyperthermia of tumors....93
4.3 Immunoconjugated magnetoliposomes for the systemic approach of magnetically mediated hyperthermia in solid tumors....101
4.3.1 Magnetoliposomes conjugated with anti-CA9 (human MN) antigen antibodies....101
4.3.2 Magnetoliposomes coupled with anti-HER2 antibodies....102
4.3.2.1 Anti-HER2 immunoconjugated magnetoliposomes and pharmaceutical

considerations associated with anti-HER2 antibodies....102
4.3.2.2 Anti-HER2 immunoconjugated magnetoliposomes and micropharmacology considerations associated with non-magnetic anti-HER2 immunoliposomes....103
4.4 Cationic magnetoliposomes in bone metastasis in a prostate cancer model....106
4.5 Neutral magnetoliposomes: targeting draining lymphatic nodes for magnetic hyperthermia 107
5 Conclusion....108
6 Acknowledgements....109
7 References....109

Chapter 2....132

1 Introduction....134
2 Materials and methods....137
2.1 Materials....137
2.2 Methods....137
2.2.1 Magnetic microparticle synthesis and characterization....137
2.2.2 Hydrogel formulations....139
2.2.2.1 Thermosensitive formulations....139
2.2.2.2 Alginate formulations....140
2.2.2.2.1 Internal gelation: preparation and mixing 140
2.2.2.2.2 External gelation: preparation, mixing and injection....141
2.2.3 Organogel formulations....141
2.2.3.1 Preparation of single-solvent formulations....141
2.2.3.2 Preparation of cosolvent formulations....141
2.3 Viscosimetry....142
2.4 In vitro injections....142
2.5 In vivo testing of the tumor model....142
2.6 Histology....144
3 Results and discussion....144
3.1 Hydrogel formulations 144
3.1.1 Thermosensitive formulations....146
3.1.2 Alginate formulations based on internal gelification....146
3.1.3 Alginate formulations based on external gelation....147
3.2 Organogel formulations....150
3.2.1 Single-solvent organogel formulations....150
3.2.2 Cosolvent organogel formulations....156
3.3 In vivo experiments....160
3.3.1 Intratumoral injection of hydrogels....162
3.3.2 Intratumoral injection of organogels....163
4 Conclusion and perspectives....169
5 Acknowledgements....170
6 References....170

Chapter 3....175

1 Introduction....177
2 Experimental details....179

2.1 Magnetic microparticles....179
2.2 Characterization methods....180
2.2.1 Pycnometry and size analysis by laser diffraction....180
2.2.2 X-ray diffraction: XRD....180
2.2.3 Transmission electronic microscopy: TEM....181
2.2.4 Scanning electron microscopy and energy-dispersive X-ray spectroscopy: SEM-EDX 181
2.3 Formulation preparation and in vitro implant formation....181
2.3.1 Liquid formulation preparations....181
2.3.1.1 Polymer solution preparations for the organogel formulation. 181
2.3.1.2 Polymer solution preparations for the hydrogel formulation....182
2.3.1.3 Magnetic microparticle incorporation....182
2.3.2 In situ formation of implants....182
2.4 Superconducting quantum interference device: SQUID....183
2.5 Heating capacities under an alternative magnetic field....183
2.5.1 Alternative magnetic field (AMF) generation and thermometry....183
2.5.2 Method A of SLP determination....185
2.5.3 Method B of SLP determination....186
3 Results and Discussion....188
3.1 Structural properties of the –SPION-silica composite microparticles....188
3.1.1 Size distribution analysis by laser diffraction....188
3.1.2 Particle analysis by TEM 189
3.1.3 Particle analysis by SEM-EDX 190
3.1.4 Crystalline structure by XRD 192
3.1.5 Magnetic properties by SQUID....194
3.2 Magnetic properties of implants (SQUID)....197
3.3 Heating capacities of implants under AMF 200
4 Conclusions....204
5 Acknowledgements....204
6 References....205

Chapter 4....209

1 Introduction....211
2 Materials and Methods....212
2.1 Magnetics beads....212
2.2 Injectable formulation....213
2.3 Alternating magnetic field generator....213
2.4 Tumor model....214
2.5 Mice....214
2.6 Implantation....215
2.7 Thermometry....215
2.8 In vivo investigation protocols....215
2.9 Histology....216
2.10 Imaging....217
2.11 Statistics....217
3 Results....218
3.1 Precipitation of the injectable formulation fills the initially necrotic core and peripheral

extensions of the tumor....218
3.2 The implant formed in situ can heat the tumor by magnetic induction at 141 kHz across the whole temperature range of moderate hyperthermia as a function of field strength....219
3.3 Above a threshold temperature, a larger delivered heat dose increases the extent of induced necro-apoptosis to whole tumor 221
3.4 Magnetically-induced heat delivery through an implant is highly efficient in treating solid tumor for a magnetic field strength of 12 mT....223
3.5 Computerized Tomography allows for precise implant imaging....224
4 Discussion....227
5 Acknowledgements....230
6 References....230

Summary and conclusions....235

Résumé....241

Abbreviations....245

Foreword

Hyperthermia is defined as a more or less localized temperature elevation in tissues, organs and the body. The therapeutic use of hyperthermia, namely *induced hyperthemia*, is mainly indicated as a adjuvant treatment in oncology. We do not consider here other applications of hyperthermia, which include treatment of tissue wounds, the surgical treatment of benign dysplasia or drug delivery. Induced hyperthermia involves temperature elevations of varying amplitude in the target area to be treated through various physical means. Hyperthermic modalities differ one from another according to the target volume, the heating amplitude and the physical means used. The general hyperthermic modality applied to the body, *whole body hyperthermia*, which is obviously limited to temperatures up to 42 °C for physiological considerations, will only be evoked to highlight the important biological aspects it shares with more-localized heating modalities, on which we will focus hereafter. Regional modalities consist in raising the temperature of a part of the body that includes both healthy tissues and the targeted lesion. Heating can be limited, for instance, to a limb or an organ, such as the liver. Regarding biological limits, the target temperatures can then reach a maximum in the vicinity of 42 – 45 °C, depending on the sensitivity of the targeted tissues. However, regarding achievable temperatures in clinical situations, it shall be noted that only temperatures up to 41 – 42 °C can be routinely reached with available devices. This temperature range denotes the upper limit for *mild hyperthermia*, for which temperatures remain below 41 – 42°C, whereas *moderate hyperthermia* describes treatments with temperatures above 42°C. Among the various physical modalities of *regional hyperthermia*, those based on external radio-frequencies, microwaves, ultrasound and lasers, are the most advanced. Techniques based on electromagnetic radiation and ultrasound can be used in interfering or minimally invasive devices to confine heating locally around the lesion, with the underlying goal of heating only the lesion itself and thus sparing the healthy tissue. This confinement to the lesion defines *local hyperthermia*.

A recent magnetically induced modality has been developed for local hyperthermia based on the interaction of magnetic biomaterials with an external alternative magnetic field. Because most components of the body do not have the required magnetic properties, this modality only heats the tissue volume that contains specific magnetic biomaterials capable of generating heat upon exposure to

an external electromagnetic or alternating magnetic field. An alternating magnetic field has the advantage of being able to reach deep-seated areas within the body with few adverse effects regarding other exposed parts of the body over electromagnetic fields, which lead more frequently to adverse side effects. We will focus here on modalities based on the use of an alternating magnetic field, discussing only the aspects of other physical modalities that are common with the magnetic modalities. Bulk and large particles of ferro- and ferrimagnetic materials were the first magnetic materials developed for use in *magnetically mediated hyperthermia*. Fine particles of these materials that were previously used in certain surgical approaches to minimize invasiveness showed promise for applications in a variety of other approaches. At the extreme level of size reduction, the magnetic behavior of extremely fine particles, i.e., nanoparticles, of ferro- or ferrimagnetic mineral phases generally switch from ferro- or ferrimagnetic behavior to superparamagnetic behavior. The iron oxide phases magnetite and maghemite are already approved as MRI contrast agents in the form of coated nanoparticles that show superparamagnetism and are generally known as Superparamagnetic Iron Oxide Nanoparticles (SPIONs). At present, they are also highly represented in the most advanced investigations concerning magnetically mediated hyperthermia modalities. It should be mentioned that the use of coated SPION suspensions, first for MRI contrasting and second for hyperthermia, namely *magnetic fluid hyperthermia*, which is the most advanced and model technique as far as magnetically mediated modalities of induced hyperthermia are concerned, are not treated here in spite of the interesting pharmaceutical challenges in improving the formulation of these suspensions. A number of excellent reviews address this subject [1-5].

In addition, more sophisticated magnetic phases have been recently developed at an experimental level that hold promising potential for further investigations. The general limit in properly delivering the heat to the lesion turns out to be crucial for magnetically mediated hyperthermia, similar to the issue of margins regarding tumor surgical resection. This limitation is due to three reasons: i) the physical efficiency in heating, ii) the biological and pathophysiological characteristics of the treated area, and iii) the interactions of a given magnetic biomaterial with the specific biological and pathophysiological environment. Tailoring these magnetic biomaterials and making the most-advanced ones more efficient for use in magnetically mediated hyperthermia therapy depends on the improvement and adaptation of their pharmaceutical formulation.

All of these important aspects are discussed in chapter 1, which is mainly based on ref. [6] (see also [7]), before coming to a critical review of pharmaceutical formulation possibilities, including a critical presentation of the original modality that our group has developed. This modality relies on injectable formulations that precipitate *in situ* as a vehicle for magnetic microparticles, thus allowing the treatment of solid tumors through local magnetically mediated hyperthermia. The magnetic microparticles can be schematically depicted as a relatively spherical porous silica matrix, of about 10 micrometers in diameter, that embeds iron oxide nanoparticles. Such particles have two main benefits for our purpose. First, the size of the embedded iron oxide particles is controlled by the porosity of the silica matrix. The embedded iron oxide nanoparticles are thus small enough to show superparamagnetic characteristics (i.e., they are SPIONs) and so are capable of efficiently converting the energy of an alternating magnetic field into heat. Secondly, the final microparticles remain discrete and dense physical entities, large enough to favor the syringeability of the injectable formulation forming implants while avoiding the unfavorable rheological characteristics generally associating with suspensions of fine particles. To generate the alternating magnetic field for heating the microparticles, we used a calibrated setup consisting of a generator coupled with a coil inductor, which was large enough to fit the investigated samples as well as the injected animal to be treated inside the coil. The frequency was fixed at 141 kHz, a value calculated to be optimal according to the size distribution of SPIONs.

Chapter 2, which is based on ref. [8], gathers the variety of pharmaceutical options we have investigated to obtain injectable formulations of superparamagnetic microparticles that can solidify *in situ*. The two main categories of formulation that we studied as vehicles for the silica microparticles with embedded SPIONs are hydrogel- and organogel-based formulations. To develop a practical understanding of the formulation issue, we attempted to identify the critical formulation parameters and to establish a parallel between *in vitro* investigations, which highlight the important physicochemical characteristics, and *in vivo* investigations, which focus on syringeability and the implant microstructure and distribution within the various tumor models incorporated.

Among the hydrogel formulations, we first investigated the thermoreversible formulations based on chitosan or poloxamer that are liquid at room temperature but become a gel at body temperature. We

also investigated alginate formulations based on aqueous alginate dispersions, whose gelation relies on ionic cross-linking by calcium cations. We tested two approaches known as external and internal gelation. External gelation consists of bringing a calcium cation solution in contact with an alginate dispersion, which causes gelation to occur rapidly and thus necessitates a special injection device. Internal gelation is intended to sufficiently delay the release of free calcium cations to give time after mixing to implement a regular injection. This formulation makes use of poorly soluble calcium salts that will slowly dissolve. We tested various calcium salts and studied the influence of particles size for carbonate and phosphate salts of calcium.

Regarding organogel-based formulations, the mechanism of gelation relies on precipitation by solvent exchange. Solutions of water-insoluble polymers in appropriate organic solvents provide a fluid formulation in which the magnetic microparticles are incorporated. Once the formulation is injected in the tissue, the tissue water diffuses into the injected mass, and the organic solvent diffuses into the surrounding tissues and blood circulation, which causes the precipitation of the polymer that entangles and entraps the magnetic microparticles and forms the solid implant *in situ*. We have investigated a broad variety of polymers in combinations with single organic solvents, preferring solvents of clinical relevance with suitable dielectric constants, solubility parameters and, most importantly, with a partial or even total water miscibility. Water miscibility will allow a proper bulk precipitation and avoid polymer micellar dispersion, although this has the disadvantage of hygroscopicity regarding the formulation process and storage. In the search of innocuousness - although local toxicity in the tumor may be desirable in our case - we also developed co-solvent organogel formulations. These last formulations consist in incorporating as much as possible a more hydrophilic solvent in partial replacement of the more toxic organic solvent constituting a single solvent organogel formulation, while preserving its essential characteristics.

In chapter 3, which is based on ref. [9], we focused on the physical, and in particular the magnetic, characterization of implants formed under *in vitro* conditions mimicking the already thoroughly studied *in vivo* conditions. We evaluated the possible degradation of the magnetic characteristics and heating properties related to the embedding of the microparticles into the implant. We selected two formulations, one based on hydrogels, the other based on organogels, while varying the microparticle

concentration.

Chapter 4, which is based on ref. [10], presents the results of the *in-vivo* feasibility investigation testing our approach of magnetically induced moderate hyperthermia by injectable formulations. We used the formulation that appeared to be the most suitable. This *in situ* forming implant formulation was injected by direct percutaneous puncture in a human colocarcinoma solid tumor subcutaneously engrafted in Swiss nude mice. The following day, we induced local hyperthermia by heating the implanted tumor by exposing the animal to the alternating magnetic field in a single session of 20 min. The first part of the study was devoted to the investigation of *in vivo* heating capacities with thermometry; the most suitable amplitude of the alternating magnetic field was at the fixed frequency of 141 kHz, with an increasing magnetic field strength of 9, 10, 10.5, 11 and 12 mT. In the second part of the study, we further tested this approach for its therapeutic potential through survival studies.

References

[1] Thiesen B, Jordan A. Clinical applications of magnetic nanoparticles for hyperthermia. Int J Hyperthermia. 2008 Sep;24(6):467-474.

[2] Latorre M, Rinaldi C. Applications of magnetic nanoparticles in medicine: magnetic fluid hyperthermia. P R Health Sci J. 2009 Sep;28(3):227-238.

[3] Jordan A, Maier-Hauff K, Wust P, Johannsen M. Nanoparticles for Thermotherapy. In: Kumar CSSR, editor. Nanomaterials for Cancer Therapy. Weinheim: Wiley-VCH; 2006.

[4] Pankhurst QA, Thanh NKT, Jones SK, Dobson J. Progress in applications of magnetic nanoparticles in biomedicine. J Phys D Appl Phys. 2009;42(22):224001.

[5] Jordan A, Wust P, Fähling H, John W, Hinz A, Felix R. Inductive heating of ferrimagnetic particles and magnetic fluids: physical evaluation of their potential for hyperthermia. Int J Hyperthermia. 1993 Feb;9(1):51-68.

[6] Le Renard P-E, Buchegger F, Petri-Fink A, Hofmann H, Doelker E, Jordan O. Formulation for local magnetically mediated hyperthermia treatment of solid tumors. Submitted to Nova Publishers;

[7] Le Renard P-E. Formulations pour le traitement local de tumeurs solides par hyperthermie à médiation magnétique. Thèse N°3505, Faculté de Pharmacie de Nancy; 2011.[1]

[8] Le Renard P-E, Jordan O, Faes A, Petri-Fink A, Hofmann H, Rüfenacht D, Bosman F, Buchegger F, Doelker E. The in vivo performance of magnetic particle-loaded injectable, in situ

1 Access to the document Thèse N°3505:
http://www.scd.uhp-nancy.fr/docnum/SCDPHA_T_2011_LE%20RENARD_POL-EDERN.pdf
http://tel.archivesouvertes.fr
http://thesepelr.wordpress.com

gelling, carriers for the delivery of local hyperthermia. Biomaterials. 2010 Feb;31(4):691-705.

[9] Le Renard P-E, Lortz R, Senatore C, Rapin J-P, Buchegger F, Petri-Fink A, Hofmann H, Doelker E, Jordan O. Magnetic and in vitro heating properties of implants formed in situ from injectable formulations and containing superparamagnetic iron oxide nanoparticles (SPIONs) embedded in silica microparticles for magnetically induced local hyperthermia. Journal of Magnetism and Magnetic Materials. 2011 Apr;323(8):1054-1063.

[10] Le Renard P-E, Buchegger F, Petri-Fink A, Bosman F, Rüfenacht D, Hofmann H, Doelker E, Jordan O. Local moderate magnetically induced hyperthermia using an implant formed in situ in a mouse tumor model. Int J Hyperthermia. 2009 May;25(3):229-239.

Chapter 1

Formulation for local magnetically mediated hyperthermia treatment of solid tumors

Submitted as a book chapter to Nova Publishers

Pol-Edern Le Renard[1], Franz Buchegger[2], Alke Petri-Fink[3], Heinrich Hofmann[4], Eric Doelker[1], Olivier Jordan[1].

[1]School of Pharmaceutical Sciences, University of Geneva, University of Lausanne, Geneva, Switzerland; [2]Service of Nuclear Medicine, University Hospital of Lausanne, Lausanne, University Hospital of Geneva, Geneva, Switzerland; [3]Department of Chemistry, University of Fribourg, Fribourg, Switzerland; [4]Laboratory for Powder Technology, École Polytechnique Fédérale de Lausanne (EPFL), Lausanne, Switzerland.

Abstract

In this chapter we review both preformulation and formulation efforts relevant to the magnetically induced hyperthermia as a new and attractive modality for the treatment of cancer lesions eligible for a thermotherapy, or for *de novo* indications in specific clinical situations. Following a pharmaceutical approach, we first introduce the general biological rationale for the use of hyperthermia, considering the technical strategies known possibilities to generate hyperthermia and then we detail several different magnetically induced heating modalities. We then review the literature on formulations in an attempt to compare their specificities, advantages and shortcomings. First, we consider formulation of glass ceramics and cement biomaterials for magnetically-mediated hyperthermia in the treatment of bone solid tumors, with respect to the biological specificities. Secondly, formulations intended for magnetically mediated hyperthermia are considered for soft tissue solid tumors, emphasizing the potential for pharmacological modulation. In the last part, we consider magnetic liposome formulations that can be equally administrated in various types of tumors. We do not detail magnetic fluid hyperthermia based on suspension of magnetic nanoparticles stabilized by various coating for biological applications. The importance of biological and immunological considerations that are associated with these formulations is outlined. Importantly, this chapter focuses on the importance of the formulation and on the highly complex interactions of formulation with hyperthermia that should be considered in various medical applications.

Chapter 1: Table of Contents

Chapter 1....7
1 Introduction: understanding the complexity of hyperthermia....10
1.1 Biological and clinical rationale for induced hyperthermia....11
1.1.1 Heat effects and toxicity at the cellular level....11
1.1.1.1 Morphostructural changes induced by heat....13
1.1.1.2 Metabolic effects of heat....22
1.1.1.3 Heat cytotoxicity and thermal dosimetry....25
1.1.1.4 Molecular biology of stress responses: heat shock, hypoxia and connections....34
1.1.2 Hyperthermia in oncology....39
1.1.2.1 Hyperthermia treatment modalities....39
1.1.2.2 Hyperthermia and solid tumor pathophysiology....41
1.1.2.3 Hyperthermic therapy combinations, emphasis on embolization procedures....48
1.1.2.4 Hyperthermia and immunological considerations....50
1.2 Current technical status of induced hyperthermia....52
1.2.1 Physical modalities for induced hyperthermia....52
1.2.2 Inductive modalities....54
1.2.3 Magnetic losses....55
1.2.3.1 Hysteresis losses....55
1.2.3.2 Losses by magnetic relaxations....56
2 Formulations for local hyperthermia treatment of hard tissue tumors....58
2.1 Magnetic ceramic, glass and glass-ceramic materials....63
2.2 Glass/ceramic particles and microspheres....70
2.3 Magnetic materials for cementoplasty....75
3 Formulations and minimally invasive procedures for magnetically mediated local hyperthermia treatment of soft tissue tumors....77
3.1 Arterial injections and arterial embolization hyperthermia (AEH)....77
3.1.1 Microparticles....80
3.1.2 Formulation forming-depot....81
3.2 Direct intratumoral injection (DIH: direct injection hyperthermia)....83
3.2.1 Formulation forming depot....83
3.2.2 Formulations forming implants in situ....84
4 Magnetic liposomes and local hyperthermia treatment of tumors....91
4.1 General characteristics of liposomes....91
4.2 Magnetoliposomes and magnetically induced local hyperthermia of tumors....93
4.3 Immunoconjugated magnetoliposomes for the systemic approach of magnetically mediated hyperthermia in solid tumors....101
4.3.1 Magnetoliposomes conjugated with anti-CA9 (human MN) antigen antibodies....101
4.3.2 Magnetoliposomes coupled with anti-HER2 antibodies....102
4.3.2.1 Anti-HER2 immunoconjugated magnetoliposomes and pharmaceutical considerations associated with anti-HER2 antibodies....102

4.3.2.2 Anti-HER2 immunoconjugated magnetoliposomes and micropharmacology considerations associated with non-magnetic anti-HER2 immunoliposomes.....103
4.4 Cationic magnetoliposomes in bone metastasis in a prostate cancer model.....106
4.5 Neutral magnetoliposomes: targeting draining lymphatic nodes for magnetic hyperthermia 107
5 Conclusion.....108
6 Acknowledgements.....109
7 References.....109

1 Introduction: understanding the complexity of hyperthermia

The purpose of induced hyperthermia in multi-modality oncology is to take therapeutic advantage of the multi-directional biological and toxicogenic effects of heat stresses [1]. This chapter will focus on the formulations and hyperthermia modalities for the local treatment of solid tumors with respect to various neoplasms. Associated treatments or therapeutic modalities will be also discussed. In this introduction, we first delineate the biological and toxicogenic effects of heat stress and stress response modulation that underly biological and clinical rationales of induced hyperthermia treatment. Pharmaceutical formulation possibilities will also be introduced. Subsequently, we present the current status of induced hyperthermia techniques and emphasize the physics of magnetically mediated hyperthermia, which lends itself to broader pharmaceutical formulation possibilities. We will present some technical and physical aspects of magnetic fluid hyperthermia (MFH), the most advanced and magnetically mediated technique. This technique is restricted to magnetic nanoparticle suspensions, which can be considered as pharmaceutical formulations but cannot be thoroughly treated here. Nonetheless, we discuss some formulations, in which similar magnetic nanoparticles or even suspensions can be found and potentially released to disperse in tissues. A number of fundamental and relevant physico-chemical or biopharmaceutical concerns for this MFH therefore intersect with the modality discussed in the following. For a deeper understanding of these aspects, specifically concerning the use of magnetic nanoparticles suspensions in MFH or as MRI contrast agent the reader will be referred to selected reviews. In the second section, we will discuss the formulations intended for local hyperthermia treatment of hard tissue tumors, i.e., magnetic bulk and particulate ceramics, glasses and glass-ceramics and cements. In the third section, we will discuss minimally invasive formulations for local hyperthermia treatment of soft tissue tumors. These include microparticle and *in situ*-forming depots or implant formulations through arterial or intratumoral injection. We dedicate the fourth section to liposomal formulations used to mediate magnetically induced hyperthermia.

1.1 Biological and clinical rationale for induced hyperthermia

The current understanding of the heat-induced biological and toxicogenic effects extent across the cellular, sub-cellular, tissue, and pathophysiological levels. We will discuss the understood molecular biological mechanisms connecting the biological effects of heat to its toxicogenic and therapeutic effects, which are indissociable one from another in cancer treatment. This overview is an important prerequisite to overcoming the contradictory appearances of clinical rationales arising from varied hyperthermia treatment modalities.

1.1.1 Heat effects and toxicity at the cellular level

As for various stresses, morphostructural and biological changes can be noted in mammalian cells exposed to heat. These effects are variable relative to the biological characteristics of the cell and increase gradually with the degree of stress. The effects of heat stress can most directly be analysed through a combination of temperature and duration parameters [2,3]. The morphostructural changes induced by small-scale stress appear limited, transient, reversible or repairable. Such stress is referred to as sub-lethal in that cell functions and development generally appear to be only temporarily affected. In contrast, alterations induced with large-scale heat stress appear prolonged. If possible, when heat stress is not too large, reversion, reparation and regeneration take time. Large heat stress affect often irreversibly cell functions, compromising survival and cell cycle progression. Ultimately, heat exposure can suppress the clonogenic activity of the cell (e.g., cytostatic and cytotoxic effects of heat) and kills cells in a stochastic manner (e.g., cytocidal effect of heat), with heat-induced cell death occurring quite rapidly [4]. As the toxicogenic effects of heat are numerous, cell death can occur in several ways: metabolic, apoptotic, autophagic, necrotic or reproductive. The “direct cell-killing effect” of induced hyperthermia usually refers to cell death during or after the heat stress (cytocidal effect). The method used to asses survival rates after a treatment can be misleading [4]. The vital stain uptake method of determining the number of dead cells allows a characterization that essentially reveal survival rate

following the "direct cell killing" or cytocidal effect of a given heat treatment. The determination of survival rate by clonogenicity measurements, in addition to being very biologically relevant for hyperthermia, reveals both the cytostatic effects of a given heat treatment and some of the direct cytocidal effects [4]. Clonogenic methods can underestimate the direct cell killing effect [5]. For clinical pertinence, both effects on survival should be kept in mind when considering the direct cytotoxicity of a given hyperthermic treatment. Remarkably, survival rates most often do not correlate with the extent of heat-induced morphostructural alterations but they do correlate with the rapidity of their reversion [4]. With the exception of particular stress conditions, in addition to direct stress response, cell population surviving a stress develops a physiological adaptation to this stress, for instance when stress is prolonged. This adaptation is less rapid but more durable than stress-induced morphostructural changes. Furthermore, this physiological adaptation results in an increased potential of morphostructural adaptation and improved capacities to endure and withstand stresses, which ultimately leads to increased survival rates. This physiological state of endurance to stress and resistance to its toxicogenic effects is referred to as tolerance. This type of tolerance applies at cell, tissues, organs, and organismal level, which will be considered later. This also applies at the pathophysiological level. The physiological aspects of tolerance development begin at the cellular level and appear as a common denominator to stresses in general, but more specifically to thermal stress. The physiological adaptation to bear thermal stress is referred to as thermotolerance. Adaptations to withstand other stresses, such as X-ray- or chemotherapy-induced stress, which are often concomitant in modern, multi-modality cancer treatment practices, can similarly be referred to as radiotolerance and chemotolerance, respectively, but are most commonly termed radioresistance and chemoresistance. The development of a tolerance following a given stress results in a period of tolerance to this stress. The amplitude and duration of tolerance depend on the extent of primary stress. Also, development of tolerance following an initial heat stress that allows increased resistance to a subsequent heat stress should be termed heat-induced thermotolerance. Alternatively, crosstalk between adaptive stress responses to some extent allows one stress to induce tolerances for various other stresses. This is likely because all stress responses evolved from a common ancestral pathway. Heat stress can thus transiently induce radiotolerance and chemotolerance to some degree, but it cannot induce multiple drug

resistance, given that the P170 glycoprotein is not induced by heat. Because hyperthermia is an adjuvant therapy, the reciprocal phenomenon, thermotolerance induction through chemotherapy or radiotherapy, is less understood. These tolerance effects are not very problematic when considering heat treatment repetitions or combined therapies to generate additive cytotoxic effects, allowing for latitude in the sequence of administration. Tolerance, however, can dramatically complicate sequence adaptations in therapy combinations aimed at obtaining specific synergistic effects, from which the greatest therapeutic gain can be expected.

1.1.1.1 Morphostructural changes induced by heat

Heat-induced pleomorphisms of cells and cytoplasmic membranes, and the temporary interruption of cyclose, indicate perturbation and rearrangement of the cytoskeleton [6]. The cytoskeleton is a highly dynamic and rapidly adaptable scaffold for eucaryotic cellular organization, functions and division. The complex cytoskeletal network is composed of various filaments: i) microfilaments (actin polymer), which determine the shape of the cell's surface and are necessary for locomotion; ii) microtubules (tubulin polymer) determine membrane-enclosed organelle positions and intracellular transport; and iii) intermediate filaments (polymers specific to metazoans: vimentine, keratins, etc...), which provide mechanical strength and resistance to shear stress [7]. A large number of accessory proteins and free intracellular Ca^{2+} ions are necessary for filament functions. The movement and function of the cell membrane relies on the cytoskeleton, especially the supportive gel-like cortical area. This is often regulated by external signals. Depending on the cell line and the extent of heat shock, rounding (Figure 1.1) or flattening of cell and membrane bleb formation can be observed. Disturbances of the cytoskeleton appear reversible after a great deal of heat stress, provided that the disturbance is not drastic and therefore lethal. In general, microfilaments (actin) are reordered in rounded cells, rounding also being observed in the early phase of apoptosis. Alternatively, microtubules and/or vimentin-intermediate filament dynamics are modified in cells that adopt a flat shape, characteristic of growth arrest [6,8]. Accessory proteins and subsequently cytoskeleton microtubules can disaggregate during heat stress and reaggregate afterwards, resulting in more or less disorganization. Tubulin is disrupted at

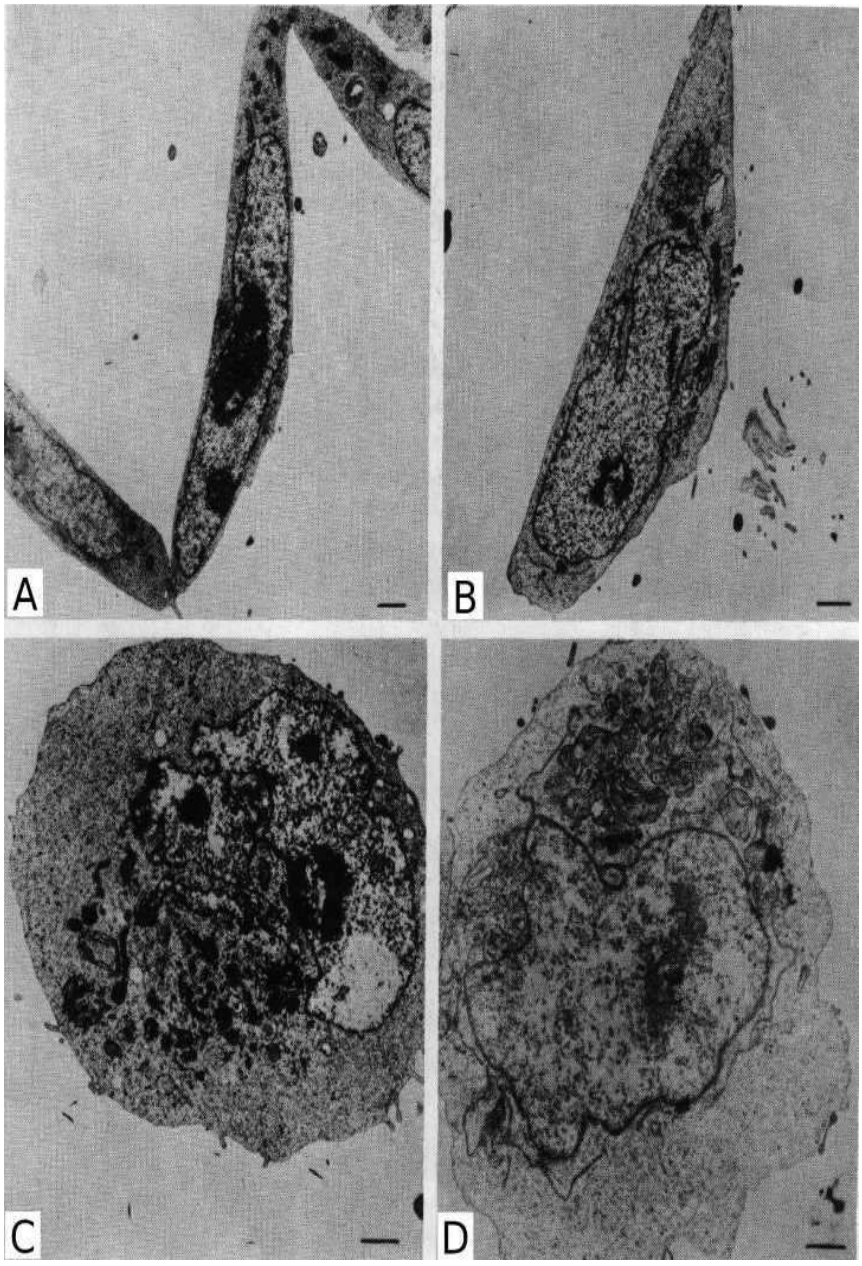

Figure 1.1*: Morphostructural effects of in vitro heat treatment of chinese hamster V79 fibroblasts from ref [2] (bar = 1 μm)*

A: Elongated and flattened morphology of untreated fibroblasts. The authors report that this morphology was not affected after heating at 42°C, even for a prolonged period. **B**: Discrete rounding of cell morphology after1 h at 43°C. **C:** After 3 h at 43°C, clear rounding of cellular morphology, nucleus fragmentations and convolutions, and perturbation of the nuclear matrix are observed. The nucleolus has lost its physiological fibrillar component. **D**: Dramatic morphostructural changes after 1 h at 45°C, cytoplasmic and nuclear matrices appear affected, organelles are concentrated at cell poles, and mitochondriae with lowered matrix densities show dilatations and interruptions at the level of the cristae.

44°C but not at 42°C. Microtubule disturbances account for a portion of the observed pleomorphisms, especially in the giant cells that result from heat treatment of melanoma cells [4]. Heat effects on microtubules are not directly linked with cell survival but can explain the considerable thermosensitivity of cells in the mitosis phase. The transient mitotic spindle is indeed very sensitive to disaggregation of microtubules, leading to tetraploidy and giant cells that cannot complete mitosis. Then, a high rate of mitotic cell death occurs immediately following heat-induced stress or possibly after one further cell cycle (octaploid cells observed). This effect explains the dramatic decrease in survival rates of heat-exposed mitotic cells [4]. Intermediate filaments, which connect microtubules to membranes, appear more sensitive to heat than microtubules themselves [4]. After 3h at 42°C, a flat morphology of rat fibroblasts was associated with the collapse of vimentin-containing intermediate filaments within the perinuclear space, whereas microtubules did not appear to have been affected [8]. Bleb formation, a typical feature of apoptosis, has been correlated with cell survival during heat stress [4,9,10]. More generally, cytoskeletal reorganization cannot be interpreted as a cause but as part of the heat shock response aimed at cell survival [6]. Cytoskeletal alterations and cell survival are indeed not directly correlative, unless irreversible damage is caused by large-scale heat stress. The capacity of cytoskeletal and cellular architecture to rapidly assume normal morphology during recovery at physiological conditions following heat shock is nonetheless correlated with increased cell survival [6,11]. This capacity also appears to be characteristic of thermotolerant cells [6]. In fact, the cytoskeleton can become resistant to heat shock in the absence of protein synthesis. This is indicative of type-I thermotolerance, a particular form of thermotolerance not dependent on protein synthesis. This was shown by the induction of thermotolerance in the presence of arsenate and amino acid analogs that impede protein synthesis [6,12]. This reveals mechanisms of stabilization within cells that can counteract thermal perturbations and that involve preexisting elements. Among the many possible biochemical interactions involved, however, few have been studied. Chaperones are a class of proteins that interact with hydrophobic areas of other proteins to avoid undesirable and deleterious hydrophobic interactions, thereby guiding and stabilizing correct protein folding [13,14]. Hydrophobic areas of proteins are accessible to adverse interactions during synthesis or following protein destabilization, such as is induced by heat stress. Chaperones first interact with hydrophobic areas to prevent harmful

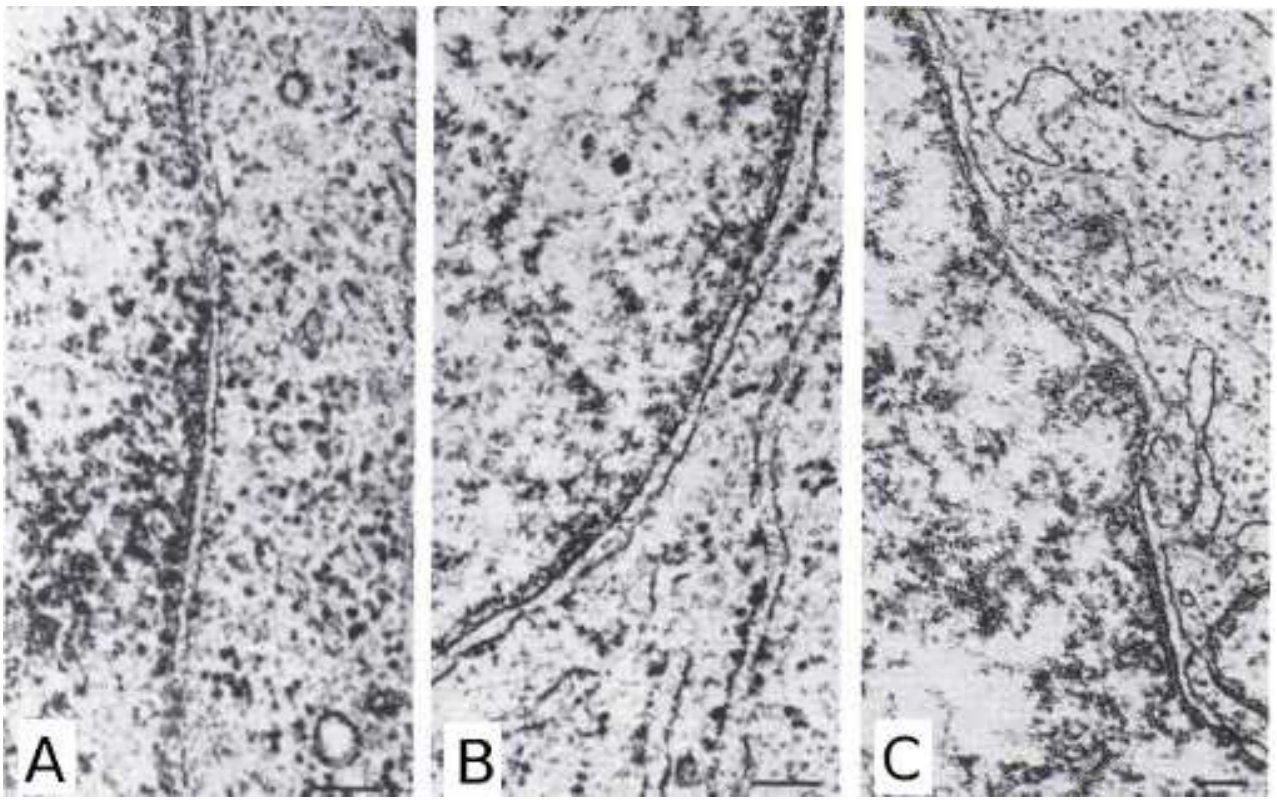

Figure 1.2: Effects of hyperthermia at the level of the nuclear envelope of Chinese hamster V79 fibroblasts *in vitro*, from ref [2](*cf.* Figure 1.1), bar = 0.1 μm.
A: Structure of the nuclear envelope of untreated fibroblasts. **B**: Irregular dilatations of the the nuclear envelope appear following 6 h hyperthermic treatment at 42°C. **C**: the nuclear envelope appears very dilated and external nuclear membrane shows numerous folds following 1 h hyperthermic treatment at 45°C.

hydrophobic interactions, and chaperone machinery subsequently guides protein folding. If proper folding cannot be catalyzed, chaperones remain bound to neutralize hydrophobic areas until the protein is delivered to proteases. Hence, chaperones are always present within the cell and critically participate to the counteraction of heat-induced protein alterations. In view of the striking morphostructural perturbations observed during heat stress, many proteins may seek chaperones. Type-II thermotolerance is particularly dependent on protein synthesis. As one of its most obvious features, intracellular levels of a particular set of proteins are remarkably increased in response to thermal stress and are therefore referred to as heat shock proteins (HSP). The various and complex molecular aspects of *HSPs* will be

discussed in a later section. Inconsistencies in the nomenclature of HSPs can complicate their discussion. Here, we will implement the nomenclature and nomenclature rules of the HUGO Gene Nomenclature committee [15] for human genes or proteins (i.e., genes italicized in all capitals, proteins in all capitals but not italicized). We will remain in accordance with NCBI Entrez Gene database for other species when necessary (i.e., first letter capitalized or uncapitalized, the following letters in lower case, respecting the previous rule of italicization to distinguish genes from proteins) and with respect to recent guidelines for HSPs [16]. Previously used common nomenclature will be referenced in brackets for clarity. Considering that HSP levels can be notably increased in response to a number of non-heat stresses and that other proteins can participate in the thermal stress response, the preferred generic term is "stress proteins", which includes all proteins involved in varied stresses responses. Consistent with their important functions in the stabilization of other proteins, many HSPs are chaperones. HSPD1 (HSP60) and HSPA8 (HSC70; HSC71; HSP71; HSP73) are the two major families of molecular chaperones in eucaryotic cells. Some noticeable morphostructural cytoskeletal changes are reported in type II thermotolerance. These changes are apparently not a cause but a consequence of the colocalization of *de novo* synthesized proteins, namely HSPs [6]. This finding would explain similar observations in cytoskeleton changes following exposure of cells to other stresses that also induce *HSP* expression. These stresses include treatments with amino acid analogues, organic solvents or heavy metals. Other remarkable cytoplasmic heat-induced perturbations affect polyribosomes, also known as polysomes. These consist of a chain of ribosomes translating a given messenger RNA (mRNA) into protein. At 42°C, two classes of polysomes are distinguishable: a somewhat inactive class related to mRNAs that were previously actively translated, and, a very active class in which high levels of "stress-induced" mRNAs are translated [8]. At 43°C, all polysomes are inactive, an effect maintained following the return to normal thermal conditions. Translation machinery relies on numerous factors and a highly sophisticated spatiotemporal orchestration, one in which the cytoskeletal matrix appears to be involved. It should be noted that the structure connecting the cytoskeleton to the nuclear envelope might also be important [4]. A treatment at 43°C triggers irregular dilatation of the nuclear envelope and perturbation of the constitutive membranes, which are no longer well defined. At 45°C, extreme nuclear envelope dilatation and multiple foldings of the external membrane are triggered (Figure 1.2) [2]. With respect to

the nucleus, heat induces marked pleomorphisms, including an increase in size and an alteration or disruption of nuclear functions [4]. An increase in the density of the nuclear matrix, similar to the cytoskeleton matrix with which it is continuous, is observed in direct response to thermal stress (after 3 h at 42°C, see [8]). This can be explained in part by intracellular redistribution of proteins that localize to the nucleus instead of other compartments or organelles [8]. Protein aggregation within the nucleus also partly contributes to increased nuclear density, which is characterized by small granular perichromatin elements [8], implying protein destabilization and the exposure of hydrophobic pockets. Both protein aggregation and increased nuclear density are certainly associated have to be related with the perturbation of nuclear functions. Transient perturbations of the dynamic equilibrium between disaggregation and reaggregation of filaments within the nuclear matrix appear very sensitive to heat stress, but the consequences on survival are not straightforward [4]. Damage of the nuclear matrix that directly impacts cell survival appears only for large-scale heat exposures. This occurs at temperatures beyond nuclear matrix thermolability, corresponding to the calorimetric transition at 48°C [17]. Occasionally, reversible actin fibrous rod-like structures, nuclear actin paracrystals, are induced by heat [3,8,11]. Comparable actin paracrystals are known to form at the expense of actin cytoplasmic stress fibers in the presence of 10 % dimethyl sulfoxide (DMSO), an organic solvent of pharmaceutical use [18-23]. Similarly to what is observed for the cytoskeleton, a remarkable reorganization of the nuclear matrix morphology occurs in thermotolerant cells, but the degree of this reorganization cannot be directly correlated with cell death [8]. The nuclear matrix plays an important role in the regulation of chromatin activities [24]. Cellular phenotypes suggesting growth arrest also reflect down-regulation of replication and transcription. For temperatures of 42 to 45°C, DNA and RNA polymerizations are known to be suddenly inhibited [3,4,8,24-26]. Notably, DNA polymerization is not simply inhibited during heat stress, but it remains decreased for prolonged periods of time relative to the scale of the stress. Perturbations in the dynamic homeostasis of the nucleo-cytoplasmic actin cycle can be also regarded as signaling stressful conditions at the chromatin level [24,27]. Inhibition of DNA polymerization appears less relevant to direct, heat-induced death of the cell than cytoskeletal damage does [4]. Among nuclear protein aggregates, various proteins, such as chaperones belonging to the HSP family, can be basally present or colocalize within the nucleus. This occurs through redistribution from

their basally distinct intracellular localization or following *de novo* synthesis, further increasing nuclear matrix density [24]. Preexisting constitutive HSPs, such as HSPB1 (HSP27, basally cytoplasmic) and HSPH (HSP110, basally in Golgi apparatus) are found to redistribute to nucleus matrix during heat shock, even in the absence of *de novo* protein synthesis (e.g., following chemical inhibition). Without detailing HSP classification, it will be here explained how one HSP category, the "prompt" HSPs, are closely associated with the nuclear matrix. As HSPs, prompt HSPs are by definition heat-inducible, but their expression level is remarkably increased during, not after, the heat exposure, whereas for other heat-inducible HSPs induction is generally subsequent [28]. The biological function of prompt HSPs remains to be determined. Nonetheless, some details of their activity are known. Their translation from pre-existing mRNA is maintained during heat exposure. These HSPs, such as lamin B, associate with nuclear intermediate filaments [29]. Other heat-inducible HSPs, not originating from pre-existing mRNA, which can be translated during heat shock, require a further synthesis step, and their levels only increase following heat shock, or possibly only during long exposures to moderate heat stress. This is the case for HSPA2 (HSP 72), which is encoded by the purely thermo-inducible *HSP* gene. This protein is associated with nuclear matrix at high levels following heat shock [3,8,30-34]. The relationship of nuclear changes with the development of thermotolerance appears to rely particularly on HSPs as a type II thermotolerance. More locally within the nucleus, the nucleolus is the most sensitive to limited temperature augmentation [4]. Heat-induced swelling and unraveling of nucleolus reveals important perturbations [8]. Nucleus-associating HSPs are especially concentrated in the nucleolus [8,34]. It is not yet understood how the nucleolus is held together and organized, but it is known to be involved in the production of RNA-protein complexes, primarily ribosomes. RNA must be intensively polymerized at the level of the nucleolus for the active transcription of ribosomal RNA (rRNA, implicating RNA-polymerase I) that assembly with numerous small proteins imported from the cytoplasm to produce ribosome subunits, which are in turn exported to the cytoplasm. Also, the high sensitivity of nucleolus to heat stress corroborates the similar sensitivity of DNA-dependent RNA polymerization [3,25]. The morphostructures of the endoplasmic reticulum (which is continuous with the nuclear envelope) and the Golgi apparatus appear relatively thermosensitive [3,4,8]. After 3 h at 42°C, the Golgi apparatus almost disappears. This is likely due to its dissociation in small vesicles [8]. This effect is potentially related to

the nuclear translocation (especially to the nucleolus) of HSPH (HSP110), which is basally associated with the Golgi apparatus. Protein glycosylation appears nonetheless to rapidly recover following heat-stress [4,8]. Mitochondria exhibit dilated and vesicular cristae after 1 h at 42°C [3,8]. After 3 h at 42°C [8] or 1 h at 43°C [2], swollen mitochondria clearly display increased intracristal space. This effect is similarly observed following chemical oxidative uncoupling [35] or electron transport inhibition, which further interferes with glycolysis [8]. Mitochondria then localize to the perinuclear space, seemingly as the intermediate filament collapse [8]. After 1 h at 45°C, mitochondria appear aggregated in the perinuclear space, the cristae are irregular and the matrix density is decreased [3]. In view of their pivotal role in cell death, mitochondria should be considered potent modulators of heat-induced toxicogenic effects. Heat also induces an augmentation of the number of lysosomes along with triggering their destabilization [4]. This was suggested as an important phenomenon related to heat-induced cell death [36]. With respect to the plasma bilipidic layer, small interruptions observed after 1 h at 42°C are reversible but transiently alter barrier function, which is noteworthy in the context of small molecules delivery (Figure 1.3) [3]. These interruptions increase proportionally with duration and temperature and are clearly evident but still reversible after 3 h at 43°C, allowing permeability to nanoparticles [3]. At 45°C, the loss of large segments is finally lethal [3]. The cell membrane as a biochemical entity is considered one of the most important cellular sites for the development of heat-induced toxicogenic and cytotoxic effects [37]. Scanning electron microscopy studies have revealed that heat can induce the removal of inter-membrane protein particles, which are composed of trans-membrane proteins that stabilize the membrane and perform important enzymatic reactions for cellular homeostasis [4]. Modulation of heat-induced cell death via membrane perturbation is further supported by the observed synergism in increasing cell lethality with heat, and agents that contribute to cytoplasmic and, potentially, intracellular membrane destabilization. These agents belong to the following categories: i) the thermosensitizers e.g., membrane-active drugs such as anesthetics (lidocaine or procaine) or phenothiazine that chiefly interact with the plasma membrane, and organic solvents (in particular ethanol); or ii) various liposomes (unilamellar and multilamellar, see later section) [3,4]. This raises critical concerns for the pharmaceutical formulations discussed herein that contain organic solvents or liposomes.

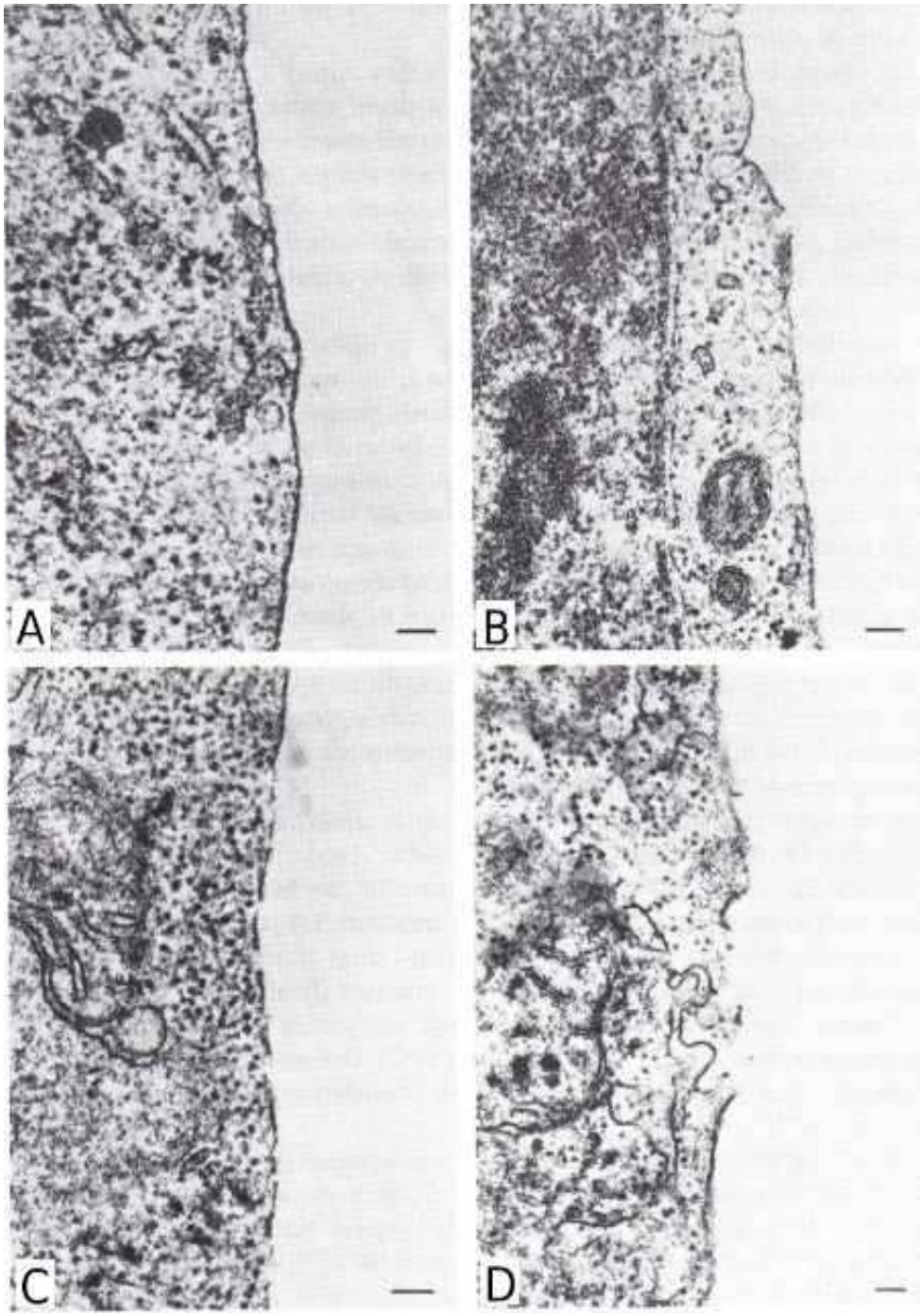

Figure 1.3: Alterations of the plasmalemma of Chinese hamster V79 fibroblasts *in vitro,* from ref [2] (*cf.* Figures 1.1 and 1.2), bar = 0.1 μm.
A: Details of the cytoplasmic membrane of an untreated fibroblast. **B:** Following hyperthermia for 1 h at 42°C, small discontinuities in the structure of the plasmalemma appear. **C:** Following hyperthermia for 3 h at 43°C, numerous interruptions of the plasma membrane are observed. **D:** After 1 h at 45°C, the plasma membrane is disrupted.

1.1.1.2 Metabolic effects of heat

Glucose catabolism is central to general cellular metabolism and is closely linked to the metabolism of lipids and a number of amino acids. Provided that enzymatic inhibition or denaturation does not occur, the energy reservoirs of heated cells (firstly ATP) are utilized and depleted to i) comply with the thermodynamic increases in metabolic reaction rates and ii) to limit the perturbations of morphostructural characteristics and ionic gradients [4]. The augmentation of K^+ efflux during heat exposure and of intracellular Ca^{2+} following heat exposure are reflective of membrane alterations but cannot be strongly correlated with cell death. Heated cells exhibit decreased ATP levels but enhanced synthesis and turnover [4]. Following severe heat damage, the high ATP content would be related to Na^+/K^+ ATPase inhibition in the context of heat shock response, but is not a primary factor in the death of the cell [38]. ATP depletion would affect ATPase enzymes, such as membrane transporters, in conjunction with membrane destabilization. Respiration at the cellular level is impaired as consumption of oxygen is dramatically reduced during heat exposure, at least for neoplastic cells [3]. Oxidative phosphorylation in the mitochondria membrane is directly dependent on oxygen, as this is the only site where molecular oxygen is consumed. Alternatively, other biochemical pathways only indirectly depend on oxygen status [4]. The inhibition of oxygen consumption thus reflects the inhibition of oxidative phosphorylation. The oxidative phosphorylation is the predominant pathway for ATP generation and NAD^+, whose the stock is particularly limited in human [39], and FAD regeneration by the oxidation of the $NADH+H^+$ or $FADH_2$, respectively. The citrate cycle taking place in mitochondrial cytosol also appears to be inhibited by heat exposure [4,40]. This impairs the capacity of mitochondria to utilize fatty acyl or acetyl CoA, a process which NAD^+ and FAD take part. Also impaired is the further generation of GTP, $NADH+H^+$ and $FADH_2$. As the first stage in glucose catabolism, the glycolysis pathway generates two pyruvate molecules. The glycolysis requires 2 NAD^+ molecules and generates 2 $NADH+H^+$ and 2 ATP, among the 30 obtained from the complete biochemical catabolism of one glucose molecule in normal and euoxic conditions [41]. Glycolysis is extremely dependent on the extra- and intracellular milieu [42,43] and is indirectly indissociable from the supply in nutrients, pH and oxygen status. Note that the capacity of oxidative phosphorylation to regenerate NADH or $FADH_2$,

relying on the capacity of citrate cycle to further metabolize pyruvate, is extremely dependent on the oxygen status. Each of these parameters in turn influences the biochemical regulation of the glycolysis, primarily through the rate of lactate accumulation [3,4,42,43]. In basal physiological conditions that allow for constant NAD^+ regeneration (i.e. euoxia and normal respiration), the NAD^+-dependent pyruvate dehydrogenase complex allows decarboxylation of pyruvate into acetyl CoA. This molecule then enters the citrate cycle at the level of mitochondria matrix [41]. When oxidative regeneration of NAD^+ is not possible, as is the case in anaerobic conditions or during heat exposure, the NAD^+ necessary for glycolysis is regenerated through the transformation of pyruvate to lactate. In the physiological context of anaerobia, accumulating lactate is exported into the extracellular compartment through a specific transporter to be drained to the liver [39]. The acidification of the milieu as a result of lactate efflux can inhibit glycolysis [3]. Alternatively, an increase in intracellular lactate, more precisely the lactate/pyruvate ratio, as well as β-hydroxybutyrate, can lead directly to a pH_i decrease that can also inhibit glycolysis [4]. The functional integrity of glycolytic enzymes appears unaffected by temperatures as high as 44°C for many biological systems [3]. Numerous, apparently contradictory reports of glycolysis inhibition can be explained in term of pH decreases mediated by milieu acidification, especially *in vitro* when the culture conditions are not adapted. These differing results can also be explained by direct or indirect intracellular acidification, which can be a consequence of acute extracellular pH decrease. Following heat exposure of normal cells, tumor cells or tumors, for which energy metabolism is almost exclusively based on glycolysis, the lactate/pyruvate ratio and, to a lesser extent, the β-hydroxybutyrate level can vary. Specifically, these values are constant for normal cell and decreased in tumor cells *in vitro* but remarkably increased in tumors [3,4,44-49]. This raises the importance of physiopathological characteristics, discussed later when considering solid tumors. The nutrient status thus appears to be of importance, and it can be concluded that glycolysis is not inhibited during heat exposure to temperatures as high as 45°C provided that glucose is available [4]. Finally, certain biochemical manipulations, for instance glycolysis oxidative phosphorylation inhibition, have revealed the potential to sensitize cells to heat [50-53]. Following exposure to heat or ethanol, the levels of intracellular thiol, particularly glutathione, decrease. This finding is important in the context of the heat shock response, intracellular acidification, toxicity of the reactive oxygen species and

thermotolerance [4,54,55]. Hyperthermia can indeed increase the steady-state concentration of reactive oxygen species (ROS) generated through oxidases (e.g., O_2^-, H_2O_2 and the more active hydroxyl radical OH^-) [3]. The accumulation of these species promotes cellular oxidation events at the protein, DNA and membrane lipids levels and represents a further important major mechanism of heat stress-induced cell injury [56]. ROS-dependent direct cytocidal and even anti-tumor effects of heat can be specifically inhibited by the addition of superoxide dismutases (SOD), catalases or DMSO, known as a ROS scavenger [57]. In parallel, a rise in Cu, Zn-SOD (SOD1) activity was shown to be associated with the development of thermotolerance following heating [58]. Reciprocally, decreased antioxidant activity is associated with increased sensitivity to heat [59]. Among the oxidases involved in purine degradation, xanthine oxidase (XO), which has O_2 for a substrate and is associated with the generation of the superoxide anion, has been shown to play a central role in heat-induced ROS production [60-62]. Xanthine dehydrogenase (XDH) is a closely related isoform of XO but catabolizes hypoxanthine to xanthine with NAD^+ as a cosubstrate. This function does not lead to superoxide generation [63]. Notably, XDH levels are already increased in tumors. Heat-induced modulations of XDH and XO activity induction seem to rely on increased cytosolic Ca^{2+}, likely due to respiration limitation in the context of ATP production [3]. This increase in cytosolic Ca^{2+} is capable of activating proteases that can convert XDH to XO [64]. One additional reason for the induction of XO activity may be linked to ischemia/reperfusion. Iron release from ferritin appears important in hyperthermic toxicity, at least in the liver [65]. A significant role for amino oxidases has been also emphasized [3]. Finally, nucleotide and amino acid incorporation is decreased during and following hyperthermia for a relatively long period, and this is especially prolonged for DNA replication and transcription [3,4]. This confirms the repression of nucleic acid and protein synthesis observed at the ultra-structural level. Some specific metabolic inhibitors of DNA and protein synthesis decrease the thermal sensitivity of HeLa cells. In contrast, agents interfering with RNA synthesis act as enhancers of hyperthermia [3,66]. This underlines the particular role of RNA synthesis in heat-induced cell damage. To our knowledge, extracellular matrix and its importance in cellular growth (as a support for cells and a reservoir of growth factors) has not been specifically studied under hyperthermic conditions.

1.1.1.3 Heat cytotoxicity and thermal dosimetry

A large part of what is known about heat cytotoxicity is from studies with cultured cells. These protocols allow finely tuned and homogeneous temperature control, conditions that are difficult to match in clinic. These fundamental *in vitro* studies are imperative to our understanding of direct cytocydal effects of heat but correspond to ideal conditions and preclude the evaluation of indirect heat effects. The following points should be emphasized with respect to physiological or pathological contexts: i) the parameters of heat shock are not finely controlled, and ii) when studying the toxicogenic effects of heat at the tissue, organ or even whole-body level, indirect biological effects contribute with direct cytotoxic effects to antitumoral effect. For example, the indirect biological effects such as physiological feedback loops or immune responses can drive the antitumoral effect of heat. Intrinsically, the direct cytocidal effect of heat can be observed in the temperature range of 42 - 47°C. Cell types can reveal variations in their sensitivity to heat over an order of magnitude [37], but no variations can specifically distinguish a malignant status [5]. Cytocide induced by a single heat exposure depends simultaneously on the temperature and time parameters, i.e., on the "thermal dose". Any biological or pharmacologically measurable effect can be represented through dose-effect curves, linking the effect to variation of one condition, the others being constant. Thermobiological *in vitro* studies, modeled after and occasionally used in combination with *in vitro* radiobiology studies, use cell survival curves to this end [67]. These models consist of a semilogarithmic plot of the survival fraction of treated cell populations following heat exposure. One of the two main parameters of heating, most often temperature, is fixed as a function of the second, e.g., the exposure time (note the interchangeability of these two parameters) [4,68]. The definition of the end point of survival should be carefully considered to understand the biological significance these studies. For proliferating cells such as malignant cells, the clonogenicity test can determine the loss of the capacity for sustained proliferation of a cell population *in vitro* or *ex vivo*. This is a very relevant endpoint in therapeutic terms, as to prevent further growth and spreading of the malignancy it is only necessary to impede cell division [4,67]. The rate of clonogenicity decreases as a function of time (i.e. the slope of the corresponding semilogarithmic survival curve) and can be understood in terms of cytotoxicity as an

anti-mitotic effect, with direct cytocidal effect contributing to this effect. Clonogenicity testing is not suitable with non proliferating cells, such as cells from normal tissues. In this case, other parameters need to be tested [67]. Above 43°C, survival curves in semi-logarithmic diagrams can appear as straight lines from the origin for almost the entire time domain, increasing in steepness when the temperature increases. This can be modeled by the one-step or one-hit equation:

$$S = S_0 \cdot e^{-k \cdot t}, \qquad (T = const), \qquad \textit{Equation 1}$$

where S is the survival fraction at any time t during a constant temperature exposure; S_0 is the number of cells in the population at the beginning of the experiment ($t = 0$), and k is a constant representing the inactivation rate at the experimental temperature T (i.e. the steepness of the linear survival curves). Based on experimentations with various temperatures, increasing the exposure temperature T, from one experiment to the other, results in a doubling of k and a halving of the exposure time necessary to achieve a given survival fraction. Survival curves can be fitted in this way over the entire temperature range only for a few cell lines. Deviations of experimental curves from exponential behavior take the form of curving toward smaller slopes. These deviations are cell line- and temperature range-dependent, appearing at experimental temperatures below 42-43°C, over a limited range at short incubation times (the shoulder [67]) and at the longest incubation times (Figure 1.4A). The adaptation capacities of cells described above allow them to gain a resistance to thermal stress, i.e. thermotolerance. This is occasionally referred to as acute thermotolerance, to be distinguished from chronic or inherited thermotolerance. The last of these forms of thermotolerance can be observed in situations when transmission of resistance to thermal stress appears to last through several cell generations, such as may occur during very long heating experiments [4,5]. To exemplify the variation with respect to cell line, it is worth noting that glioblastoma cells do not appear to be capable of developing thermotolerance [69]. More sophisticated mathematical models developed from radiobiology, such as the multi-target or linear quadratic models [67], can better fit experimental deviations to exponential behavior. These models, however, may not translate in a biologically significant way to hyperthermia, and it must be understood that thermal cytotoxicity arises from totally different mechanisms than radiation cytotoxicity [4]. A recent two step model, converting initially heat-induced non-lethal lesions to lethal lesions in a second step, may be more valuable [70-72]. Nonetheless, the parameter D developed in

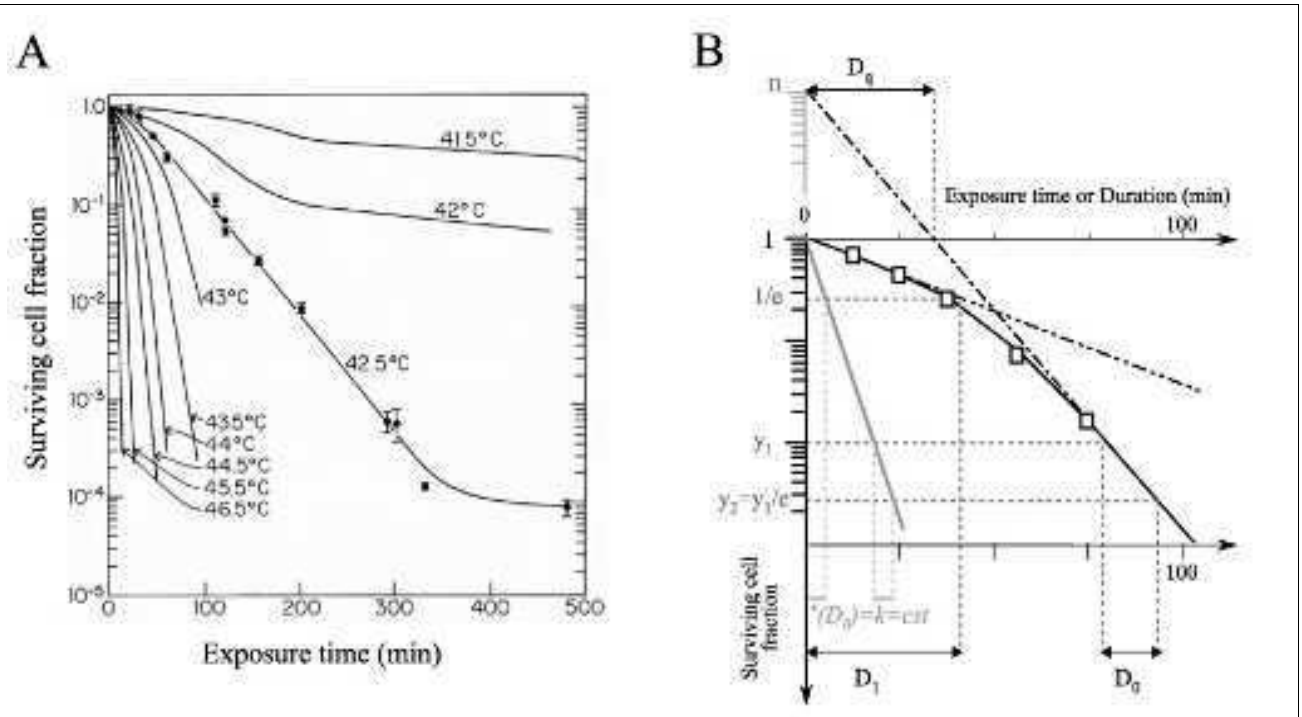

Figure 1.4: Effect of heat: survival curves and multi-target model

A. Survival curves as a function of exposure time of CHO cells treated *in vitro* by hyperthermia separately and at various temperatures. For temperatures > 43°C, curves tend ideally toward a straight line, which can be modeled by equation 1 ($S = S_0 \cdot e^{-k \cdot t}$, *S:* survival fraction, *t*: time, $S_0 = S(t = 0)$, *k:* inactivation rate). Note that for 43°C and lower temperatures, deviations from the ideal curve, such as shoulders at short incubation times and plateaus for long exposure times, allow for thermotolerance.

B. Graphical demonstration of the formalism associated with the multi-target model, which is helpful for the comparison of non-ideal curves.

D_1 is the time to reduce the survival fraction from 1 to 0.37 (reduction from S_0 to $1/e$). It is also the reciprocal of the initial slope at the very initial part of the curve, corresponding to the shoulder deviation.

D_0 relates strictly to the exponential portion of the curve that follows the shoulder. It still defines the time to reduce survival by a $1/e$ factor and represents the reciprocal of the slope of the straight-line portion following the shoulder.

D_q, or n, define from the extrapolated portion of straight-line corresponding to exponential decay as the time at which the line crosses the X-axis and the ordinate at the origin, respectively. It represents the width of the shoulder of the curve and can be viewed as a threshold to reach the main cytotoxic regime within the heat treatment.

radiobiology with a multi-target model (*D* for ionizing radiation dose) can be adapted for hyperthermia as "duration" of exposure at a given temperature, corresponding to the time necessary during heating at a given temperature for the surviving fraction of cells to be reduced by 1/*e* (i.e., 0.37 or 37 %) (Figure 1.4B). It can be then very helpful to compare various curves with a shoulder deviation by focusing on the characteristics of the subsequent exponential decay. The type of survival curve at given temperature, which is not an ideal exponential curve in that it presents a shoulder, can be thus described by three values of *D*: D_1, D_0, and D_q (*D* being constant for ideal curves, equivalent to *k*) [4,67]. D_1 is the time to reduce the survival fraction from 1 to 0.37 and is also the reciprocal of an initial slope. This parameter therefore reflects the initial part of the curve. In contrast, D_0 is the reciprocal of the slope with respect to the exponential part of the curve. D_0 is still defined as the time to reduce survival by 1/*e*, but it is measured at a point of the well exponential part of the curve that corresponds to the subsequent straight line portion in semi-logarithmic diagram (i.e., from 0.1 to 0.037, or from 0.01 to 0.0037, etc.). Finally, D_q represents the width of the shoulder of the curve. It is occasionally referred to as *n* and can be viewed as a threshold. The Arrhenius equation [73], a model of heat activation assuming thermodynamic equilibrium, makes use of D_0 in a very useful formalism for compiling survival curves:

$$\frac{1}{D_0} = k = A \cdot e^{\frac{-E}{RT}}, \qquad \textit{Equation 2}$$

where *k* (the in/activation rate) is $1/D_o$; *A* is a constant; *E* is the energy of activation (occasionally referred to as simply activation); *R* is the perfect gas constant; and *T* is the absolute temperature applied as a constant parameter during the heat treatment, which led to the survival curve and D_o value [4,68]. Synthetic representation using a linear Arrhenius plot allows one to compile in a two dimensional-semilogarithmic plot a set of survival curves corresponding to experiments at different temperatures (Figure 1.5). This representation consists of plotting the logarithm of the reciprocal of D_o for all survival curves against the reciprocal of the temperature used. This Arrhenius representation reveals an inflection point, a "breakpoint" temperature between 42 and 43°C (often averaged at 42.5°C for general considerations), whereupon cytotoxicity of an *in vitro* single-exposure heat treatment is markedly higher [4,5,68,74]. In terms of rate theory [75], this breakpoint translates to the difference in activation energy above and below this temperature and reflects variation in cellular mechanisms of heat damage [4,5,37]. Above breakpoint temperature (i.e., 43°C), the calculated activation energies associated with

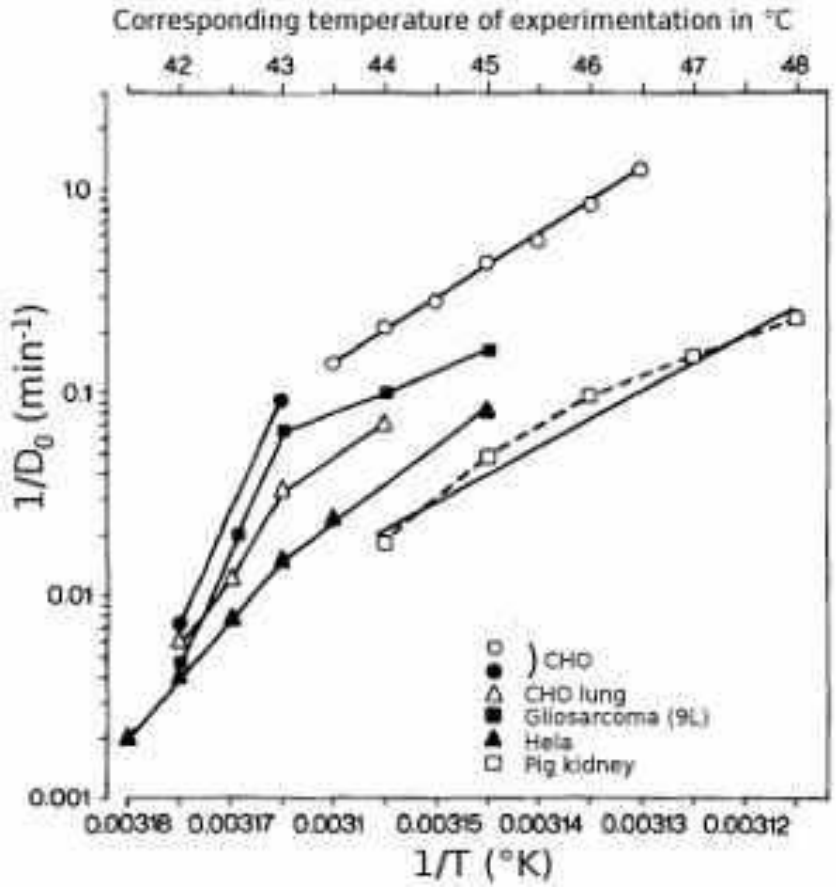

Figure 1.5: Examples illustrating the Arrhenius diagram representation of heat-induced inactivation for i) cells in varied biological samples in vitro and ii) the in vivo, heat-induced inactivation of an organ, illustrated for the pig kidney (from reference [4]).

marked heat-induced cytotoxicity are reproducible for many cell lines, close to the enthalpy of protein denaturation (140 kcal·mol^{-1}) [76,77]. Below the breakpoint temperature (i.e., 42.5°C), activation energies are more variable and generally higher. This indicates that proteins, rather than other macromolecules, are the central mediators of heat-induced cytotoxicity. The conformation of nucleic acids is stable with respect to heat. Only above 45°C, can sufficient localized energy be deposited into the DNA molecule for a direct induction of DNA strand breaks. This becomes measurable only after effective cytotoxicity, when severe cytocidal effects (i.e., less than 1% cell survival) have occurred [4,78]. It is noteworthy that the activation energy deduced from the DNA-damaging effect of heat is similar to protein denaturation, implicating the protein machinery associated with DNA as the true

effectors of heat-induced DNA perturbations. Beyond the possibility of assessing *ex vivo* clonogenicity, Arrhenius diagrams can be drawn for *in vivo* biological effects once an endpoint relevant to the effects being considered is defined, such as tumor growth delay in the treatment of solid tumors (Figure 1.5 and 1.6) [79-81]. It therefore appears that there is i) a lowering of the inflection point *in vivo* to approximately 41.5°-42.5°C, as compared to the same cell line *in vitro*; ii) a superimposition of *in vitro* and *in vivo* activation energies above, but not below inflection; and iii) a wide range of *in vivo* activation energies that differ slightly from the *in vitro* activation energies. This suggests that intratumoral toxic effects can profitably take place at lower temperatures than *in vitro*. This finding reinforces the above-emphasized hypothesis of *in vivo* modulation of heat effects, which will be discussed below. Because a simple dose parameter that multiplies time by temperature fails to predict heat cytotoxic effects, the "thermal isoeffect dose" (TID) concept has been introduced [82]. This concept converts heat exposure to equivalent heating minutes at an index temperature of 43°C (*EM*43) producing an equal biological effect through:

$$EM\,43 = tC^{T-43}, \qquad \textit{Equation 3}$$

where t is the exposure time at a given temperature T and C is a constant. $C = 2$ above 43°C and C = 4 below this point. These two distinct exponential constants for the two temperature domains reflect distinct activation energies [9,37,68]. *EM*43 accurately predicts *in vitro* cell survival following diverse single-exposure heat treatment schemes. In the case of varying T, a summation of thermal dose with respect to the temperature T and its variation in time, Δt, leads to the cumulative equivalent heating at 43°C, CEM43. Apart of considerations of thermotolerance, CEM43 is very useful for more complex heat exposure paradigms, such as those encountered in the clinic [4,68,74,83]. *In vivo*, tissue necrosis can be also well prognosticated when temperature distribution in the tissue volume is considered. Such is the case with CEM43 T_{90}, which is the CEM43 calculated for the ninetieth percentile of the temperature distribution in the target volume [5,68]. Moreover, thermodosimetry parameters applied in clinical situations are very helpful in prognosticating tumor response [68,74,84,85] and benefit from constant improvements in thermometry techniques [86]. The cytotoxic effect of a heat dose depends on the phase of the cell cycle. M- and S-phases are most sensitive to heat. This sensitivity is due to inhibition of nucleic acid polymerization and to alterations of chromosomes and mitotic machinery.

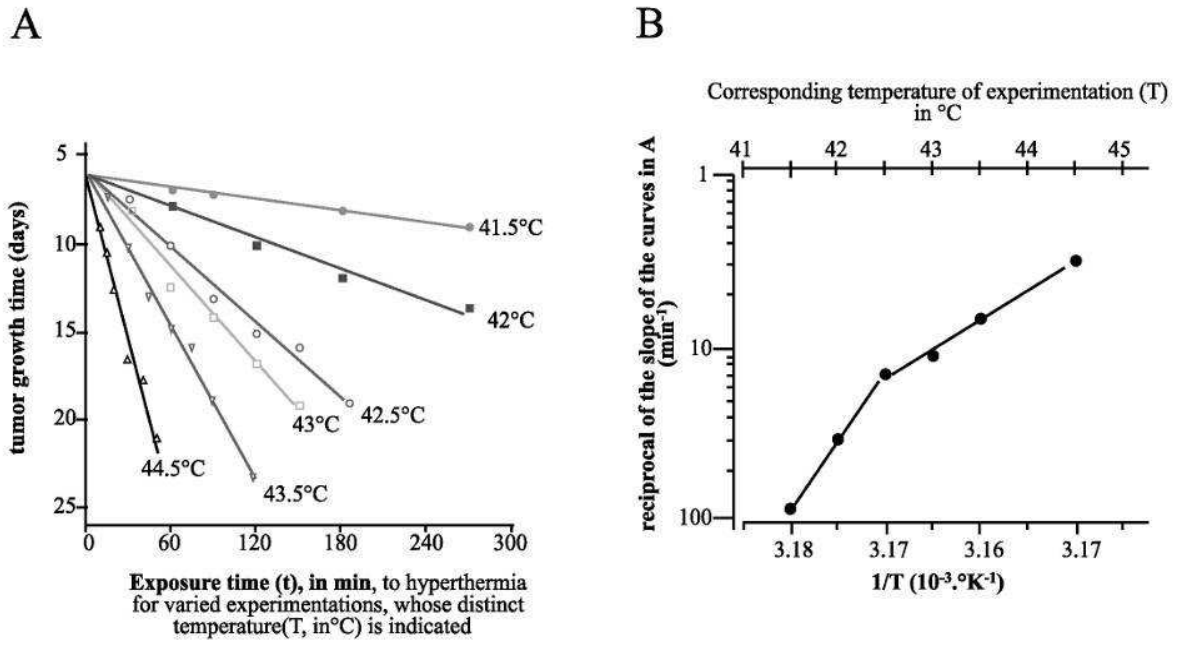

Figure 1.6: Application of the Arrhenius representation to the dose-effect curves obtained from an *in vivo* model of hyperthermic treatment of solid tumors in mice.
A: Double linear graphic with dose-effect curves of tumor growth time (Y-coordinate) following hyperthermic treatment as a function of exposure time for separate experiments at distinct temperatures (T, in °C). Here, curves are straight lines and slopes are the inactivation rates.
B: Corresponding Arrhenius diagram. On the abscissa in a linear scale is the reciprocal of the experimental temperature (1/T, in °K-1) used to obtain the curves in A. A supplementary axis on top of the graph indicates the corresponding experimental temperature T in °C. The Y-coordinate, using a logarithmic scale, is the reciprocal of the inactivation rate determined in A (in min-1), or the slope of the curves in A. An inflexion appears at 42.5°C, reflecting a transition to a regime of hyperthermia with more marked inhibitory effects on tumor growth. (From ref [83]).

Cell death apparently occurs principally in the cell cycle during which cell was exposed to heat [37]. *In vitro* and theoretically *in vivo*, rapidly cycling tumor cells, frequently in M- or S-phases, are killed selectively by hyperthermia when compared to the slowly cycling cells in normal tissues, which are primarily in G_1 or G_0 [5]. In contrast, M- and S- phases, notably late S-phase, are the most resistant to radiotherapies, and cells die primarily by reproductive cell death at the end of cell cycle. This can partly explain the benefits from combining hyperthermia and radiotherapy [5]. Nonetheless, cells in either G-phase, in other words differentiated cells, are less severely affected by heat and are unaffected by radiotherapies. More extreme heat exposure in either G-phase can still trigger cell death, which occurs

faster than for cells exposed in M- or S-phases [37,87]. Hyperthermia is able to induce both apoptosis and necrosis with increasing temperatures. Susceptibility to apoptosis appears important below the consensus temperature of 43°C, whereas necrosis appears more likely above this point [37]. This effect is also tied to the pivotal importance of mitochondria in cell death pathways. When considering clonogenicity in addition to direct cell death, it is important to note that heat prolongs the cell cycle. This effect is more pronounced when heat is applied to the G_1- or early S-phases, and increasing temperature increases the number of cell that never divide [4]. Heat can trigger arrests in G_2- or S_0-phases. Cells arrested in S_0-phase die immediately following the cell cycle, displaying specific chromosomal aberrations thought to be due to disaggregation of the DNA synthesis machinery [4]. In contrast, G_2-arrested cells appear resistant and thus participate in thermotolerance [9].

In addition to considerations relating to cell characteristics, conditions of the cell environment have also been assessed. When tumor cells grown *in vivo* as tumor xenografts were heated *in situ*, clonogenicity (determined *ex vivo*) was decreased by a factor of 10^2 when compared to the clonogenicity of the same cells grown and treated *in vitro*. This was even more pronounced 5 h after treatment if treated xenografts were remained *in situ* during this delay [88-90]. This delay had already been shown to allow the full recovery of engrafting capacities, in experiments assessing the ability of tumor cells from heat-treated xenograft to regraft [91]. This finding further suggests that thermosensitivity is higher *in vivo* than *in vitro* and raises the issue of the tumor microenvironment. The tumor microenvironment is a complex entity resulting from the interaction of several factors [92], including the following: i) tumor perfusion; ii) oxygenation status of the tumor; iii) pH distribution; and iv) metabolic-bioenergetic status, all of which are mutually interactive, as discussed below. In attempting to dissect the basis of thermosensitization *in vivo*, many interesting studies have assessed heat-induced cytotoxicity in conditions generally characteristic of tumors, i.e., hypoxia, nutrient deprivation and acidic pH. Under acute hypoxic conditions, thermosensitivity is generally only slightly affected [4,42]. In contrast, chronic hypoxia can increase thermosensitivity [4,43]. This suggests that decreased oxygen content is not directly responsible for thermosensitization but rather that it is a consequence of the sensitivity of a cellular metabolism that has adapted to hypoxic conditions [4,42]. Chronically hypoxic cells found in tumor area are also at a lower pH (i.e., acidic). When assessing the *in vitro* effects of acidic pH

conditions, a comparable 10^2-factor in clonogenicity decrease can be obtained as *in vivo* [93]. When extracellular pH (pH_e) is lowered during heat exposure, thermosensitization effects occur only transiently. Notably, these effects are occasionally less pronounced in normal cells [4]. In contrast, when cells are further maintained *in vitro* in acidic conditions following heat treatment, thermosensitivity appears maximal 5 h after heat treatment [93]. Therefore, the pH effect appears to depend on intracellular pH (pH_i) [4,42,43,94]. When cells are grown in acidic conditions prior to heat exposure, the thermosensitivity effect disappears. This suggests that tumor cells may adapt to maintain their pH_i near physiological values (i.e., 7.4). Two primary mechanisms of intracellular pH homeostasis involve intracellular buffer systems and the incorporation of H^+ in the form of NH_4^+ in amino acid turnover. Also important for pH regulation are transport enzymes, which notably are ATP-dependent and have been identified from experiments using pH inhibitors. These transport enzymes include i) vacuolar-type H^+ ATPase, an ion transporter (inhibited by bafilomycin and oximidine); ii) H^+/lactate co-transport exchanger (blocked by amiloride and quercetin); iii) Na^+/dependent Cl^-/HCO_3^- exchanger (blocked by disulfonic derivatives, DIDS); iv) the NHE sodium-proton exchanger family (blocked by amiloride and its derivative, cariporide); and v) electrogenic Na^+-HCO_3^- co-transporter [42]. The determining factor appears to be the decrease in pH_i, but this is not yet clear [4,42]. In Arrhenius plots, breakpoint temperatures lower with decreased pH_i [4,68]. This suggests that proteins are more easily altered by the joint effects of heating and acidification, which in turn is likely related to intracellular variations in ionic strength [4]. Acidification has been also shown to abrogate the heat shock response in melanoma cells, with deviations due to acute thermotolerance vanishing from survival curves [54]. To illustrate the intricateness of these factors in response to heat exposure, it is worth noting that pH_i decreases under acute hypoxic conditions and that this effect is already pronounced for heat exposure at 41°C [4]. Nutrient deprivation is also capable of increasing thermosensitivity, reflecting complex interrelations and metabolic changes, which will be considered in more detail later in discussion of tumor pathophysiology.

1.1.1.4 Molecular biology of stress responses: heat shock, hypoxia and connections

A wide variety of stresses induce the stress responses. These stressors range from phases of the cell cycle, differentiation and growth to inhibitors of energy metabolism. Stressors also include toxins, various biophysical agents and, above all, heat. The first stress proteins were discovered as gene products that are strongly induced by heat shock and thus referred to as heat shock proteins (HSPs). Presently, among the growing number of genes classified in the highly conserved group of heat shock genes (*HSP*s), some encode the most abundant proteins of normal cells, representing approximately 50% of cellular proteins, but baseline levels depend on the animal (e.g., levels are often higher in human). In particular, HSPs levels are increased in a wide variety of cancer cells. HSPs have important and manifold biological functions in normal cells. It should be restated here that the chaperone functions consist of direct interactions with proteins and involve ATP-dependent folding stabilization. As previously described, chaperone function is crucial for the folding of nascent proteins. This importance derives from conditions of high intracellular protein concentrations and from the need to stabilize and repair partially denatured proteins. Moreover, cellular homeostasis requires the housekeeping functions of certain HSPs for protein trafficking, translocation and turnover, and coated vesicle or receptor (steroids) stabilization [95]. Depending on whether HSPs or other chaperones exist intracellularly, at the membrane level, or in extracellular fluid environment, recent “moonlighting” functions unrelated to folding, but rather related to signaling are now recognized [13,96-98]. HSPs are first classified by molecular weights in conserved families [99]. As mentioned above, the nomenclature of heat shock proteins according to [16], the HUGO Gene Nomenclature Committee and the Entrez Gene database is emphasized. Nomenclature may be followed in parentheses by the commonly used alias. A few remarkable HSPs, chaperones or non-HSP but heat-inducible proteins should be noted [95,99-104]: the small HSPs, such as UBB (ubiquitin) or HSPE1 (HSP10) and HSPB1 (HSP27), of which the latter two are tissue-specific; HMOX1 (heme oxygenase 1, HSP32 or HO-I); SERPHIN1 (HSP47), which is associated with collagen and is a product of a heat-inducible endoreticular serin peptidase paralog; HSPD1 (HSP60), of importance for mitochondria and innate immunity; and HSPA8 (HSC70; HSC71; HSP71; HSP73), which is constitutively expressed. HSPA1A and HSPA1B (HSP70

and HSP72, respectively) are the most heat-inducible of HSPA family. They differ by two amino acids but are believed to be fully interchangeable at the biological level. HSC1 (HSP90) and HSPH1 (*HSP100/105*) are important chaperones. HSPA8 (HSC70; HSC71; HSP71; HSP73) is the major chaperone found basally in normal cells. Synthesis of HSPA1 isoforms: HSPA1A (HSP70-1; HSP72; HSPA1) and HSPA1B (HSP70-2) is very low in the absence of stress or pathology and increases following heat shock, after which they comprise the most abundant protein fractions of a normal cell. Numerous stressful conditions lead to destabilization and spoilage of a subset of proteins and call for the essential chaperone function of *HSP*s. Thus, beyond responsiveness to heat shock, HSPs are actually stress proteins synthesized in response to any proteotoxic stress [95,100,105]. Distinct biophysical stressors, all inducing HSPs, are classified into three groups with respect to their mechanism of action [106], although all converging on protein denaturation. These stressors include the following: i) induction of non-native proteins, specifically triggered by amino acid analogues or ethanol; ii) alteration of proteins conformation, including protein denaturation triggered by organic solvents; iii) some heavy metal ions (Cd^{2+}, Cu^{2+}, Hg^{2+}, Zn^{2+}), chelating agents and thiol-reactive compounds, which lead through redox reactions to protein thiolation or to protein-protein disulfide bond formation (these treatments and agents are elsewhere qualified in terms of altering protein conformation); and iv) free radicals and recovery from anoxia, both to be distinguished from oxidative stress. This latter stressor induces HSPs chiefly through direct or redox-mediated protein fragmentation, involving principally the powerfully hydroxyl radical (•OH). *HSPs* are transcribed directly into mRNA without the requirement for post-transcriptional modifications. Furthermore, *HSPC1* and *HSPA1* (*HSP90* and *HSP70*) do not require post-translational modifications (unlike *HSPC4* (*GP96*), for which a glycosylation step is necessary). The induction of *HSP* genes can thus trigger very rapid and transient transcription and quickly increase certain protein levels that are maintained for long durations (ca. 48 h, peaking at 24 h). For example, a treatment of HeLa cells at 42°C for 4 h leads to maximal *HSPs* transcription within 30 – 60 min and declines thereafter. The rapidly produced mRNAs are maintained during exposure to heat through a further stabilizing effect of heat shock and reach maximal levels later in the heat response, within 2 hours for *HSA1* mRNA levels. HSPA1 (HSP70) protein levels are maximal within 3 h [107]. Interestingly, the authors note that at 43°C, neither attenuation of *HSP*

transcription nor HSP translation occurs. Nevertheless, following return to a normal temperature, *HSP*s will inescapably be induced because of the occasioned cell injuries [12]. Heat shock transcription factors (HSFs), of which there are three homologs in mammals (HSF1, 2 and 4) are central to the regulation of *HSP* genes. HSFs recognize and bind to the heat shock element DNA sequence *HSE* and promote transcription. HSF1 is the primary regulator of the entire repertoire of stress-inducible *HSP*s [108], for the canonical genes *HSPB1*, *HSPA1* and *HSC1 (HSP27*, *HSP70* and *HSP90*) and for other genes as well [109]. Notably, promoters of the *SOD* gene, which encodes superoxide dismutases, and the promoter of *ABCB1*, which is involved in multi-drug resistance genes, both have *HSF* binding sites [110,111]. Some protein not fully considered HSPs, such as HLA proteins (or MHC-I) involved in human antigen processing, appear to be transcriptionally upregulated by heat shock. An exception to this is ubiquitin (UBB), which is classified as a HSP. Recently, this upregulation was reported specifically for two inducible subunits of the proteasome, PSMB9 (or lmp2) and PSMB8 (or lmp7), in relation with increased antigen presentation [112]. Cytosolic monomeric HSF1 is the repressed state. HSC1 (HSP90) associates to cytosolic monomeric HSF1 and maintain repression. The derepression elicited by thermal or other stresses activates HSFs. Subsequently, phosphorylation, trimerization and translocation of HSFs to the nucleus (stress-induced intranuclear granules) allow the binding of these factors to the *HSE* site and activation of *HSP* genes [108]. One possible initiating event linked with proteotoxic stress is the recruitment of HSC1 (HSP90), which dissociates from HSF1. High rates of transcription are maintained only when HSF1 trimers remain bound to the *HSE* site. Conversion of HSF1 trimers to monomers, either following removal of the stress signal or when damaged proteins are no longer generated, is associated with attenuation of HSP synthesis and thus of the heat shock response [113]. HSA1 (HSP70), which has the best-described chaperoning function, binds to denatured proteins (recognizing hydrophobic areas exposed by denaturation) and attempts to restore their tertiary structure and enzymatic activity through an ATP-dependent function. The interactions between induced HSPs with HSFs very likely allow autoregulation of *HSP* genes activity through a feedback regulatory loop. The repression of HSF1 by HSA1 (HSP70) has been clearly demonstrated [107]. At the genome-wide level, binding of HSF1 to DNA was neither necessary nor sufficient for heat shock-induced transcription [109]. Post-transcriptional mechanisms, such as changes in mRNA processing or stability

during or following heat shock, may contribute to the increased transcript levels of HSF1-independent but heat-inducible genes. With respect to these genes, the authors suggest that either i) their regulation is HSF1-independent (on the basis of previous reports [114,115]) or that ii) they are part of a secondary response that occurs in a subset of cells after failure of the primary heat shock response. Alternatively, HSF1 repressive activity is strongly suggested for genes binding HSF1 but not activated by heat. An important consideration regarding *HSPA1* is the apparent discordance between mRNA transcription and protein translation. This seeming paradox reinforces the suggestion that the regulation of protein levels also depends on downstream regulation mechanism, likely at the translational level [12]. Notably, the pool of intracellular HSPA1 (HSP70) is basally over-expressed in cancer cells. This is generally reported to be independent of *HSF1* (invoking translational regulation or the participation of other HSF isoforms), but recent studies have shown a possible mechanism of HSF1 activation through horizontal signaling at the membrane level. In this situation, HSF1 would be activated via inhibition of constitutive repressing kinase GSK3 at the end of the phosphorylation cascade activated by neuregulins, such as the malignant EGF-like growth factor NRG1 (or Heregeulin β1). This neuregulin is able to facilitate homo- and heterodimerization of each member of the four epidermal growth factor receptors (EGFRs) [116-118]. The heat shock response, similar to most stress responses, is multi-faceted and complex. Cross-regulations of stress pathways allow one pathway to sensitize another and to elicit a response under unspecific conditions. For example, the response to hypoxic stress relies on the central oxygen-sensing stress pathway. However, expression of *HSP* genes is necessary for a complete response [119]. Notably, HSPA9 (GRP75) and HSPA5 (GRP78) are known oxygen-regulating factors [99]. The hypoxic stress response results from acute changes in oxygen status, such as during ischemia/reperfusion, a very frequent phenomenon in tumors. This response should be distinguished from the stress response associated with chronic hypoxia. Ischemia, which corresponds to the first phase of oxygen deficiency, should also be distinguished from reperfusion, which corresponds to the return to normal oxygen conditions with generation of an ROS burst. It shall be noted that although the ischemia/perfusion phenomenon is associated with oxidative stress, the regulation of the oxygen-sensing stress pathway (by definition dependent on oxygen levels) is distinct from the regulation of the oxidative stress pathway (defined as ROS-dependent), for which H_2O_2 appears to play the role of

signaling molecule [40]. This distinction is still matter of debate [120]. Nonetheless these differences should be kept in mind when considering their relationship with the thermal stress response. For example, oxidative stress has been shown to induce thermotolerance in the absence of HSP induction (type-I thermotolerance) [12]. Hypoxia-inducible factor 1 (HIF1, heterodimer of protein HIF1A and HIF1B) is activated by oxygen deprivation, as occurs during ischemic pathology or very frequently in tumors. Oxygen deprivation also prevents HIF1A from its normally rapid degradation, an example of post-translational regulation. HIF1 and the proteins it regulates, also known as oxygen-regulated proteins, including p53 protein and VEGFs, play a fundamental role in cancer [121-124], notably in tumor aggressiveness [125]. HIF1 induces the expression of a number of important genes involved in vasomotor regulation (nitric oxidase); glucose transport; glycolysis; erythropoiesis; angiogenesis (VEGFs and angiopoietin); insulin-like growth factor production; extracellular matrix remodeling; and cell cycle regulation [126]. The HIF1-regulated enzymes that catalyze intermediary steps of glycolysis are GLUT-1, type I hexokinase, aldolase A, lactate dehydrogenase, phosphofructokinase L, phosphoglycerate kinase 1 and pyruvate kinase M. HIF1 further upregulates SOD and heme oxygenases (HMOX1 (HSP32) and HMOX2), which are central to ROS scavenging and thus to oxidative stress [127]. These enzymes catalyze the Fenton reaction that requires iron and contributes to iron metabolism, recently found to be important in tumor pathophysiology [128]. HIF1 also upregulates carbonic anhydrases (CA), which counteract intracellular acidification and therefore would also participate in tumor pathophysiology [129]. HIF1A can be used as an endogenous marker of acute hypoxia at the time of biopsy, such as the transient perfusion-limited hypoxia, because of its short half-life. However, its use in this respect can be difficult. Because of their longer half-lives, CA9 and Glut1 can be more easily used as endogenous markers and may be more representative of long-term or diffusion-limited hypoxia [130]. It was shown in Drosophila that the binding of conserved element response sequences within the *Hsf1* promoter to sima (homologue to human HIF1A) induces also an increase in transcript level of *Hsf1* mRNA, which is necessary for full *Hsp*s induction during hypoxia [131]. This cross-regulation reflects complex aspects of the heat shock response. This intricacy appears to originate from evolutionary adaptation to protect cells from diversified forms of stresses, lethal signals and cell death signals. In particular, HSPB1, HSPA1 and HSPC1 (HSP27, HSP70 and HSP90)

have extremely complex inhibitory roles in the regulation of apoptosis. Physical interactions with apoptotic molecules appear responsible for apoptosis inhibition (caspases, cyclin dependent kinases, BAG3) [101,132], although overwhelming stress can still induce necrosis. The resistance to cell death associated with high HSP levels likely participates in the increased survival that characterizes cancer cells. This resistance is also likely associated with the limitation of therapeutic modalities based on apoptosis induction, such as chemotherapy, radiation and hyperthermia. Moreover, the parallel between HSPs with thermotolerance is almost certain but remains to be clearly understood. Recently, HSPA1 (HSP70) was shown to participate in the protection of lysosomal membranes that prevent autophagic cell death. This protection occurs in cancer cells [133].

1.1.2 Hyperthermia in oncology

To understand the true rationales of hyperthermia in oncology, its effects should be considered beyond the cellular level. The complexity of hyperthermia's effects at the tissue, organ and organismal levels, how it relates to pathophysiology, and the therapeutic frame are all addressed.

1.1.2.1 Hyperthermia treatment modalities

Thermal therapy, or thermotherapy, encompasses all therapeutic treatments based on the transfer of thermal energy into or out of the body [134]. Induced hyperthermia as a therapeutic approach consists of raising the temperature of i) the whole body (i.e., whole body hyperthermia (WBH)); ii) part of the body, referred to as regional hyperthermia; or, iii) a specific tissue, referred to as local hyperthermia [135]. When the heating is more localized, the applicable temperature increases, consequently influencing the therapeutic effects of heat. Hyperthermia as adjuvant therapy in oncology is gaining interest in clinical practice and is the main indication of hyperthermia [37,136-140]. Thermoablation, also used for hyperplasia, is a particular modality that consists of raising the temperature of a delimited

tissue volume above 47°C. This modality, which is associated with direct and intense tissue necrosis and coagulation, is indicated when access by surgery is difficult [141]. In contrast, whole body hyperthermia is limited to 41°C for obvious toxicity consideration (maximal temperatures of extreme WBH reach 42°C). Between these applications, temperatures up to 46°C can be envisaged with regional or local hyperthermia modalities. Tumor growth delay can be observed at temperatures as low as 39°C [9], whereas only temperatures above 42-43°C can have a direct cytocidal effect as previously discussed. This raises extremely important considerations of solid tumor pathophysiology and suggests: i) that thermal sensitivity of tumor or normal cells is higher exclusively within the tumor environment [142]; and ii) that hyperthermia has indirect toxicogenic and anti-tumor effects. Mild hyperthermia is a modality limited to intratumoral temperatures of up to 42°C, which can routinely be achieved in the clinic. By contrast, intratumoral temperatures ranging from 42 – 43°C to 46°C are defined as moderate hyperthermia. Anti-tumor effects of heat generally increase substantially with temperature, but response to hyperthermia appears to depend on tumor volume [43]. It is also frequently observed that hyperthermia treatment of deep-seated tumor raises tumor temperature to a target temperature range while leaving surrounding, healthy tissues at lower temperature [4,42,143,144]. Quasi-selective damage of the tumor lesion can be achieved by regional or local heating to temperature between 40 and 44°C [145]. Moreover, when hyperthermia is used as a sensitizing agent to additional therapies in multi-modality approaches, the differential heating effect is of first importance in terms of therapeutic gain [5,9,37,146,147]. Clinical studies of the association of hyperthermia with ionizing radiation have established the potential of heat in radiosensitization [5]. At this cellular level, the therapeutic gain is explained by complementarity in terms of both cell cycle sensitivity and synergy in DNA damage. Synergistic radiosensitization by heat can nonetheless be fully understood only when taking into account alterations of the tumor microenvironment, as will be discussed below [148]. Heat can also sensitize the tumor and tumor cells to certain chemotherapies. This, however, depends on the mechanism of action of the drug and on subtle pharmacodynamic or pharmacokinetic interactions, which are intensively investigated [5,146,149]. It is very interesting, that local hyperthermia can further target the action of the drug [5]. Our understanding of heat-based modulations of the immune response to the tumor is constantly increasing. These effects explain indirect consequences of local heat within

an organism and suggest an important role for loco-regional modalities and whole body hyperthermia in immunotherapy protocols.

1.1.2.2 Hyperthermia and solid tumor pathophysiology

Among the intricacies of tumor pathophysiology, the intratumoral heterogeneity of which is not taken into account frequently enough, the central roles played by abnormal tumor vascularization and the microenvironment are crucial to hyperthermia [148,150-155]. Thermal sensitivity is dependent on the tumor microenvironment through bioenergetic, metabolic, pH, nutrient and oxygen statuses that further depend on the supplying and draining microcirculation. It is worth noting the underline the central importance of the microenvironment in our current understanding of cancer etiology. The microenvironment is one that favors genetic instability (epigenetic) and further mutations (mutating phenotype). For example, both mutated and normal cells adopt a common phenotype in a given tumor microenvironment [156]. Alternatively, the temperature that can be achieved within a tumor is dependent on heat dissipation by convection. This is primarily a factor of fluid conduction and its regulation, principally via blood perfusion. An inverse correlation between deep-seated tumor temperature and the average degree of perfusion has been often reported [157]. Thus, an evaluation of the average blood flow (the thermal clearance or washout method) consists of measuring the short-term temperature decrease just after heating [158-163]. Fairly accurate techniques of blood flow measurement can assess different aspects of this process, e.g., average blood flow, regional blood flow and accurate measures of blood flow distribution [158]. Very frequently, tumor perfusion differs significantly from normal tissue perfusion. Despite the fact that higher basal average tumor blood flows (TBFs) are often documented for smaller tumors, this metric cannot be strictly correlated to tumor volume, and low-flow tumors should be distinguished from high-flow ones. Basal blood-flow patterns show important intratumoral heterogeneity, especially for larger tumors with a high perfusion in the periphery in comparison to the tumor core [42,43,145,164]. Intertumor variations in blood flow also depend on the method of determination and the accuracy of the measurement technique, together with the complication of intra-tumor variability. Ultimately, average TBFs range from 0.01 to 1-2 $ml \cdot g^{-1} \cdot min^{-}$

[1]. The highest values are reported for liver metastases, breast cancers and in some instance for colorectal cancers. Each of these tumor types can actually show greater value of blood flow than for normal tissues [164]. Generally, inappropriate distribution and deficiencies of tumor microcirculation impede supply (diffusion limited to about 100-200 μm) and drainage. This effect leaves some tumor areas chronically deprived and hypoxic, the physiological ability to use oxygen being unimpaired [42,121]. It should be noted that pO_2 distribution merely reflects the TBF pattern [43]. Tumor microvasculature arises from varied mechanisms [42,165-167]: i) co-option of normal vessels that preexist and are somewhat preserved during tumor colonization (co-opted vessels); ii) vasculogenesis involving the colonization of circulating endothelial or other cells primarily from the bone marrow, the importance of which was recently emphasized in etiology [168]; iii) angiogenesis, or neoangiogenesis, resulting from the sprouting and proliferation of endothelial cells from local vessels; and iv) pseudoangiogenesis, which consists of tumor cells adopting or forming an architecture composed of lumens, known as pseudo-vessels [169]. It is important to note that tumor angiogenesis is strongly dependent on HIF. Newly formed tumor microvasculature is highly tortuous, with cul-de-sac vessels, excessive branching, and shunts. Vessels are sharply bent, twisted in coiled structures and highly dilated in basal conditions, almost maximally dilated to meet the high nutrient demand of the tumor [93]. The endothelial lining and elastic basement of tumor vessels are frequently interrupted, allowing tumor cells to be in contact with circulating cells. Neovessels lack smooth muscle and pericytes [169]. The tumor vasculature shows increased permeability with abundant sinusoidal openings that are closed in normal tissue vasculature under normothermic conditions [93]. As lymphatic drainage is very low, tumor interstitial fluids accumulate and occupy 30 – 60 % of the tumor volume [42,170-172]. This consequent volume fraction is not negligible in comparison with normal tissue, where extracellular water accounts for 20-25% of the total water [170,171]. Tumor interstitial fluids, especially those in necrotic areas, are collagen-rich and show specific biochemical characteristics. Blood in the tumor, representing 1-10% of tumor volume [173], also has an increased viscosity, which is associated with hemoconcentration and a pH-dependent decrease in erythrocyte elasticity. Frequent stops in blood microcirculation are due to the blocking and aggregation of these erythrocytes, platelet clots, coagulation and collapse, or the invasion of proliferating cells [42,169]. The high interstitial pressure within tumors (55 mmHg) is associated

with a restricted diffusion (of oxygen, nutrients and noteworthy drugs) [171], transient vascular collapse and even occasionally a local reversal of the blood flow [42]. Tumor vascularization generally shows altered regulation. TBF is not regulated according to metabolic demand as in normal tissue [42,150]. In addition to basal restriction of diffusion, transient microcirculation stops result in the ischemia/reperfusion phenomenon. This produces transient acute hypoxia and nutrient deprivation of downstream areas, whereas chronic hypoxia concerns tumor areas more distant from a vessel. Regarding vascular thermoregulation, the capacity of vasodilatation of neo-formed tumor microvasculature is lower than co-opted vessels or normal tissue vasculature [93]. This is because neovessels, under intense development and constantly reorganized, are devoid of smooth cells and are not innervated [93,164]. During hyperthermic treatment, TBF can be increased, decreased or unchanged. The incidence of these effects depends on the tumor, basal TBF, thermal dose, heating rate and heating technique. The exact mechanisms are not clearly understood. Moreover, variations in TBF can occur in the course of hyperthermic treatment. This essentially concerns a subsequent shutdown of an initially increasing TBF upon hyperthermia. Moreover, after heating, changes in TBF can endure to some extent. It is worth noting that higher heat damage can be generally expected with low blood flow tumors [43]. The vascular responses to hyperthermia with respect to average TBF and TBF distribution are difficult to predict. Furthermore, the involvement of vasculature in the tumor's response to heat is often difficult to decipher [43]. When TBF is decreased in response to heat (above the indicative temperature of approximately 43°C), higher tumor damage can be achieved. This is because blood flow deprivation in tumor worsens the microenvironment. Moreover, decreased cooling effects allow a further increase in the temperature and effective toxigenicity of heat. The tumor vasculature is also damaged by treatment, and TBF further decreases until stasis occurs [37]. When TBF increases in response to hyperthermia (generally observed for moderate hyperthermia, below 43°C), the increases in TBF are generally not greater than a 1.5 to 2.0-fold, whereas normal tissue blood flow can increase by 10 to 15-fold in healthy tissues [145]. Following the initial increase, a decrease in TBF can be observed to various extents. This occurs more or less rapidly with respect to thermal dose (temperatures ranging approximately from 41 to 43°C). At the end of the TBF decline, stasis can be observed, whereas stasis is never observed in healthy tissue for temperatures lower than 45-47°C, durations shorter than 30-60

min and heating rates below 0.7°C·min^{-1} [93,164]. In addition to thermoregulation characteristics, each of above-mentioned abnormalities in tumor vasculature can be involved in more complex vascular events in response to hyperthermia [42]. Considering that neovessels lack thermoregulation and that their basal usage is near capacity, the following specific mechanisms have been advanced to explain increase in TBF: i) involvement of coopted vessels; ii) mechanical or passive dilatation by increase in blood inflow from adjacent normal tissue; iii) an increase in cardiac output, often observed during local hyperthermia and involving the secretion of vasomotor agents, such as bradykinin or histamine [93]. To explain a decrease in TBF and stasis, various mechanisms have often been suggested, including the following: i) swelling of endothelial cells; ii) flow stop by leucocyte sticking, which is observed at the post-venule level by intravital microscopy; iii) an increase in blood viscosity and in the frequency of erythrocyte stasis, an effect of pH modulation through hyperthermic treatment; iv) focal vasoconstrictor reflexes of the short portions of the normal vasculature, immediately upstream of tumor vasculature in series geometry and/or steal effects in parallel or mixed geometry; v) degenerative effects, such as lysis of endothelial or tumor cells for some vessels; and vi) blood leakage [42,93,145,164]. Mechanisms corresponding to point iv), v) and vi) are prominent in explaining immediate decrease in TBF upon heating. Occlusions and stasis are frequently irreversible [93], and tumor vasculature is generally more vulnerable to heat than normal vasculature [42,145]. When stasis occurs, further degenerative effects appear remarkably dose-dependent. This is possibly associated with lowering of the toxic threshold and is preferential for proliferative endothelial cells. In contrast, healthy tissue vasculature is spared up to temperatures of 45-47°C, reflecting not only the general resistance of endothelial cells to heat but also a likely protective cooling through the increased luminal flow of colder blood (10 to 15-fold increase). With respect to damage at the vascular level, the role of concentrated organic solvent solutions, especially ethanol, as sclerotic agents in interventional radiology should be noted [174]. In addition to tumor particularities, systematic studies in animal tumor models have focused on the kinetic of the TBF changes induced by a 1-h heat treatment at various temperatures while guarding against tumor variability [175,176]. During heating at 42.5°C, TBF increased during treatment and declined within 5 h to control levels. Heating at 43.5°C produced an initial increase in perfusion over the first 30 min followed by a pronounced reduction during treatment. In this case, basal TBF was not completely

recovered 24 h after heating. Upon 44.5°C hyperthermia, only a decrease in TBF occurred, which became even more pronounced after heating was complete. In contrast, normal tissue vasculature recovered to basal blood flow levels more rapidly following hyperthermic treatment. With heating repetition, tumor blood vessels have shown the capacity to acquire a thermal adaptation to reheating that consists of improvements in positively regulating blood flow in response to thermal stress. This phenomenon, referred to by Song as vascular thermotolerance, only refers to the observed blood-flow increase in tumor vessels in response to reheating, not the reduction observed during initial heating [176,177]. Vascular thermotolerance remains incompletely understood and speculative [42] and should be distinguished from cellular thermotolerance [12], which is defined by the resistance to heat-induced cell death, as previously discussed. This does not exclude the possibility, however, that cells constituting tumor vessels can develop individual cellular thermotolerance. Further characteristic tumor reactions to hyperthermia are i) peritumoral inflammatory infiltration of leukocytes following recruitment and extravasation and ii) interstitial edema with even increased interstitial pressures [42]. The recruitment of leukocytes can be explained by the heat-induced up-regulation of adhesion molecules, which are usually down-regulated in tumor endothelial cells [178]. The increase in interstitial pressure can be related to increased vascular wall permeability and leakage because of stress fiber rearrangement. This is variable and depends on the extent of associated connective tissue [42]. The capacity of hyperthermia to increase cellular membrane permeability may be highly relevant for pharmaceutical formulations that rely on extravasation for tumor and cellular delivery. For further considerations of heat effects within tumor tissues, the importance of several interconnected factors is still debated: blood flow, metabolism, oxygen and pH. The basal characteristics of tumor important for tumor treatment, at least in crucial tumor regions, include acidosis, substrate restriction, accumulation of metabolic waste products, energy depletion and hypoxia. The role of hypoxia, in the most general sense [121] and not simplified in terms of oxygen partial pressures, is dramatic in its effect on intrinsic tumor functional metabolism. Hypoxia is also critical in understanding thermosensitization. One striking metabolic abnormality of cancer cells specific to the tumor microenvironment is their capacity to metabolize carbohydrates primarily by anaerobic glycolysis even under aerobic conditions [42]. This metabolic behavior is the result of hypoxic adaptation and *HIF1*-dependent upregulation of the many enzymes involved in the

intermediate reactions of glycolysis, as previously discussed. Many acidic catabolic wastes accumulate in the large and poorly drained tumor interstitium (where characteristic precipitates are observed in histology), including acetoacetic acid, β-hydroxybutyrate, lactic acid, and H^+ [42,43]. Median lactate levels in the tumor increase notably with tumor size, as does the hypoxic cell fraction. Moreover, pH_e values ranging from 5.7 to 7.6 are observed, whereas physiologic pH_e is 6.8 [42,43,179]. Cytosolic acidification is a common feature associated with acute hypoxia [121], but cells adapted to chronic hypoxia show a pH_i adaptation to more physiologic values. At the very least, acidosis in tumors may contribute to cell death, even in the absence of therapy [43]. Basally, the pH gradient between pH_e and pH_i is the most specific characteristic in discriminating between tumor and healthy tissues [180]. As a general rule, $pH_i > pH_e$ in tumor tissues, whereas in healthy tissue $pH_i < pH_e$. These acidic conditions are known to substantially increase the delay and decrease the magnitude of thermotolerance, an immediate beneficial consequence [93]. Regarding previous *in vitro* and *ex vivo* cell survival studies, it should be noted that an acidic pH can enhance thermosensitivity, especially when changes in pH are acute. This is in contrast to chronic acidification within the tumor and adaptation of tumor cells that do not demonstrate increased thermosensitivity, suggesting that tumor thermosensitivity *in vivo* depends on more complex mechanisms [42]. A very remarkable response common to many local hyperthermia treatments consists of a marked tumor acidification during and after treatment. This occurs regardless of the effects of the treatment on TBF and tissue oxygenation and regardless of the dose and temperature range. This effect is even more pronounced at the lower temperature range corresponding to mild hyperthermia, in contrast to the higher temperature range of moderate hyperthermia [42]. Moreover, the maximal pH decrease after treatment completion occurs within about 5 h [93]. This time point is approximately the landmark for thermosensitization discussed above and further explains the observed advantage of certain relevant tumor treatment fractionation sequences, with respect to thermotolerance. These observations are so central to the rationales of *in vivo* hyperthermia that they warrant detailed explanations, although these effects are still far from being understood. When hyperthermia treatment results in a lower TBF, e.g., for high temperature range of moderate hyperthermia, in addition to reductions in heat dissipation that favor heating, there is an intensification of thermal damage that is thought to rely on reductions in pH_e and/or pH_i. This later effect is coincident

with the enlargement of hypoxic regions (chronic hypoxic areas plus adjacent enlarging areas of acute hypoxia) and the destruction of tumor tissue, chiefly by necrosis. Each of these phenomena further contribute to acute tumor acidosis [42]. When hyperthermia treatment results in a higher TBF, e.g., for treatments by mild hyperthermia, there is an increase in supplied and dissolved oxygen and glucose concentrations. These events result in better oxygenation of the tumor, especially of the hypoxic areas. The increased pO_2 available for respiration leads oxidative phosphorylation and the abnormal glycolytic catabolism (only inhibited for high temperatures) to produce high levels of acidic catabolites [43]. These are then committed to excretion pathways. Nevertheless, because of the limited drainage of deep tumor interstitium, even in the presence of increased blood flow (interstitium volume increasing upon hyperthermia), interstitial lactate levels are particularly heightened, which relates to pH_e acidification [4,42,43,145]. Furthermore, a general increase in the lactate/pyruvate ratio reflects intracellular acidification [4]. Precisely concomitant with hyperthermia treatment, the acute phase of pH_e and/or pH_i decrease may explain the specific thermosensitization of the tumor *in vivo* upon a single heat exposure that is never observed in *in vitro* models or *in vivo* models of tumors devoid of blood flow [90]. It is important to note that an enhancement of radiation-induced damage is expected in a higher oxygenation environment. It should also be noted that radiosensitization is higher for normal tissue, abolishing therapeutic gain. Therefore, treatment sequences where hyperthermia follows radiation are preferable, in that radiation thermosensitizes the tumor through vascular damage [5,93]. Without detailing other, considerably important hyperthermia-induced alterations in tumor metabolism and the importance of nucleotide trihosphate, especially ATP, should be mentioned. An immediate drop in tumor ATP levels occurs during heating, the lowest concentration being reached 12 h following treatment [43]. As a clear, indirect antitumoral activity of hyperthermic treatment, angiogenesis inhibition has been clearly attributed to the heat-induced activation of serpin peptidase inhibitor 1 (SERPINE1), also known as Plasminogen Inhibitor Activator I (PAI-I). This protein counteracts plasmin formation and subsequent fibrinolysis of the blood clot, knowing that the latter blood clot plays a central role in tumor angiogenesis [181]. Perturbations of hemostasis, thrombolysis and fibrinolysis should be also considered when some pharmaceutical formulation that occasion transient release of organic solvent and thus acute hypocoagulable state, as known for ethanol, are injected [182,183].

1.1.2.3 Hyperthermic therapy combinations, emphasis on embolization procedures

Hyperthermia is known as the most potent cellular radiosensitizer [184-186]. The strength of this effect is continuously improving with increased understanding of heat effects. Also important for these advances is the adaptation of thermoradiotherapy sequences to obtain desired effect combinations. One important, straightforward rational for thermoradiotherapy sequence is the observed heat-induced inhibition of the DNA damage repair system. The mechanisms of this effect are still not fully understood but are gaining significance [5,187]. Most combined thermoradiotherapy protocols rely on positive modulation of tumor oxygenation. This aims to increase the oxygen enhancement ratio, thereby obtaining an increased therapeutic index from ionizing radiation. For external radiation in hyperthermic conditions, blood-flow modulation and the differential kinetics of blood flow between tumor and normal tissue are crucial for sequence adaptation to achieve therapeutic gains, maximal additive effects or even synergistic effects [188-190]. Vascular thermotolerance appears most desirable in this context. With respect to confining the treatment to the lesion, the association with brachytherapy appears straightforward, but sequence adaption and especially possibilities for fractionation are more restricted, even if this technique is now minimally invasive [191,192]. Other modalities combining hyperthermia and chemotherapies (thermochemotherapy) can be extremely advantageous depending on the chemotherapeutic agent [9,146]. This combination effect is more complex and far less understood for thermochemotherapy than for thermoradiotherapy. The effect depends on the many parameters that heat variably affects, such as tumor and/or compound metabolism parameters; very important but difficult-to-predict pharmocodynamic and pharmacokinetic parameters; and a direct and strong pH-dependency for many compounds (Table 1.1)[193]. Photodynamic therapy depends on oxygen levels and on the pharmacodynamics and pharmacokinetics of the photosensitizer. This method has a prominent synergy with hyperthermia and is indeed often intrinsically generated by the devices used [43,194,195]. Ultimately, hyperthermia appears to be a potent method to cope with the clinical issue of hypoxic tumor areas, which are responsible for relapses and failures of many treatments. For the treatment of problematic hypoxic tumor areas that escape hyperthermic treatment or other tumor oxygenation methods [196,197], hypoxic toxins have gained increased interest [198,199]. Their selectivity relies on

Table 1.1: Influence of pH and temperature on the activity of important chemotherapeutic agents.

conditions of temperature	37°C			Hyperthermia		
pH	**< 7.0**	**7.0 –7.4**	**>7.4**	**< 7.0**	**7.0–7.4**	**>7.4**
Chemoterapeutic agent						
Cyclophosphamide	++	+				
4-hydroxyperoycyclophosphamide	++	+				
Mafosamide	++	+				
Meclorethamine	++	+				
Melphalan	++	+				
Chlorambucil	++	-				
Nor-Nitrogen mustard	++	+				
Ifosfamide	+	+				
Triethylenemelamine	++	+				
Thiophosphamide	++	+				
Methylmethane sulfonate (MMS)	+	+	+	+++	++	
Bis-chloroethylnitrosourea (BCNU)	+	+	+	++++	++	+
Cyclophexylchloroethyl-nitrosourea (CCNU)	+	++				
Thiotepa	++	+				
Methotrexate	+	+	+	++	+	+
5-fluorouracil	++	+				
Bleomycin	+	+	+	++++	++	+
Mitomycin C	++	+				
Amphotericin B	+	+	+	+++	++	+++
Doxorubicin	+	++				
Mitoxantrone	+	++				
Vinblastine	+	++				
$PtCl_4(Fastblack)_2$	++	+		+++	++	
Cisplatine	+++	+		++++	++	+
1,2.diamono-r-nitrobenzene) dichloroplatinum(II) (Plato)	+	+		+	++	
trans-bis(2-amino-5-nitrothiazole)dichloroplatinum(II) (Plant)	++	+		++	+	
Paclitaxel	+	+		+	++	

Legend: This table shows how variations in pH and temperature can greatly modulate the efficacy of chemotherapy. It should be noted that these parameters vary within the tumor, depending on the pathophysiological characteristics of the region considered and on differences between the intracellular to extracellular compartments. This variability is known to be further modulated by hyperthermia (as discussed above). Moreover, variation within a single cell should also be considered. For instance, doxorubicin, a basic drug, may be trapped within an acidic vesicle as a mechanism of resistance. When considering acidic tumor regions, it has been reported that the effects of methylmethane sulfonate (MMS), bis-chloroethylnitrosourea (BCNU), bleomycin and amphotericin B may strongly benefit from hyperthermia. These molecules would therefore be ideal candidates for drug delivery systems that are also capable of generating hyperthermia. To a lesser extent, this holds true for methotrexate and platinum derivatives, which are in widespread use. Adapted from [193].

intracellular metabolic conversion, and entrapment in an active form is only possible in the reducing conditions associated with hypoxia. Notably, the effects of tirapazamine, a well-established hypoxic cytotoxin, have been shown to be inhibited by DMSO, because this organic solvent is a ROS scavenger [198]. In turn, modulations of physiological parameters and/or the tumor microenvironment have been more recently proposed as adjuvants to hyperthermia. Systemic blood flow manipulations have shown positive results [200]. It should be emphasized that some techniques allowing for locally blood flow manipulation are relevant to the pharmaceutical formulation presented below. Clamping procedures that can stop tumor's a blood supply have demonstrated a drastic dose diminution for an isoeffect of hyperthermic treatments. A tumor treated by clamping procedures appears approximately 2-fold more thermosensitive. Moreover, there is a vanishing of the transition at 42.5°C in the Arrhenius representation, indicating that thermotolerance is suppressed [42,201]. In terms of complete tumor responses, a delay of 60 min between clamping and subsequent heating appears far more beneficial than 30 minutes. Importantly, no cures were observed when heat was applied immediately before clamping or after the release of the clamp. When clamping is not possible, similar results can be obtained with chemoembolization, the alternative technique of choice detailed in section 3.

1.1.2.4 Hyperthermia and immunological considerations

As previously outlined, interactions of HSFs with other transcription factors account for the complex regulations of the heat shock response [95,119]. Activation of HSF1 by the transcription factor nuclear factor associated with IL-6 (NF-IL6) and by the INF-γ–associated transcription factor STAT-1 (opposite to STAT-3) may account for capacity of these two cytokines to activate stress response genes [202]. In turn, HSFs can inhibit the activating nuclear translocation of the transcription factor NF-κB [203], which regulates transcription of several pro-inflammatory cytokines and chemokines (e.g., TNF-α, IL-1 and IL-8). This effect was reversed 6 h after heat-shock, concomitantly with the return of HSFs (primarily HSF1) to the inactive state. NF-κB is central to the inflammatory process [204,205]. Moreover, most documented protective anti-inflammatory aspects associated with stress response genes can be related to the HSP-independent, anti-inflammatory effect of HSF activation by compounds or

stress factors, including hyperthermia itself [127]. HSPs, notably HSPA8 (HSC70; HSC71; HSP71; HSP73) and/or HSPA1A and HSPA1B (HSP70-1 or HSP72 and HSP70-2, respectively), are factors of intracellular and extracellular importance in cancer biology [156,206]; the antitumoral immune response [207]; several inflammatory diseases; neurodegenerative diseases [208]; transplant rejection [209]; and as therapeutic marker, targets or immunoadjuvants [210]. Augmentation of HSP levels is correlated with various disease features [95]. HSPs are involved distinctly in the pathophysiological contexts of inflammatory and autoimmune diseases and cancer. Inflammatory diseases such as asthma are based on the sustained antigen presentation, which is associated with increased HSP levels. In these circumstances, the pro-inflammatory aspects of HSPs appears to result from the increased viability of cells involved in the deleterious deregulation of immune response. The increase in viability and antigen presentation, a result of high HSP levels, leads to self-perpetuation of the inflammatory disease. In contrast, tumors of primary interest for hyperthermia treatment may certainly be inflammatory, but a decrease in the body's immune response to the tumor contributes to this pathophysiological process. Heightened levels of HSPs and the possibility of localization to the surface membrane are noticeable characteristics of cancer cells [127]. Evidence of the importance of HSPs is that most tumor-infiltrating lymphocytes (TILs) recognize HSPA1A (HSP70-1 or HSP72, the canonical heat-inducible isoform). Moreover, the basal expression of HSPA1A on the extracellular surface of tumor cells is able to induce non-specific cellular immune responses involving MHC-independent cell lysis. This occurs through γδTcR and/or NK cells, neither of which are MHC-restricted. Apoptosis triggered by NK cells is primarily mediated by the Fas-ligand, and this event has been shown to be independent of HSPs levels. Other apoptosis pathways, however, are inhibited by HSPs, as previously discussed. HSPA8 (HSC70; HSC71; HSP71; HSP73) and many other HSPs, including HSPA1A (HSP70-1; HSP72) and HSPA1B (HSP70-2), lack the hydrophobic leader sequence necessary for addressing proteins to the cytoplasmic membrane, and the mechanisms of their surface membrane localization are not clearly understood [127]. Hyperthermia can potentiate surface membrane localization of HSPs through their induction or upregulation, through the heat-induced cytotoxicity, morphological alterations and abnormal protein localization, as discussed previously. One debated explanation of HSP relocalization at extracellular membrane level relies on cell death and membrane disruption [211]. This mechanism could be

prominent for hyperthermia. In conjunction with *HSP*s induction, this mechanism would be enhanced to an even greater extent given that cytotoxic temperatures can be focally reached during local hyperthermia treatments. In other contexts, interactions of HSPAs (HSP70 family) with normal and aberrant proteins are emerging as a unifying theme of membrane anchorage [127]. In the context of cancer therapy, a very profitable aspect of extracellular HSPs complexes relies on the striking capability of peptide-HSPs to trigger immune responses. Peptide-HSPs complexes are extensively studied as ideal cancer vaccines that, as described by the homonculus theory, allows for non-MHC-restricted, specific immune responses [212]. This concept is of particular importance for the hyperthermic treatment of cancer because of i) the important hyperthermia-induced modulation of the immune response to the tumor and ii) it could further explain the indirect antitumoral efficacy of hyperthermia.

1.2 Current technical status of induced hyperthermia

1.2.1 Physical modalities for induced hyperthermia

Whole-body hyperthermia is generally achieved through a heating jacket or bath. Regional hyperthermia can be achieved through heated perfusion or the interaction of non-ionizing electromagnetic radiations (EM) with tissues. The types of EM radiations include radio frequencies (RF, hundreds of kilohertz to a few megahertz) and microwaves (MW, hundreds of megahertz to ca. ten gigahertz). Ultrasound (US) can also be used for regional hyperthermia [134]. The interaction of the electric and/or magnetic components of the EM radiations with body tissues locally deposits energy that ultimately turns into heat, i.e., an increase of kinetic energy at the molecular level. This thermal effect requires a high electromagnetic field (EMF) exposure to be associated with the desired temperature increase for significant biological effects. The marginal biological effects associated with “athermal” and “nonthermal” modes, specifically observed at low-level exposures, are unclear and primarily debated for occupational safety concerns [134,213]. Below approximately 1 MHz, the dominant action of EMF relies on the induction of electric currents in the body. A possible effect of

EMF at low frequencies is thought to be related to the ability, through magnetic induction, to stimulate eddy currents at cell membranes and in tissue fluids [134]. Common EM and US modalities poorly confine heat deposition to the targeted tissue volume and difficultly reach deep-seated localization within the human body. EMF treatments are especially impeded by adverse inductive effects (e.g., hot spots, burns of the body's surface, which increase with body radius) [84]. To achieve the deep localizations and to better confine heating when RF, MW and US are used, the basic single-element devices of the early 1980s evolved into adjustable, multi-element devices based on spatially precise constructive interference. These devises are recently used or in final stages of development.

Alternative approaches capable of confining energy deposition from an external power source make use of an implantable or injectable dedicated material, referred to as seed. Injectable air or gas microbubbles used as contrast agents can be used for deposition of US energy through cavitation [214]. Gold nanoparticles can enhance heat conversion with RF and photo-thermal therapy [215]. Power deposition through ferro- and ferrimagnetic material, which can concentrate magnetic flux much more efficiently than endogenous paramagnetic tissues, is also possible when the external source is an EMF or an alternating magnetic field (AMF), the latter often being preferable in some respects [216]. This technique is commonly referred to as magnetically induced or magnetically mediated hyperthermia. As mentioned, potentially deleterious effects, such as external fat layer burns and hot spots, can be observed when magnetic induced hyperthermia is clinically applied. These effects are associated with electric fields and related currents induced by AMF. As a first approach, the induced current density can be taken as proportional to the product of the magnetic field strength H and frequency f. The $H \cdot f$ product is generally considered to be the best predictor of these side effects. Specifically in clinical situations, when AMFs were applied for the treatment of human prostate tumors, values above $5 \cdot 10^8$ $A \cdot m^{-1} \cdot s^{-1}$ were associated with hot spots in the particularly sensitive pelvic fold [217-220]. In other locations, higher values of $13.5 \cdot 10^8$ $A \cdot m^{-1} \cdot s^{-1}$ could be clinically applied for hyperthermic treatment of glioblastomas without triggering side effects during skull exposition [217,221]. Higher values were only applied in less relevant experimental contexts (e.g., in mice or *ex vivo*) [222,223]. These limits should be kept in mind when evaluating the clinical potential of formulations intended for hyperthermia treatment. Experimentally, higher values of $H \cdot f$ ($81 \cdot 10^8$ $A \cdot m^{-1} \cdot s^{-1}$) in the form of pulses of very high

amplitude have been reached without adverse effects in mice [224].

1.2.2 Inductive modalities

The first inductive approaches were based on heating via Joule effect of eddy currents induced in a metallic conductor, which were produced by the magnetic component of an external EMF. This was applied to metallic elements used for other indications (orthopedic elements, stents) and to dedicated material specially developed for this use, known as thermoseeds [225]. Ceramics and glasses, already clinically applied in bone surgery, can be made to be inductively heated through the incorporation of metallic constituents, rendering them useful for further treatment of bone neoplasias. Implantable rods have also been developed for soft tissue indications. *In situ*, a thermoseed acts as a focal heat source, rapidly reaching very high temperatures that are associated with a steep temperature gradient in the surrounding tissue. Thus, homogeneous heating of the target volume requires the insertion of thermoseeds in adequate number and in the correct pattern. The limit of this approach is the poor control of heat distribution, with focal underheating and overheating. Soft magnetic materials have been used to interact more specifically through magnetic induction with low-frequency EMFs and pure AMFs [216,226,227]. Among these materials, ferro- and ferri-magnetic iron oxides (maghemite, magnetite) are recognized as the most biocompatible. This approach benefits from the development of pure AMFs, which have the advantage of reaching deep-seated locations with significantly less induction of adverse eddy currents typically encountered with using high-frequency EMFs. Magnetization depends on the magnetic permeability of the material, which in turn depends on the temperature. Above a specific temperature, corresponding to a threshold thermal energy that overcome spin lattice organization, namely the Curie point (or Néel temperature), the material loses its magnetic permeability. This annihilates magnetization and magnetic interactions, and heat dissipation ceases. This occurs for common magnetic materials at high temperature. Hematite, magnetite and maghemite have curie points of 956, 850 and 820 – 986°C, respectively. For alloys, however, the Curie point may be lower depending on the lattice composition. This property allows the development of so-called self-regulating thermoseeds, which are composed of alloys with a Curie point set precisely at the maximum

temperature desired for clinical applications [228,229]. Barium is classically used in such alloys but is toxic. Alternatively, when considering pure magnetic interactions with AMFs, the mechanisms of heating rely on mesoscopic and microscopic magnetic considerations. Observation of different magnetic samples at this level, in the field-free state, reveals uniformly magnetized regions or domains, with a randomized orientation pattern [230]. This is best described by statistical mechanics with magnetic domain theory [230]. One domain in a lattice is represented by a population of molecular dipoles with isotropic orientations (magnetic molecular fields). These domains are of finite size and are enclosed by a bordering population of molecular dipoles with anisotropic orientation, or domain walls [230]. The randomly patterned magnetic domains have a resultant zero magnetization at the macroscopic level. An isolated domain, referred to as a single domain, is only possible below a minimal domain wall size that depends on the lattice composition [216]. Above this critical size, the domain walls divide the lattice into a multi-domain structure. This accounts for an important distinction between multi-domain and single-domain magnetic structure of ferri- and ferromagnetic materials at mesoscopic levels. The domain structure also drastically changes the magnetization process in static or dynamic conditions. As a consequence, the mechanisms of heat dissipation primarily contributing to heat losses in an AMF (alternating or rotating) should be considered separately [231].

1.2.3 Magnetic losses

1.2.3.1 Hysteresis losses

A multi-domain magnetic microstructure is characterized by hysteresis losses. Magnetization processes occur through domain-wall displacement such that domains preferentially oriented along the axis of magnetic induction grow at the expense of the other, non-preferentially oriented domains. Domain wall displacement occurs through the rotation of each constitutive molecular dipole. Withdrawing the magnetic induction will not return the sample to its initial state but will result in an axial remnant magnetization at macroscopic level. The amplitude of this macroscopic magnetization depends on the amplitude of the magnetic induction up to a limit referred to as the saturation magnetization (M_s),

characteristic of ferro- and ferrimagnetic spinels. If the axial magnetic induction is inverted, as occurs with an AMF, the same process takes place in the opposite direction, and macroscopic magnetization will decrease. The amplitude of the magnetic field necessary to reach zero macroscopic magnetization is referred to as coercivity (H_c) (Figure 1.7C). Larger amplitudes of magnetic induction will allow remagnetization of the sample in the inverted direction, still involving the motion of domain walls. This defines a hysteresis cycle, experimentally characterized by static magnetometry using loop measurements. Graphically, the loop encloses an area referred to as the hysteresis area. The characteristic parameters of loop measurements, remnant magnetization, coercivity and hysteresis area can be linked to the heat loss obtained in dynamic conditions. Therefore, hysteresis area and power loss will critically depend on the amplitude of the AMF, which should be specified with material characterization. Thermal energy is specifically dissipated by domain wall motion through orbital friction during molecular dipole reorientation. Understanding and modeling heat dissipation more precisely remains a challenge that requires precise characterization of complex systems, such as those developed for medical applications.

1.2.3.2 Losses by magnetic relaxations

When converging on a single domain, the collective reaction of the molecular dipoles of the domain to the magnetic field can be regarded as that of a single magnetic moment. This representation allows for the description of magnetic relaxations of isolated single domains following magnetic moment reorientation itself resulting from the changes in the direction of magnetic induction. This can explain two striking characteristics of ferri- and ferromagnetic material, which are comprised of isolated single domains devoid of interactions at temperatures, frequencies and time scales of interest in hyperthermia applications (room or body temperatures, frequencies up to the low MHz range). First, the magnetic dipole moment of the domains can relax freely following removal of magnetic induction, and no remnant magnetization or coercivity is observed. Such ferri- or ferromagnetic materials appear therefore to adopt a pseudo-paramagnetic behavior referred to as superparamagnetism. In

pharmaceutical applications, superparamagnetic behavior is desired to prevent adverse magnetic aggregation in the body, which is especially critical for the intravenous route. These magnetic relaxations also account for the heat dissipation in AMFs, which is known to be highly efficient [232]. Magnetic relaxations of superparamagnetic materials comprise two contributing mechanisms: Néel relaxation and Brownian relaxation [233]. Néel relaxation is based on cooperative rotation of each individual molecular dipole of a static lattice. The dipoles' population collectively relaxes into a random orientation and thermal energy arises from orbital friction and dissipation to the environment. It is worth emphasizing that Néel relaxations require no displacement of the domain within the lattice or in space, which should be consider for fine particles of magnetic material free to move. In contrast, for such magnetic particles in a viscous environment, the Brownian relaxation is purely based on the displacement in space of the whole domain, i.e., the magnetic particle, without any magnetic dipole individual rotation. Brownian mechanism of relaxation is not possible when single domains are immobilized [233]. Energy dissipation during Brownian relaxation is based on heat loss though viscous friction within the milieu, the temperature of which then rises. The magnitude of Brownian relaxation of particulate magnetic materials decreases with increasing hydrodynamic radius of the particles and with the viscosity of the environment [234], Brownian relaxation impeded for exceeding values for radius or viscosity are substituted by Néel relaxation [235]. The magnetic iron oxides maghemite or magnetite [236] are the two ferrimagnetic materials now in clinical use. Mono-domain particles are referred to as superparamagnetic iron oxide nanoparticles (SPIONs). Reproducible SPION synthesis methods are available [236], but highly controlled, mono-dispersed, mono-domain magnetic particle dispersion is still a challenge. Practically, this has strong repercussions for heat dissipation capacities [237,238]. As for raw magnetite SPIONs, the protonation and deprotonation of the surface oxygen groups and OH^- adsorption [239] explain the variation of the zeta potential value with pH (0 mV at pH = 6.5, positive at lower pH and negative at higher, biological pH) [240]. Because of their high surface energy, SPIONs agglomerate rapidly (4h) and irreversibly. This results in a loss of superparamagnetism from dipole-dipole attractions, leading to ferrimagnetic behavior characteristic of larger particles. The cytotoxicity of bare SPIONs has been demonstrated [241] but can be prevented by suitable coatings. This fact illustrates the importance of stabilizing agents or coatings to control biological interactions

(see review by Gupta [242]). The FDA has approved the clinical use of coated magnetite (Fe_3O_4) SPIONs as MRI contrast agents in products such as Endoderm™, Feridex® and Resovist®. Numerous formulations embed mono-domain particles into therapeutic systems for modulation by static magnetic fields [243]. If the SPIONs are not durably coated or entrapped, dispersion of SPIONs in the body should be considered. Magnetic fluid hyperthermia is currently the most advanced clinical modality of magnetically mediated hyperthermia. This treatment is based on the injection of dextran-coated SPIONs that generate heat dissipation in the presence of a very controlled AMF (Mag-Force®), which is safe for human exposure. This technique, which is outside of the scope of this paper, has been recently reviewed [217,244,245].

As discussed in the following sections, both multi- and single-domain magnetic microstructures may contribute to the development of complex pharmaceutical formulations appropriately designed for magnetically mediated hyperthermia in physiopathological situations. Ceramics, glasses, glass-ceramics and cements are developed for the application of hyperthermic treatment in hard-tissue pathologies associated with solid tumors. Injectable formulations carrying magnetic particles are interesting for magnetically mediated hyperthermic treatments of soft-tissue tumors. Liposomal formulations have been also extensively investigated for use in both types of tumors.

2 Formulations for local hyperthermia treatment of hard tissue tumors

Glasses, ceramics and glass-ceramics compose one group of biomaterials used in the treatment of bone pathologies, notably in cases of tumor lesions. Cements comprise a second group [246].

The first group is classically and broadly defined by broad inorganic/non-metallic compositions.These materials can be synthesized by thermal processing. Five classes are distinguished with respect to microstructure criteria [247]: i) glass (rapid melt quenching); ii) cast or plasma-sprayed polycrystalline ceramics (high temperatures but short exposition time); iii) liquid-phase sintered (vitrified) ceramics

that are highly resistant to mechanical stress; iv) solid-state sintered ceramics; and v) polycrystalline glass-ceramics. Alternatively, wet chemical synthesis methods allow for the formation of very homogeneous glasses and ceramics at temperatures well below the normal temperatures required to sinter high-density bodies with uniform microstructures [248]. Two basic methods for wet-synthesis are precipitation from colloidal suspension (usually spray-drying) and sol-gel phase transition. The latter technique is used to create "sol-gel" glasses at room temperature. Macroporosity and interconnected microporosity are important parameters for osteointegration [247], and porogens can be used during processing to introduce and control porosity. With increasing porosity, the strength of material decreases rapidly [247]. The material is often represented by its final composition after processing, also referred to as composition system. In one standard system, for example, SiO_2, CaO, P_2O_5, and Na_2O can be obtained by thermal processing of precursor components, such as Na_2CO_3, $CaCO_3$, SiO_2 and $CaHPO_4$. Certain composition systems have shown the capability to bond bone (or soft tissues for certain glasses) and are considered bioactive [249](Figure 1.7A). This is well known for mineral phases such as calcium phosphates (monetite, brushite, whitlockite, tricalcium phosphate, hydroxyapatite) and calcium ionosilicate (Wollastonite). In a biological environment, highly localized surface chemical reactions, primarily dissolution and precipitation, act on silanol groups and crystallites that chiefly contain calcium. This process ends with the formation of a hydroxyapatite-rich layer and implant bonding to the bone (osteointegration). Slight changes in composition are known to dramatically affect the bioactivity spectra. Even trace level of multivalent cations, such as Al^{3+}, Ti^{4+} and Fe^{3+}, can interfere with the complex reaction chain that permits bioactivity [247]. Iron components should therefore be carefully introduced into the composition of bioactive systems [250]. Only 3% w/w of Fe_2O_3 can dramatically slow the formation of the hydroxyapatite-like layer that contributes to bone bonding and bioactivity in commonly used ceramics [251]. The versatility in the composition and processing of these materials allows for an infinite variety of original magnetic materials. Crystallization, however, may require precise, delicate control to obtain magnetic phases relevant for *in vivo* applications. Such care would, for instance, be required for the generation of clinically approved magnetite or maghemite and for original formulations with efficient heating properties. Elemental iron has been observed following the processing of the iron oxide precursor, not only in populations of magnetite particles,

Figure 7 (on opposite page): Processing, microstructure and magnetic properties of glasses, ceramics, glass-ceramics, bulk or particulate materials, intended for magnetically-mediated hyperthermic treatment of solid tissue tumors.

A. Top, left: Ternary diagram illustrating the compositional dependence of bone and soft tissue bonding on Na_2O-CaO-P_2O_5-SiO_2, with constant 6 wt % P_2O_5 (adapted from ref [247]); fabrication of interesting bulk, particulate and biphasic materials. Circular curves within the diagram depict the iso-index line of bioactivity (I_B). The continuous gray line depicts the limit isocurve for bioactivity ($I_B = 0$), thus enclosing bioactive systems. The dotted gray line delimits $I_B = 2$. The dashed gray line is the isocurve for $I_B = 5$. The black line is the isocurve for $I_B = 8$, large enough to allow soft tissue bonding. The bold black line is the isocurve for $I_B = 10$. Region *: resorbable glasses that disappear within 10 days (bioactivity is limited to a surface hydration layer of SiO_2, type I or II response). Region **: nearly inert material. Region ***: technically impractical and therefore not tested as implants. On the basis of this material, iron precursors are added to obtain composite glass-ceramics with magnetic iron oxide. The obtained ferromagnetic material with multi-domain magnetic microstructures (simple arrows depicting molecular moment) can be used as implants in surgery. The solid solution is marked by (+). When crushed, it can be injected or incorporated into biphasic materials. These materials will heat through hysteresis losses in AMFs (see panel **C**). The hysteresis losses depend on the area under the hysteresis curve. Multi-domain magnetic characteristics appear for diameters larger than Ds (single-domain diameter, depending on the phase). The magnetization curve of a multi-domain magnetic material is depicted as the black line in the magnetization sketch. The gray line corresponds to demagnetization by cycling, with decreasing amplitude of the static magnetic field, illustrating how hysteresis curves depend highly on history and measurement conditions.

B. Sol-gel processing: iron precursors are precipitated in the pores of the silica matrix, directly in magnetic iron oxides or in non-magnetic iron oxides that are subsequently oxidized into magnetic iron oxides. In particular, the mesoporosity of silica processed in this way allows for generation of magnetic iron oxides small enough to be superparamagnetic, SPIONs. The corresponding magnetization curve is depicted as a dotted black line in the B-H magnetization graph (**see panel C**). This curve, with negligible coercivity, corresponds to a pure superparamagnetic behavior, for particles smaller than a critical diameter D_p (depending on phase). A single superparamagnetic nanoparticle is depicted as an arrow encircled in an oval white area, suggesting the molecular moments acting together as a large, resultant dipole free to rotate. Most often, a final crushing step is applied, resulting in glass microparticles that embed several SPIONs. Alternatively, pre-synthesized superparamagnetic nanoparticles can be incorporated in a silica matrix through sol-gel processing. In a last approach, pre-synthesized silica microparticles can be used as templates and grafted with SPIONs. All these materials show superparamagnetic behavior. Heat dissipation from superparamagnetic nanoparticles can occur through two types of magnetic relaxations in AMFs: i) Brownian and ii) Néel relaxations. i) Particles with a hydrodynamic radius small enough to dissipate heat through Brownian relaxations do so through whole particle reorientation. Brownian relaxations are impeded by high viscosity of the medium and large hydrodynamic radii. ii) When considering immobilized particles, only Néel relaxations are possible. Here, all magnetic dipoles populating the mono-domain reorient synchronously in a free direction following magnetic excitation, as is often depicted by the free rotation of the macroscopic dipole. This applies to large microparticles that carry several, not interacting mono-domain magnetic particles.

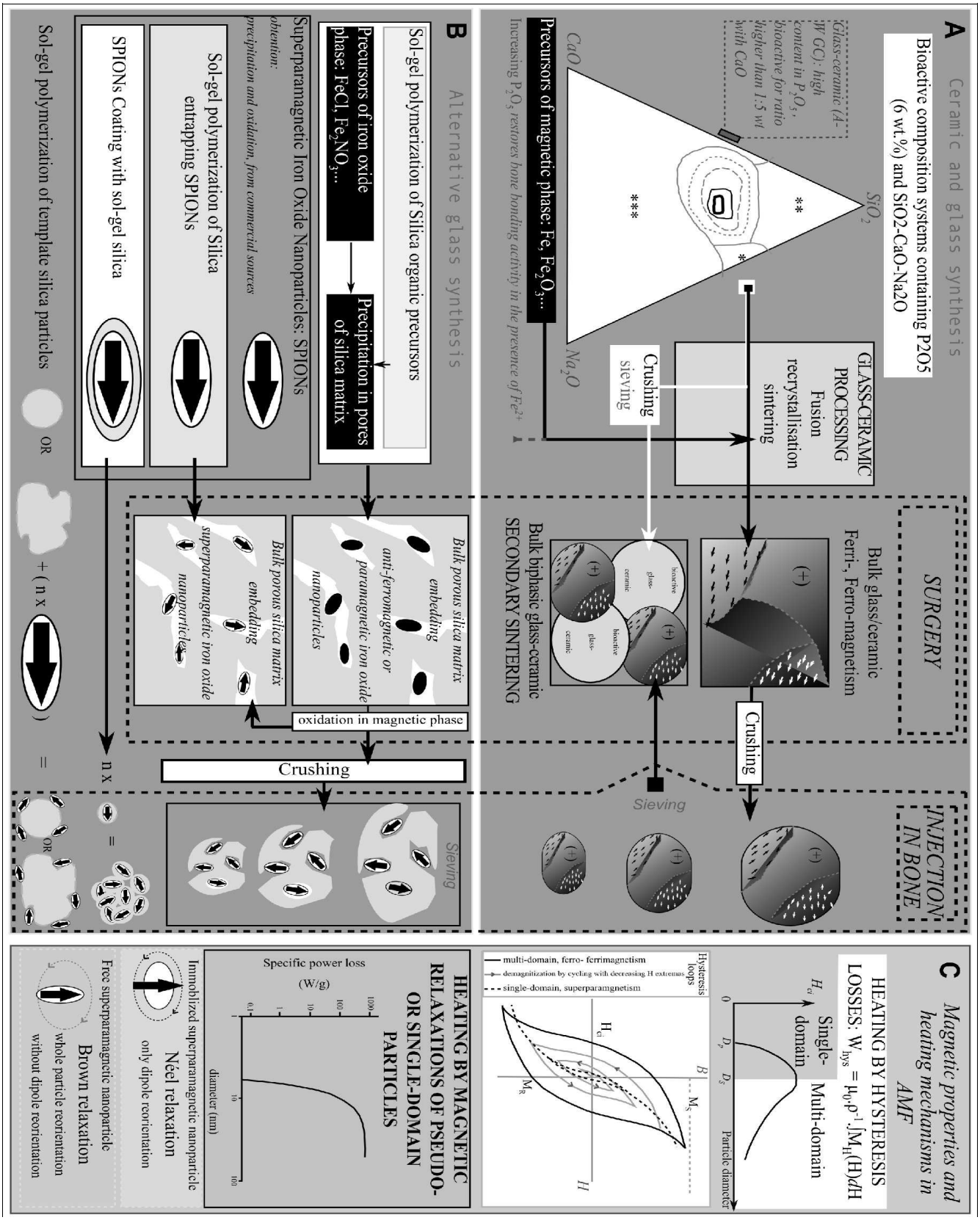
A
Ceramic and glass synthesis
Bioactive composition systems containing P2O5 (6 wt.%) and SiO2-CaO-Na2O
SiO2
CaO
Na2O
Glass-ceramic (4-HF GC): high content in P2O5, bioactive for ratio higher than 1:5 wt with CaO
GLASS-CERAMIC PROCESSING
Fusion
recrystallisation
sintering
Crushing
sieving
Precursors of magnetic phase: Fe, Fe2O3...
Increasing P2O5 restores bone bonding activity in the presence of Fe2+
SURGERY
Bulk glass/ceramic
Ferri-, Ferro-magnetism
Crushing
Bulk biphasic glass-ceramic
SECONDARY SINTERING
Sieving
INJECTION IN BONE
B
Alternative glass synthesis
Sol-gel polymerization of Silica organic precursors
Precursors of iron oxide phase: FeCl, Fe2NO3...
Precipitation in pores of silica matrix
Superparamagnetic Iron Oxide Nanoparticles: SPIONs
obtention:
precipitation and oxidation, from commercial sources
Sol-gel polymerization of Silica entrapping SPIONs
SPIONs Coating with sol-gel silica
Sol-gel polymerization of template silica particles
OR
+ (n x
Bulk porous silica matrix
embedding
anti-ferromagnetic or paramagnetic iron oxide nanoparticles
Bulk porous silica matrix
embedding
superparamagnetic iron oxide nanoparticles
oxidation in magnetic phase
Crushing
Sieving
n x
=
OR
C
Magnetic properties and heating mechanisms in AMF
HEATING BY HYSTERESIS LOSSES: W_hys = μ0.p-1.∫MH(H)dH
Single-domain
Multi-domain
Particle diameter
multi-domain, ferro- ferrimagnetism
demagnitization by cycling with decreasing H extremas
single-domain, superparamagnetism
Hysteresis loops
HEATING BY MAGNETIC RELAXATIONS OF PSEUDO-OR SINGLE-DOMAIN PARTICLES
Specific power loss (W/g)
diameter (nm)
Immobilized superparamagnetic nanoparticle
Néel relaxation
only dipole reorientation
Free superparamagnetic nanoparticle
Brown relaxation
whole particle reorientation
without dipole reorientation

with ferri- and superparamagnetic properties depending on the volume of crystallite, but also less desirably as paramagnetic Fe^{2+} [252]. Iron can be also found in numerous less desirable phases (such as anti-ferrimagnetic hematite) and minor contaminating phases responsible for Fe^{3+} leaching out and impeding bioactivity. Historically, iron was incorporated in a metallic state, exactly as for thermoseeds, or in biocompatible but nearly inert glasses or ceramics with limited hysteresis heat losses in AMFs, allowing for proof of concept [253]. Constant improvements in composition and processes now allow for the generation of bioactive forms of these magnetic materials. These contain well-defined magnetic iron oxide crystallite phases that can heat efficiently in AMF. This heating principally occurs through hysteresis losses or superparamagnetic relaxations. Bulk glasses or ceramics are often implanted by invasive surgery. The invasiveness is reduced by the administration of injectable particles (with excellent packing ability under shear stress) of these materials into voids, where they sustain only moderate mechanical stresses, but the osteointegration is enhanced by increased implant-bone contact area [247]. Here, wet chemistry synthesis methods (e. g. by spray drying) appear more appropriate than crushing to produce defined and controlled particle populations [248]. The potential of ceramic and glass matrices formulated into microspheres is also under investigation [254]. These can be mixed with organic phases, such as organoapatites, designed to mimic some aspects of the natural bone matrix [248]. Most of these biomaterials have been investigated as drug delivery systems [255], but few have been tested with respect to local delivery of magnetically induced hyperthermia. Both the bulk and particulate glass ceramic materials discussed in the two following subsections are summarized in a contextual sketch (Figure 1.7). Syringeable cements belong to the second group, allowing for minimally invasive direct injection into bones or bone tumors and osteoinduction. They will be addressed in detail in a subsequent section.

2.1 Magnetic ceramic, glass and glass-ceramic materials

The first inert glass ceramic ferrimagnetic material was introduced in a heterotopic mouse model for magnetically induced hyperthermia treatment of subcutaneous "syngeneic" murine mammary carcinoma, known to frequently metastasize in the bone. This glass-ceramic contained hematite and lithium ferrite [253]. Milled to particles with a diameter of 1.5 μm (ρ = 3.5 g·cm^{-3}), it could be injected through 22-26-gauge needles with high tolerability (up to 1 g intramuscular). Following direct intra-tumoral injection of 0.1 g and exposure to AMF (10 kHz, 39.8 kA·m^{-1}), temperatures could be raised by only 9°C (up to ~ 43.5°C) in 10 min. With a specific absorption rate in this AMF of only 1 W·g^{-1}, heating capacities were relatively low for *in vivo* application. No marked cytotoxicity was reported, and this approach was encouraged by a significant increase in survival rate and a number of complete responses. Following works were aimed at developing bioactive materials and improving heating capacities. The heating capacities of ferrimagnetic glass-ceramics developed using the system of CaO, SiO_2, Fe_2O_3 (hematite, as precursor of magnetite Fe_3O_4), B_2O_3 and P_2O_5 were investigated in healthy animal bone [256]. After two heat treatments, heat-generating glass-ceramic was crushed into granules for insertion in bone. This glass-ceramic contained wollastonite and 10 nm-diameter magnetite (Fe_3O_4) crystallites dispersed in a glassy matrix of CaO-SiO_2. This material had a saturation magnetization of 32 A·m^2·kg^{-1}, a coercivity of 9.5 kA·m^{-1} (± 796 kA·m^{-1} loop measurement) and a specific loss power (SLP) of 10^{-2} W·kg^{-1}, most often expressed in W·g^{-1}, here 10 W·g^{-1}, in a 100 kHz, 23.9 kA·m^{-1} AMF. SLP is occasionally referred to in literature by the less appropriate nomenclature of specific absorption rate (SAR). *In vivo*, the implanted bone reached the target temperature of 45°C, which was maintained for 30 min by modulating AMF amplitude. The surrounding muscles and distant bone reached 42°C. No hydroxyapatite layer was formed because of the leaching out of iron ions, as previously discussed [250,251]. Some bioactivity, however, was observed *in vivo*, as bone bonding and increased resistance to failure load with implantation time from 8 to 25 weeks, in contrast to basic glass. Wollastonite dissolution from the hydrated, glassy matrix, and interactions with biological fluids were proposed as

the mechanisms of bone bonding. Still, this slow increase in bonding may not be suitable for rapidly growing tumoral lesions. The antitumoral potential of heat produced in AMFs by ferrimagnetic glass-ceramics was then tested in an animal model of metastatic bone tumor animal model. This model consisted of an undifferentiated squamous cell carcinoma VX2 tumor strain grafted into the medullary canal of the rabbit tibiae [257]. Glass ceramics in thise system [256] were processed as described above [258] and were later studied in detail [259]. Glass-ceramic pins were inserted in medullary tibia canal, which bore tumors for both the sham operated and hyperthermia treatment groups. Control animals received no implantation. AMF was applied for 50 min. The ceramic surface reached a plateau temperature of 50°C within 10 min, whereas the extracortical bone surface reached only 42.5°C. Histological analysis 5 weeks after treatment revealed extensive tumor necrosis when compared to healthy tissues, whereas both control and sham groups displayed large vital, tumor tissue invading the bone. In radiological follow-up, the fracture rate was significantly lower in heated bone of the treated group than in the control or sham groups. When compared to controls, the displacement rate was significantly reduced in both ceramic-implanted groups, with or without hyperthermia treatment. These findings link the intrinsic value of hyperthermia for local tumor control to the functional benefits of ceramics in bone cancer lesions.

The microstructure, magnetic properties and bioactivity of a glass-ceramic material in the composition system 45% SiO_2, 45% CaO and 10% Fe_2O_3 (mol%) added with 3% w/w Na_2O was thoroughly studied by Real et al [260]. This glass-ceramic material contained a main crystalline phase consisting of wollastonite and a minor phase consisting of ϵ-$CaSiO_3$, both made of small crystallites. X-ray diffraction showed the absence of any crystalline iron oxide. *In vitro* testing demonstrated little iron leaching out and demonstrated bioactivity at days 20 and 40. On the basis of crystallography and Mössbauer spectroscopy results, the authors determined that ferroan-wollastonite ($CaSiO_3 \cdot Fe^{II}SiO_3$) and ϵ-$(Fe^{II},Ca)SiO_3$ were the main softer magnetic phase and the minor harder magnetic phases, respectively. In contrast, Fe^{III} would remain trapped in the glassy matrix at the initial 800°C glass melting step because of its high oxidation state. No hysteresis area or SLP in AMF has been reported. In addition, by adding a bioactive sol-gel glass phase to the magnetic glass phase before secondary heating, an original biphasic material was synthesized with improved bioactivity [261,262]. One phase

consisted of the previously studied magnetic glass with the composition 45% SiO_2, 45% CaO and 10% Fe_2O_3 (mol%), with 3% w/w Na_2O. The other bioactive sol-gel glass, with the composition 58% SiO_2, 6% P_2O_5 and 36% CaO (mol%), was obtained by hydrolysis and polycondensation of tetraethyl orthosilicate and triethyl phosphate (TEP) with $Ca(NO_3)_2$·$4H_2O$. Each phase was pulverized, and size fractions between 32 and 64 μm were selected. Powder from the sol-gel bioactive material was subjected to a final stabilization step by heating at 700°C. The glass-glass biphasic material was then obtained by mixing, pressing and heating the two pulverized glasses in 5:1, 2:1 and 1:1 mass ratios of magnetic glass to bioactive sol-gel glass. This biphasic glass-glass ceramic was micro- and mesoporous with a specific area more similar (or higher) to that of the melt glass than to that of sol-gel glass (14 $m^2 \cdot g^{-1}$). The only crystalline phase present was wollastonite (50 nm diameter). No crystalline phase derived from iron oxide was detectable, strongly suggesting the formation of the solid solution $CaSiO_3$.$FeSiO_3$ (ferroan wollastonite) as the primary magnetically ordered phase. Only the 1:1 biphasic glass ceramic material showed improved bioactivity. The low fraction of iron atoms in the final material led to low saturation magnetization between 0.012 to 0.021 $emu \cdot g^{-1}$. This is approximately one order of magnitude lower than for the model glass-ceramic previously studied, or for what can be extrapolated for 5% w magnetite spinel. A coercivity of 400 Oe (from +/- 20 kOe hysteresis loop) was reported. The possibility of hysteresis losses appeared to limit *in vivo* applications. The authors proposed to increase the iron oxide fraction in the magnetic glass system with the aim of increasing saturation magnetization, thereby allowing higher heating capacities. This was implemented in subsequent *in vitro* biocompatibility studies of similar biophasic glass-glass ceramics obtained from the same sol-gel phase. This phase was mixed in various proportion to a magnetic glass phase using a similar ptrotocol as described previously but with 20 mol% Fe_2O_3.[263] During the first days of incubation, there was a decrease in cell proliferation when compared with controls, reflecting perturbations of ionic exchange, chemical reactions and cell viability in a closed system. Nonetheless, this effect rapidly reverted and cell proliferation rate equalized after 7 days levels to those observed for TCP. Moreover, the large surface of magnetic glass grains was demonstrated to be the most favorable for cell proliferation.

More recent *in vitro* studies have examined ferrimagnetic glass-ceramic materials of the bioactive composition system SiO_2-Na_2O-CaO-P_2O_5-FeO-Fe_2O_3. These studies have helped to elucidate the

impact of nanoscale material structure and magnetic properties on heating capacity as a function of AMF [264-267]. Important results are summarized in Table 1.2. Ref. [264], describes the preparation of a ferrimagnetic glass-ceramic material through coprecipitation of water-soluble precursors in a basic medium. This step is followed by melting for 30 min at 1500°C and quenching by cooling at room temperature. Two concentrations of iron oxide precursors, 35 and 45 wt % exhibited striking discrepancies in microstructure (as determined by SEM, XRD and DTA), magnetic properties at room temperature (Vibrating Sample Magnetometry) and heat loss in AMF. The ceramic material with 45 %wt of iron oxide precursors revealed one primary iron oxide phase composed of magnetite nanoparticles of approximately 54 nm in diameter. The ceramic material with 35 %wt of iron oxide precursors had a final constitution 20 %wt magnetite nanoparticles of approximately 34 nm in diameter. The remaining 15 %wt of precursors presumably formed a solid solution. The increase in magnetite concentration clearly explains increasing saturation magnetization but is also known to decrease coercivity through anisotropic effects of the packing of nanoparticles [216]. Decreases in coercivity have also been linked to an increase in crystallite size and lower internal stress in the crystal phase generated during cooling [216]. Measurements of heat losses in AMF are frequently done with values of AMF parameters that are not in the acceptable range for clinical application (*cf.* paragraph 1.2.1). Here, one should keep in mind an approximate upper limit acceptable for humans in the value of the product of magnetic field strength with frequency, $H \cdot f$, of $5 - 13.5 \cdot 10^8$ $A \cdot m^{-1} \cdot s^{-1}$. Keeping $H \cdot f$ under the above range prevents adverse effects, including non-selective tissue heating induced by eddy currents (external fat layer burns and hot spots). The calculated $H \cdot f$ values for the AMF used by Bretcanu et al., as high as $170 \cdot 10^8$ $A \cdot m^{-1} \cdot s^{-1}$, would be difficult to apply clinically. Interestingly, however, the authors compared calorimetric determinations of heat loss under a dynamic magnetic field (40 $kA \cdot m^{-1}$, 500 Oe in the text, at 440 kHz.) to the determination of heat loss based on hysteresis curve loop measurements under two static magnetic field condition, one for ± 796 $kA \cdot m^{-1}$ (10 kOe), most often used for material characterization, and another for ± 39.8 $kA \cdot m^{-1}$ (500 Oe), much closer to clinically used values although too high for clinical applications. At ± 796 $kA \cdot m^{-1}$ (10 kOe), magnetization of the ferrimagnetic ceramic material reached saturation. Moreover, the integrated hysteresis loop area was higher with 45 % wt than with 35 % wt of iron oxide precursors (Table 1.2) because of the predominant

Table 1.2: Summary of the works of Bretcanu et al. with magnetic glass-ceramic materials.

Method of synthesis			Coprecipitation [a]		Traditional [b]				Coprecipitation [c]				Coprecipitation [d]
Proportion of iron oxide precursors °			35 % wt	45 % wt	45 % wt				45 % wt				45 % wt
Melting temperature (°C)			1500	1500	1400	1450	1500	1550	1400	1450	1500	1550	1500
Phase determined by XRD	Crystalline	magnetite	Main	Main	comp.	Main	Main	Pure	Main	Main	Pure	Main	Main
		indicative intensity of main peak §	8	14	3	5	7	9	4.5	5	6	4	*
		hematite	-	-	comp.	Minor	Minor	-	Minor	Minor	-	Minor	-
		indicative intensity of main peak	-	-	4	3.5	1	-	1	0.5	-	> 0	-
		Ca Silicate	-	-	-	Minor	Minor	-	-	-	-	-	-
		indicative intensity of main peak	-	-	-	0.1	0.1	-	-	-	-	-	-
	Amorphous at small angle		yes	yes	yes	yes	yes	yes	yes	yes	yes	yes	yes
Amount of magnetic phase (%wt)			20	45	20	22	24	34	36	39	46	42	45
Averaged size of crystallite in nm (XRD)			34	54	56	59	79	83	-	-	-	-	53
Saturation Magnetization, Ms (emu/g)			15	33	18.6	20.5	22.3	31.5	26	28	33	30	34
Field allowing saturation (Oe)			4000	2000	4000	4001	4002	4003	Not specified (~4000)				4000
Coercivity, Hc (Oe)			144	82	83	122	180	35	151	147	82	220	85
Remnant magnetization, Mr (emu/g)			4.45	2.45	1.62	2.8	7.4	1.07	3.86	3.73	2.45	5.83	2.4
Interpolated hysteresis area (erg/g of ceramic) for:		Loop ± 10 kOe (796 kA/m)	6150	14400	4900	7400	9100	4200	12000	13600	14450	20250	14500
		Loop ± 500 Oe (39.8 kA/m)	3850	1750	1500	2050	5150	900	2300	2700	1750	3000	1700
		Loop ± 60 Oe (4.8 kA/m)	-	-	-	-	-	-	-	-	-	-	15
ΔT °C/g of ceramic (1g in 20ml H2O)			93	36	40	41	87	27	39	40	36	41	35
Specific power loss in W/g of ceramic in AMF: 40kA/m, 440 kHz			65	20	28	29	61	19	27	28	25	29	25
Bioactivity *in vitro*			-	-	-	-	-	-	-	-	-	-	yes

Legend: References: a) [264], b) [266], c) [265], d) [267]. All magnetic properties were measured at room temperature. °corresponding composition of precursor systems: i) For 35% iron oxide precursor Na_2O (15.9), CaO (15.9), SiO_2 (29.3), P_2O_5 (3.9), FeO (10.9), Fe_2O_3 (24.1) (%wt). ii) For 45% iron oxide precursor, Na_2O (13.5), CaO(13.5) , SiO_2 (24.7), P_2O_5 (3.3), FeO (14), Fe_2O_3 (31) (%wt). § intensity of the ((311) at 35°) reflection of magnetite in XRD. * very detailed XRD characterization, cf ref [266].

effect of saturation magnetization. In contrast, at ± 39.8 $kA \cdot m^{-1}$ (500 Oe) the magnetic ceramic materials did not reach saturation, and the integrated loop area was higher with 35 wt % of iron oxide precursors (Table 1.2) because of the predominant effect of coercive fields. This percentage of iron oxide precursors was associated with a striking increase in SLP (65 $W \cdot g^{-1}$) when compared to 45 wt % iron oxide (20 $W \cdot g^{-1}$). The smaller crystallite size was demonstrated to be more efficient for heating in AMFs with lower field strengths, whereas larger sizes would more efficient in AMFs with larger field strengths. Three subsequent papers have further investigated the impact of varying melting temperatures from 1400 to 1550°C on microstructure, magnetic properties and heating capacities of ferrimagnetic glass-ceramic materials. These materials had a 45 wt % iron oxide proportion and were subjected to two processing methods: i) by melting coprecipitated precursors [265,267], as described previously, and (ii) a traditional melting process consisting in melting based on chemical-grade precursors [266] (see Table 1.2). Coprecipitated precursors of high purity and reactivity are entirely converted into magnetite at 1500°C, as demonstrated in [264], with a mean diameter of 54 nm [267] and high saturation magnetization (33 $A \cdot m^2 \cdot kg^{-1}$, or $emu \cdot g^{-1}$). This was in contrast to traditional melted glass-ceramic, with magnetite particles averaging 56 to 83 nm in diameters with increasing melting temperature. In this condition, precursors were not entirely converted in magnetite because of the formation of solid solutions, as in [261,262]. When the melting temperature was 1500°C, coercivity and remnant magnetization were highest, 14.3 $kA \cdot m^{-1}$ (180 Oe) and 7.4 $A \cdot m^2 \cdot kg^{-1}$ ($emu \cdot g^{-1}$), respectively. These high values were not observed at other melting temperatures. With a static magnetic field strength corresponding to that of AMF used for calorimetric experimentations, the integrated area of the hysteresis loop was strongly predictive of the SLP for all ferrimagnetic glass-ceramics incorporating 45 % w/w iron oxide precursors. For this composition system of precursors, glass-ceramics processed by coprecipitation and melting at 1550°C had the highest coercivity but intermediate remnant magnetization among various processes [265,266]. The corresponding area under the hysteresis curve for ± 796 $kA \cdot m^{-1}$ (10 kOe) is the highest, but this area is intermediate for ± 398 $kA \cdot m^{-1}$ (500 Oe), in accordance with the determined intermediate SLP. These observations are consistent with Hergt's findings with respect to magnetic particle size [238], demonstrating that the main parameter empirically describing hysteresis losses is coercivity. Eventually, the calculation of hysteresis losses can

be refined by taking saturation magnetization (M_s) into account [237].

Taking these results into consideration, the authors of the studies mentioned above made important proposals regarding materials and magnetic characteristics. First, variations in SLPs under AMFs are linked through to magnetic coercivity variations with crystalline phase, crystallite size, and number and homogeneity of the static magnetic domains [264]. The maximum heat dissipation associated with large coercivity can be explained by a microstructure that the authors proposed to be at the limit between pseudo-single domains and multi-domains, i.e. crystallites of 79 nm [266]. This size seems to relate to the static magnetic domain, which is larger than the dynamic domain (several hundreds and 170 Å, respectively [216]). Thus, considering the domains under dynamic conditions, TEM observations of single crystals of approximately 10 nm [267] correspond to a dynamic pseudo-single domain and, in agreement with [216], the magnetic relaxation would substantially change. In our opinion, highly efficient Néel relaxations could then be considered (Brownian relaxation excluded). With respect to the discrepancies resulting from variations in the processing method, the authors originally consider the contributions of eddy current and anomalous losses to AMF-induced heat dissipation. Anomalous losses are explained by the non-homogeneous structure of the magnetic domain, irregular movements of the domain walls, and impurities and stresses in the crystal lattice [264]. Finally, other important investigations have contributed to a better understanding of the microstructure and magnetism of magnetic glass-ceramic materials. These studies, however, were unfortunately not placed in context with studies of the heating capacities of these materials [268-272]. A great deal of work has been devoted to the incorporation of novel magnetic phase compositions in glass-ceramics. This effort aims to generate materials with larger saturation magnetization and, as for self-regulating thermoseeds of adequate Curie temperatures, above which heat dissipation ceased to avoid overheating. The phases described are not yet accepted for clinical use [273].

2.2 Glass/ceramic particles and microspheres

Ceramic materials can be also found in various particulate forms intended for direct use or as fillers. These materials can find application in minimally invasive surgical bone treatment procedures and include crushed powders, granules, microparticles and microspheres. These formulations are developed to allow syringeability and to preserve *in-situ* properties such as bioactivity. As stated above, all glass-ceramic materials can be advantageously used in this form, although most published work on these materials relates to the bulk material. Unfortunately, only a few studies have investigated syringeability, as the chief concern is often the characterization at the bulk level as a function of processing conditions. In most *in vivo* investigations glass-ceramic particles are pressed into bulk samples and inserted, instead of injected, to avoid variability related to the injection. Micron-sized particulate systems have large advantages in terms of syringeability. The size is large enough to have high packing and flowing ability but small enough to be compatible with minimally invasive devices as small as catheters.

An injectable ceramic powder material with a specific magnetic phase has been tested in model agar spheres [274]. Here, the specific biocompatible magnetic phase was $Mg_{1+x}Fe_{2-2x}Ti_xO_4$, where the values of x are 0.35 and 0.38 and the Curie temperatures are approximately 77 and 42°C, respectively. It should be stressed once more that when the particle reaches the Curie temperature, magnetic properties are lost and heat dissipation stops, preventing overheating. The precursors, MgO, Fe_2O_3 and TiO_2 were pre-sintered for 22 h at 703°C, pelletized, pressed into the shape of a disk and sintered at 1200°C. Lastly, particles of 8 μm in diameter were obtained by crushing in a mortar. Particles were dispersed in a spherical agar phantom as a tumor model, embedded in a larger agar gel as a model for surrounding tissue, and submitted to AMF at a frequency of 230 kHz and magnetic field strengths varying from 1.6 to above 16 $kA \cdot m^{-1}$ (20 to above 200 Oe). The hysteresis loss was calculated using the area enclosed by hysteresis loop curve in a static magnetic field, although no field value was reported. The SLP was derived from the gradient of the experimentally determined temperatures. The saturation magnetization and Curie temperature were decreased by increasing the stoichiometric parameter x. When submitted to

AMF with increasing magnetic field strengths, the ceramic powder reached an increasing equilibrium temperature, asymptotically approaching T_c. Below 8 $kA \cdot m^{-1}$ (100 Oe), hysteresis losses were strikingly predictive of the experimentally determined SLP, demonstrating that hysteresis loss is the unique mechanism of heat generation. Independently of the magnetic field strength, both hysteresis loss and SLP decrease linearly when the proportion of Ti atoms in the composition increases, i.e., increasing *x* decreases T_c. This effect is explained by the linear decrease in magnetization capacities. In this ideal model, where particles are homogeneously distributed in the 2-cm spherical agar tumor model, temperature elevation could be accurately predicted by solving the heat conduction equation. Temperatures above 44°C, adequate for hyperthermia treatment, could be obtained near the sphere surface.

Glass-ceramic microspheres are spherical microparticles produced by specific processing that allow for the control of particle size, such as aerosol-assisted wet chemistry (i.e., spray-drying methods). The development of ferromagnetic ceramic materials in such particulate forms is fairly recent.

Glass-ceramic microspheres with a diameter 20-30 µm have already found biomedical applications [275]. Clinically approved radioactive ceramic microspheres are used for cancer treatment to combine radiotherapy with embolization techniques, which will be discussed below. Ferrimagnetic ceramic microspheres with diameters of 20 to 30 µm suitable for embolization are currently being developed to magnetically induce local hyperthermia [276,277]. Kawashita *et al.* [276] prepared microspheres by melting magnetite (Fe_3O_4) powders in high frequency induction thermal plasma or by precipitating iron on the surface of 10-µm silica microbeads. Both methods end with a heat treatment to ensure complete oxidation of the iron-containing phase into a magnetic iron oxide, here primarily magnetite. The plasma method led to microspheres of pure Fe_3O_4 with a crystallite diameter of 1 µm, whereas precipitation led to microspheres with a FeOOH rust layer on the surface, the thickness of which could be tailored by the time of contact with solution of iron precursors (24 days were required to reach 25 µm in diameter). With respect to hyperthermia treatment, the precipitation method resulted in more appropriate magnetic characteristics and heating capacities than the plasma method: the coercivity was 9.5 $kA \cdot m^{-1}$ (120 Oe) instead of 4 $kA \cdot m^{-1}$ (50 Oe) and the saturation magnetization was 53 $A \cdot m^2 \cdot kg^{-1}$ ($emu \cdot g^{-1}$) instead of 92 $A \cdot m^2 \cdot kg^{-1}$ ($emu \cdot g^{-1}$) and the SLP calculated for AMF at 100 kHz and 23.9 $kA \cdot m^{-1}$ (300 Oe) was 41 $W \cdot g^{-1}$

instead of 10 $W \cdot g^{-1}$. Only microspheres produced by the precipitation method were examined for their *in vitro* heat generation capabilities [277]. Here, slight changes in processing prevented the occurrence of dehydration-induced cracks. TEM showed crystallites that appeared cubic, suggesting that maghemite was the most likely magnetic phase. Crystallites revealed a broadened size range, from 100 to 300 nm, with an estimated averaged size of 206 nm. The microspheres dispersed uniformly at 2% w/w in an agar phantom could only raise rise the agar temperature by 2°C. In contrast, when microspheres were concentrated in a restricted volume of the agar phantom, the temperature could be increased by 20°C. This experimental design raises a very important concern with respect to heat delivery by injectable material. These two extreme particle distribution patterns (i.e., diffuse or concentrated) reflect the variability inherent in the injection route when compared to the controlled implantation of bulk materials. The expected SLP of 41 $W \cdot g^{-1}$ was not confirmed by calorimetry. The authors emphasized that maghemite crystallite size could be optimally reduced to the size corresponding to single domain spherical crystallites. This would allow for maximum coercivity and would corroborate the experimental considerations of Bretcanu *et al.* With respect to glass-ceramic materials containing magnetite (see above discussion, [266]). Larger, hollow magnetite particles (500 μm in diameter) were prepared via enzymatic decomposition of urea within alginate gel template particles [278]. An aqueous solution containing iron nitrate, urease and ammonium alginate was added drop-wise into an aqueous solution of iron nitrate and urea. The precipitation of iron into an amorphous oxide was triggered by enzymatic urea decomposition on the drop surface and led to large hollow particles 2 mm in diameter. The subsequent crystallization step, consisting of heat treatment in a CO_2/H_2 atmosphere, resulted in shrinking of the hollow particles to 500 μm in diameter, with sparse cracks. Another interesting point was debated. The large hollow particles of this study have a lower density than the smaller, previously described microspheres [276,277]. The importance of this consideration is chiefly with respect to injection of these materials into the vascular bed and concerns of embolizing capacities, as particles behave quite differently in the blood stream as a function of their density. Considering what is currently known, this will not impact their use with respect to injection into bone. Particles heat-treated at 800°C in a 50/50 % of CO_2/H_2 atmosphere had a high saturation magnetization of 52 $A \cdot m^2 \cdot kg^{-1}$ ($emu \cdot g^{-1}$) and a coercivity of 14.6 $kA \cdot m^{-1}$ (183 Oe). These particles were

thought to have highest hysteresis loss in AMF conditions (a SLP of 45 $W \cdot g^{-1}$ was calculated from static magnetic characterization, but no calorimetry study was performed). For particles heated at 600°C and 700°C instead of 800°C, Fe_3O_4 also appears very likely to form and XRD peak broadening was typical of nanocrystallites, arguing for superparamagnetic properties. The latter particles heated at 600°C and 700°C were discarded because of their low saturation magnetization and coercivity, the authors predicting their low heating capabilities in AMF. However, this prediction accounted only for hysteresis losses, and the possibility of other magnetic relaxations, such as Néel relaxation, could result in significant heat generation.

Among numerous magnetic particles initially designed for other purposes (e.g., separation, catalysis or drug delivery), some candidates would be promising for magnetically mediated hyperthermia. Thus, magnetic nanocomposite mesoporous silica materials, also referred to as mesoporous magnetic carriers, could be considered for bone tumor indications. For instance, micron-sized ferromagnetic cores (3 µm in diameter, M_s = 80 $A \cdot m^2 \cdot kg^{-1}$ or $emu \cdot g^{-1}$)) can be coated with mesoporous silica (100 nm in thickness) [279] or, conversely, mesoporous silica can be coated with magnetic nanoparticles [280] (see Figure 1.7B). Most interestingly, magnetic cores (Fe_3O_4 and Fe) of 120 nm in diameter with a mesoporous silica shell were recently synthesized [281]. These 270 nm spherical particles have a magnetization of 27.3 $emu \cdot g^{-1}$ and a large hysteresis area based on a 5 kOe loop measurement.

Most of the glass ceramic materials yet developed for hyperthermia in AMF are based on heat dissipation through hysteresis losses. An alternative approach to this paradigmatic design is to synthesize superparamagnetic silica glass microparticles. Thanks to the versatility of processing through sol-gel silica chemistry, several SPIONs (superparamagnetic iron oxide nanoparticles) can be homogeneously embedded in a silica matrix to limit magnetic moments coupling and preserve superparamagnetism. Two approaches were used to this end by our group [282]. In the first approach, iron nitrate was mixed with silica precursors that were hydrolyzed to form a porous silica gel at 50°C. The iron nitrate precipitated in the pores of the silica gel matrix, which further controlled size of iron oxide crystallites. This bulk matrix was ground into microparticles and subsequently thermally treated in air (24 h at 500°C or 1h at 700°C) to oxidize *in situ* the precipitated iron crystallites into magnetic nanoparticles, most likely maghemite. This processing results in microparticles composed of a silica

matrix entrapping magnetic iron oxide crystallites. These crystallites had XRD and magnetic diameters of approximately 13 nm. In the second approach, superparamagnetic microparticles were obtained by dispersing bare SPIONs prepared by classical coprecipitation method in a solution of silica precursors. The gelation was allowed as previously described at 50°C. The gel was crushed into microparticles and submitted to heat treatment at 800°C for 1 h. The diameters of SPIONs determined by XRD, TEM and magnetic characterization were approximately 11 nm. With such superparamagnetic microparticles, the mechanism of heat dissipation under AMF changes from hysteresis losses associated with multi-domain magnetic particles to magnetic moment relaxations associated with sub-domain particles, known to be more efficient. Specifically, the spin reorientation in space is only driven by spin system reorientation in the lattice, i.e., Néel relaxations. Brown relaxations are negligible with SPIONs embedded in a solid matrix. In contrast, this would not hold true for particles with hydrodynamic radii smaller than one micrometer, such as SPIONs, dispersed in a liquid medium of low viscosity, e.g., ferrofluids. Mesoporous silica microspheres embedding 5 - 7-nm diameter SPIONs were synthesized by evaporation self-assembly in an aerosol-assisted manner from a mix of aqueous ferrofluid in ethanol, with silica precursors and Pluronic® as surfactants [283]. The highly spherical microspheres had diameter between 0.3 and 3 μm and smooth surfaces that would be highly beneficial for syringeability and clinical use. Up to 40 wt % of maghemite SPIONs could be embedded. Superparamagnetism was determined by hysteresis loop measurements at 795 $kA \cdot m^{-1}$ (10 kOe) and, for a representative sample containing 10 wt % of maghemite the saturation magnetization was 57 $A \cdot m^2 \cdot kg^{-1}$ (or $emu \cdot g^{-1}$), compared to a value of 62 $A \cdot m^2 \cdot kg^{-1}$ (or $emu \cdot g^{-1)}$ for the bare ferrofluid. Microspheres could be loaded with model drug ibuprofen by diffusion into the mesopores. The drug was released from compacted microspheres in a simulated body fluid (SBF), showing 50 % release during the first hour (burst effect) followed by sustained release during 100 h and reaching a plateau at 70 % of release. A recent confocal microscopy study revealed that these magnetic microspheres were internalized without manifestations of cytotoxicity in the absence of heating [284]. The authors underline that this is due to the size of these particles, all of which are larger than 200 nm, avoiding the cytotoxicity that smaller particles trigger by interaction with organelles [285]. Notably, the fraction of particles that are internalized and observed in the cytoplasm appears to correspond to a diameter of approximately 1.3 μm. These magnetic

microspheres were shown to generate efficient heating under magnetic induction (42°C could be reached in an AMF), killing 50% of the cells.

Originally, bioactive polymeric microspheres (i.e., those able to form apatite surface layer in SBF), have been prepared by means of coating with a solution of calcium silicate and subsequent soaking in SBF [286]. This approach could be very fruitful for magnetically mediated hyperthermia treatment of bone tumors if combined with important findings from the field of polymeric magnetic particles.

2.3 Magnetic materials for cementoplasty

Syringeable cements are composed of "polymerizable" mineral components or organic components. Mineral calcium phosphate cements consist of a powder phase of calcium and/or phosphate salts that, together with an aqueous phase in given liquid to powder ratios, react at ambient or body temperatures to form a calcium phosphate precipitate. This precipitate sets by the entanglement of bone-like hydroxyapatite crystals. Organic cements, often poly(methyl methacrylate) (PMMA) cements, consist of monomers and prepolymers whose final polymerization step is triggered before injection by mixing with polymerization initiator. The polymerization lasts through the injection and *in situ*. Cements injections are very suitable for vertebra treatment, through percutaneous vertebroplasty and kyphoplasty techniques [287]. Many ceramic, glass and glass-ceramic crushed particles can be used as filler, such as pre-polymerized PMMA fillers. These can be in cement or mixed with polymers, as in the most recent generation of composite biomaterials, Cortoss® (Orthovita Inc., Malvern, PA, USA). Ferromagnetic cements are based on a resin composed of bis-α-glycidyl methacrylate and triethylene-glycol dimethyl-acrylate mixed with filler. This filler consists of powders of magnetite particles (Fe_3O_4, 13 μm in diameter) and silica particles (SiO_2, 3 μm in diameter) [288]. Mixing equal parts of paste incorporating the dissolved polymerization initiator (benzoyl peroxide, 0.1 wt%) and paste incorporating the dissolved activator (N,N-dimethyl-p-toluidine, 0.1 wt%) initiates polymerization before molding. Syringeability was not investigated. *In vitro*, in a 100 kHz AMF and field strength of 6.4 $kA \cdot m^{-1}$ (80 Oe), cement containing 80 % w/w magnetite reached a maximum temperature of 61°C, falling below 40°C when the

magnetite content was lower than 50 % w. To investigate their *in vivo* hyperthermia potential, cements were surgically placed in rabbit tibias inoculated with VX2 tumor cells and submitted to AMF at 100 kHz under thermometry control. The magnetic field strength was varied to achieve temperatures of 50 - 60°C. Bone surrounding the implant could thus be maintained in a temperature range of 43 - 45°C, demonstrating a tumoricidal effect while not damaging healthy tissue. This effect was observed one day, one month and three months after treatment. Moreover, the mechanical strength of the implant would allow for stabilization of the bone fracture. This work demonstrated that magnetically induced heat delivery by the cement to engrafted bone tumors dramatically lowers tumor-induced bone pathological fracture and cortical bone destruction [289].

A recent non-randomized clinical trial investigated repeated magnetically induced hyperthermia of bone metastases to the extremities from various primary cancers. These hyperthermia treatments were performed following reconstructive surgery. During the surgery, a mix of 40 wt % magnetite particles (Fe_3O_4, 13 µm in diameter) with calcium phosphate cement (Biopex®-R Pentax Corp., Tokyo, Japan; [290]) was injected as a magnetic material in conjunction with other magnetic materials that were prosthesis, plaques or nails [291]. Unfortunately, the ferromagnetic cement formulation alone could not be investigated. The scope of this study was also limited because of eligibility restrictions for ill-defined criteria and because of the technical impossibility of exposing the most proximal location in the femur to AMF. Two control groups were constituted of patients undergoing the operation alone or combined with radiotherapy. In the hyperthermia group, lesions were exposed to AMF at 1.5 MHz 10 times during 15 min. Power output was adjusted to achieve a temperature of 43°C as ascertained by thermometric monitoring of the cortical bone surface. This study revealed comparable outcomes for clinical and radiographic assessments in the hyperthermia *vs*. radiotherapy groups; both improved when compared to the operation-alone control group.

In other contexts, an injectable magnetic formulation of calcium sulfate cement was tested for injection into bone metastasis *in vivo* [292]. The cement was composed of $CaSO_4$ powder, a degradable mineral matrix, mixed with 3 % w/w bare magnetic nanoparticle (70 nm in diameter) in water. Degradation of the matrix began at day 8 of implantation and after two weeks was replaced by a cellular fibrous tissue containing numerous monocytes and multinucleated cells. Released magnetic nanoparticles were found

internalized in parallel with $CaSO_4$ particles, primarily within cells of the monocyte lineage. These cells are involved in bone osteoclasis and extracellular matrix degradation. These cells could be then selectively killed by magnetically induced hyperthermia with the goal of impeding tumor expansion in the bone [293]. Importantly, this type of approach would likely benefit from progress in SPIONs surface chemistry and coating to improve interactions with cells [294,295].

3 Formulations and minimally invasive procedures for magnetically mediated local hyperthermia treatment of soft tissue tumors

Two administration routes and the related formulations are discussed: intra-arterial and intratumoral injections.

3.1 Arterial injections and arterial embolization hyperthermia (AEH)

The concept of arterial embolization is based on the selective use of a therapeutic agent that can embolize the vessels of a tumor's arterial supply. For physiological considerations, the model indication is the treatment of metastatic lesions of the liver in the absence of other contraindications [296,297]. Normal hepatic parenchyma derives approximately 80 % of its blood supply from the portal vein, whereas hepatic malignancies receive the majority of, if not virtually their entire, blood supply from the hepatic artery [298]. This allows selective targeting of tumor tissue through the afferent artery and relatively spares healthy hepatic tissue (Figure 1.8). In case of hyper-vascular tumor, arterial embolization through super-selective catheterization may be considered in other organs such as the kidney, pancreas, lung [299]. It is worth noting that no targeting of tumor tissues can be awaited as in the case of hepatic lesion. Importantly, the protective cooling of healthy tissue by the portal vein in the

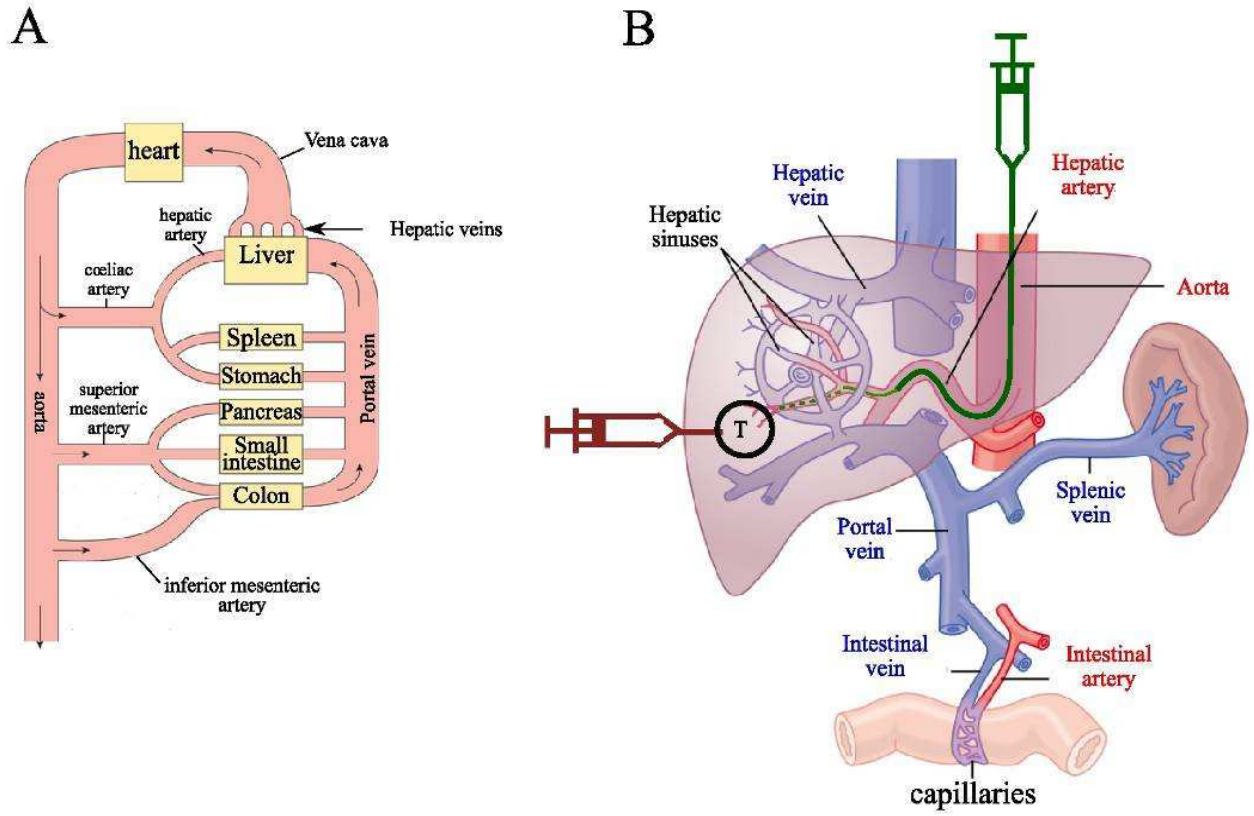

Figure 1.8: The liver and the approach of therapeutic embolization.

A: Schema representing the location of the liver and related organs in the general circulation and showing the double blood supply to the liver. Blood enters through the hepatic artery and the portal vein, the latter collecting blood from other organs, and notably involved in digestion.

B: Illustration of the embolization techniques used for liver tumor treatment as presently indicated in the clinic. Within the healthy hepatic parenchyma (purple) is a tumor (T). The blood vascularization of hepatic tumors, notably metastases, derives almost exclusively from the artery arising from and fed by the hepatic artery. In contrast, the healthy hepatic parenchyma derives the largest part of its blood supply from the portal vein.
The technique of embolization through arterial injection, depicted in green, takes advantage of this particularity to target the tumor lesion, efficiently sparring healthy hepatic parenchyma. The green line from the green syringe depicts the trajectory of catheterization, which can lead relatively close to the lesion depending on the material used.
An alternative approach for precisely localized tumor embolization is direct intratumoral injection (e.g., percutaneous), as depicted by the brown line and syringe, which is applied in a number of clinical tumor locations.
(A: adapted from: Barrett KE, Barman SM, Boitano S, Brooks H. Ganong's Review of Medical Physiology. 23rd ed. McGraw-Hill Medical; 2009. B: adapted from: Guyton AC, Hall JE. Textbook of Medical Physiology. 11th ed. Saunders; 2005.)

case of liver will be absent for the other envisaged organs. Arterial embolization has been fruitfully combined with chemotherapy or radiotherapy in the treatment of inoperable liver tumors. We will now present the established formulations and discuss them in view of hyperthermic treatment.

3.1.1 Microparticles

Micron-sized particles of sufficient mechanical strength are able to embolize vessels of a similar diameter [300]. For example, microparticles over 10 μm in diameter are able to deposit in the pre-capillaries arterial vessel. Commercially available microspheres, reviewed in [301], have diameters ranging from 40 to 1200 μm. For intratumoral embolization or chemoembolization, the ideal diameter is tumor-dependent and has to be determined by the operator. For radioembolization, SIR-spheres® (Sirtex Medical Ltd, Lane Cove NSW, Australia) and Teraspheres® (MDS Nordion, Kanata, ON, Canada) are respectively radioactive ceramic and glass microspheres (30 μm or slightly less, respectively) used as carriers of radiation to liver tumors [297]. It is worth noting that such methods are not based on the effects of ischemia but on the antitumoral effects of radiation. The deposition achieves advantageous selectivity by matching the formulation to the pathophysiology of the liver lesion. Sub-domain (SPIONs) or multi-domain ferromagnetic small particles that are generally less than l μm in diameter are able to flow through capillaries. Many efforts have been made to combine microparticle arterial embolization with magnetically induced hyperthermia as described in [302]. These efforts benefit from significant formulation advances in the field of microparticles for biopharmaceuticals, particularly SPION microencapsulation for drug delivery. Jones and coworkers have developed 20 - 45 μm-diameter microspheres of Biopol®, a copolymer of (R)-3-hydroxybutyric acid and (R)-3-hydroxyvaleric acid. These microspheres encapsulate ferromagnetic nanoparticles and have been investigated for arterial embolization followed by AMF-induced local hyperthermia in an animal kidney model [303]. This model has vascularization characteristics comparable to a tumor. The investigation was further led in animal model of liver tumor [304]. This latter work provides evidence of selective tumor embolization and demonstrate an encouraging microparticle distribution ratio of tumor to healthy parenchyma. This was evidenced by microspheres located primarily in and around the peripheral rim of tumor, including in the neovascularization, with only few microspheres distributed in healthy hepatic parenchyma. In the control group, which did not received a hyperthermic treatment, liver infusion with

microspheres had few side effects and did not alter tumor growth. Microsphere distribution was a key parameter for the efficiency of AMF-induced heating [304]. Notably, microsphere embolization could limit cooling by reducing blood flow [303].

3.1.2 Formulation forming-depot

Formulations of iodized derivatives of poppy-seed oil emulsified in water-soluble X-ray contrast medium are used for lymphography contrast and demonstrate long-lasting retention in hepatocellular carcinoma. Formulations should be distinguished owing by droplet size and viscosity. Lipiodol® (Ethiodol® in the US) has a viscosity of 430 mPa·s. Lipiodol Ultra-Fluid®, a first choice for arterial embolization of carcinoma or colorectal carcinoma liver metastasis, has a viscosity of 25 mPa·s (with a droplet diameter range of 20 - 200 μm) [296]. Formulations of iodized derivatives have been further used as lipophilic antineoplastic agents or for radioactive iodine treatments of hepatic or breast tumors [305]. Some cellular uptake has been reported following deposition and emulsification on the cell surface [306]. Radioembolization is possible for the radiopharmaceutical ^{131}I (Lipiocis®) [297]. Lipiodol® was successfully investigated *in vivo* as a vehicle for SPIONs, resulting in a straightforward formulation for arterial embolization and local, magnetically induced hyperthermia with AMF. In a rabbit liver tumor model, the embolized tumor could be heated to a temperature of 42 - 43°C while preserving adjacent tissue, improving tumor necrosis and local control of the tumor lesion [307,308]. Notably, increasing the iron oxide particle doses from 25 to 100 mg resulted in lower iron oxide content ratios of tumoral to distant, normal hepatic tissue. The authors found that the deposition of the ferromagnetic particle Lipiodol® formulation was confined to the vascular lumen. The possibility of extra-vascular deposition was excluded in a later work [309]. This treatment was also associated with non-specific embolization of the biliary, extra-hepatic system, such as gallbladder, which is also supplied by hepatic artery. In a clinical situation, this possibility would require catheter placement as near as possible to the liver. This can be achieved today by super-selective catheterization of the hepatic

artery, but still necessitates ligation of the upstream gastroduodenal artery and prophylactic cholecystectomy [296]. Marginally, necrotic areas in the normal hepatic parenchyma were observed even in the absence of formulation and were due to oxygen and nutrient deprivation associated with the embolization procedures. Recently, Takamatsu *et al.* mixed Lipiodol® with a clinically approved SPION suspension: the MRI contrast agent Ferrucarbotran®. This formulation intended for embolization and magnetically induced hyperthermia showed significant heat loss under AMF and clearly demonstrated in pre-clinical investigation a better tumor control than untreated controls [310]. Moreover, the authors highlight that the formulation of the same SPIONs in gelatin microparticles (Gelfoam®, instead of Lipiodol®) was less efficient at heating the tumor graft. The authors argued that the microparticle embolization pattern inadequately limited the distribution of the magnetic seeds to the largest vessels, in contrast to Lipiodol®, which could better fill capillaries. The kidney is an end organ and is not eligible in a clinical situation for intra-arterial injection of embolizing materials, but it constitutes a model of hypervascular tumors. Regarding arterial embolization of the kidney, Mitsumori *et al.* [311] performed a comparative study of two formulations of 70-nm diameter superparamagnetic dextran-magnetite complexes (including SPIONs of 7-nm diameter Fe_3O_4) mixed with either Lipiodol® emulsion or with 40-nm degradable starch microspheres and Iopamiron® as a contrast agent. There was no encapsulation. The authors reported equivalent distribution of both formulations, both of which were strictly confined to the capillaries. Compared with multi-domain ferromagnetic particles, the higher specific absorption rate of the SPIONs used here allowed for rapid temperature increase selectively in the kidney, irrespective of SPION formulation. Both formulations used in this study are equivalent for arterial embolization hyperthermia.

3.2 Direct intratumoral injection (DIH: direct injection hyperthermia)

3.2.1 Formulation forming depot

Intratumoral deposition of magnetic particles can be realized by direct tumor puncture. This approach requires tumor visualization either directly or radiographically. Formulations forming a depot *in situ*, such as Lipiodol®, previously used for arterial embolization, can also cause tumor embolization through direct intratumoral injection. In a mouse model hepatocellular carcinoma, Muraoka *et al*. embolized the tumor vascular bed and induced local hyperthermia by direct puncture and injection of a suspension of magnetic particles in Lipiodol® [312]. When submitted to AMF, the microparticles of magnesium ferrite (2-5 μm in diameter) produced heat through hysteresis losses, with overheating controlled by a Curie temperature T_c of 77°C. The authors were able to heat tumors to 42-43°C, allowing for specific tumor necrosis and sustained decrease in volume. This was even more marked with systemic administration of doxorubicin.

Using a model of the VX2 carcinoma line tumor engrafted in the rabbit liver, Moroz *et al.* investigated tumor response after embolization treatment with magnetically-induced hyperthermia using an arterially-injected microparticle formulation in one group and, in a second group, using intratumoral direct injection of depot-forming formulation based on Lipiodol® [313]. Maghemite nanoparticles of 100 - 200 nm were incorporated by encapsulation in 32-μm-diameter microparticles of polyester of valeric and butyric acids for microparticle formulation, or by suspension in 2:1 v/v Histoacryl®-Lipiodol® mixture for the depot-forming formulation. Following treatment by embolization and magnetically mediated hyperthermia, the authors found a higher efficacy in tumor growth control with arterially-injected microparticle formulation when compared to intratumoral injection with the Lipiodol® based formulation. This was thought to be due to the distribution of heat and magnetic particles. But, as discussed above, this effect is also related to the parameters of the injection procedure, such as selectivity and specificity to the tissues composing the tumor lesion. Selectivity and specificity

are lower in the case of the direct injection procedure. Control of tumor growth is also primarily dependent on thermometry parameters and heat loss mechanisms. Moreover, more subtle relationships between the injection procedure and heating have to be taken into consideration here, especially with respect to arterial embolization. Firstly, an effect on tumor growth by oxygen and nutrient deprivation is not negligible, even if not corroborated by control injections with particles, in accordance with [304]. Secondly, a decrease in the cooling capacity of blood flow is very likely. Unfortunately, the design of this study did not permit the differentiation of the impacts of the formulation and the procedure.

In this respect, studies comparing the same formulation administered through both routes, using Lipiodol® or microparticles for instance, could be highly valuable to the field.

3.2.2 Formulations forming implants *in situ*

Further injectable formulations that solidify *in situ* could be beneficial for direct intratumoral injections or arterial injections targeting solid tumors. Such formulations are currently developed for aneurysm treatments in vascular interventional radiology [314] and offer alternatives in vertebroplasty. They are also used as bulking agents in urology [315]. Hydrogels and organogel-based formulations have been tested for direct percutaneous intratumoral injection as carriers of tailor made silica microparticles. These particles embed SPIONs that would allow for subsequent heating using AMF [316]. Investigated mechanisms of implant formation are based on polymer precipitation or cross-linking through ionic or thermal processes. To further assess the *in vivo* heating capacities of intratumoral injection, the organogel formulation of ethylene-vinyl alcohol (EVAL) in DMSO (8% w/v) was preferred. This formulation, similar to the commercial formulation Onyx® used for aneurysm embolization, has the largest incorporable proportion of magnetic microparticles (up to 40 % w/v) and preserves syringeability and viscosity [317]. The mechanism of implant formation occurs via precipitation through exchange of the organic solvent with tissue water followed by entanglement of collapsing polymer chains (Figure 1.9). The systemic toxicity of organic solvents limits the injection volume to 0.25 mL in our Swiss Nude mouse model subcutaneously of engrafted human colocarcinoma. With

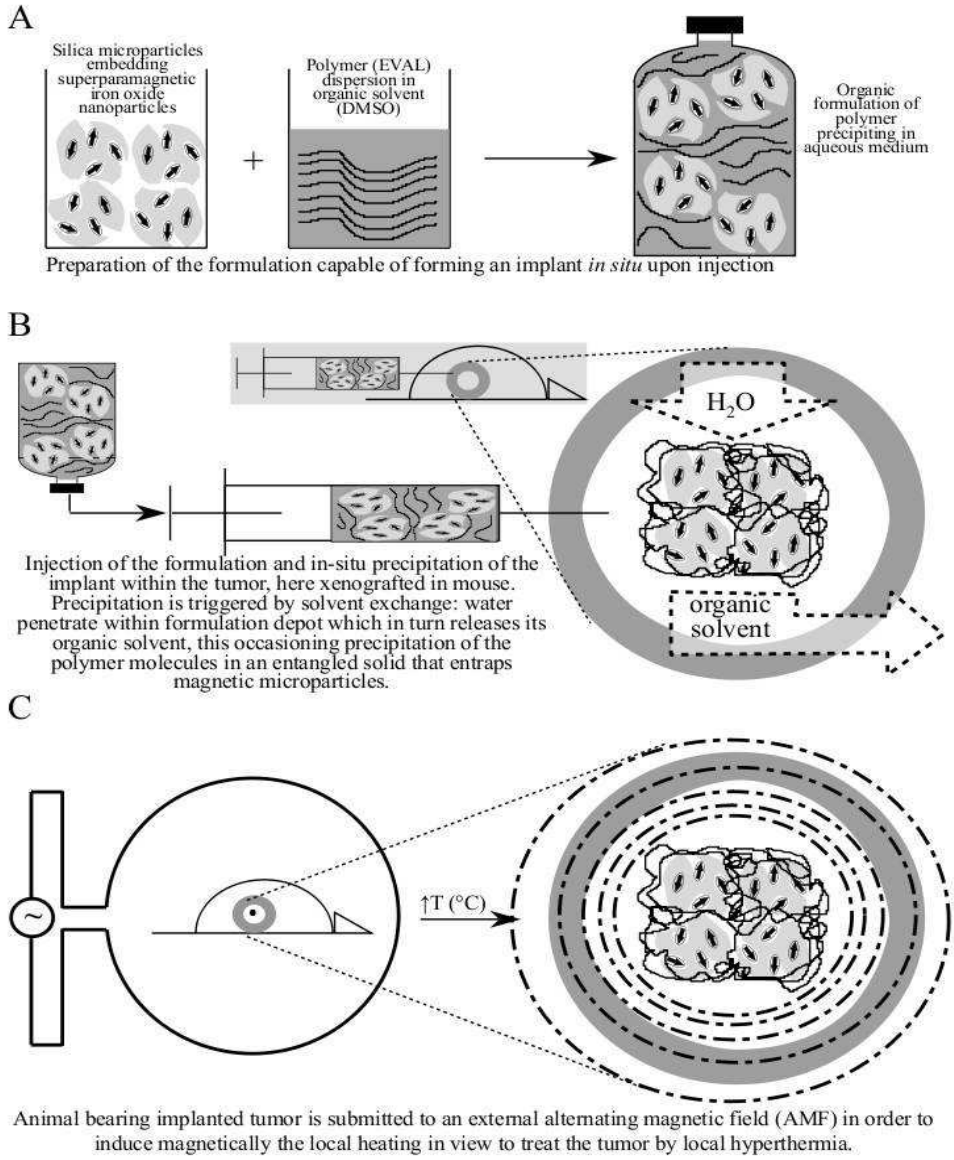

Figure 1.9: Injectable organogels that form an implant *in situ*, entrapping magnetic microparticles for local, magnetically-induced moderate hyperthermia treatment of solid tumors.
Schema of preparation and injection of organogel formulations forming an implant in situ and entrapping silica microparticles that embed superparamagnetic iron oxide nanoparticles (see section 2.2 of this chapter and Figure 1.7). These formulations are intended for intratumoral use followed by magnetically-induced heating to treat solid tumors by local moderate hyperthermia, as discussed in the section 3.2.2 of this chapter. **A**: preparation of the formulation, **B**: injection, here in a xenograft tumor model in Swiss Nude mice (human colocarcinoma Co112 cell line), **C:** induction of local hyperthermia through an external alternating magnetic field

respect to entanglement, this volume was large when compared to the mean tumor volume of 200 mm^3. In the injected control group without hyperthermia, as for direct tumor injection with Lipiodol (in contrast to arterial injection), the implant localized in the necrotic core with interstitial prolongations in the peripheral vital rim of the tumor. It was also localized in the pseudo-stromal capsule of the smallest dense tumor nodules. Tumor capillaries were scarcely embolized when compared to Lipiodol®, which is known as previously described for its capability to diffuse into the vascular lumen and occlude capillaries. An embolizing effect through vasculature collapse could not be excluded. Microparticles were efficiently entrapped in the polymer matrix formed *in situ* and dissemination was avoided. The local reaction to intratumoral injection consisted of edema at the tumor site. This effect was reversible within 24 hours and resulted in the development of a non-specific inflammatory rim of phagocytes surrounding the implant. Elsewhere, this reaction was reported for various organogels and injectable formulations of hydrogels forming *in situ* implants [316]. The day following the injection of the 8% w/v EVAL/DMSO treated groups were submitted to 20-min treatment in AMF at 141 kHz for increasing field amplitudes of 9, 10, 10.5, 11 and 12 mT. Mean intratumoral temperatures rose rapidly (within 5 min) to 40, 42.5, 42.9, 43.5 and 47.8°C, respectively and were maintained for the duration of treatment (Figure 1.10). As revealed by histology, heat-induced necrosis was related to the distribution of the formulation. Extensive tumor necrosis was observed only for the 12mT-treated group. In parallel survival studies, median survival times were 12, 21, 27, and 37 days for uninjected controls, injected but not heated controls, and 10- and 12-mT treated groups, respectively. For 10- and 12-mT treated groups, we observed complete responses in 1 of 7 and 5 of 11 treated animals, respectively (Figure 1.10). In light of biological considerations, these results can be further discussed with respect to the effects of organic solvents. Cell survival studies reported by Hahn *et al.* [318] revealed that cells cultured with hydrophilic organic solvents, such as DMSO and dimethyl formamide, show evidence of thermotolerance induction. Solvent were used at doses of 1 or 2% in the medium, a level associated with intermediate solvent cytotoxic doses. Thermotolerance induction begins after 8 h of contact and is fully developed between 18 and 24 h. The mechanism of thermotolerance induction appears more complex than for lipophilic aliphatic organic solvents. This latter effect almost exclusively involves the cell membrane, as strongly suggested by the fact that the concentration of aliphatic solvent used to

Figure 1.10, inset A and B (inset C and legend on the following page)

A

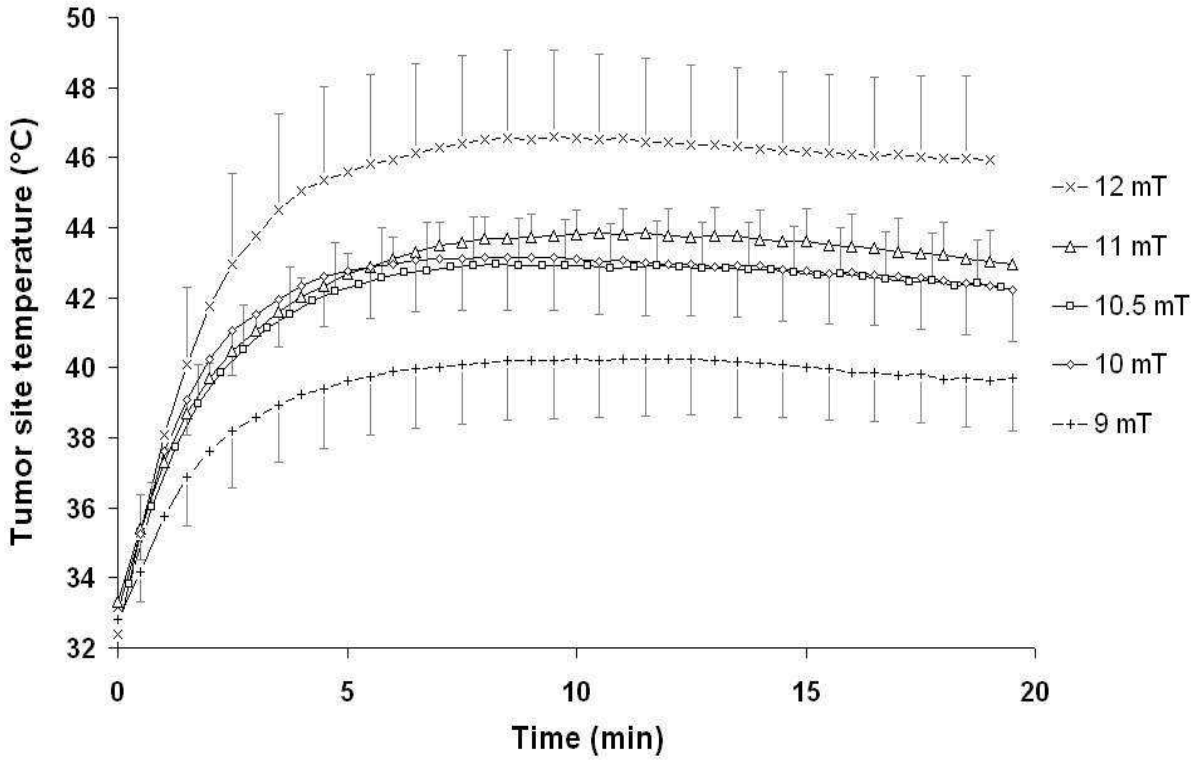

B

Field strength (mT)	9 (n = 5)	10 (n = 4)	10.5 (n = 5)	11 (n = 3)	12 (n =5)
Initial tumor volume (mm^3)	217 ± 254	110 ± 40	129 ± 88	279 ± 60	220 ± 104
Tumor ET (°C)	40.0 * ± 3.1	42.7 † ± 3.0	42.8 § ± 2.6	43.5 ‖ ± 1.6	47.8 *†§‖ ± 2.2
Tumor AUC (°C·min)	131.1 * ± 44.3	180.1 † ± 45.1	177.3 § ± 40.1	183.8 ‖ ± 34.0	282.5 *†§‖ ± 40.0
Skin ET (°C)	38.6 *‡ ± 3.0	42.0 † ± 3.4	42.2 §‡ ± 2.2	43.5 ‖ ± 2.0	48.4 *† §‖ ± 2.0
Tumor necrosis (%)	67 ± 25	65 ± 21	54 ± 23	52 ± 13	78 ± 6

The U Mann-Withney test was used to evaluate statistical significance between the groups of mice. *§P < 0.001, †‖‡P < 0.05.

C

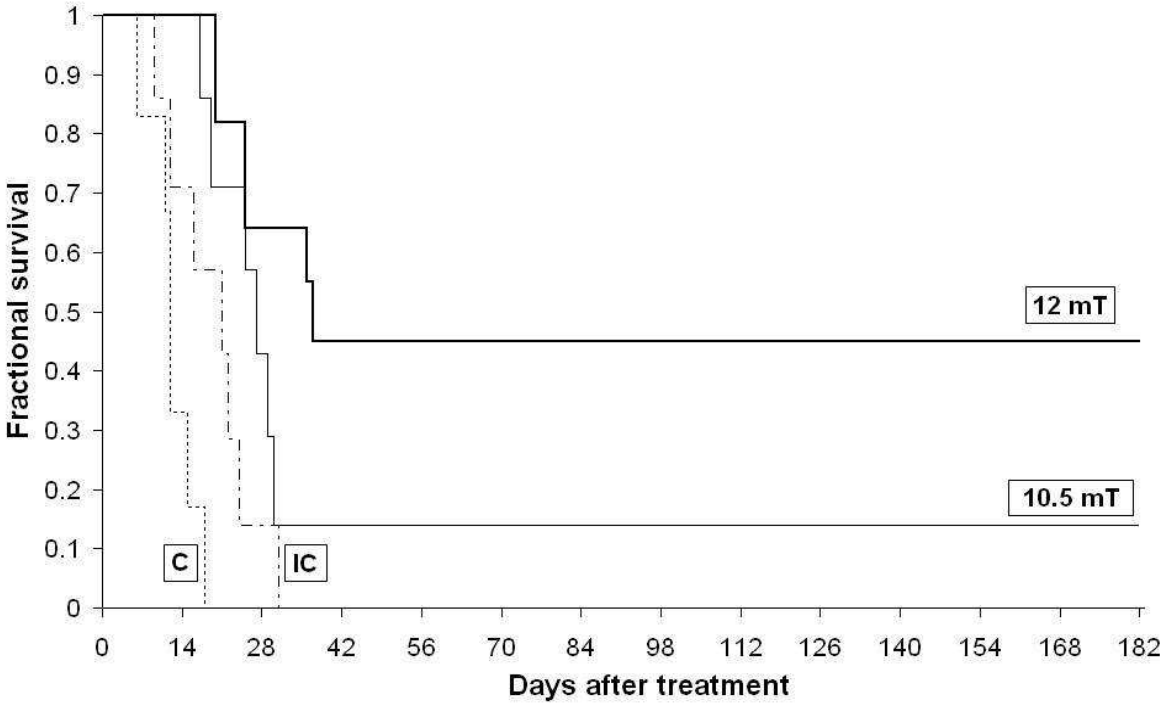

Figure 1.10: *In vivo* investigations of organogels entrapping magnetic microparticles forming *in situ* an implant for intratumoral injection and local magnetically induced hyperthermia treatment of solid tumor model**.** ***(this figure gathers important figures of chapter 4)***

A volume of organogel formulation of 0.25 ml was injected in human Co112 cell-line tumors subcutaneously engrafted in mouse. Magnetically induced hyperthermia was applied one day after injection by exposing animal 20 min. to AMF at the constant frequency 141 kHz with varying amplitude of magnetic field strength. The temperature was monitored through fluoroptic thermoprobes placed in the tumor or append to skin upon tumor site. Adapted from ref [314].

A. *See also chapter 4, Figure 4.1*. Thermograms representing tumor temperature as a function of time, during single 20-min magnetically induced hyperthermic treatments in an alternating magnetic field, for magnetic field strengths of 9 mT (n =5, grey line), 10 mT (n = 4, black line), 10.5 mT (n = 5, dashed bold grey line), 11 mT (n = 3, bold grey line), 12 mT (n = 5, bold black line). Note the leveling of mean temperatures reported for 10, 10.5 and 11 mT to about 43°C. In opposition for 12 mT with 46°C. We hypothesize an important role of cooling effect of neovasculature in relation with the likely thermotolerance induced by organic solvent (see text).

B. *See also chapter 4, Table 4.2*. Table summarizing corresponding important parameters (mean ± SD). (ET) is the equilibrium temperature defined as the averaged temperature over the final 15 min of magnetic field application. AUC, the area under thermogram curve, was correlated with heat quantity.

C. *See also chapter 4, Figure 4.3*. Independent survival investigations. Dotted line: control group (C), n = 6; dashed line: implanted control group (IC), n = 7; normal line: 10.5-mT treated group, n = 7; bold line 12-mT treated group, n = 11. Note that in the group treated with a 12-mT alternating magnetic field, 5 of 11 mice survived 12 months after treatment without tumor relapse.

Note: no significant changes in peripheral body temperature was recorded.

achieve maximal thermotolerance, normalized by the partition coefficient between the membrane and the culture medium, is constant. In this case, thermotolerance fully develops within the first hours and is tightly correlated with higher synthesis rates of HSPs, e.g., HSPA1 (HSP70), HSPC1 (HSP87) and HSPH2 (HSP110). The DMSO partition coefficient in the membrane is not negligible but is low, and the authors propose the possibility of a cytosolic mechanism to induce thermotolerance following treatments with hydrophilic organic solvents. As discussed in the introduction, the hydrophilicity of DMSO allows one to suppose that *HSP* expression may be induced by interference with protein synthesis, leading to the accumulation of non-native proteins, such as is the case for ethanol treatment. The level of HSPs were unfortunately not determined in this study but may be supposed to have been higher. This scenario can be envisaged following injection of organogels, through slow solvent elimination and exchange *in situ*. Larger solvent doses could be used to cause increased direct cellular cytotoxicity. This effect may partly explain the local edema and the delay of tumor regrowth in the injected but non-heat-treated control group. It is also possible that cells surviving DMSO exposure can present HSPA1 (HSP70) at the membrane and, as described in the introduction, trigger NK cell-mediated cytotoxicity. Importantly, these cells are still present in immunodeficient athymic mice, such as Swiss Nude mice. Notably, the ischemia and hypoxia that embolization may generate, is known to induce *HSP* expression [119]. It was also reported to interfere in the kinetic of heat-induced thermotolerance given that the nutrient deficiency is known to slow the rate of thermotolerance acquisition *in vitro* [319]. Nonetheless, in the implanted and treated groups of the study, at the time of hyperthermia treatment, the injection of organogel appears most likely to have induced thermotolerance. Indeed, tumor tissue appears protected against moderate doses at temperatures below 45°C, whereas very important appears at higher temperatures and heat doses. Similarly, thermotolerant cells with high levels of HSPs are protected from apoptosis at moderate heat doses but are sensitive to necrosis at higher temperature. It is worth noting that thermotolerance can have a protective effect on healthy tissues. Indeed, no damage was observed in the underlying muscle or peritoneal layer but the skin was affected similarly to the tumor at the highest heat doses. The leveling of temperatures reported for AMF amplitudes below 12 mT contrasts with the higher temperatures reported at 12 mT (Figure 1.10A). This leads us to consider the effect of heat on the vasculature of the tumor. Also considered are

the effects of the surrounding healthy tissue on cooling in relation to the likely induction of thermotolerance at the tumor site following organogel injection. We believe that thermotolerance of the tumoral vasculature induces a shift from 42°C to 44 - 45°C in the landmark temperature for sensitivity to irreversible heat damage, similar to thermosensitive healthy tissue. Above 44 - 45°C, the direct necrotic effect of heat, thermoablation, can no longer be prevented by the thermotolerance state independently of HSP levels. At this point, the irreversible damage to tumor vasculature and concomitant annihilation of its cooling effect could allow the recorded temperatures to reach as high as an average of 47.8°C. With respect to the surrounding healthy tissues, thermotolerance because of solvent diffusion appears clear, unless heat damages to underlying tissue and to the thin overlying skin is divergent. Damage of the skin can involve anatomical considerations with respect to prior direct injury by organic solvents. Taking these considerations into account, important complementary investigations are necessary for hyperthermia using organogels. Instructive investigations of immunological effects in relation with complex *HSP* induction would require immunocompetent animal models. For hyperthermia treatment based on organogels intended for direct cytotoxicity, the sequence should be definitively adapted to the time of injection of the organic solvent formulations, owing to the kinetics of thermotolerance induction. Hydrogel formulations would be interesting with respect to embolization effects, but their heating capacities should be improved. Organogel formulations can be adapted by the addition of less toxic co-solvents, such as propylene glycol or polyethylene glycol [316]. The generally lower solid fraction that can be accommodated by co-solvent formulation would benefit from the recent development of glass-ceramic particulate systems to improve heating efficiency. The effects of thermotolerance at the tumor vasculature level should be further assessed through investigations of tumor blood perfusion to confirm an increased cooling effect. The drawbacks of an increase in tumor blood flow and cooling capacity in achieving cytotoxic hyperthermia can be turned advantageous. This could be beneficial in terms of: i) synergy with radiotherapy or photodynamic therapy, through increase in oxygenation [320]; ii) a supra-additive pharmacokinetic effect with chemotherapy; and iii) passive targeting by raising tumor biological availability. Following the spontaneous decay of thermotolerance, the cytotoxic capacities of hyperthermia would be recover.

To conclude, theoretical work [321,322] ascribes impacts of the formulation on heat generation primarily to magnetic seed distribution and heat dissipation through blood flow modulation. So far, no data have been presented that evaluate residual blood perfusion remaining following direct intratumoral injection of the examined formulations. Knowledge of this effect could allow further formulation adaptation for hyperthermic treatment and could contribute to solving the problem of poor control in the delivery of cytotoxic heat doses.

4 Magnetic liposomes and local hyperthermia treatment of tumors

4.1 General characteristics of liposomes

Liposomes are small vesicles (20 to 4000 nm) consisting of a single or multilamellar lipid bilayer that separates an aqueous internal cavity from the aqueous environment [323]. Lipids with varying composition and charge, usually glycero-phospholipids and lecithins, are used. Three categories of liposomes are distinguished based on the surface charge of vesicles: neutral, anionic and cationic liposomes [324]. Various lipids can be used to prepare these liposomes. Classically, phosphatidylcholine is a major component of neutral liposomes. Dimyristoyl-phosphatidylglycerol (DMPG) and dipalmitoyl-phosphatidylglycerol (DPPG) are often found in the composition of anionic liposomes. Octadecylamine (or stearylamine) and N-(2,3-Dioleoyloxy-1-propyl)trimethylammonium methylsulfate (DOTAP) are representatives of the first and second generation class of cationic lipids, respectively [325]. *In vivo*, liposomes are known to adsorb many biological macromolecules, especially plasma protein (such as apolipoprotein A) and components of the immune system (e.g., complement, immunoglobulins, especially when they are aggregated by heat) [326]. For medical applications, liposomes are widely used as vehicles for nucleic acids or drugs. Hydrophilic drugs are loaded in the aqueous cavity, and neutral or hydrophobic drugs are sequestered in the lipid membrane. Liposomes

also constitute potent immunoadjuvants. Pharmacokinetic modulations depend on liposome size and charge (accounting for surface adsorption) and on the administration route [327]. Liposome pharmacokinetic profiles can be compared to free drug. When compared to free drug, liposomes are known to have i) enhanced circulation time, ii) high accumulation in tissues rich in macrophages, iii) longer retention in tissue and iv) the capacity to protect drug from metabolism degradation and elimination. Chiefly administered by parenteral routes, liposomes can remain intact for relatively long periods of time, depending on the parenteral route chosen. This property has been used for synovial infiltration, subcutaneous injection (liposomes are known to last as long as 600 h in mouse skin) and for intratumoral injection. Intravenously, conventional liposomes have short plasma half-life due to non-specific uptake, with notably high uptake by the macrophagic system [327]. Plasma half-life can be improved by PEGylation, which also increases syringeability by preventing aggregation [324]. The presence of negative charges on the surface of liposomes increases their capability to extravasate from fenestrated endothelium, which is found physiologically in liver, spleen and bone and in pathological conditions such as inflammation or solid tumors [328]. Cationic liposomes interact with the negatively charged membrane and are preferred for intracytoplasmic delivery (e.g., nucleic acids). They were also observed to have affinity for tumor endothelial cells [324]. Here, combinations of hyperthermia with liposomal drug delivery need to be distinguished from formulations of liposomes as carrier of magnetic particles intended to generate hyperthermia by magnetic induction, as detailed in a very informative review by Kong and Dewhirst [329]. It is also important to bear in mind that interactions of liposomes with cells may involve very distinct mechanism [330]: i) fusion with biological membranes; ii) endocytosis of intact vesicles; iii) adsorption of vesicles or fragments of vesicles to the cell surface without true incorporation of vesicle components; iv) transfer or exchange of phospholipids and proteins between the vesicle and the plasma membrane; and v) any combination of these mechanisms. Unilamellar and multilamellar liposomes are distinguishable because disruption or degradation of outermost lamella results in release of internal aqueous compartment or of inner vesicles, respectively. The inner vesicles are then able of further interactions, for instance with organelle membranes, primarily of lysosomes [330]. Special lipid composition even showed capability to target mitochondria [331]. The important ability of the internal vesicles composing a multilamellar liposome to take part in

intracellular interactions may account for the synergistic cytotoxic effect of hyperthermia, which is observed with empty multilamellar but not with unilamellar cationic liposomes. These results are reported in [332].

4.2 Magnetoliposomes and magnetically induced local hyperthermia of tumors

Liposomes containing magnetic particles, referred to as magnetoliposomes (MLs), allow for the induction of hyperthermia in AMFs. Generally, direct procedures of ML preparation lead to encapsulation of a ferrofluid in the aqueous cavity. Incorporation in membrane has been rarely reported [240] and was originally suggested in [329] to trigger burst release of an encapsulated drug through AMF-induced membrane disruption.

The extensive work of Kobayashi *et al.* addressed many aspects of magnetically-induced hyperthermia mediated by cationic magnetoliposomes (CMLs) and investigated neutral magnetoliposomes (NMLs).

CMLs were prepared by encapsulating colloidal magnetite nanoparticles in liposomes made of a combination of N-α-trimethyl-ethylamonioacetyl dodecyl-D-glutamate chloride: dilaurylphosphatidylcholine: dioleyl-phosphatidylethanolamine, 1:2:2, through sonication. Although not specified, a multilamellar structure is most likely for this fabrication process, considering the absence of a specific removal step [333-335]. Encapsulated magnetic particles ranged from 35 nm in early reports to 10 nm [336-340]. In agar phantom, 5 mg of magnetite per gram of cationic magnetic liposome formulation was the minimal concentration of magnetite (35-nm diameter) required to raise the temperature above 42°C was [336]. T9 rat glioma cells were incubated for 4 h in the medium mixed with the formulation to a magnetite concentration of 22 mg/ml (above which cytotoxicity was observed in culture). The cell pellet demonstrated a concentration of 5 mg/ml of pellet (23 % of cellular uptake), translating to a concentration to 55 pg per counted cell. Because of favorable interactions with negatively charged cell membranes, this concentration was ten-fold higher than when neutrally charged magnetoliposomes were used. When the cell pellet was submitted to AMF, controlling the amplitude to maintain 42°C for 30 min, cell survival was largely decreased. Interestingly, the authors reported that

the dose-effect curve did not follow the expected Arrhenius law [81]. The general ability of liposomes to fuse with membranes and alter the physicochemical properties of plasmalemma or possibly organelle membranes may synergize with membrane destabilization and hyperthermia-induced damages, accounting for cytotoxicity. This interaction with intracellular membranes was specifically described for multilamellar liposomes [332]. Following subcutaneous injection in rats, the cell pellet containing CMLs was subsequently submitted to the AMF regimen for 60 min. AMF was applied once or three times at 12-h intervals, and the formation of tumor nodules was prevented in 80 % and 100% of the animals, respectively [337]. All tumor nodules were formed at day 11, as compared to day 6 for the control group without AMF. Subsequent *in vivo* investigations with tumor nodules used direct intratumoral injection to ensure high intratumoral CML concentration and heating capacities. In the T9 rat glioma heterotopic model, the sequence of hyperthermic treatments was investigated for single AMF (11 days after CML injection). The AMF amplitude was modulated to maintain a temperature of 44°C at the upper skin level, and was performed once or twice at 24-h intervals [338,339]. The intratumoral distribution of CMLs was highly confined around the injection trajectory. Efficient heating allowed the target temperature to be reached rapidly and caused tumor necrosis after a single induction of hyperthermia. Tumor necrosis matched the distribution of CMLs, leaving more distant areas of the tumor unaffected. As generally reported for heat delivery, inhomogeneities in CML distribution are associated with non-uniform heat distribution. Nevertheless, after hyperthermic treatment repetition, necrosis spread over the whole tumor. This led to an increased rate of complete regression and survival probability. The CMLs seemed to fade from their confinement toward the injection trajectory. Spreading of necrosis to the whole tumor was attributed by the authors to CML migration through a so-called “thermal bystander effect”, which describes a spread of magnetic fine particles injected in tissues treated with magnetically induced hyperthermia,. This would not occur in control animals, injected with CMLs but not submitted to hyperthermia treatment. So far, no solid evidence supports this hypothesis. An unequivocal histological demonstration by Berlin blue coloration of CMLs in the spleen was unfortunately not applied to the repeatedly treated tumors. The thermal bystander effect was also reported for magnetic fluid hyperthermia with dextran-coated magnetic nanoparticles, but not in the case of an aminosilane-based coating [244,341,342]. Another biological aspect of hyperthermia

described in [343] may participate in the spreading of necrosis. This *in vitro* study was conceived to understand the spreading of skin burns to unheated cells during some photodynamic therapies. In the absence of any direct heating, heat diffusion, or cell-to-cell contact, DNA damage, apoptosis and decreased survival were demonstrated for non-heated cells when cultured with previously heated cells and separated from them by an insert. This distinct effect was named active the thermal bystander effect (ATBE). This effect should rely on a molecular factor of the medium that both cells share across the porous separation. This factor is not known, but the authors plan experiments to investigate a potential role of ROS (personal communication). We believe that an additional hypothesis may also account for the spreading of necrosis across tumors. In addition hyperthermia-induced necrosis triggered by direct cytocidal effect, other factors should be considered, including concomitant acute inflammation because of necrosis of the tumor tissues; hyperthermia itself; damage from cytokines produced by immune cells; and increased killing of tumor cells by cytolytic T cells and NK. A reactivation of occult active immunity or enhancement of innate or natural immunity is suggested by rechallenge experiments (e.g., through tumor re-injection as the mentionned above) and further investigations by Kobayashi's group [339,340]. Almost all animals for which complete tumor regression was observed in response to magnetic liposomes mediated hyperthermia were resistant to subsequent tumor engrafting challenge. Animals for which tumor responded partially to the treatment or relapsed after a period of regression were demonstrated to develop tumor after rechallenge experiments [339,340]. Furthermore, residual immunity induced by hyperthermia appeared specific for tumor-associated transplantation antigens (TATA, [344]) of the cell line treated (T9 glioblastoma). This was evidenced by the fact that rechallenging with other (TATA-negative) transformed cells lines did not show cross-reactivity. The role of the immune system was further supported by complementary experiments with bilateral, subcutaneous engrafting in this animal model. After regression of one treated tumor on a given flank, the non-CML injected, untreated contralateral tumor was shown to regress. Using exactly the same model, these results were not seen in athymic rats, strongly supporting the existence of a cell-mediated immune response as the underlying mechanism. Immunohistochemical analysis revealed a possible scenario involving activation of NK cells and T lymphocytes positive for CD-3, -4 and -8. These cells were observed in the necrotic tissue and vital rim of the treated tumor and were able to infiltrate the

contralateral tumor. Importantly, these cells were absent in the controls. Infiltration by these lymphocytes is a clinical criterion of favorable prognosis [345-348]. The *in vitro* cytotoxicity of harvested spleen lymphocytes was specific to and enhanced by the hyperthermic treatment. Two antigen-presentation mechanisms important for adaptive cellular immune response tumor were investigated for CML-mediated hyperthermia [349,350], although innate immunity may play a role [344]. First, the influence of cytostatic but non-necrotic hyperthermia on the adaptive immune response was investigated through two important mediators of antigenic determinant processing dependent on the major histocompatibility complex class I (MHC-I), referred to as MHC-I restricted [349]: i) classical proteins constituting the MHC-I, and ii) HSPA1 isoforms A and B, and HSPA8 (i.e., the heat-inducible and constitutive HSP70 isoforms). MHC-I is associated with the final step of intracellular antigen processing, which is to incorporate the antigenic determinant and to bind it to the CD8 T-cell receptor of cytotoxic lymphocytes. The low expression of MHC-I in tumors is associated with escape from immune surveillance [351]. With respect to the animal model used for investigation of CML-mediated hyperthermia (which is not syngeneic *stricto sensu*), it is important to understand that MHC-I is simultaneously involved in the histocompatibility immune response and in the tumor-specific immune response [344]. As discussed in the introduction, both HSPA1A and HSPA1B (heat-inducible isoforms of HSP70) and HSPA8 (HSC70, constitutive), which we will here gather under the abbreviation HSPA1/8, both play important roles in hyperthermia and thermotolerance, although the details differ. Intracellular and extracellular populations of these proteins have pivotal implications in cancer cell biology [156,206], the immune response to cancer [207], transplant rejection [209], and for the immunoadjuvant effect [210]. Ito *et al.* [349] examined *in vitro* the impact of CML-mediated heating of T9 glioma cells on the function of HSPA1/8 in chaperoning and directing chaperoned proteins or peptides to the MHC class I-restricted presentation of antigenic determinants (including those from tumors) to CD8+ T cells (see [344]). Although immunochemitry did not discriminate between both isoforms, hyperthermic treatment of T9 glioma cells essentially increased HSPA1/8 expression levels, which then decreased from a maximum expression at 24 h. In parallel, MHC-I expression levels increased and peaked at 48 h. MCH-I expression was enhanced in transfected cells over-expressing HSPA1. Cells having either high levels of HSPA1/8 or MCH-I expression led to similar

delays in tumor growth following subcutaneous injection in immunocompetent animals. Conversely, an alternative mechanism for triggering the immune response, namely through the extracellular function of the HSPA1/8-peptide complex released after cell death was addressed in [350] (see also [344]). One day after CMLs were injected into the subcutaneously engrafted tumor, hyperthermia was induced by AMF for 30 min. The tumor temperature reached 42°C in 3 min and increased continuously to 45°C at 30 min. As described above, necrosis was observed to spread with repeated hyperthermic treatment. HSPA1/8 immunostaining appeared to follow the heat gradient and the necrosis pattern within the tumor. Expression was positive in necrotic tissue and strongly positive in the vital rim of the tumor surrounding the necrosis. Expression was not observed, however, in the opposite, more distant tumor vital areas. No significant apoptotic cells could be found in the detection assay by TdT-mediated dUTP nick end-labeling (TUNEL). Interestingly, double immunostaining for macrophages and HSPA1/8 showed a macrophage engulfing a corpuscle containing HSPA1/8. This finding can be considered in connection with the remarkable capacity of liposomes to target macrophages [352,353] and to interact specifically with the intracellular trafficking of MHC-I-restricted processes [354]. An immune challenging following immunization with HSPA1/8-peptide complexes from T-9 rat gliomas treated with hyperthermia revealed significantly lower rates of tumor growth when compared to non-immunized controls or controls immunized with HSPA1/8-peptide complexes purified from naive rat liver. Following *in vitro* CML-mediated hyperthermia, cell necrosis (apoptosis excluded by FACS analysis) was related to the high level of HSP70 released in the supernatant. The *in vivo* protocol for this experiment consisted of subcutaneous injection of T-9 glioma cells with MCLs followed immediately by AMF-induced heating at 42°C for 30 min. The formation of the tumor nodule was strongly suppressed. One week later, immunological challenging revealed that tumor growth was suppressed for 50% of the animals and delayed for others when compared to control growth. This was enhanced for *HSPA1*-transfected clones that demonstrated high expression of all HSPA1/8 constituent proteins, confirming the dose dependency reported in [355]. This suggests that MCL-mediated hyperthermia can trigger immunization through HSPA1/8-peptide complexes (the so-called “danger response” [344]) that are released specifically by cell necrosis [356]. Extracellular stress-proteins in fact have immunological activities in antigen transfer and the induction of T and NK cell responses. These

response are also very efficiently mediated by dendritic cells (DC), which acquire antigens from the surrounding environment and upregulate co-stimulatory molecules and conditioning cytokines [357]. This process is depicted in [358] as a delivery of intracellular HSPs from the tumor cell's interior to the extracellular space. The authors emphasize that this process ultimately depends on the heat dose, its distribution and its ability to trigger necrosis. They also suggest that temperatures allowing cell necrosis may be achieved focally within a treated tumor even for mild hyperthermia treatment. It is thus worth considering recent results showing the intrinsic cytotoxicity of magnetic and non-magnetic cationic liposomes in the absence of hyperthermia [359,360]. There is some evidence that cationic lipid-mediated destabilization of the plasma membrane results in an augmentation of cytoplasmic ROS and Ca^{2+} as cytotoxic effectors. These effectors ultimately would lead to apoptosis, and, when considering concomitant hyperthermia, the destabilization of the plasma membrane would perhaps facilitate cell necrosis. In [360], it was emphasized that inhibition of vesicles fusion did not prevent cytotoxicity, demonstrating that the cationic lipid exchange from adhering liposome to plasma membrane is the primary mechanism of cationic lipid-mediated cytotoxicity. Moreover, CMLs have a large heating potential when intratumorally injected and large mammary carcinoma tumors engrafted in mice completely regressed following *ad hoc* repetition of hyperthermia induction. This effect, however, did require repeated CMLs injections [361]. CML-mediated hyperthermia has also been investigated for the treatment in a mouse model of B-16 melanoma [362]. Three treatment schemes were investigated: two single hyperthermia treatments generated by exposure to 30 min of AMF at 118 kHz, with amplitude modulated to reach 43°C or 46°C, and a repetition of the 46°C treatment. For single and repeated 46°C hyperthermia groups, 40 and 90% of animals achieved complete regression, respectively. This was accompanied with significant increases in survival after 120 days of observation, reaffirming the potential of hyperthermia treatment. Spleen cells extracted from cured animals showed increased cytotoxic activity against B16 cells cultured *in vitro*. One month after hyperthermia treatment, cured animals rechallenged with B16 melanoma did not develop tumor nodules in the following month, as opposed to naive mice. Respective HSPA1 (HSP70) levels of 1.6 and 1.3 ng per mg of tumor tissue were reported for hyperthermic treatments at 43°C and 46°C. The authors proposed that the lower HSPA1 levels were due to necrosis. CMLs were also directly injected in a hamster osteosarcoma tumor

model [363]. Here, a tumor temperature of 42°C was maintained for 30 min by exposure to an AMF of 118 kHz with amplitude modulation on days 1, 2 and 3 after tumor injection. A slight increase in the tumor volume was observed up to days 4-10 before a sharp decrease with complete regression (3-month observation) for all animals in the treated group, whereas tumors in the control group showed rapid and uninterrupted increases in volume.

Collectively, these results show that efficient therapeutic responses are achievable in various tumor models using CML-based modality. Ito *et al.* reviewed the contributing mechanisms with respect to the effect of local hyperthermia on the immune response, in terms of cell death and antigen determinant presentation (Figure 1.11) [364]. It would be very instructive to further investigate the cellular actions of magnetic liposomes on membrane biology [365] and on intracellular trafficking, all with respect to the magnetic nanoparticles themselves [241,366]. It would be also beneficial to examine vesicles with or without entrapped magnetic nanoparticles that, as mentioned above, can destabilize plasma membrane or intracellular organelles [367-369]. Considering the number of immunological investigations with various hyperthermic modalities, and the variability of the effects of thermal stress [358,370], the convincing results obtained with liposomal formulations suggest a powerful combination with hyperthermia in inducing an immune response to cancer. Considering the high affinity liposomes have for macrophages, synergy at the level of this professional antigen-presenting cell is likely. The exceptional capacities of liposomes to adsorb and exchange a variety of constituents of biological systems (e.g., soluble or membrane-anchored elements such as lipids or proteins) and to modify the membranes with which they interact, may enhance the ability of hyperthermia to transfer tumor antigens to antigen-presenting cells. Such interactions with macrophages, monocytes or dendritic cells would increase immune response to the tumor. It would be beneficial in future investigations of liposome-mediated hyperthermia to incorporate classic techniques of membrane labeling [323,365,371,372]. As conceptually formulated by Humphries regarding the use of liposomes for studying membrane antigens as immunogens and as targets for immune attack [373], the “language reference frame” of the cell membrane can be modulated by the liposomes in many ways. This effect may occur to some extent via the hypothesized membrane eddy currents.

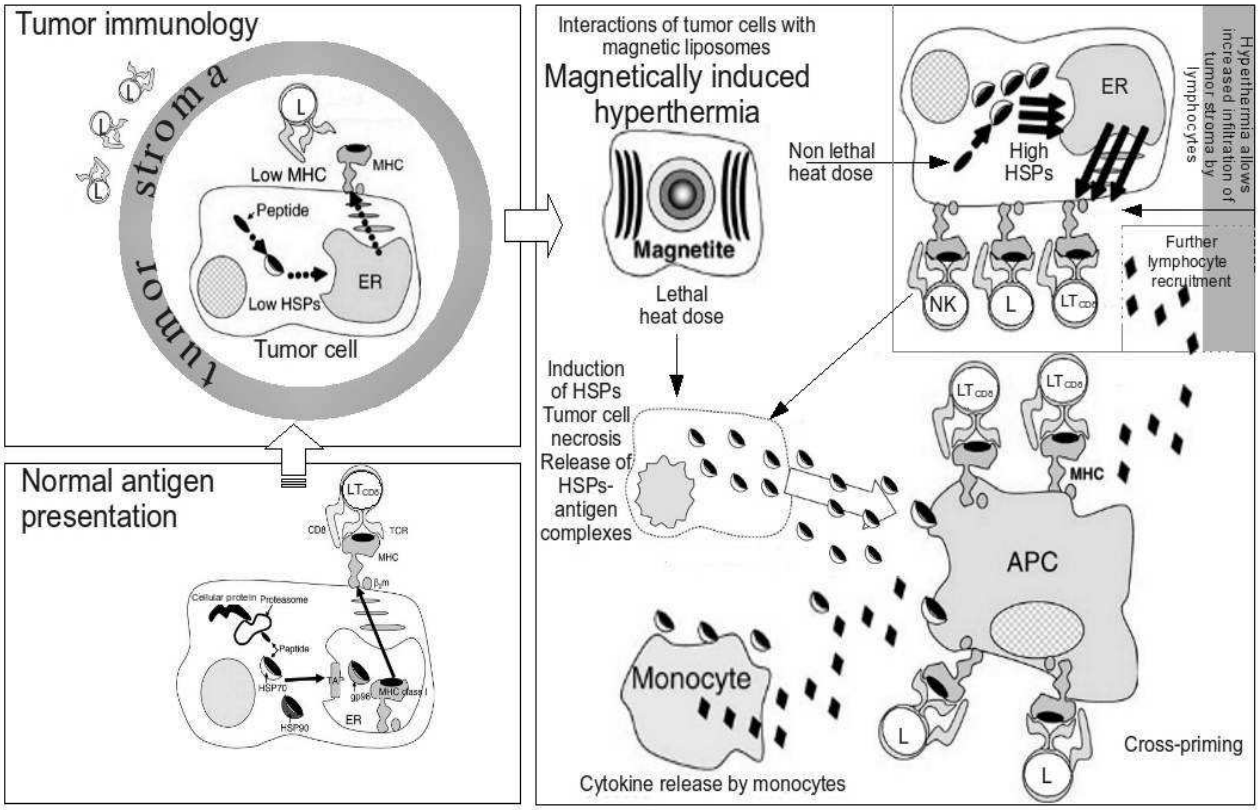

Figure 1.11: Effects of magnetically induced hyperthermia mediated by magnetic liposomes on the anti-tumor immune response, adapted from ref [361].

Bottom left: Implication of heat shock proteins (HSPs, depicted as crescents) in the presentation mechanism of antigenic peptides (depicted as black ellipses) in association with molecules of the MHC I (major histocompatibility complex I). This depicts the process as it occurs for the presentation of self-antigens by healthy cells or the presentation of abnormal antigens by naturally senescent cells to cytotoxic T lymphocytes (LT_{CD8}) through the T cell receptor (TCR), triggering physiological cytotoxic response. In these cases, in constrat to a cell infected by a virus, antigens are processed through the endogenous pathway (involving the endoplasmic reticulum (ER), glycoprotein 86 (gp86), transporter associated with antigen processing (TAP) and $\beta_2$microglobuline (β_2m:)). **Top left**: Mechanisms of immune response impairments by which solid tumors can escape immune attack: impairment of lymphocyte (L) infiltration in the tumor stroma; low MHC expression in tumor cells; low levels of certain HSPs (to some degree); and impairment of tumor abnormal antigen presentation through the endogenous pathway. **Right**: Magnetic liposomes in the tumor allow magnetic induction of hyperthermia, inducing HSPs. Depending on the heat dose, cells can survive or necrose. Antigen presentation would be increased by surviving cells or by antigen-HSP complexes that are highly immunogenic. In both cases, increased non-specific and specific immune responses, involving NK cells, antigen presenting cells (APCs) and CD-4 and -8 T lymphocytes (LT_{CD4} and LT_{CD8}) enhance anticancer immune response. This occurs in conjunction with cytokine secretion (depicted as small, filled lozenges).

4.3 Immunoconjugated magnetoliposomes for the systemic approach of magnetically mediated hyperthermia in solid tumors

4.3.1 Magnetoliposomes conjugated with anti-CA9 (human MN) antigen antibodies

In a quasi non-invasive alternative to intratumoral injection, magnetic liposomes were conjugated with human $F(ab')_2$ antibody fragment anti CA9, also known as carbonic anhydrase IX or human MN antigen (hMN) [374]. This was performed with the aim of hyperthermic treatment after intravenous injection of mouse renal cell carcinoma cells transfected with hMN cDNA in a balb/c mouse orthotopic model [375]. The CA9 protein is also an important marker of cervical carcinomas [376]. This transmembrane protein belongs to the carbonic anhydrases enzyme family, which is specifically induced by hypoxia, as previously discussed. CA9 is an increasingly important factor and target in tumor molecular biology of. CA9 can maintain intracellular pH at physiological values in the frequently acidic environment within solid tumors [129]. This feature and its particular role in cell adhesion, likely mediated by its proteoglycan extramembrane domain, are associated with increased tumor growth and high metastasizing potential. In the CA9-transfected xenograft mouse model, half of the systemically injected dose of anti-CA9 immuno-magnetoliposomes were recovered from the tumor at 48 h. The remainder of the dose was essentially recovered from liver and blood cells. This biodistribution appears specific when compared to control experiences with non-conjugated magnetoliposomes or with control tumor grafts consisting of a non-transfected cell line, for which no accumulation of antibody-conjugated MLs was observed. The distribution within the transfected tumor was not investigated thoroughly, but iron-specific histological coloration revealed marked areas of ribbed appearance that suggests a tight relationship with vascularization or possibly glandular architecture. The accumulation at the tumor site is likely, but the precise localization needs to be investigated further. As a general example, the accumulation of immunoliposomes targeted against colon adenocarcinoma in a liver metastatic tumor site has been reported to be selective for macrophages and not the targeted epitope

[328]. In an AMF of 118 kHz and 30.6 $kA \cdot m^{-1}$ (384 Oe), the SLP of liposome formulation was 94 $W \cdot g^{-1}$. The heating was efficient as demonstrated by superficial skin temperatures of 43°C, which were reached in 10 min and plateaued (intratumoral temperature would be higher). The sequence of three hyperthermic treatments led to extensive necrosis surrounding the appreciable aggregate of the liposome formulation at the level of vessels. Finally, this specifically targeted hyperthermia sequence modality allowed for increased in survival to a mean of 64 days, as compared to 35 days for controls. The two control groups consisted of i) mice injected with non-immuno-conjugated magnetoliposomes 48 h after engraftment with the transfected renal carcinoma cell line over-expressing CA9 and ii) mice injected with anti-CA9 immuno-conjugated magnetoliposomes 48 h after engrafting with non-transfected renal carcinoma cells.

4.3.2 Magnetoliposomes coupled with anti-HER2 antibodies

4.3.2.1 Anti-HER2 immunoconjugated magnetoliposomes and pharmaceutical considerations associated with anti-HER2 antibodies

Preliminary feasibility investigations demonstrated the high potential for magnetoliposomes coupled with anti-HER2 antibodies [377], such as trastuzumab (Herceptin®) for antitumoral treatment with hyperthermia. These antibodies interact with the extracellular domain of the human epidermal growth factor tyrosine kinase receptor 2 *(*HER2), which is expressed in some types of breast cancer cells in 25 % of breast cancers [378]. This faculty appears not to be affected once these antibodies are conjugated with magnetoliposomes. This argues for partial preservation of its understood anti-neoplastic effects on tumor cells. These effects consist of i) diminished receptor signaling; ii) G1 arrest by accumulation of $p27^{kip1}$, a cyclin-dependent kinase inhibitor; iii) the induction of apoptosis; and iv) inhibition of angiogenesis [379]. There is also an immune effect described for anti-HER2 antibodies, involving NK cells in antibody-dependent cellular cytotoxicity (ADCC). The ADCC is mediated by the Fc fragment of the antibody and could be impeded if the fragment is made inaccessible following conjugation with

the lipid vesicle in a liposomal formulation. The large capacity of ligand-stimulated receptor-mediated endocytosis characterizing HER2 would also lead to a high internalization capacity for the conjugated system. Notably, shedding of the extracellular domain of HER2 occurs through hydrolysis. This shedding is not thought to be a mechanism of resistance to trastuzumab, but ongoing evaluation of its role should be taken into account for immunoliposome formulation. Some trastuzumab treatment failure have been associated with altered receptor-antibody interaction resulting from affinity-decreasing mutations of the HER2 extra-cellular domain. This is reported for cases of trastuzumab treatment failure with high levels of HER2 expression and would affect immunoconjugated liposomes as well. It appears that the shed, soluble form of the extracellular domain does not lead to competitive inhibition with trastuzumab. Two other possible explanations for trastuzumab treatment failure implicate i) the HER2 dimerization status and ii) upregulation of the downstream signal cascade. With respect to the former possibility, studies of the dimerization status have revealed how pertuzumab, an antibody anti-HER2 that inhibits dimerization, can be an alternative or act synergistically with trastuzumab in patients refractory or only partially responding to trastuzumab. Evidence of resistance relating to heterodimerization with other tyrosine kinase receptors, such as epithelium growth factor receptor (EGFR), is also reported. With respect to the latter possibility underlying trastuzumab failures (upregulation of the signalization cascade downstream HER2), decreased $p27^{kip1}$ activity or increased insulin-like growth factor-I receptor (IGF-IR) signaling, which share a common pathway with HER2 signal transduction, were involved. This suggests an increased therapeutic potential of antibodies with defined cross-reactivity against two pivotal receptors.

4.3.2.2 Anti-HER2 immunoconjugated magnetoliposomes and micropharmacology considerations associated with non-magnetic anti-HER2 immunoliposomes

The possibility of anti-HER2 immunoconjugated magnetoliposomes for magnetically mediated hyperthermia should be discussed in light of the distribution and microdistribution studies with very comparable, long-circulating immunoliposomes conjugated with anti-HER2 monoclonal antibody fragments. These studies show therapeutic benefit when formulation was intended as a vehicle for

doxorubicin [380], but the results of these studies completely overturns the paradigm of antibody targeting of particulate vectors [381]. Using a model of xenografted tumors expressing high levels of HER2 (breast adenocarcinoma), as well as those with basal levels of expression, such as in normal tissue, distribution studies revealed no difference in tumor uptake between conjugated and non-conjugated liposomes, both of which were found in limited amounts compared to the injected dose. In both cases, only 7 to 8 % of the systematically injected dose was passively retained in the tumors. Nonetheless, microdistribution studies of the fractional taken-up in the tumor with low-power magnification microscopy revealed the capacity of extravasation into tumor nodules [382]. These analyses also demonstrated the overcoming of the micropharmacological barrier in the diffusion of antibodies into the tumor at the tissue level, the so-called binding site barrier [383,384]. This diffusion barrier is related to the high affinity of the antibody-antigen interactions. At intermediate magnifications, non-conjugated liposomes displayed uneven or patchy distribution, reminiscent of the distribution observed previously with non-immuno-conjugated CMLs by Kobayashi's group [339,340], including the observation of Ito *et al.* [349,350]. In contrast to non-conjugated liposomes, the same limited levels of up-taken immuno-conjugated liposomes were homogeneously distributed throughout the cellular organization of the tumor nodule. The immuno-conjugated liposomes reached all levels of the tumor nodule's organization, including the peripheral pseudo-stroma, the intermediate vital layer where neovascularization is the largest, and the central necrotic area. At high magnifications, internalized conjugated liposomes had a perinuclear localization, specifically in cells of the xenografted tumor cell line. This was in contrast to host cells present within the entire cell population of the nodule, as evidenced by parallel flux cytometry investigation. Alternatively, non-conjugated liposomes accumulated predominantly within the tumor stroma, either in extracellular interstices or into tumor-resident macrophages, consistent with [382,385]. As emphasized by the authors, the classical paradigm of active targeting in explaining the therapeutic gain from this therapeutic formulation has to be reconsidered. The mode of action of the therapeutic agent should also be carefully considered. For doxorubicin, this action takes place at the chromatin level and leads to inhibition of the ribosomal DNA synthesis. With antibody targeting, the therapeutic gain should not be attributed at the pharmacokinetic level in terms of its higher biological availability to the tumor, as is commonly assumed, but at the

pharmacodynamic levels. Of the small fraction retained passively in the tumor, the therapeutic gain can be entirely explained by the 6-fold increase in the even smaller fraction of internalized therapeutic agent, a process reflective of the only intrinsic activity of the vector, i.e., receptor-mediated endocytosis from the extracellular milieu. The situation is complicated at pharmaceutical level with respect to magnetically induced hyperthermia and necessitates a fundamental distinction between the active principle, heat, and the therapeutic agent, the magnetic seed, for example SPIONs. Even more complicating are the diffusive characteristics of the applied heat. The direct dependence of heating intensity on the volume concentration of magnetic seeds is the most important factor for local, magnetically mediated treatment of solid tumors. that has to be large enough for reliable heating of the volume targeted. The heating capacity of diluted SPIONs would not succeed in increasing the tissue temperature to effective levels for hyperthermia unless the amplitude of AMF was dramatically increased. Nevertheless, if the corresponding small amount of SPIONs is concentrated in a microscopic focus within this volume, heating could focally reach temperatures of biological significance. When reconsidering magnetoliposomes in this respect, their uptake into the tumor remains the prevailing issue of systemic administration. This route must achieve large intratumoral concentration to provide heating capacities sufficient to generate hyperthermic effects at the level of the tumor volume, as demonstrated by the large amounts obtained with direct injection in the tumor. Thus, the extrapolated dose of anti-HER2 immuno-conjugated magnetoliposomes (developed by Ito *et al* [377]) required to reach tumoral concentrations similar to those obtained with direct intratumoral injection appears unrealistic and would lead to adverse effects. An important advantage specific to magnetoliposomes is the possibility of magnetic concentration at the tumor site based on attraction by a magnetic gradient [371]. It is also evident that magnetic induction must be confined to the tumor site because of the distal accumulation of magnetoliposomes (immuno-conjugated or not) following systemic administration. Regardless, the methods employed by Ito *et al* [375] still resulted in a portion of the tumor response observed with direct intratumoral injection, though AMF amplitude seemed somewhat increased. CA9 is not a cell membrane receptor and is not reported as capable of ligand-induced receptor-mediated endocytosis as is HER2. However, even fluid-phase or adsorptive endocytosis and constitutive receptor-mediated internalization are conceivable. Focal concentration can explain the partial hyperthermic effects

through of focal heatings with an anti-CA9 immuno-conjugated magnetoliposome formulation. With respect to micropharmacology [382-385], histology microphotographs show that anti-CA9 immuno-conjugated magnetoliposomes were concentrated at foci, which may correspond to vascular and perivascular spaces at the level of tumor neovasculature. Focal heating could damage this vasculature, further contributing to confining heat dissipation in the tumor. In that particular case, the spreading of liposomes throughout the tumor could be unfavorable. Notably, with respect to macroscopic heating, intracellular hyperthermia is equivalent to extracellular hyperthermia [386], to an even lesser degree *in vitro* [387]. This fact, however, must be placed in a biological perspective. For example, Rabin consider the heat dissipated by one SPION at the nanoscale to be physically negligible [386]. Fortin *et al*, however, refines these considerations in an intracellular environment by describing the significant heating of nanofoci, which consist of a group of nanoparticles packed in an endosome [387], evoking a striking parallel with magnetoliposomes.

4.4 Cationic magnetoliposomes in bone metastasis in a prostate cancer model

The introduction of CMLs is pertinent to each modality of hyperthermia aiming at accumulation in a specific subset of the cellular population involved in a pathophysiological process. This population subset is very often macrophages [388], but CMLs are also very relevant for targeting osteoclasts in solid bone tumors, as proposed by Fraysinnet et al. [292].

Recently, CMLs were investigated by intratumoral injection for magnetically induced hyperthermic treatment of “syngeneic” prostate tumors. The tumor was heterotopically grafted in subcutaneous tissue affixed to cranial bone as a model for prostate cancer bone metastasis. A control group received abdominal subcutaneous engraftments, representing the absence of the participation of bone in the pathological process [389]. A high occurrence of death in the injected and heated group was reported, even if adapting the complex sequence of repeated AMF hyperthermic treatment, such as by reducing exposure time (30 to 15 min) or AMF amplitude. The temperature reached equilibrium at 44°C during each AMF session. No complete regression was observed. The area of necrosis was effectively associated with CML concentration, but distribution was inhomogeneous and the authors noted that

injection from both sides of the tumor was preferred. Osteoclasts were identified by tartrate-resistant acid phosphatase (TRAP) histochemistry, and proliferating cell nuclear antigen (PCNA) was used as a marker of cell proliferation [390]. Interestingly, the number of TRAP-positive osteoclasts at the engrafted bone site was decreased in the case of hyperthermic treatment. Without hyperthermia (with or without CMLs), tumor cells were strongly positive for PCNA at the tumor/bone interface, more than at the abdominal localization. With CML and hyperthermia treatment, the number of PCNA-positive cells decreased at the tumor/bone interface but not in the abdominal tumor. This was related to decreased bone destruction rate, explained by the inactivation of osteoclasts through heating. This raises the potential of hyperthermia to modulate osteolytic processes in the pathophysiological interactions of prostate cancer metastases with bone [293]. Considering the HSP-independent possibility of HSF-1 to inhibit NF-κB discussed in the introduction, this for of modulation is especially pertinent in this paracrine disorder or other that involve the receptor activator of NF-κB (RANK) [391-396]. In other respects, the high lethality was likely due to adverse CNS injuries. This finding would oblige further studies and formulation adaptations to find indication for the vertebral metastases.

4.5 Neutral magnetoliposomes: targeting draining lymphatic nodes for magnetic hyperthermia

Following a completely different approach, neutral magnetoliposomes (phosphatidylcholine : phosphatidyl-ethanolamine, 2:1, 94.1 nm in diameter) in combination with local hyperthermia were tested *in vivo* by submucosal or intramuscular injection in the tongue to target anatomically associated cervical lymph nodes hosting metastases [397]. One day after injection, neutral magnetoliposomes were found in higher concentrations in cervical lymph nodes than in the tongue, blood, spleen or liver. In an AMF of 30.6 $kA \cdot m^{-1}$ (384 Oe) at 118 kHz, the node reached 44°C. Lymph nodes treated for 40 min at 42.5°C revealed a significant increase in the necrotic area and apoptosis index. It is worth mentioning that hyperthermia can increase homing of lymphocytes in lymphoid organs [398], which are known as

key sites for promoting antitumor immune responses [399].

5 Conclusion

A growing number of magnetically-mediated modalities proposed for hyperthermia have reached the technical level and meet variable medical needs. The constantly evolving magnetic materials being developed can also constitute biomaterials. This is particularly true for magnetic glass-ceramic materials that have the desired high heating efficiency and bioactivity for clinical applicability in hard tissue cancer pathologies. For glass-ceramics embedding magnetic iron oxide, the problematic release of the iron ion was compensated by the addition of phosphate or increase in its concentration. Original magnetic phases are being developed that have the promise of continuously increasing heating efficiency. Alternatives, for example the confinement of SPIONs within a glass-ceramic matrix, offer the advantage of superparamagnetic behavior, i.e., high conversion of external power to heat dissipation and safe parenteral use because of the absence of remnant magnetization. The microparticle systems based on glass-ceramic materials allow for further combinations with varied implantable and injectable biomaterials. The combination of the parenteral therapeutic approach with magnetically mediated hyperthermia has demonstrated strong potential in the case of liver tumor embolization. With the constant improvement of minimally invasive interventional techniques, more of the tumor could be reached and therefore be eligible for this type of intervention in a broadening window of clinical situations. In combination with a robust, magnetically mediated hyperthermic modality, some local surgical interventions could be made less invasive. The formulation of the material plays a pivotal role, as illustrated with Lipiodol® and microspheres. Our group has demonstrated that the formulation of superparamagnetic microparticles with an injectable, *in situ* forming implant allows for efficient, local magnetically mediated hyperthermia. The versatility of the injectable organogels and hydrogels that form an implant *in situ* provides many possibilities for further formulation improvements to treat tumors that can be intratumorally injected. Experimental evidence supports a high potential for magnetoliposomes injected intratumorally, although the low syringeability reported for liposome

formulations used in these experimentations must be carefully considered. Moreover, magnetoliposomes benefit from the wide array of knowledge accumulated for liposomes as drug carriers. Some systemic modalities for magnetoliposome-based treatments of local solid tumor are attractive, but would require specific micropharmacological properties. The well-known action of liposomes as immunoadjuvants at the level of the immune system makes magnetoliposomes very promising for magnetically mediated hyperthermia intended for solid tumor treatment with the intention to promote an immune response.

6 Acknowledgements

We acknowledge the financial support of the Swiss National Science Foundation (grant 3200B0-104508), Switzerland.

7 References

[1] van der Zee J. Heating the patient: a promising approach? Ann. Oncol. 2002 Aug;13(8):1173-1184.

[2] Arancia G, Crateri Trovalusci P, Mariutti G, Mondovì B. Ultrastructural changes induced by hyperthermia in Chinese hamster V79 fibroblasts. Int J Hyperthermia. 1989 Jun;5(3):341-350.

[3] Pietrangeli P, Mondovi B. On the Biochemical Basis of Tumour Damage by Hyperthermia. In: Hyperthermia in cancer treatment. Springer; 2006. p. 110-118.

[4] Christian Streffer. Molecular and Cellular Mechanism of Hyperthermia. In: Thermoradiotherapy and thermochemotherapy - Volume 1: Biology, Physiology, and Physics. Springer; 1995. p. 47-74.

[5] Hall EJ, Giaccia AJ. Hyperthermia. In: Radiobiology for the radiologist. Lippincott Williams & Wilkins; 2006. p. 469-490.

[6] Coss RA, Linnemans WAM. The effects of hyperthermia on the cytoskeleton: a review. Int J Hyperthermia. 1996 Jan;12(2):173-196.

[7] Alberts B, Johnson A, Lewis J, Raff M, Roberts K, Walter P. Chapter 16. The cytoskeleton. In: Molecular Biology of the Cell. New York: Garland Science, Taylor & Francis Group; 2002. p. 907-982.

[8] Welch WJ, Suhan JP. Morphological study of the mammalian stress response: characterization of changes in cytoplasmic organelles, cytoskeleton, and nucleoli, and appearance of intranuclear actin filaments in rat fibroblasts after heat-shock treatment. J. Cell Biol. 1985 Oct;101(4):1198-1211.

[9] Hildebrandt B, Wust P. The biologic rationale of hyperthermia. Cancer Treat. Res. 2007;134:171-184.
[10] Borrelli MJ, Wong RS, Dewey WC. A direct correlation between hyperthermia-induced membrane blebbing and survival in synchronous G1 CHO cells. J. Cell. Physiol. 1986 Feb;126(2):181-190.
[11] Wachsberger PR, Coss RA. Effects of hyperthermia on the cytoskeleton and cell survival in G1 and S phase Chinese hamster ovary cells. Int J Hyperthermia. 1990 Jan;6(1):67-85.
[12] Kregel KC. Heat shock proteins: modifying factors in physiological stress responses and acquired thermotolerance. J. Appl. Physiol. 2002 May;92(5):2177-2186.
[13] Csermely P, Söti C, Blatch G. Chaperones as Parts of Cellular Networks. In: Molecular Aspects of the Stress Response: Chaperones, Membranes and Networks. 2007. p. 55-63.
[14] Bukau B. Molecular chaperones and folding catalysts. CRC Press; 1999.
[15] HUGO Gene Nomenclature Comittee Home Page [Internet]. [cited 2010 Jun 11];Available from: http://www.genenames.org/
[16] Kampinga HH, Hageman J, Vos MJ, Kubota H, Tanguay RM, Bruford EA, et al. Guidelines for the nomenclature of the human heat shock proteins. Cell Stress Chaperones. 2009 Jan;14(1):105-111.
[17] Lepock JR, Frey HE, Heynen ML, Senisterra GA, Warters RL. The nuclear matrix is a thermolabile cellular structure. Cell Stress Chaperones. 2001 Apr;6(2):136-147.
[18] Fukui Y, Katsumaru H. Dynamics of nuclear actin bundle induction by dimethyl sulfoxide and factors affecting its development. J. Cell Biol. 1980 Jan;84(1):131-140.
[19] Fukui Y. Intranuclear actin bundles induced by dimethyl sulfoxide in interphase nucleus of Dictyostelium. J. Cell Biol. 1978 Jan;76(1):146-157.
[20] Fukui Y, Katsumaru H. Nuclear actin bundles in Amoeba, Dictyostelium and human HeLa cells induced by dimethyl sulfoxide. Exp. Cell Res. 1979 May;120(2):451-455.
[21] Jelke E, Oertel B. DMSO induces the formation of microfilament bundles in nuclei of zoospores of Phytophthora infestans (Mont.) De Bary (Oomycetes, Pythiaceae). Acta Histochem. Suppl. 1990;39:435-442.
[22] Sanger JW, Sanger JM, Kreis TE, Jockusch BM. Reversible translocation of cytoplasmic actin into the nucleus caused by dimethyl sulfoxide. Proc. Natl. Acad. Sci. U.S.A. 1980 Sep;77(9):5268-5272.
[23] Sanger JW, Gwinn J, Sanger JM. Dissolution of cytoplasmic actin bundles and the induction of nuclear actin bundles by dimethyl sulfoxide. J. Exp. Zool. 1980 Aug;213(2):227-230.
[24] Roti Roti JL, Kampinga HH, Malyapa RS, Wright WD, vanderWaal RP, Xu M. Nuclear matrix as a target for hyperthermic killing of cancer cells. Cell Stress Chaperones. 1998 Dec;3(4):245-255.
[25] Strom R, Santoro AS, Crifo' C, Bozzi A, Mondovi' B, Fanelli AR. The biochemical mechanism of selective heat sensitivity of cancer cells - IV. Inhibition of RNA synthesis. Eur J Cancer. 1973 Feb;9(2):103-112.
[26] Mondovi' B, Agro' AF, Rotilio G, Strom R, Moricca G, Fanelli AR. The biochemical mechanism of selective heat sensitivity of cancer cells - II. Studies on nucleic acids and protein synthesis. Eur J Cancer. 1969 May;5(2):137-146.
[27] Gieni RS, Hendzel MJ. Actin dynamics and functions in the interphase nucleus: moving toward

an understanding of nuclear polymeric actin. Biochem. Cell Biol. 2009 Feb;87(1):283-306.

[28] Reiter T, Penman S. "Prompt" heat shock proteins: translationally regulated synthesis of new proteins associated with the nuclear matrix-intermediate filaments as an early response to heat shock. Proc. Natl. Acad. Sci. U.S.A. 1983;80:4737-4741.

[29] Zhu W-G, Roberts ZV, Dynlacht JR. Heat-induced modulation of lamin B content in two different cell lines. J. Cell. Biochem. 1999;75(4):620-628.

[30] Arrigo AP, Suhan JP, Welch WJ. Dynamic changes in the structure and intracellular locale of the mammalian low-molecular-weight heat shock protein. Mol. Cell. Biol. 1988 Dec;8(12):5059-5071.

[31] Mizzen LA, Welch WJ. Characterization of the thermotolerant cell. I. Effects on protein synthesis activity and the regulation of heat-shock protein 70 expression. J. Cell Biol. 1988 Apr;106(4):1105-1116.

[32] Welch WJ, Mizzen LA. Characterization of the thermotolerant cell. II. Effects on the intracellular distribution of heat-shock protein 70, intermediate filaments, and small nuclear ribonucleoprotein complexes. J. Cell Biol. 1988 Apr;106(4):1117-1130.

[33] Welch WJ, Suhan JP. Cellular and biochemical events in mammalian cells during and after recovery from physiological stress. J. Cell Biol. 1986 Nov;103(5):2035-2052.

[34] Welch WJ, Feramisco JR. Nuclear and nucleolar localization of the 72,000-dalton heat shock protein in heat-shocked mammalian cells. J. Biol. Chem. 1984 Apr 10;259(7):4501-4513.

[35] Buffa P, Guarriera-Bobyleva V, Muscatello U, Pasquali-Ronchetti I. Conformational changes of mitochondria associated with uncoupling of oxidative phosphorylation in vivo and in vitro. Nature. 1970 Apr 18;226(5242):272-274.

[36] Turano C, Ferraro A, Strom R, Cavaliere R, Fanelli AR. The biochemical mechanism of selective heat sensitivity of cancer cells: III. Studies on lysosomes. Eur J Cancer. 1970 Apr;6(2):67-72.

[37] Hildebrandt B, Wust P, Ahlers O, Dieing A, Sreenivasa G, Kerner T, et al. The cellular and molecular basis of hyperthermia. Crit. Rev. Oncol. Hematol. 2002 Jul;43(1):33-56.

[38] Burdon RH, Kerr SM, Cutmore CM, Munro J, Gill V. Hyperthermia, Na+K+ATPase and lactic acid production in some human tumour cells. Br. J. Cancer. 1984 Apr;49(4):437-445.

[39] Thews G, Mutschler E, Vaupel P. Anatomie, Physiologie, Pathophysiologie des Menschen. 6th ed. Wissenschaftliche Verlagsges.; 2007.

[40] Storey KB. Functional metabolism: regulation and adaptation. Wiley-IEEE; 2004.

[41] Nelson DL, Cox MM. Lehninger Principles of Biochemistry. 4th ed. W. H. Freeman; 2004.

[42] Baronzio GF, Gramaglia A, Baronzio A, Freitas I. Influence of tumor microenvironment on thermoresponse: Biological and clinical implications. In: Hyperthermia in cancer treatment. Springer; 2006. p. 68-91.

[43] Vaupel PW, Kelleher DK. Metabolic status and reaction to heat of normal and tumor tissue. In: Thermoradiotherapy and thermochemotherapy - Volume 1: Biology, Physiology, and Physics. Springer; 1995. p. 159-176.

[44] Mondovì B, Rotilio G, Strom R, Finazzi-Agrò A, Cavaliere R, Moricca G, et al. Biochemical mechanism of selective heat sensitivity of tumour cells: preliminary results. Ital. J. Biochem. 1968 Apr;17(2):101-106.

[45] Lee SY, Ryu KH, Kang MS, Song CW. Effect of hyperthermia on the lactic acid and beta-

hydroxybutyric acid content in tumour. Int J Hyperthermia. 1986 Jun;2(2):213-222.
[46] Streffer C. Aspects of metabolic change after hyperthermia. Recent Results Cancer Res. 1988;107:7-16.
[47] Streffer C. Biological basis of thermotherapy (with special reference to oncology). In: Biological basis of oncologic thermotherapy. Springer-Verlag; 1990.
[48] Streffer C, van Beuningen D. The biological basis for tumour therapy by hyperthermia and radiation. Recent Results Cancer Res. 1987;104:24-70.
[49] Streffer C. Biological basis for the use of hyperthermia in tumour therapy. Strahlenther Onkol. 1987 Jul;163(7):416-419.
[50] Song CW, Clement JJ, Levitt SH. Cytotoxic and radiosensitizing effects of 5-thio-D-glucose on hypoxic cells. Radiology. 1977 Apr;123(1):201-205.
[51] Kim SH, Kim JH, Hahn EW. Selective potentiation of hyperthermic killing of hypoxic cells by 5-thio-D-glucose. Cancer Res. 1978 Sep;38(9):2935-2938.
[52] Kim JH, Kim SH, Alfieri AA, Young CW. Quercetin, an inhibitor of lactate transport and a hyperthermic sensitizer of HeLa cells. Cancer Res. 1984 Jan;44(1):102-106.
[53] Kim SH, Kim JH, Alfieri AA, He SQ, Young CW. Gossypol, a hyperthermic sensitizer of HeLa cells. Cancer Res. 1985 Dec;45(12 Pt 1):6338-6340.
[54] Coss RA, Storck CW, Daskalakis C, Berd D, Wahl ML. Intracellular acidification abrogates the heat shock response and compromises survival of human melanoma cells. Mol. Cancer Ther. 2003 Apr;2(4):383-388.
[55] Will O, Mahler HC, Arrigo AP, Epe B. Influence of glutathione levels and heat-shock on the steady-state levels of oxidative DNA base modifications in mammalian cells. Carcinogenesis. 1999 Feb;20(2):333-337.
[56] Biesalski HK, Franklin J. Antioxidants in cancer therapy: is there a rationale to recommend antioxidants during cancer therapy? In: Pompella A, Bánhégyi G, Wellman-Rousseau M, editors. Thiol metabolism and redox regulation of cellular functions. IOS Press; 2002. p. 252-264.
[57] Yoshikawa T, Kokura S, Tainaka K, Itani K, Oyamada H, Kaneko T, et al. The role of active oxygen species and lipid peroxidation in the antitumor effect of hyperthermia. Cancer Res. 1993 May 15;53(10 Suppl):2326-2329.
[58] Loven DP, Leeper DB, Oberley LW. Superoxide dismutase levels in Chinese hamster ovary cells and ovarian carcinoma cells after hyperthermia or exposure to cycloheximide. Cancer Res. 1985 Jul;45(7):3029-3033.
[59] Omar RA, Yano S, Kikkawa Y. Antioxidant enzymes and survival of normal and simian virus 40-transformed mouse embryo cells after hyperthermia. Cancer Res. 1987 Jul 1;47(13):3473-3476.
[60] Skibba JL, Quebbeman EJ, Kalbfleisch JH. Nitrogen metabolism and lipid peroxidation during hyperthermic perfusion of human livers with cancer. Cancer Res. 1986 Nov;46(11):6000-6003.
[61] Lin PS, Quamo S, Ho KC, Gladding J. Hyperthermia enhances the cytotoxic effects of reactive oxygen species to Chinese hamster cells and bovine endothelial cells in vitro. Radiat. Res. 1991 Apr;126(1):43-51.
[62] Powers RH, Stadnicka A, Kalbfleish JH, Skibba JL. Involvement of xanthine oxidase in oxidative stress and iron release during hyperthermic rat liver perfusion. Cancer Res. 1992 Apr 1;52(7):1699-1703.

[63] Permyakov E. Metalloproteomics. Wiley-Interscience; 2009.
[64] McCord JM. Oxygen-derived free radicals in postischemic tissue injury. N. Engl. J. Med. 1985 Jan 17;312(3):159-163.
[65] Skibba JL, Gwartney EA. Liver hyperthermia and oxidative stress: role of iron and aldehyde production. Int J Hyperthermia. 1997 Apr;13(2):215-226.
[66] Strom R, Santoro AS, Crifo' C, Bozzi A, Mondovi' B, Fanelli AR. The biochemical mechanism of selective heat sensitivity of cancer cells. IV. Inhibition of RNA synthesis. Eur J Cancer. 1973 Feb;9(2):103-112.
[67] Hall EJ, Giaccia AJ. Cell survival curves. In: Radiobiology for the radiologist. Lippincott Williams & Wilkins; 2006. p. 30-46.
[68] Dewhirst MW. Thermal dosimetry. In: Thermoradiotherapy and thermochemotherapy - Volume 1: Biology, Physiology, and Physics. Springer; 1995. p. 123-138.
[69] Sneed PK, Stea B. Thermoraditherapy for brain tumors. In: Thermoradiotherapy And Thermochemotherapy - Volume 2: Clinical Applications. Springer Verlag; 1996.
[70] Jung H. A generalized concept for cell killing by heat. Radiat. Res. 1986 Apr;106(1):56-72.
[71] Jung H. A generalized concept for cell killing by heat. Effect of acutely induced thermotolerance and decay of thermosensitization. Radiat. Res. 1994 Sep;139(3):280-289.
[72] Jung H. A generalized concept for cell killing by heat. Effect of chronically induced thermotolerance. Radiat. Res. 1991 Sep;127(3):235-242.
[73] G Pincus, A Fischer. The growth and death of tissues cultures exposed to supranormal temperatures. J. Exp. Med. 1931;54:323-332.
[74] Dewhirst MW, Viglianti BL, Lora-Michiels M, Hanson M, Hoopes PJ. Basic principles of thermal dosimetry and thermal thresholds for tissue damage from hyperthermia. Int J Hyperthermia. 2003;19(3):267.
[75] F.H. Jonhson, H. Eyring, M.J. Polisar. The kinetic basis of molecular biology. John Wiley, New York; 1954.
[76] Bischof JC, He X. Thermal stability of proteins. Ann. N. Y. Acad. Sci. 2006;1066:12-33.
[77] Privalov PL, Tiktopulo EI, Tischenko VM. Stability and mobility of the collagen structure. J. Mol. Biol. 1979 Jan 15;127(2):203-216.
[78] Jorritsma JB, Konings AW. The occurrence of DNA strand breaks after hyperthermic treatments of mammalian cells with and without radiation. Radiat. Res. 1984 Apr;98(1):198-208.
[79] Rofstad EK, Brustad T. Arrhenius analysis of the heat response in vivo and in vitro of human melanoma xenografts. Int J Hyperthermia. 1986 Dec;2(4):359-368.
[80] Dewey WC. Arrhenius relationships from the molecule and cell to the clinic. Int J Hyperthermia. 1994 Aug;10(4):457-483.
[81] Dewey WC. Arrhenius relationships from the molecule and cell to the clinic. Int J Hyperthermia. 2009;25(1):3 - 20.
[82] Sapareto SA. A workshop on thermal dose in cancer therapy: introduction. Int J Hyperthermia. 1987 Aug;3(4):289-290.
[83] Sapareto SA. Thermal isoeffect dose: addressing the problem of thermotolerance. Int J Hyperthermia. 1987 Aug;3(4):297-305.
[84] Lagendijk JJW. Hyperthermia treatment planning. Phys Med Biol. 2000;45(5):R61-R76.

[85] Field SB, Morris CC. The relationship between heating time and temperature: its relevance to clinical hyperthermia. Radiother Oncol. 1983 Nov;1(2):179-186.
[86] Baiotto B, Marini P. Thermometry: Clinical Aspects and Perspectives. In: Hyperthermia in cancer treatment. Springer; 2006. p. 19-26.
[87] Vidair CA, Dewey WC. Two distinct modes of hyperthermic cell death. Radiat. Res. 1988 Oct;116(1):157-171.
[88] Rofstad EK, Brustad T. Effect of hyperthermia on human melanoma cells heated either as solid tumors in athymic nude mice or in vitro. Cancer. 1982 Oct 1;50(7):1304-1308.
[89] Song CW, Kang MS, Rhee JG, Levitt SH. The effect of hyperthermia on vascular function, pH, and cell survival. Radiology. 1980 Dec;137(3):795-803.
[90] Kang MS, Song CW. The effect of hyperthermia on cell survival in a mouse tumour without blood flow. Br J Radiol. 1980 Jun;53(630):606-607.
[91] Crile G. The effects of heat and radiation on cancers implanted on the feet of mice. Cancer Res. 1963 Mar;23:372-380.
[92] Kallinowski F, Schlenger KH, Runkel S, Kloes M, Stohrer M, Okunieff P, et al. Blood Flow, Metabolism, Cellular Microenvironment, and Growth Rate of Human Tumor Xenografts. Cancer Res. 1989 Jul 15;49(14):3759-3764.
[93] Song CW. Effect of Local Hyperthermia on Blood Flow and Microenvironment: A Review. Cancer Res. 1984 Oct 1;44(10_Supplement):4721s-4730.
[94] Li JH, Liu FF. Intracellular pH and heat sensitivity in two human cancer cell lines. Radiother Oncol. 1997 Jan;42(1):69-76.
[95] Latchman DS, editor. Stress Proteins. Berlin: Springer; 1999.
[96] Henderson B. Integrating the cell stress response: a new view of molecular chaperones as immunological and physiological homeostatic regulators. Cell Biochem. Funct. 2010;28(1):1-14.
[97] Soti C, Pál C, Papp B, Csermely P. Molecular chaperones as regulatory elements of cellular networks. Curr. Opin. Cell Biol. 2005 Apr;17(2):210-215.
[98] Novartis Foundation. The biology of extracellular molecular chaperones. John Wiley and Sons; 2008.
[99] Sharp FR, Massa SM, Swanson RA. Heat-shock protein protection. Trends Neurosci. 1999 Mar 1;22(3):97-99.
[100] Eden W van, Young DB. Stress proteins in medicine. Informa Health Care; 1996.
[101] Arrigo A-P, Müller WEG. Small stress proteins. Springer; 2002.
[102] Csermely P, Korcsmáros T, Sulyok K. Stress responses in biology and medicine. Blackwell Pub.; 2007.
[103] Csermely P, Vígh L. Molecular aspects of the stress response. Springer; 2007.
[104] Multhoff G. Heat shock proteins in immunity. Handb Exp Pharmacol. 2006;(172):279-304.
[105] Morimoto RI, Santoro MG. Stress-inducible responses and heat shock proteins: new pharmacologic targets for cytoprotection. Nat. Biotechnol. 1998 Sep;16(9):833-838.
[106] Feige DU. Stress-inducible cellular responses. Birkhäuser; 1996.
[107] Shi Y, Morimoto RI. Autoregulation of the heat shock response. In: Latchman DS, editor. Stress Proteins. Berlin Heiselberg New York: Springer- Verlag; 1999. p. 225-241.
[108] Anckar J, Sistonen L. Heat Shock Factor 1 as a Coordinator of Stress and Developmental

Pathways. In: Molecular Aspects of the Stress Response: Chaperones, Membranes and Networks. 2007. p. 78-88.

[109] Trinklein ND, Murray JI, Hartman SJ, Botstein D, Myers RM. The role of heat shock transcription factor 1 in the genome-wide regulation of the mammalian heat shock response. Mol. Biol. Cell. 2004 Mar;15(3):1254-1261.

[110] Yoo HY, Chang MS, Rho HM. The activation of the rat copper/zinc superoxide dismutase gene by hydrogen peroxide through the hydrogen peroxide-responsive element and by paraquat and heat shock through the same heat shock element. J. Biol. Chem. 1999 Aug 20;274(34):23887-23892.

[111] Vilaboa NE, Galán A, Troyano A, de Blas E, Aller P. Regulation of multidrug resistance 1 (MDR1)/P-glycoprotein gene expression and activity by heat-shock transcription factor 1 (HSF1). J. Biol. Chem. 2000 Aug 11;275(32):24970-24976.

[112] Callahan MK, Wohlfert EA, Ménoret A, Srivastava PK. Heat shock up-regulates lmp2 and lmp7 and enhances presentation of immunoproteasome-dependent epitopes. J. Immunol. 2006 Dec 15;177(12):8393-8399.

[113] Rossi A, Ciafrè S, Balsamo M, Pierimarchi P, Santoro MG. Targeting the heat shock factor 1 by RNA interference: a potent tool to enhance hyperthermochemotherapy efficacy in cervical cancer. Cancer Res. 2006 Aug 1;66(15):7678-7685.

[114] Li T, Spearow J, Rubin CM, Schmid CW. Physiological stresses increase mouse short interspersed element (SINE) RNA expression in vivo. Gene. 1999 Nov 1;239(2):367-372.

[115] Liu XD, Liu PC, Santoro N, Thiele DJ. Conservation of a stress response: human heat shock transcription factors functionally substitute for yeast HSF. EMBO J. 1997 Nov 3;16(21):6466-6477.

[116] Khaleque MA, Bharti A, Sawyer D, Gong J, Benjamin IJ, Stevenson MA, et al. Induction of heat shock proteins by heregulin [beta]1 leads to protection from apoptosis and anchorage-independent growth. Oncogene. 2005 Jun 13;24(43):6564-6573.

[117] Stove C, Bracke M. Roles for neuregulins in human cancer. Clin. Exp. Metastasis. 2004;21(8):665-684.

[118] Escribá PV, González-Ros JM, Goñi FM, Kinnunen PKJ, Vigh L, Sánchez-Magraner L, et al. Membranes: a meeting point for lipids, proteins and therapies. J. Cell. Mol. Med. 2008 Jun;12(3):829-875.

[119] Nishizawa J, Nagata K. Regulation of heat shock transcription factors by hypoxia or ischemia/reperfusion in heart and brain. In: Latchman DS, editor. Stress Proteins. Berlin: Springer; 1999. p. 201.

[120] Michiels C, Minet E, Mottet D, Raes M. Regulation of gene expression by oxygen: NF-kappaB and HIF-1, two extremes. Free Radic. Biol. Med. 2002 Nov 1;33(9):1231-1242.

[121] Hockel M, Vaupel P. Tumor Hypoxia: Definitions and Current Clinical, Biologic, and Molecular Aspects. J. Natl. Cancer Inst. 2001 Feb 21;93(4):266-276.

[122] Quintero M, Mackenzie N, Brennan PA. Hypoxia-inducible factor 1 (HIF-1) in cancer. Eur J Surg Oncol. 2004 Jun;30(5):465-468.

[123] Mabjeesh NJ, Amir S. Hypoxia-inducible factor (HIF) in human tumorigenesis. Histol. Histopathol. 2007 May;22(5):559-572.

[124] Semenza GL. HIF-1 and tumor progression: pathophysiology and therapeutics. Trends Mol Med. 2002;8(4 Suppl):S62-67.
[125] Hockel M, Vaupel P. The prognostic significance of hypoxia in cervical cancer: a radiobiological or tumor biological phenomenon? In: Molls M, Vaupel P, editors. Blood perfusion and microenvironment of human tumors. Springer; 2000. p. 73-79.
[126] Hypoxia-inducible factor. In: Cancer Biology. Oxford University Press, USA; 2007. p. 204.
[127] Bachelet M, Multhoff G, Vignola M, Himeno K, Polla BS. Heat shock proteins in inflammation and immunity. In: Stress Proteins. Berlin Heiselberg New York: Springer- Verlag; 1999. p. 281-303.
[128] Freitas I, Boncompagni E, Vaccarone R, Fenoglio C, Barni S, Baronzio GF. Iron accumulation in mammary tumor suggests a tug of war between tumor and host for the microelement. Anticancer Res. 2007 Oct;27(5A):3059-3065.
[129] Chiche J, Ilc K, Laferriere J, Trottier E, Dayan F, Mazure NM, et al. Hypoxia-Inducible Carbonic Anhydrase IX and XII Promote Tumor Cell Growth by Counteracting Acidosis through the Regulation of the Intracellular pH. Cancer Res. 2009 Jan 1;69(1):358-368.
[130] Lunt SJ, Hill RP. Tumor Oxygenation and Treatment Response. In: Cancer drug resistance. Totowa, New Jersey: Humana Press; 2006. p. 43-66.
[131] Baird NA, Turnbull DW, Johnson EA. Induction of the heat shock pathway during hypoxia requires regulation of heat shock factor by hypoxia-inducible factor-1. J. Biol. Chem. 2006 Dec 15;281(50):38675-38681.
[132] Li G, Mivechi N. Heat shock protein 70. In: Latchman DS, editor. Stress Proteins. Berlin: Springer; 1999. p. 43.
[133] Kirkegaard T, Roth AG, Petersen NHT, Mahalka AK, Olsen OD, Moilanen I, et al. Hsp70 stabilizes lysosomes and reverts Niemann-Pick disease-associated lysosomal pathology. Nature. 2010 Jan 28;463(7280):549-553.
[134] Habash RWY, Bansal R, Krewski D, Alhafid HT. Thermal therapy, part 1: an introduction to thermal therapy. Crit Rev Biomed Eng. 2006;34(6):459-489.
[135] Glossary of terms for thermal physiology. J. Therm. Biol. 2003 Jan;28(1):75-106.
[136] Luk KH, Hulse RM. Hyperthermia in Cancer Therapy. West J Med. 1980 Mar;132:179.
[137] Engin K. Biological rationale and clinical experience with hyperthermia. Control Clin Trials. 1996 Aug;17(4):316-342.
[138] Falk MH, Issels RD. Hyperthermia in oncology. Int J Hyperthermia. 2001 Feb;17(1):1-18.
[139] Baronzio GF, Hager ED. Hyperthermia in cancer treatment. Springer; 2006.
[140] Dewhirst MW, Jones E, Samulski T, Vujaskovic Z, Li C, Prosnitz L. Clinical Hyperthermia. In: Cancer Medicine. B.C. Decker; 2003.
[141] Habash RWY, Bansal R, Krewski D, Alhafid HT. Thermal therapy, Part III: ablation techniques. Crit Rev Biomed Eng. 2007;35(1-2):37-121.
[142] Urano M, Douple EB. Thermal effects on cells and tissues. VSP; 1988.
[143] LeVeen HH, Wapnick S, Piccone V, Falk G, Ahmed Nafis. Tumor eradication by radiofrequency therapy. Responses in 21 patients. JAMA. 1976 May 17;235(20):2198-2200.
[144] Hiraoka M, Jo S, Akuta K, Nishimura Y, Takahashi M, Abe M. Radiofrequency capacitive hyperthermia for deep-seated tumors. I. Studies on thermometry. Cancer. 1987 Jul 1;60(1):121-

127.
[145] Kelleher DK, Vaupel PW. Vascular effects of localized hyperthermia. In: Hyperthermia in cancer treatment. Springer; 2006. p. 99-109.
[146] Hildebrandt B, Wust P. Interactions between hyperthermia and cytotoxic drugs. Cancer Treat. Res. 2007;134:185-193.
[147] Dieing A, Ahlers O, Hildebrandt B, Kerner T, Tamm I, Possinger K, et al. The effect of induced hyperthermia on the immune system. Prog. Brain Res. 2007;162:137-152.
[148] Molls M, Vaupel P, editors. Blood perfusion and microenvironment of human tumors. Springer; 2000.
[149] Urano M, Douple EB. Chemopotentiation by Hyperthermia. VSP; 1994.
[150] Vaupel P, Kallinowski F, Okunieff P. Blood flow, oxygen and nutrient supply, and metabolic microenvironment of human tumors: a review. Cancer Res. 1989 Dec 1;49(23):6449-6465.
[151] Gautherie M, Streffer C, Vaupel P, Hahn GM. Biological basis of oncologic thermotherapy. Springer-Verlag; 1990.
[152] Vaupel P, Schlenger K, Hoeckel M. Blood flow and tissue oxygenation of human tumors: an update. Adv. Exp. Med. Biol. 1992;317:139-151.
[153] Vaupel PW, Kelleher DK. Pathophysiological and vascular characteristics of tumours and their importance for hyperthermia: Heterogeneity is the key issue. Int J Hyperthermia. 2010 Mar 26;
[154] Vaupel P. Physiological properties of malignant tumours. NMR Biomed. 1992 Oct;5(5):220-225.
[155] Baronzio G, Fiorentini G, Cogle CR. Cancer Microenvironment and Therapeutic Implications: Tumor Pathophysiology Mechanisms and Therapeutic Strategies. Springer; 2009.
[156] Ruddon RWR. Cancer Biology. 4th ed. Oxford University Press, USA; 2007.
[157] Ward KA, Jain RK. Response of tumours to hyperglycaemia: characterization, significance and role in hyperthermia. Int J Hyperthermia. 1988 Jun;4(3):223-250.
[158] Feldmann HJ, Molls M, Vaupel P. Clinical investigations on blood perfusions in human tumors. In: Molls M, Vaupel P, editors. Blood perfusion and microenvironment of human tumors. Springer; 2000. p. 47-62.
[159] Waterman FM, Nerlinger RE, Moylan DJ, Leeper DB. Response of human tumor blood flow to local hyperthermia. Int. J. Radiat. Oncol. Biol. Phys. 1987 Jan;13(1):75-82.
[160] Waterman FM, Tupchong L, Liu CR. Modified thermal clearance technique for determination of blood flow during local hyperthermia. Int J Hyperthermia. 1991 Oct;7(5):719-733.
[161] Samulski TV, Fessenden P, Valdagni R, Kapp DS. Correlations of thermal washout rate, steady state temperatures, and tissue type in deep seated recurrent or metastatic tumors. Int. J. Radiat. Oncol. Biol. Phys. 1987 Jun;13(6):907-916.
[162] Lagendijk JJ, Hofman P, Schipper J. Perfusion analyses in advanced breast carcinoma during hyperthermia. Int J Hyperthermia. 1988 Oct;4(5):479-495.
[163] Feldmann HJ, Molls M, Hoederath A, Krümpelmann S, Sack H. Blood flow and steady state temperatures in deep-seated tumors and normal tissues. Int. J. Radiat. Oncol. Biol. Phys. 1992;23(5):1003-1008.
[164] Vaupel P. Tumor blood flow. In: Molls M, Vaupel P, editors. Blood perfusion and microenvironment of human tumors. Springer; 2000. p. 41-45.
[165] Schwab M. Encyclopedia of Cancer. 2nd ed. Springer; 2008.

[166] Döme B, Hendrix MJC, Paku S, Tóvári J, Tímár J. Alternative vascularization mechanisms in cancer: Pathology and therapeutic implications. Am. J. Pathol. 2007 Jan;170(1):1-15.
[167] Papetti M, Herman IM. Mechanisms of normal and tumor-derived angiogenesis. Am. J. Physiol., Cell Physiol. 2002 May;282(5):C947-970.
[168] Kioi M, Vogel H, Schultz G, Hoffman RM, Harsh GR, Brown JM. Inhibition of vasculogenesis, but not angiogenesis, prevents the recurrence of glioblastoma after irradiation in mice. J Clin Invest. 2010 Mar 1;120(3):694-705.
[169] Konerding MA, van Ackern C, Fait E, Steinberg F, Streffer C. Morphological aspects of tumor angiogenesis and microcirculation. In: Molls M, Vaupel P, editors. Blood perfusion and microenvironment of human tumors. Springer; 2000. p. 5-17.
[170] Freitas I, Baronzio GF, Bono B, Griffini P, Bertone V, Sonzini N, et al. Tumor interstitial fluid: misconsidered component of the internal milieu of a solid tumor. Anticancer Res. 1997 Feb;17(1A):165-172.
[171] Baxter LT, Jain RK. Transport of fluid and macromolecules in tumors. I. Role of interstitial pressure and convection. Microvasc. Res. 1989 Jan;37(1):77-104.
[172] Baxter LT, Jain RK. Transport of fluid and macromolecules in tumors. II. Role of heterogeneous perfusion and lymphatics. Microvasc. Res. 1990 Sep;40(2):246-263.
[173] Baxter LT, Zhu H, Mackensen DG, Jain RK. Physiologically based pharmacokinetic model for specific and nonspecific monoclonal antibodies and fragments in normal tissues and human tumor xenografts in nude mice. Cancer Res. 1994 Mar;54(6):1517–1528.
[174] Funaki B, Lorenz J, Ha TV, editors. Teaching Atlas of Vascular and Non-Vascular Interventional Radiology. Thieme; 2007.
[175] Shakil A, Osborn JL, Song CW. Changes in oxygenation status and blood flow in a rat tumor model by mild temperature hyperthermia. Int. J. Radiat. Oncol. Biol. Phys. 1999 Mar 1;43(4):859-865.
[176] Song CW, Lin JC, Chelstrom LM, Levitt SH. The kinetics of vascular thermotolerance in SCK tumors of A/J mice. Int. J. Radiat. Oncol. Biol. Phys. 1989 Oct;17(4):799-802.
[177] Song CW, Chelstrom LM, Sung JH. Effects of a second heating on blood flow in tumors. Radiat. Res. 1990 Apr;122(1):66-71.
[178] Evans SS, Frey M, Schleider DM, Bruce RA, Wang W-chao, Repasky EA, et al. Regulation of leukocyte-endothelial cell interactions in tumor immunity. In: The biology of tumors. Springer; 1998. p. 273-286.
[179] Stubbs M. Tumor pH. In: Molls M, Vaupel P, editors. Blood perfusion and microenvironment of human tumors. Springer; 2000. p. 113-120.
[180] Gerweck LE, Seetharaman K. Cellular pH gradient in tumor versus normal tissue: potential exploitation for the treatment of cancer. Cancer Res. 1996 Mar 15;56(6):1194-1198.
[181] Roca C, Primo L, Valdembri D, Cividalli A, Declerck P, Carmeliet P, et al. Hyperthermia inhibits angiogenesis by a plasminogen activator inhibitor 1-dependent mechanism. Cancer Res. 2003 Apr 1;63(7):1500-1507.
[182] Spoerke N, Underwood S, Differding J, Van P, Sambasivan C, Shapiro D, et al. Effects of ethanol intoxication and gender on blood coagulation. J Trauma. 2010 May;68(5):1106-1111.
[183] Seth D, Hogg P, Gorrell M, Mccaughan G, Haber P. Direct effects of alcohol on hepatic

fibrinolytic balance: Implications for alcoholic liver disease. Journal of Hepatology. 2008 Apr;48(4):614-627.

[184] Kampinga HH, Dikomey E. Hyperthermic radiosensitization: mode of action and clinical relevance. Int. J. Radiat. Biol. 2001;77(4):399.

[185] Seegenschmiedt MN, Fessenden P, Vernon CC. Thermoradiotherapy And Thermochemotherapy - Volume 2: Clinical Applications. Springer Verlag; 1996.

[186] Douple EB. Biology of thermal potentiation of radiotherapy. VSP; 1989.

[187] Iliakis G, Wu W, Wang M. DNA double strand break repair inhibition as a cause of heat radiosensitization: re-evaluation considering backup pathways of NHEJ. Int J Hyperthermia. 2008 Feb;24(1):17-29.

[188] Song CW, Park HJ, Lee CK, Griffin R. Implications of increased tumor blood flow and oxygenation caused by mild temperature hyperthermia in tumor treatment. Int J Hyperthermia. 2005;21(8):761.

[189] Song CW, Park H, Griffin RJ. Improvement of tumor oxygenation by mild hyperthermia. Radiat. Res. 2001 Apr;155(4):515-528.

[190] Vujaskovic Z, Song CW. Physiological mechanisms underlying heat-induced radiosensitization. Int J Hyperthermia. 2004 Mar;20(2):163-174.

[191] Urano M, Douple EB. Interstitial hyperthermia. VSP; 1992.

[192] Hall EJ, Giaccia AJ. Radiobiology for the radiologist. Lippincott Williams & Wilkins; 2006.

[193] Song CW, Griffin R, Park HJ. Influence of Tumor pH on Therapeutic Response. In: Cancer drug resistance. Totowa, New Jersey: Humana Press; 2006. p. 21-42.

[194] Chen B, Roskams T, de Witte PAM. Enhancing the antitumoral effect of hypericin-mediated photodynamic therapy by hyperthermia. Lasers Surg Med. 2002;31(3):158-163.

[195] Freitas I. Role of hypoxia in photodynamic therapy of tumors. Tumori. 1985 Jun 30;71(3):251-259.

[196] Siemann DW, Horsman MR, Chaplin DJ. Modification of oxygen supply. In: Molls M, Vaupel P, editors. Blood perfusion and microenvironment of human tumors. Springer; 2000. p. 209-218.

[197] Grau C, Overgaard J. Significance of hemoglobin concentration for treatment outcome. In: Molls M, Vaupel P, editors. Blood perfusion and microenvironment of human tumors. Springer; 2000. p. 101-112.

[198] Brown JM. The potential benefit of hypoxic cytotoxins in radio-oncology. In: Molls M, Vaupel P, editors. Blood perfusion and microenvironment of human tumors. Springer; 2000. p. 219-229.

[199] Bache M, Kappler M, Said HM, Staab A, Vordermark D. Detection and specific targeting of hypoxic regions within solid tumors: current preclinical and clinical strategies. Curr. Med. Chem. 2008;15(4):322-338.

[200] Song CW. Modification of blood flow. In: Molls M, Vaupel P, editors. Blood perfusion and microenvironment of human tumors. Springer; 2000. p. 193-208.

[201] Field SB. In vivo aspects of hyperthermic oncology. In: Field SB, Hand JW, editors. An Introduction to the practical aspects of clinical hyperthermia. Nwe York, London, Philadelphia: Taylor & Francis; 1990. p. 55-68.

[202] Regulation of heat shock genes by cytokines. In: Stress Proteins. Berlin: Springer; 1999. p. 153.

[203] Rossi A, Elia G, Santoro MG. Inhibition of nuclear factor kappa B by prostaglandin A1: an effect

associated with heat shock transcription factor activation. Proc. Natl. Acad. Sci. U.S.A. 1997 Jan 21;94(2):746-750.

[204] Baeuerle PA, Baltimore D. NF-kappa B: ten years after. Cell. 1996 Oct 4;87(1):13-20.

[205] Baldwin AS. The NF-kappa B and I kappa B proteins: new discoveries and insights. Annu. Rev. Immunol. 1996;14:649-683.

[206] Schmitt E, Gehrmann M, Brunet M, Multhoff G, Garrido C. Intracellular and extracellular functions of heat shock proteins: repercussions in cancer therapy. J. Leukoc. Biol. 2007 Jan;81(1):15-27.

[207] Wells AD, Malkovsky M. Heat shock proteins, tumor immunogenicity and antigen presentation: an integrated view. Immunol. Today. 2000 Mar;21(3):129-132.

[208] Sherman MY, Goldberg AL. Cellular Defenses against Unfolded Proteins: A Cell Biologist Thinks about Neurodegenerative Diseases. Neuron. 2001 Jan;29(1):15-32.

[209] Pockley AG, Muthana M. Heat shock proteins and allograft rejection. Contrib Nephrol. 2005;148:122-134.

[210] Segal BH, Wang X-Y, Dennis CG, Youn R, Repasky EA, Manjili MH, et al. Heat shock proteins as vaccine adjuvants in infections and cancer. Drug Discov. Today. 2006 Jun;11(11-12):534-540.

[211] Muthukrishnan L, Warder E, McNeil PL. Basic fibroblast growth factor is efficiently released from a cytolsolic storage site through plasma membrane disruptions of endothelial cells. J. Cell. Physiol. 1991 Jul;148(1):1-16.

[212] Srivastava M. Heat shock protein-peptide interaction: Basis for a new generation of vaccines against cancers and intracellular infections. In: Latchman DS, editor. Stress Proteins. Berlin Heiselberg New York: Springer- Verlag; 1999. p. 403-414.

[213] Habash R. Bioeffects and Therapeutic Applications of Electromagnetic Energy. Boca Raton: CRC Press; 2008.

[214] Kaneko Y, Maruyama T, Takegami K, Watanabe T, Mitsui H, Hanajiri K, et al. Use of a microbubble agent to increase the effects of high intensity focused ultrasound on liver tissue. Eur Radiol. 2005 Jul;15(7):1415-1420.

[215] Day ES, Morton JG, West JL. Nanoparticles for thermal cancer therapy. J Biomech Eng. 2009 Jul;131(7):074001.

[216] Cullity BD, Graham CD. Introduction to Magnetic Materials. Wiley-IEEE; 2008.

[217] Thiesen B, Jordan A. Clinical applications of magnetic nanoparticles for hyperthermia. Int J Hyperthermia. 2008 Sep;24(6):467-474.

[218] Johannsen M, Gneveckow U, Thiesen B, Taymoorian K, Cho CH, Waldöfner N, et al. Thermotherapy of prostate cancer using magnetic nanoparticles: feasibility, imaging, and three-dimensional temperature distribution. Eur. Urol. 2007 Dec;52(6):1653-1661.

[219] Johannsen M, Gneveckow U, Taymoorian K, Thiesen B, Waldöfner N, Scholz R, et al. Morbidity and quality of life during thermotherapy using magnetic nanoparticles in locally recurrent prostate cancer: results of a prospective phase I trial. Int J Hyperthermia. 2007 May;23(3):315-323.

[220] Wust P, Gneveckow U, Johannsen M, Böhmer D, Henkel T, Kahmann F, et al. Magnetic nanoparticles for interstitial thermotherapy--feasibility, tolerance and achieved temperatures. Int J Hyperthermia. 2006 Dec;22(8):673-685.

[221] Maier-Hauff K, Rothe R, Scholz R, Gneveckow U, Wust P, Thiesen B, et al. Intracranial thermotherapy using magnetic nanoparticles combined with external beam radiotherapy: results of a feasibility study on patients with glioblastoma multiforme. J. Neurooncol. 2007 Jan;81(1):53-60.

[222] Hilger I, Andrä W, Hergt R, Hiergeist R, Schubert H, Kaiser WA. Electromagnetic heating of breast tumors in interventional radiology: in vitro and in vivo studies in human cadavers and mice. Radiology. 2001 Feb;218(2):570-575.

[223] Hilger I, Hiergeist R, Hergt R, Winnefeld K, Schubert H, Kaiser WA. Thermal ablation of tumors using magnetic nanoparticles: an in vivo feasibility study. Invest Radiol. 2002 Oct;37(10):580-586.

[224] Ivkov R, DeNardo SJ, Daum W, Foreman AR, Goldstein RC, Nemkov VS, et al. Application of high amplitude alternating magnetic fields for heat induction of nanoparticles localized in cancer. Clin. Cancer Res. 2005 Oct 1;11(19 Pt 2):7093s-7103s.

[225] Brezovich IA, Meredith RF. Practical aspects of ferromagnetic thermoseed hyperthermia. Radiol. Clin. North Am. 1989 May;27(3):589-602.

[226] Jiles D. Introduction to magnetism and magnetic materials. CRC Press; 1998.

[227] Cornell RM. The Iron Oxides: Structure, Properties, Reactions, Occurrence and Uses. Weinheim [etc.]: VCH; 1996.

[228] Tucker RD. Use of interstitial temperature self-regulating thermal rods in the treatment of prostate cancer. J. Endourol. 2003 Oct;17(8):601-607.

[229] Deger S, Taymoorian K, Boehmer D, Schink T, Roigas J, Wille AH, et al. Thermoradiotherapy using interstitial self-regulating thermoseeds: an intermediate analysis of a phase II trial. Eur. Urol. 2004 May;45(5):574-579; discussion 580.

[230] Hubert AE, Schäfer R. Magnetic Domains. Berlin Heidelberg: Springer-Verlag; 1998.

[231] Hergt R, Andrä W. Magnetic Hyperthermia and Thermoablation. In: Magnetism in Medicine: A Handbook. Weinheim: Wiley-VCH; 2007. p. 550.

[232] Jordan A, Wust P, Fähling H, John W, Hinz A, Felix R. Inductive heating of ferrimagnetic particles and magnetic fluids: physical evaluation of their potential for hyperthermia. Int J Hyperthermia. 1993 Feb;9(1):51-68.

[233] Hergt R, Hiergeist R, Hilger I, Kaiser WA, Lapatnikov Y, Margel S, et al. Maghemite nanoparticles with very high AC-losses for application in RF-magnetic hyperthermia. J Magn Magn Mater. 2004 Apr;270(3):345-357.

[234] Feyen M, Heim E, Ludwig F, Schmidt AM. Magnetic Nanorotors with Tailored Field-Induced Dynamics. Chem Mater. 2008 May 1;20(9):2942-2948.

[235] Levy M, Wilhelm C, Siaugue J-M, Horner O, Bacri J-C, Gazeau F. Magnetically induced hyperthermia: size-dependent heating power of γ-Fe2O3 nanoparticles. J Phys Condens Matter. 2008;20(20):204133.

[236] Schwertmann U. Iron Oxides in the Laboratory: Preparation and Characterization. 2nd ed. Weinheim: Wiley-VCH; 2000.

[237] Ma M, Wu Y, Zhou J, Sun Y, Zhang Y, Gu N. Size dependence of specific power absorption of Fe3O4 particles in AC magnetic field. J Magn Magn Mater. 2004 Jan;268(1-2):33-39.

[238] Hergt R, Dutz S, Roder M. Effects of size distribution on hysteresis losses of magnetic

nanoparticles for hyperthermia. J Phys Condens Matter. 2008;20(38):385214.
[239] Giri J, Guha Thakurta S, Bellare J, Kumar Nigam A, Bahadur D. Preparation and characterization of phospholipid stabilized uniform sized magnetite nanoparticles. J Magn Magn Mater. 2005 May;293(1):62-68.
[240] Bakandritsos A, Bouropoulos N, Koutoulogenis A, Boukos N, Fatouros DG. Synthesis and Characterization of Iron Oxide Nanoparticles Encapsulated in Lipid Membranes. J Biomed Nanotechnol. 2008 Sep;4:313-318.
[241] Lewinski N, Colvin V, Drezek R. Cytotoxicity of nanoparticles. Small. 2008 Jan;4(1):26-49.
[242] Gupta A, Gupta M. Synthesis and surface engineering of iron oxide nanoparticles for biomedical applications. Biomaterials. 2005 Jun;26(18):3995-4021.
[243] Hafeli U. Magnetically modulated therapeutic systems. Int J Pharm. 2004 Jun;277(1-2):19-[24.
[244] Jordan A, Maier-Hauff K, Wust P, Johannsen M. Nanoparticles for Thermotherapy. In: Kumar CSSR, editor. Nanomaterials for Cancer Therapy. Weinheim: Wiley-VCH; 2006.
[245] Pankhurst QA, Thanh NKT, Jones SK, Dobson J. Progress in applications of magnetic nanoparticles in biomedicine. J Phys D Appl Phys. 2009;42(22):224001.
[246] Bickels J, Dadia S, Lidar Z. Surgical Management of Metastatic Bone Disease. J Bone Joint Surg Am. 2009 Jun 1;91(6):1503-1516.
[247] Ratner BD. Biomaterials Science: An Introduction to Materials in Medicine. 2nd ed. Amsterdam [etc.]: Elsevier Academic Press; 2004.
[248] Jones D. Synthesis and evaluation of ceramic, polymer, and composite biomaterials. In: Encyclopedic Handbook of Biomaterials and Bioengineering. Part A: Materials. New York: Marcel Dekker, Inc.; 1995. p. 141.
[249] Hench LL, Wilson J. An Introduction to bioceramics. World Scientific; 1993.
[250] Ohura K, Nakamura T, Yamamuro T, Ebisawa Y, Kokubo T, Kotoura Y, et al. Bioactivity of CaO·SiO2 glasses added with various ions. J Mater Sci Mater Med. 1992 Mar;3(2):95–100.
[251] Ebisawa Y, Kokubo T, Ohura K, Yamamuro T. Bioactivity of CaO·SiO2-based glasses:in vitro evaluation. J Mater Sci Mater Med. 1990 Nov;1(4):239–244.
[252] Auric P, Van Dang N, Bandyopadhyay AK, Zarzycki J. Superparamagnetism and ferrimagnetism of the small particles of magnetite in a silicate matrix. J Non Cryst Solids. 1982 Jun;50(1):97-106.
[253] Luderer AA, Borrelli NF, Panzarino JN, Mansfield GR, Hess DM, Brown JL, et al. Glass-ceramic-mediated, magnetic-field-induced localized hyperthermia: response of a murine mammary carcinoma. Radiat Res. 1983;94(1):190–8.
[254] Kawashita M. Ceramic Microspheres for Biomedical Applications. Int J Appl Ceram Technol. 2005;2(3):173–183.
[255] Habraken WJEM, Wolke JGC, Jansen JA. Ceramic composites as matrices and scaffolds for drug delivery in tissue engineering. Adv. Drug Deliv. Rev. 2007 May;59(4-5):234–248.
[256] Ohura K, Ikenaga M, Nakamura T, Yamamuro T, Ebisawa Y, Kokubo T, et al. A heat-generating bioactive glass-ceramic for hyperthermia. J Appl Biomater. 1991;2(3):153–159.
[257] Ikenaga M, Ohura K, Yamamuro T, Kotoura Y, Oka M, Kokubo T. Localized hyperthermic treatment of experimental bone tumors with ferromagnetic ceramics. J. Orthop. Res. 1993;11(6):849–855.

[258] Ebisawa Y, Kokubo T, Ohura K, Yamamuro T. Bioactivity of Fe2O3-containing CaO-SiO2 glasses: in vitro evaluation. J Mater Sci Mater Med. 1993 May;4(3):225–232.

[259] Ebisawa Y, Miyaji F, Kokubo T, Ohura K, Nakamura T. Bioactivity of ferrimagnetic glass-ceramics in the system FeO-Fe2O3-CaO-SiO2. Biomaterials. 1997 Oct;18(19):1277–1284.

[260] Real RP del, Arcos D, Vallet-Regi M. Implantable magnetic glass−ceramic based on (Fe,Ca)SiO3 solid solutions. Chem Mater. 2002;14(1):64–70.

[261] Arcos D, Real RP del, Vallet-Regí M. Biphasic materials for bone grafting and hyperthermia treatment of cancer. J Biomed Mater Res A. 2003;65A(1):71–78.

[262] Arcos D, Real RP del, Vallet-Regí M. A novel bioactive and magnetic biphasic material. Biomaterials. 2002;23(10):2151 – 2158.

[263] Serrano MC, Portolés MT, Pagani R, de Guinoa JS, Ruiz-Hernández E, Arcos D, et al. In vitro positive biocompatibility evaluation of glass-glass ceramic thermoseeds for hyperthermic treatment of bone tumors. Tissue Eng Part A. 2008 May;14(5):617-627.

[264] Bretcanu O, Spriano S, Verné E, Cöisson M, Tiberto P, Allia P. The influence of crystallised Fe3O4 on the magnetic properties of coprecipitation-derived ferrimagnetic glass-ceramics. Acta Biomater. 2005 Jul;1(4):421–429.

[265] Bretcanu O, Verné E, Cöisson M, Tiberto P, Allia P. Temperature effect on the magnetic properties of the coprecipitation derived ferrimagnetic glass-ceramics. J Magn Magn Mater. 2006 May;300(2):412–417.

[266] Bretcanu O, Verné E, Cöisson M, Tiberto P, Allia P. Magnetic properties of the ferrimagnetic glass-ceramics for hyperthermia. J Magn Magn Mater. 2006 Oct;305(2):529–533.

[267] Bretcanu O, Spriano S, Vitale C, Verné E. Synthesis and characterization of coprecipitation-derived ferrimagnetic glass-ceramic. J Mater Sci. 2006 Feb 1;41(4):1029-1037.

[268] Leventouri T, Kis AC, Thompson JR, Anderson IM. Structure, microstructure, and magnetism in ferrimagnetic bioceramics. Biomaterials. 2005 Aug;26(24):4924–4931.

[269] Singh RK, Kothiyal GP, Srinivasan A. Magnetic and structural properties of CaO-SiO2-P2O5-Na2O-Fe2O3 glass ceramics. J Magn Magn Mater. 2008 Apr;320(7):1352–1356.

[270] Tiberto P, Coisson M, Vinai F, Allia P, Bretcanu O, Vern E. Magnetic Relaxation in Ferrimagnetic Glass-Ceramics Obtained by Co-Precipitation at Different Temperatures. IEEE Trans. Magn. 2007 Jun;43(6):2471-2473.

[271] Abdel-Hameed SAM, Hessien MM, Azooz MA. Preparation and characterization of some ferromagnetic glass-ceramics contains high quantity of magnetite. Ceram Int. 2009 May;35(4):1539–1544.

[272] Eniu D, Cacaina D, Coldea M, Valeanu M, Simon S. Structural and magnetic properties of CaO-P2O5-SiO2-Fe2O3 glass-ceramics for hyperthermia. J Magn Magn Mater. 2005 Jul;293(1):310–313.

[273] Apostolova I, Wesselinowa JM. Possible low-TC nanoparticles for use in magnetic hyperthermia treatments. Solid State Commun. 2009 Jul;149(25-26):986–990.

[274] Shimizu T, Matsui M. New magnetic implant material for interstitial hyperthermia. Sci. Technol. Adv. Mater. 2003 Sep;4(5):469–473.

[275] Kawashita M. Ceramic Microspheres for Biomedical Applications. Int J Appl Ceram Technol. 2005;2(3):173–183.

[276] Kawashita M, Tanaka M, Kokubo T, Inoue Y, Yao T, Hamada S, et al. Preparation of ferrimagnetic magnetite microspheres for in situ hyperthermic treatment of cancer. Biomaterials. 2005 May;26(15):2231–2238.

[277] Kawashita M, Domi S, Saito Y, Aoki M, Ebisawa Y, Kokubo T, et al. In vitro heat generation by ferrimagnetic maghemite microspheres for hyperthermic treatment of cancer under an alternating magnetic field. J Mater Sci Mater Med. 2008 May;19(5):1897–1903.

[278] Kawashita M, Sadaoka K, Kokubo T, Saito T, Takano M, Araki N, et al. Enzymatic preparation of hollow magnetite microspheres for hyperthermic treatment of cancer. J Mater Sci Mater Med. 2006 Jul;17(7):605–610.

[279] Wu P, Zhu J, Xu Z. Template-assisted synthesis of mesoporous magnetic nanocomposite particles. Adv Funct Mater. 2004;14(4):345-351.

[280] Lu A-H, Li W-C, Kiefer A, Schmidt W, Bill E, Fink G, et al. Fabrication of magnetically separable mesostructured silica with an open pore system. J. Am. Chem. Soc. 2004 Jul 1;126(28):8616-8617.

[281] Zhao W, Gu J, Zhang L, Chen H, Shi J. Fabrication of uniform magnetic nanocomposite spheres with a magnetic core/mesoporous silica shell structure. J. Am. Chem. Soc. 2005 Jun 1;127(25):8916-8917.

[282] Chastellain M, Petri A, Gupta A, Rao KV, Hofmann H. Superparamagnetic silica-iron oxide nanocomposites for application in hyperthermia. Adv Eng Mater. 2004 Apr;6(4):235–241.

[283] Ruiz-Hernandez E, Lopez-Noriega A, Arcos D, Izquierdo-Barba I, Terasaki O, Vallet-Regi M. Aerosol-assisted synthesis of magnetic mesoporous silica spheres for drug targeting. Chem Mater. 2007 Jul;19(14):3455–3463.

[284] Martín-Saavedra FM, Ruíz-Hernández E, Boré A, Arcos D, Vallet-Regí M, Vilaboa N. Magnetic mesoporous silica spheres for hyperthermia therapy. Acta Biomater. 2010 Dec;6(12):4522-4531.

[285] Chen M, von Mikecz A. Formation of nucleoplasmic protein aggregates impairs nuclear function in response to SiO2 nanoparticles. Exp. Cell Res. 2005 Apr 15;305(1):51-62.

[286] Leonor IB, Balas F, Kawashita M, Reis RL, Kokubo T, Nakamura T. Biomimetic apatite deposition on polymeric microspheres treated with a calcium silicate solution. J. Biomed. Mater. Res. Part B Appl. Biomater. 2009 Oct;91(1):239-247.

[287] Lieberman IH, Togawa D, Kayanja MM. Vertebroplasty and kyphoplasty: filler materials. Spine J. 2005;5(6, Supplement 1):S305–S316.

[288] Takegami K, Sano T, Wakabayashi H, Sonoda J, Yamazaki T, Morita S, et al. New ferromagnetic bone cement for local hyperthermia. J Biomed Mater Res. 1998;43(2):210–4.

[289] Kusaka M, Takegami K, Sudo A, Yamazaki T, Kawamura J, Uchida A. Effect of hyperthermia by magnetite cement on tumor-induced bone destruction. J Orthop Sci. 2002;7(3):354–7.

[290] Matsumine A, Kusuzaki K, Matsubara T, Okamura A, Okuyama N, Miyazaki S, et al. Calcium phosphate cement in musculoskeletal tumor surgery. J Surg Oncol. 2006;93(3):212–220.

[291] Matsumine A, Kusuzaki K, Matsubara T, Shintani K, Satonaka H, Wakabayashi T, et al. Novel hyperthermia for metastatic bone tumors with magnetic materials by generating an alternating electromagnetic field. Clin. Exp. Metastasis. 2007 May;24(3):191–200.

[292] Frayssinet P, Combacau M, Gougeon M, Rouquet N. Histological evaluation of a new biomaterial releasing magnetite nanoparticles inside bone metastases for thermotherapy. Key Eng. Mater.

2008;:1211–14.
[293] Shimamura T, Amizuka N, Li M, Freitas PHL, White JH, Henderson JE, et al. Histological observations on the microenvironment of osteolytic bone metastasis by breast carcinoma cell line. Biomed Res. 2005 Aug;26(4):159–172.
[294] Gupta AK, Naregalkar RR, Vaidya VD, Gupta M. Recent advances on surface engineering of magnetic iron oxide nanoparticles and their biomedical applications. Nanomedicine. 2007 Feb;2(1):23-39.
[295] Gazeau F, Lévy M, Wilhelm C. Optimizing magnetic nanoparticle design for nanothermotherapy. Nanomedicine. 2008 Dec;3(6):831-844.
[296] Gunvén P. Liver embolizations in oncology: A review. Part I. Arterial (chemo)embolizations. Med. Oncol. 2008 Mar;25(1):1–11.
[297] Gunvén P. Liver embolizations in oncology: A review. Part II. Arterial radioembolizations, portal venous embolizations, experimental arterial embolization procedures. Med. Oncol. 2007;24(3):287–296.
[298] Garrean S, Hering J, Helton WS, Espat NJ. A primer on transarterial, chemical, and thermal ablative therapies for hepatic tumors. Am. J. Surg. 2007 Jul;194(1):79–88.
[299] Lindemayr S, Lehnert T, Korkusuz H, Hammerstingl R, Vogl TJ. Transpulmonary chemoembolization: A novel approach for the treatment of unresectable lung tumors. Tech Vasc Interv Radiol. 2007 Jun;10(2):114–119.
[300] Laurent A. Microspheres and nonspherical particles for embolization. Tech Vasc Interv Radiol. 2007 Dec;10(4):248–256.
[301] Kettenbach J, Stadler A, Katzler I, Schernthaner R, Blum M, Lammer J, et al. Drug-loaded microspheres for the treatment of liver cancer: Review of current results. Cardiovasc Intervent Radiol. 2008 May;31(3):468–476.
[302] Sako M, Hirota S. [Embolotherapy of hepatomas using ferromagnetic microspheres, its clinical evaluation and the prospect of its use as a vehicle in chemoembolo-hyperthermic therapy]. Gan To Kagaku Ryoho. 1986 Apr;13(4 Pt 2):1618–1624.
[303] Jones SK, Winter JG. Experimental examination of a targeted hyperthermia system using inductively heated ferromagnetic microspheres in rabbit kidney. Phys Med Biol. 2001;46(2):385–98.
[304] Jones SK, Winter JG, Gray BN. Treatment of experimental rabbit liver tumours by selectively targeted hyperthermia. Int J Hyperthermia. 2002;18(2):117–28.
[305] Sweetman SC. Martindale: The Complete Drug Reference. 34th ed. Pharmaceutical Press; 2005.
[306] Chou FI, Fang KC, Chung C, Lui WY, Chi CW, Liu RS, et al. Lipiodol uptake and retention by human hepatoma cells. Nucl Med Biol. 1995 Apr;22(3):379–386.
[307] Moroz P, Jones SK, Winter J, Gray BN. Targeting liver tumors with hyperthermia: Ferromagnetic embolization in a rabbit liver tumor model. J Surg Oncol. 2001;78(1):22–29.
[308] Moroz P, Pardoe H, Jones SK, Pierre TGS, Song S, Gray BN. Arterial embolization hyperthermia: hepatic iron particle distribution and its potential determination by magnetic resonance imaging. Phys Med Biol. 2002 May;47(9):1591–1602.
[309] Moroz P, Metcalf C, Gray BN. Histologic analysis of liver tissue following hepatic arterial infusion of ferromagnetic particles in a rabbit tumour model. BioMetals. 2003;16(3):455–464.

[310] Takamatsu S, Matsui O, Gabata T, Kobayashi S, Okuda M, Ougi T, et al. Selective induction hyperthermia following transcatheter arterial embolization with a mixture of nano-sized magnetic particles (ferucarbotran) and embolic materials: feasibility study in rabbits. Radiat Med. 2008 May;26(4):179–187.

[311] Mitsumori M, Hiraoka M, Shibata T, Okuno Y, Masunaga S, Koishi M, et al. Development of intra-arterial hyperthermia using a dextran-magnetite complex. Int J Hyperthermia. 1994;10(6):785–93.

[312] Muraoka A, Takeda S, Matsui M, Shimizu T, Tohnai I, Akiyama S, et al. Experimental study of a novel thermotherapy for hepatocellular carcinoma using a magnesium ferrite complex powder that produces heat under a magnetic field. Hepato-Gastroenterology. 2004 Dec;51(60):1662–1666.

[313] Moroz P, Jones SK, Gray BN. Tumor response to arterial embolization hyperthermia and direct injection hyperthermia in a rabbit liver tumor model. J Surg Oncol. 2002;80(3):149–56.

[314] Jordan O, Doelker E, Rufenacht DA. Biomaterials used in injectable implants (liquid embolics) for percutaneous filling of vascular spaces. Cardiovasc Intervent Radiol. 2005;28(5):561–569.

[315] Jordan O, Doelker E, Defabiani N, Caviezel A, Iselin C. Novel injectable urethral bulking agents for the treatment of urinary incontinence. J Mater Sci Mater Med. 2004;15(4):519–522.

[316] Le Renard P-E, Jordan O, Faes A, Petri-Fink A, Hofmann H, Rüfenacht D, et al. The in vivo performance of magnetic particle-loaded injectable, in situ gelling, carriers for the delivery of local hyperthermia. Biomaterials. 2010 Feb;31(4):691-705.

[317] Le Renard P-E, Buchegger F, Petri-Fink A, Bosman F, Rüfenacht D, Hofmann H, et al. Local moderate magnetically induced hyperthermia using an implant formed in situ in a mouse tumor model. Int J Hyperthermia. 2009 May;25(3):229-239.

[318] Hahn GM, Shiu EC, West B, Goldstein L, Li GC. Mechanistic implications of the induction of thermotolerance in Chinese hamster cells by organic solvents. Cancer Res. 1985 Sep;45(9):4138-4143.

[319] Li GC, Hahn GM. A proposed operational model of thermotolerance based on effects of nutrients and the initial treatment temperature. Cancer Res. 1980 Dec 1;40(12):4501-4508.

[320] Bussink J, Kaanders JHAM, van der Kogel AJ. Tumor hypoxia at the micro-regional level: clinical relevance and predictive value of exogenous and endogenous hypoxic cell markers. Radiother Oncol. 2003 Apr;67(1):3-15.

[321] Tsafnat N, Tsafnat G, Lambert TD, Jones SK. Modelling heating of liver tumours with heterogeneous magnetic microsphere deposition. Phys Med Biol. 2005 Jun;50(12):2937–2953.

[322] Granov AM, Muratov OV, Frolov VF. Problems in the local hyperthermia of inductively heated embolized tissues. Theor. Found. Chem. Eng. 2002;36(1):63–66.

[323] Knight CG. Liposomes, From Physical Structure to Therapeutic Applications. Elsevier; 1981.

[324] Dass CR. Drug Delivery in Cancer Using Liposomes. In: Jain KK, editor. Drug Delivery Systems. Humana Press; 2008. p. 177-182.

[325] Campbell RB, Ying B, Kuesters GM, Hemphill R. Fighting cancer: from the bench to bedside using second generation cationic liposomal therapeutics. J Pharm Sci. 2009 Feb;98(2):411–429.

[326] Scherphof G, Damen J, Hoeckstra D. Interaction of Liposomes With Plasma Proteins and Components of the Immune System. In: Knight CG, editor. Liposomes, From Physical Structure

to Therapeutic Applications. Elsevier Biomedical Press; 1981. p. 299-322.
[327] Juliano RL. Pharmacokinetics of Liposome-Encapsulated Drugs. In: Knight CG, editor. Liposomes, From Physical Structure to Therapeutic Applications. Elsevier Biomedical Press; 1981. p. 391-407.
[328] Kamps J, Scherphof G. Biodistribution and Uptake of Liposomes In Vivo. In: Düzgüneş N, editor. Liposomes Part D. Amsterdam: Elsevier Academic Press; 2003. p. 257.
[329] Kong G, Dewhirst MW. Hyperthermia and liposomes. Int J Hyperthermia. 1999;15(5):345–70.
[330] Poste G. The interaction of lipid vesicles (liposomes) with cultured cells and their use as carriers for drugs and macromolecule. In: Liposomes in Biological Systems. Chichester: J. Wiley; 1980. p. 101-151.
[331] Yamada Y, Harashima H. Mitochondrial drug delivery systems for macromolecule and their therapeutic application to mitochondrial diseases. Adv. Drug Deliv. Rev. October;60(13-14):1439-1462.
[332] Laudonio N, Marcocci L, Arancia G, Calcabrini A, Del Bufalo D, Greco C, et al. Enhancement of hyperthermic damage on M14 melanoma cells by liposome pretreatment. Cancer Res. 1990 Aug 15;50(16):5119-5126.
[333] Szoka F, Papahadjopoulos D. Liposomes: Preparation and characterization. In: Knight CG, editor. Liposomes, From Physical Structure to Therapeutic Applications. Elsevier Biomedical Press; 1981. p. 323-348.
[334] Düzgüneş N. Preparation and quantitation of small unilamellar liposomes and large unilamellar reverse-phase evaporation liposomes. In: Düzgüneş N, editor. Liposomes Part A. Amsterdam [etc.]: Elsevier Academic Press; 2003.
[335] Gregoriadis G. Liposome Technology: Liposome Preparation and Related Techniques. CRC Press; 2006.
[336] Shinkai M, Yanase M, Honda H, Wakabayashi T, Yoshida J, Kobayashi T. Intracellular hyperthermia for cancer using magnetite cationic liposomes: in vitro study. Jpn. J. Cancer Res. 1996 Nov;87(11):1179-1183.
[337] Yanase M, Shinkai M, Honda H, Wakabayashi T, Yoshida J, Kobayashi T. Intracellular hyperthermia for cancer using magnetite cationic liposomes: ex vivo study. Jpn. J. Cancer Res. 1997 Jul;88(7):630-632.
[338] Yanase M, Shinkai M, Honda H, Wakabayashi T, Yoshida J, Kobayashi T. Intracellular hyperthermia for cancer using magnetite cationic liposomes: an in vivo study. Jpn. J. Cancer Res. 1998 Apr;89(4):463-469.
[339] Shinkai M, Yanase M, Suzuki M, Hiroyuki Honda, Wakabayashi T, Yoshida J, et al. Intracellular hyperthermia for cancer using magnetite cationic liposomes. J Magn Magn Mater. 1999 Apr;194(1-3):176-184.
[340] Yanase M, Shinkai M, Honda H, Wakabayashi T, Yoshida J, Kobayashi T. Antitumor immunity induction by intracellular hyperthermia using magnetite cationic liposomes. Cancer Sci. 1998;89(7):775-782.
[341] Jordan A, Scholz R, Wust P, Fähling H, Krause J, Wlodarczyk W, et al. Effects of magnetic fluid hyperthermia (MFH) on C3H mammary carcinoma in vivo. Int J Hyperthermia. 1997 Dec;13(6):587-605.

[342] Johannsen M, Thiesen B, Jordan A, Taymoorian K, Gneveckow U, Waldöfner N, et al. Magnetic fluid hyperthermia (MFH)reduces prostate cancer growth in the orthotopic Dunning R3327 rat model. Prostate. 2005 Aug 1;64(3):283-292.

[343] Purschke M, Laubach H-J, Anderson RR, Manstein D. Thermal injury causes DNA damage and lethality in unheated surrounding cells: active thermal bystander effect. J Invest Dermatol. 2009 Jul 9;130(1):86-92.

[344] Ruddon RW. Tumor immunology. In: Cancer Biology. Oxford University Press, USA; 2007. p. 400.

[345] Straten PT, Becker JC, Guldberg P, Zeuthen J. In situ T cells in melanoma. Cancer Immunol. Immunother. 1999;48(7):386-395.

[346] Hiraoka K, Miyamoto M, Cho Y, Suzuoki M, Oshikiri T, Nakakubo Y, et al. Concurrent infiltration by CD8+ T cells and CD4+ T cells is a favourable prognostic factor in non-small-cell lung carcinoma. Br J Cancer. 2006 Jan 17;94(2):275-280.

[347] Couzin J. T cells a boon for colon cancer prognosis. Science. 2006 Sep 29;313(5795):1868-1869.

[348] Galon J, Costes A, Sanchez-Cabo F, Kirilovsky A, Mlecnik B, Lagorce-Pages C, et al. Type, Density, and Location of Immune Cells Within Human Colorectal Tumors Predict Clinical Outcome. Science. 2006 Sep 29;313(5795):1960-1964.

[349] Ito A, Shinkai M, Honda H, Wakabayashi T, Yoshida J, Kobayashi T. Augmentation of MHC class I antigen presentation via heat shock protein expression by hyperthermia. Cancer Immunol. Immunother. 2001 Dec;50(10):515-522.

[350] Ito A, Shinkai M, Honda H, Yoshikawa K, Saga S, Wakabayashi T, et al. Heat shock protein 70 expression induces antitumor immunity during intracellular hyperthermia using magnetite nanoparticles. Cancer Immunol. Immunother. 2003 Feb 1;52(2):80-88.

[351] Marincola FM, Jaffee EM, Hicklin DJ, Ferrone S. Escape of Human Solid Tumors from T-Cell Recognition: Molecular Mechanisms and Functional Significance. In: Frank J. Dixon, editors. Academic Press; 1999. p. 181-273.

[352] Fidler IJ. Macrophages and metastasis--a biological approach to cancer therapy. Cancer Res. 1985 Oct;45(10):4714-4726.

[353] Killion JJ, Fidler IJ. Therapy of cancer metastasis by tumoricidal activation of tissue macrophages using liposome-encapsulated immunomodulators. Pharmacol. Ther. 1998 Jun;78(3):141-154.

[354] Rao M, Rothwell S, Alving C. Trafficking of Liposomal Antigens to the Trans-Golgi Complex in Macrophages. In: Düzgüneş N, editor. Liposomes Part C. Amsterdam [etc.]: Elsevier Academic Press; 2003.

[355] Udono H, Srivastava PK. Comparison of tumor-specific immunogenicities of stress-induced proteins gp96, hsp90, and hsp70. J. Immunol. 1994 Jun 1;152(11):5398-5403.

[356] Melcher A, Todryk S, Hardwick N, Ford M, Jacobson M, Vile RG. Tumor immunogenicity is determined by the mechanism of cell death via induction of heat shock protein expression. Nat Med. 1998 May;4(5):581-587.

[357] Zeng Y, Graner M, Katsanis E. Chaperone-rich cell lysates, immune activation and tumor vaccination. Cancer Immunol. Immunother. 2006 Mar 1;55(3):329-338.

[358] Milani V, Noessner E. Effects of thermal stress on tumor antigenicity and recognition by immune

effector cells. Cancer Immunol. Immunother. 2006 Mar;55(3):312-319.
[359] Filion MC, Phillips NC. Toxicity and immunomodulatory activity of liposomal vectors formulated with cationic lipids toward immune effector cells. Biochim. Biophys. Acta. 1997 Oct 23;1329(2):345-356.
[360] Soenen SJH, Brisson AR, De Cuyper M. Addressing the problem of cationic lipid-mediated toxicity: The magnetoliposome model. Biomaterials. 2009 Aug;30(22):3691-3701.
[361] Ito A, Tanaka K, Honda H, Abe S, Yamaguchi H, Kobayashi T. Complete regression of mouse mammary carcinoma with a size greater than 15 mm by frequent repeated hyperthermia using magnetite nanoparticles. J. Biosci. Bioeng. 2003;96(4):364-369.
[362] Suzuki M, Shinkai M, Honda H, Kobayashi T. Anticancer effect and immune induction by hyperthermia of malignant melanoma using magnetite cationic liposomes. Melanoma Res. 2003 Apr;13(2):129-135.
[363] Matsuoka F, Shinkai M, Honda H, Kubo T, Sugita T, Kobayashi T. Hyperthermia using magnetite cationic liposomes for hamster osteosarcoma. Biomagn Res Technol. 2004 Mar 25;2(1):3.
[364] Ito A, Honda H, Kobayashi T. Cancer immunotherapy based on intracellular hyperthermia using magnetite nanoparticles: a novel concept of "heat-controlled necrosis" with heat shock protein expression. Cancer Immunol Immunother. 2005 Aug;55(3):320-328.
[365] Findlay JBC, editor. Biological Membranes: A Practical Approach. Oxford: IRL Press; 1987.
[366] Kuhn SJ, Hallahan DE, Giorgio TD. Characterization of superparamagnetic nanoparticle interactions with extracellular matrix in an in vitro system. Ann Biomed Eng. 2006 Jan;34(1):51-58.
[367] Nir S, Nieva J. Uptake of liposomes by cells: experimental procedures and modeling. In: Düzgüneş N, editor. Liposomes Part B. Amsterdam [etc.]: Elsevier Academic Press; 2003. p. 235.
[368] Smolen J. Liposomes in study of membrane fusion in neutrophils. In: Düzgüneş N, editor. Liposomes Part B. Amsterdam [etc.]: Elsevier Academic Press; 2003. p. 300.
[369] Scott B, Van Komen J, Liu S, Weber T, Melia T, McNew J. Liposome fusion assay to monitor intracellular membrane fusion machines. In: Düzgüneş N, editor. Liposomes Part B. Amsterdam [etc.]: Elsevier Academic Press; 2003. p. 274.
[370] Noessner E. Thermal stress-related modulation of tumor cell physiology and immune responses. Cancer Immunol. Immunother. 2006 Mar 1;55(3):289-291.
[371] Martina M-S, Wilhelm C, Lesieur S. The effect of magnetic targeting on the uptake of magnetic-fluid-loaded liposomes by human prostatic adenocarcinoma cells. Biomaterials. 2008 Oct;29(30):4137-4145.
[372] Düzgüneş N. Fluorescence assays for liposome fusion. In: Düzgüneş N, editor. Liposomes Part B. Amsterdam [etc.]: Elsevier Academic Press; 2003. p. 260.
[373] Humphries GM. The use of liposomes for studiying membranes antigens as immunogens and as targets for immune attack. In: Gregoriadis G, Allison AC, editors. Liposomes in Biological Systems. Chichester: J. Wiley; 1980. p. 345-376.
[374] Le B, Shinkai M, Kitade T, Honda H, Yoshida J, Wakabayashi T, et al. Preparation of tumor-specific magnetoliposomes and their application for hyperthermia. J Chem Eng Jpn. 2001;34(1):66-72.

[375] Shinkai M, Le B, Honda H, Yoshikawa K, Shimizu K, Saga S, et al. Targeting hyperthermia for renal cell carcinoma using human MN antigen-specific magnetoliposomes. Jpn. J. Cancer Res. 2001 Oct;92(10):1138-1145.

[376] Liao SY, Aurelio ON, Jan K, Zavada J, Stanbridge EJ. Identification of the MN/CA9 protein as a reliable diagnostic biomarker of clear cell carcinoma of the kidney. Cancer Res. 1997 Jul 15;57(14):2827-2831.

[377] Ito A, Kuga Y, Honda H, Kikkawa H, Horiuchi A, Watanabe Y, et al. Magnetite nanoparticle-loaded anti-HER2 immunoliposomes for combination of antibody therapy with hyperthermia. Cancer Lett. 2004 Aug 30;212(2):167-175.

[378] Dinh P, de Azambuja E, Cardoso F, Piccart-Gebhart MJ. Facts and controversies in the use of trastuzumab in the adjuvant setting. Nat Clin Pract Oncol. 2008 Nov;5(11):645-654.

[379] Nahta R, Esteva FJ. Herceptin: mechanisms of action and resistance. Cancer Lett. 2006 Feb 8;232(2):123-138.

[380] Park JW, Hong K, Kirpotin DB, Colbern G, Shalaby R, Baselga J, et al. Anti-HER2 Immunoliposomes. Clin. Cancer Res. 2002 Apr;8(4):1172-1181.

[381] Kirpotin DB, Drummond DC, Shao Y, Shalaby MR, Hong K, Nielsen UB, et al. Antibody targeting of long-circulating lipidic nanoparticles does not increase tumor localization but does increase internalization in animal models. Cancer Res. 2006 Jul 1;66(13):6732-6740.

[382] Yuan F, Leunig M, Huang SK, Berk DA, Papahadjopoulos D, Jain RK. Mirovascular permeability and interstitial penetration of sterically stabilized (stealth) liposomes in a human tumor xenograft. Cancer Res. 1994 Jul 1;54(13):3352-3356.

[383] Juweid M, Neumann R, Paik C, Perez-Bacete MJ, Sato J, van Osdol W, et al. Micropharmacology of monoclonal antibodies in solid tumors: Direct experimental evidence for a binding site barrier. Cancer Res. 1992 Oct 1;52(19):5144-5153.

[384] Graff CP, Wittrup KD. Theoretical analysis of antibody targeting of tumor spheroids: Importance of dosage for penetration, and affinity for retention. Cancer Res. 2003 Mar 15;63(6):1288-1296.

[385] Huang SK, Lee K-D, Hong K, Friend DS, Papahadjopoulos D. Microscopic localization of sterically stabilized liposomes in colon carcinoma-bearing mice. Cancer Res. 1992 Oct 1;52(19):5135-5143.

[386] Rabin Y. Is intracellular hyperthermia superior to extracellular hyperthermia in the thermal sense? Int J Hyperthermia. 2002 Jun;18(3):194-202.

[387] Fortin J-P, Gazeau F, Wilhelm C. Intracellular heating of living cells through Néel relaxation of magnetic nanoparticles. Eur. Biophys. J. 2008 Feb 1;37(2):223-228.

[388] Gordon S, editor. The macrophage as therapeutic target. Springer; 2003.

[389] Kawai N, Futakuchi M, Yoshida T, Ito A, Sato S, Naiki T, et al. Effect of heat therapy using magnetic nanoparticles conjugated with cationic liposomes on prostate tumor in bone. Prostate. 2008 May 15;68(7):784-792.

[390] Yamashita S. Heat-induced antigen retrieval: mechanisms and application to histochemistry. Prog Histochem Cytochem. 2007;41(3):141-200.

[391] Boyce BF, Xing L. Functions of RANKL/RANK/OPG in bone modeling and remodeling. Arch. Biochem. Biophys. 2008 May 15;473(2):139-146.

[392] Lynch CC, Hikosaka A, Acuff HB, Martin MD, Kawai N, Singh RK, et al. MMP-7 promotes

prostate cancer-induced osteolysis via the solubilization of RANKL. Cancer Cell. 2005 May;7(5):485-496.

[393] Thiolloy S, Halpern J, Holt GE, Schwartz HS, Mundy GR, Matrisian LM, et al. Osteoclast-derived matrix metalloproteinase-7, but not matrix metalloproteinase-9, contributes to tumor-induced osteolysis. Cancer Res. 2009 Aug 15;69(16):6747-6755.

[394] Keller ET, Brown J. Prostate cancer bone metastases promote both osteolytic and osteoblastic activity. J. Cell. Biochem. 2004 Mar 1;91(4):718-729.

[395] Armstrong AP, Miller RE, Jones JC, Zhang J, Keller ET, Dougall WC. RANKL acts directly on RANK-expressing prostate tumor cells and mediates migration and expression of tumor metastasis genes. Prostate. 2008 Jan 1;68(1):92-104.

[396] Ando K, Mori K, Rédini F, Heymann D. RANKL/RANK/OPG: key therapeutic target in bone oncology. Curr Drug Discov Technol. 2008 Sep;5(3):263-268.

[397] Hamaguchi S, Tohnai I, Ito A, Mitsudo K, Shigetomi T, Ito M, et al. Selective hyperthermia using magnetoliposomes to target cervical lymph node metastasis in a rabbit tongue tumor model. Cancer Sci. 2003;94(9):834–9.

[398] Skitzki JJ, Chen Q, Wang WC, Evans SS. Primary immune surveillance: some like it hot. J. Mol. Med. 2007 Dec;85(12):1361-1367.

[399] van Mierlo GJ, Boonman ZF, Dumortier HM, den Boer AT, Fransen MF, Nouta J, et al. Activation of dendritic cells that cross-present tumor-derived antigen licenses CD8+ CTL to cause tumor eradication. J. Immunol. 2004 Dec 1;173(11):6753-6759.

Chapter 2

The in vivo performance of magnetic particle-loaded injectable, in situ gelling, carriers for the delivery of local hyperthermia.

published in Biomaterials, 31 (2010), 691–705

Pol-Edern Le Renard[1], Olivier Jordan[1], Antonin Faes[2], Alke Petri-Fink[2], Heinrich Hofmann[2], Daniel Rüfenacht[3], Frederik Bosman[4], Franz Buchegger[5], and Eric Doelker[1].

[1]School of Pharmaceutical Sciences, University of Geneva, University of Lausanne, Geneva, Switzerland; [2]Laboratory for Powder Technology, Ecole Polytechnique Fédérale de Lausanne (EPFL), Lausanne, Switzerland; [3]Neuroradiology-NeuroCenter, Hirslanden Clinic, Zurich, Switzerland; [4]Department of Pathology, University Hospital of Lausanne, Lausanne, Switzerland; [5]Service of Nuclear Medicine, University Hospital of Lausanne, Lausanne, University Hospital of Geneva, Geneva, Switzerland.

Abstract

We investigated the use of in situ implant formation that incorporates superparamagnetic iron oxide nanoparticles (SPIONs) as a form of minimally invasive treatment of cancer lesions by magnetically induced local hyperthermia. We developed injectable formulations that form gels entrapping magnetic particles into a tumor. We used SPIONs embedded in silica microparticles to favor syringeability and incorporated the highest proportion possible to allow large heating capacities. Hydrogel, single-solvent organogel and cosolvent (low-toxicity hydrophilic solvent) organogel formulations were injected into human cancer tumors xenografted in mice. The thermoreversible hydrogels (poloxamer, chitosan), which accommodated 20% w/v of the magnetic microparticles, proved to be inadequate. Alginate hydrogels, however, incorporated 10% w/v of the magnetic microparticles, and the external gelation led to strong implants localizing to the tumor periphery, whereas internal gelation failed in situ. The organogel formulations, which consisted of precipitating polymers dissolved in single organic solvents, displayed various microstructures. A 8% poly(ethylene-vinyl alcohol) in DMSO containing 40% w/v of magnetic microparticles formed the most suitable implants in terms of tumor casting and heat delivery. Importantly, it is of great clinical interest to develop cosolvent formulations with up to 20% w/v of magnetic microparticles that show reduced toxicity and centered tumor implantation.

Keywords: in situ forming implant; intratumoral injection; physical gels; hydrogels; organogels; magnetic induced hyperthermia; superparamagnetic nanoparticles; silica composite microparticles.

Chapter 2: Table of Contents

1 Introduction....134
2 Materials and methods....137
2.1 Materials....137
2.2 Methods....137
2.2.1 Magnetic microparticle synthesis and characterization....137
2.2.2 Hydrogel formulations....139
2.2.2.1 Thermosensitive formulations....139
2.2.2.2 Alginate formulations....140
2.2.2.2.1 Internal gelation: preparation and mixing....140
2.2.2.2.2 External gelation: preparation, mixing and injection....141
2.2.3 Organogel formulations....141
2.2.3.1 Preparation of single-solvent formulations....141
2.2.3.2 Preparation of cosolvent formulations....141
2.3 Viscosimetry....142
2.4 In vitro injections....142
2.5 In vivo testing of the tumor model....142
2.6 Histology....144
3 Results and discussion....144
3.1 Hydrogel formulations....144
3.1.1 Thermosensitive formulations....146
3.1.2 Alginate formulations based on internal gelification....146
3.1.3 Alginate formulations based on external gelation....147
3.2 Organogel formulations....150
3.2.1 Single-solvent organogel formulations....150
3.2.2 Cosolvent organogel formulations....156
3.3 In vivo experiments....160
3.3.1 Intratumoral injection of hydrogels....162
3.3.2 Intratumoral injection of organogels....163
4 Conclusion and perspectives....169
5 Acknowledgements....170
6 References....170

1 Introduction

Formulations forming implants in situ are attractive systems for controlled drug delivery in systemic treatments and minimally invasive approaches in localized therapies. They also offer an alternative in interventional radiology for embolization procedures [1,2] where optimization and control of the vessel lumen filling are critical. Vascular lesion filling is of specific interest in cases of vascular arteriovenous malformations and fistulae, cerebral aneurysms, endoleaks of aortic aneurysms and vascularized tumors. In addition, these formulations have found applications in tissue engineering [3]. In particular, implants formed in situ from preformed polymers have expanded the therapeutic possibilities in fields where in situ polymerizing systems are applied.

For the purpose of tumor treatment by magnetically induced local hyperthermia [4-6], a significant amount of superparamagnetic iron oxide nanoparticles (SPIONs) must be brought to the target tissue area. The present work has been dedicated to the development of injectable formulations that can form in situ physical gels containing magnetic particles and are suitable for injection into intratumoral vascular and necrotic spaces aiming at a tumor casting. These SPIONs allow secondary heating through exposure to an alternative magnetic field, i.e., the so-called magnetically induced hyperthermia. Silica microparticles (beads) embedding SPIONs maintain the superparamagnetic properties of the nanoparticles and favor syringeability of the carriers, in comparison with free iron oxide nanoparticles. Moreover, after injection, the formed implant traps the magnetic microparticles, avoiding potentially deleterious distant migration. This injectable type of formulation that carries magnetic microparticles holds promise in the treatment of solid tumors by combining both the embolization and hyperthermia approaches. The purpose of this study was to develop a formulation resulting in a functional implant that incorporates the highest magnetic microparticle load to ensure a temperature increase reaching cytotoxic levels.

In the first part of the present formulation work, we investigated hydrogels as magnetic microparticle carriers (Fig. 2.1A). We first opted for thermosensitive formulations based on two pharmaceutical grade polymers, namely, chitosan and poloxamer. Such macromolecular solutions are liquid below a

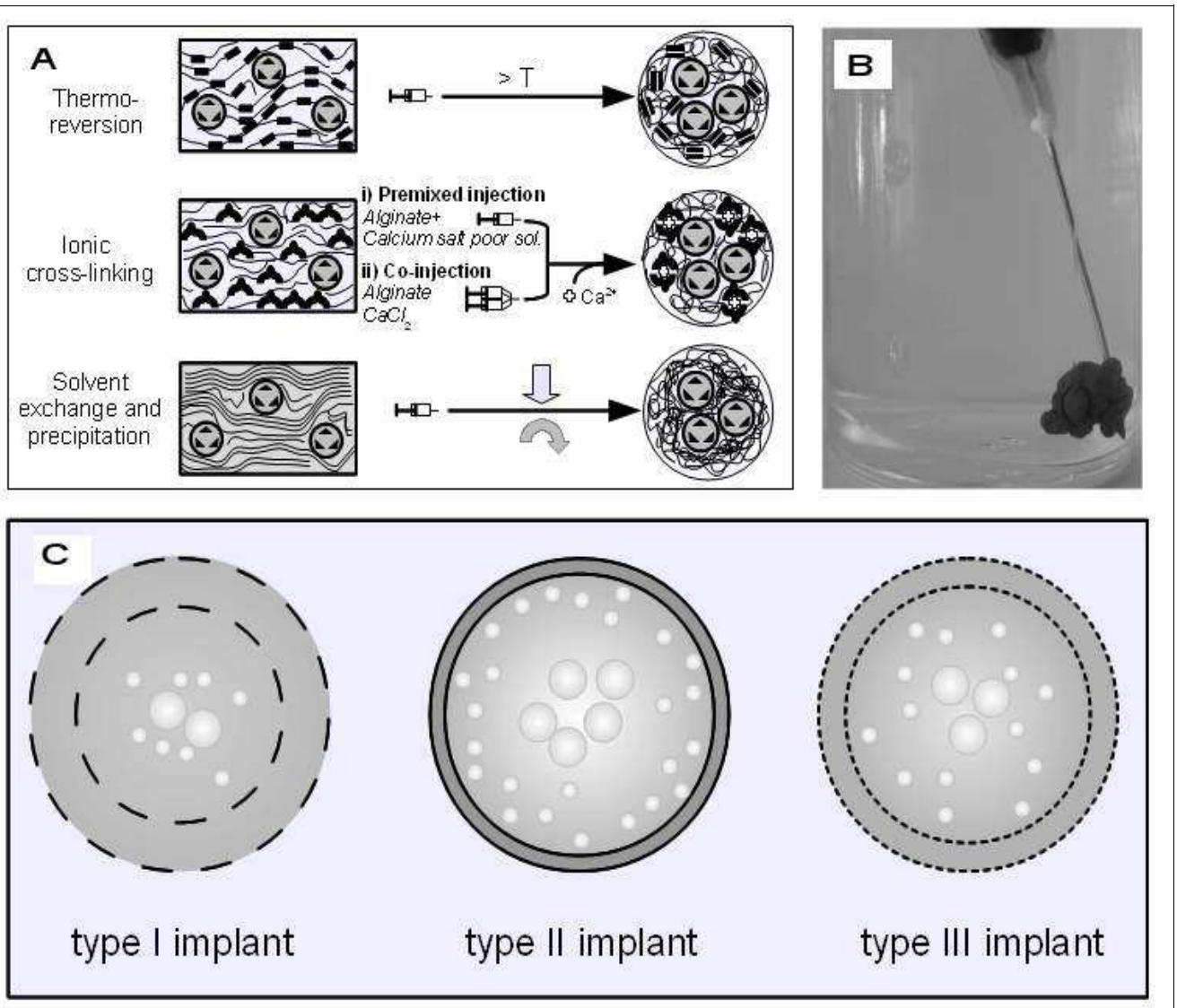

Figure 2.1. Proposed implant formation mechanism following the injection of magnetic particle-loaded injectable carriers and an organogel implant microstructure.

A. Schematic representation of three distinct sol-gel transition processes allowing injectable liquid carriers to form an implant *in situ,* entrapping the magnetic microparticles loaded. **B.** Picture of precipitating formulation, based on poly (ethylene-*co*-vinyl alcohol) 8% in DMSO, incorporating 40% w/v magnetic microparticles (containing brownish maghemite nanoparticles appearing here black) injected *in vitro*. **C.** The three types of implant microstructures found after single solvent formulation *in vitro* injection (cf text).

certain transition temperature interval (33 to 36°C) and undergo a sol-gel transition at higher temperatures, such as body temperature after injection, through interactions of hydrophobic segments [7-9]. We also studied formulations of the water-soluble sodium alginate with calcium as ionic cross-linker and developed injectable formulations for two gelation modalities described as internal or external (Figure 2.1B). Internal gelation is obtained in situ by slow dissolution of a poorly soluble calcium salt dispersed in the alginate solution just before injection. Thus, using calcium sulfate with limited solubility at physiological pH, we optimized the gelation time by adapting the particle size and by adding a delaying agent. Since it is only soluble in acidic environments, carbonate calcium was associated with δ-gluconolactone to ensure a controlled Ca2+ ion generation through slow lactone hydrolysis after suspension. External gelation of the alginate solution is obtained rapidly after contact with a calcium chloride solution, injected through a double-barreled syringe with a mixing device (Duplojet© injection system).

The second part of the formulation work has dealt with organogels based on precipitating polymers as carriers for magnetic microparticles. These polymers are soluble in organic solvents but not in water. Thus, after injection, solvent diffusion through exchange with tissue and circulating water triggers precipitation of polymers, resulting in an entangled network trapping magnetic microparticles (Figure 2.1A and B). In synthetic membrane science, this phenomenon is referred to as immersion precipitation or wet casting [10]. We investigated polymers already in clinical use [11] (polyurethanes, polyacrylates, ethylene vinyl acetate copolymer [12-14] and cellulose esters [15-17]) in solution in various organic solvents (N-methylpyrrolidone, dimethylsulfoxide or glycofurol that are used for parenterals, as well as dimethylisosorbide). In parallel, we developed cosolvent formulations prepared by adding to these single-solvent solutions a more hydrophilic solvent used in intravenous injection (polyethylene glycol, propylene glycol or hydroxyethyl-lactamide), in order to diminish systemic toxicity. This would also limit induction of heat shock proteins, amongst which a few chaperones are implicated in thermotolerance. In the last part of the study, relevant formulations were tested in vivo to prove implantation capacities in solid tumors generated through xenografting of human cancer cell lines, Skov, SK-BR-3, LN229, T380 and Co112.

2 Materials and methods

2.1 Materials

Table 2.1 lists the polymers used to prepare both the hydrogels and organogels, with their source and relevant characteristics such as molecular weight when available. The solvents and cosolvents used for the organogels can be found in Table 2.2. Those cosolvents that failed in vitro testing are not included. Other compounds used were trisodium phosphate, sodium chloride, calcium sulfate, calcium carbonate, calcium chloride and D(+)-glucuronic acid δ-lactone (δ-glucurolactone) (Fluka, Buchs, Switzerland), disodium β-glycerophosphate hydrate (Sigma, Buchs, Switzerland) and dipotassium phosphate (Merck, Dietikon, Switzerland). Water was bidistilled and ultrafiltered (Milli-Q, Millipore, Zug, Switzerland).

2.2 Methods

2.2.1 Magnetic microparticle synthesis and characterization

Micron-sized silica particles were synthesized to embed SPIONs as previously described [18]. Their volume median diameter, measured using a Malvern Mastersizer, was 0.9 μm. The particle sizes of the embedded SPIONs were obtained from transmission electron microscopy (TEM), magnetic measurements and X-ray diffraction (XRD). The embedded SPION size ranged from 6 to 20 nm (from TEM observations) and 14.2 ± 1.5 nm (magnetic measurements) to 15.5 ± 1.3 nm (XRD) depending on the measurement method. Differences in the applied statistics also explain discrepancies in mean diameter, with d(volume) > d(number). These microparticles contained 32% w/w of nanometric iron oxide particles. The Specific Absorption Ratio (SAR), which reflects the heating capacities and is conventionally defined as the slope of the initial temperature rise multiplied by the specific heat capacity, was on the order of 18 W/g iron oxide for the magnetic field applied in this investigation (magnetic field strength of 9660 A/m, frequency 144 kHz).

Table 2.1. Polymers used for hydrogel and organogel formulations, with relevant information

Polymer	Brand name (manufacturer or supplier)	abbreviation	Characteristics
Hydrogels			
Chitosan	Sigma (Buchs, Switzerland)	Chitosan	High MW, 0.8 to 2 Pa.s for 1% w/v in 1% acetic acid, 82.7% deacetylated
Poloxamer 407	Pluronic® F 127 (BASF, Ludwigshafen, Germany)	Poloxamer	Ca. 70% wt polyoxyethylene
Sodium alginate, standard grade	Fluka (Buchs, Switzerland)	SG-ALG	65-75% Glucuronic acid; low viscosity (100 to 200 mPa.s for % aq)
Sodium alginate, medical grade	Medipol (Lausanne, Switzerland)	MG-ALG	Low viscosity, 80 mPa.s at 2% w/v aq (after sterile filtration)
Organogels			
Poly(ethylene- *co*-vinyl alcohol)	EVAL E-105 B (EVAL Europe, Zwijndrecht, Belgium)	EVAL	44 mol % ethylene (ensuring flexibility), clinical use for embolization (Onyx ®).
Aromatic polyether-based polyurethane	Tecothane-TT1075D (Thermedics, Wilmington, MA, USA)	Tecothane	Higher shore hardness, medical grade (use in prosthetics)
Aliphatic polyether-based polyurethane	Tecogel TG 500-V (Thermedics, Wilmington, MA, USA)	Tecogel	Medical grade, absorbs equilibrium water contents up to 500% of the dry resin weight
Acrylic copolymer	Paraloid A12 (Rohm and Haas, Philadelphia, USA)	MMA/EA	Poly(methyl methacrylate- *co*-ethyl acrylate)
Cellulose acetate	CA-320S (Eastman, Rochester, NY, USA)	CA-320S	32.0% Acetyl, 8.7% hydroxyl, *M*n = 38000
Cellulose acetate	CA-398-3 (Eastman, Rochester, NY, USA)	CA-398-3	39.2% Acetyl, 3.5% hydroxyl, *M*n = 30000, semi-crystalline
Cellulose acetate butyrate	CAB-381-2 (Eastman, Rochester, NY, USA)	CAB-381-2	38% Butyryl, 1.3% hydroxyl, *M*n = 40000

Table 2.2: Solvents and cosolvents used for organogel formulations, with toxicity data.

Name	Viscosity (mPa·s)	Brand name (manufacturer or supplier)	Abbreviation	LD50 (mL/kg body weight)
Solvents				
Dimethyl sulfoxide	2.0	Gaylord	DMSO	6.9 (iv./m),12.6 (ip./m), 15 (po./m)
N-methylpyrrolidone	1.7	Fluka (Buchs, Switzerland)	NMP	4.4 (ip./m)
Glycofurol	13.0	Glycofurol 75 (Roche, Basle, Switzerland)	Glycofurol	3.5 (iv./m)
Dimethyl isosorbide	6.0	Uniquema (New Castle, USA)	DMI	8.54 (iv./r)
2-Pyrrolidone	13.3	Soluphor (BASF, Ludwigshafen, Germany)	NP	0.328 (po./r)
Cosolvents				
Propylene glycol	40.4	Fluka (Buchs, Switzerland)	PG	6.4 (iv./m), 9.3 (ip./m), 13 (po./m)
Polyethylene glycol 200	50	Merck (Dietikon, Switzerland)	PEG	7.6 (iv./m), 12.9 (ip./m), 26 (po./m)
N-(2-hydroxyethyl) lactamide	-	TCI Europe (Zwijndrecht, Belgium)	HELA	16.3 (ip./m), 24 (po./m), 16.1 (sc./r)

Legend: Toxicity data: LD50 stands for lethal doses for 50% of animal; iv., ip., po. stands for intravenous, intraperitoneal, per os, respectively, and m for mouse, r for rat.

2.2.2 Hydrogel formulations

2.2.2.1 Thermosensitive formulations

The 2% w/v chitosan aqueous solution was prepared under aseptic conditions, according to the method described by Chenite et al. [7,19] and adapted by Jarry et al. [20]. Briefly, from 4 mL autoclaved aqueous suspension containing 2% w/v chitosan, solubilization was triggered by adding 0.5 mL of ultrafiltered 1M HCl (Fluka, Buchs, Switzerland). The autoclaved magnetic microparticles could be dispersed only after complete chitosan dissolution. The chitosan solution was then neutralized with 0.5 mL of a 560 g/L disodium β-glycerophosphate (Sigma, Buchs, Switzerland) solution at 4°C.

The 17% w/w poloxamer 407 aqueous solution was first sterile filtered and then aseptically mixed with the sterile magnetic microparticles. According to the manufacturer, the viscosity of a 17% w/w (20.5% w/v) aqueous solution will increase from 100 mPa·s at 20°C to 1800 mPa·s at 35 °C. This allows injection at room temperature and implant formation at mouse peripheral temperature (34-36 °C).

2.2.2.2 Alginate formulations

The aqueous solutions of standard grade alginate (SG-ALG) were ultrafiltered before incorporating the sterile magnetic microparticles and autoclaving the resulting formulation. A 2% w/v aqueous SG-ALG solution had a Newtonian viscosity of 226 mPa·s (80 mPa·s after sterile filtration). The Newtonian viscosity of the 2% w/v medical grade alginate (MG-ALG) aqueous solution, which was only used for the formulation based on external gelation, was 80 mPa·s (33 mPa.s after sterile filtration). Preparation and incorporation of the sterile magnetic microparticles were carried out aseptically.

2.2.2.2.1 Internal gelation: preparation and mixing

Based on the work of Kuo and Ma [21], two different calcium salts were used to control alginate gelation, namely, the sparingly water-soluble calcium sulfate dihydrate and the practically water-insoluble calcium carbonate (both from Fluka, Buchs, Switzerland).

For calcium sulfate, two particle size fractions were considered. The raw powder (modal diameter 630 μm) was designated as coarse powder. The < 32 μm fraction, designated as fine powder, was obtained using a vibratory sieve shaker (Analysette, Fritsch, Germany). A calcium sulfate aqueous suspension was prepared at a doubled concentration with the selected adjuvant, trisodium phosphate (Fluka, Buchs, Switzerland) or dipotassium phosphate/sodium chloride (Merck, Zug, Switzerland; Fluka, Buchs, Switzerland). This suspension was then steam sterilized, while the sodium alginate and magnetic microparticles were gathered in distinct suspensions. The two suspensions were loaded into two separate syringes. The contents were mixed by directly connecting the two syringes through a Luer-LockTM 3-way stopcock (BD Connecta, Becton Dickinson Infusion therapy, Sweden). The resulting mixture was retained in one syringe for injection.

Calcium carbonate and δ-gluconolactone (Fluka, Buchs, Switzerland) can be used for controlled internal gelation of alginate [21,22]. The suspension of these two components sterilized by dry heat must be prepared extemporaneously. Mixing was carried out as described above for calcium sulfate.

2.2.2.2.2 External gelation: preparation, mixing and injection

The sodium alginate aqueous dispersion that incorporated magnetic particles was mixed in the dual-syringe injection device Duploject© (gift from Baxter, Austria) with a calcium chloride (Fluka, Buchs, Switzerland) aqueous solution. Two identical syringes, filled respectively with the calcium chloride solution and the alginate and magnetic microparticle dispersion, were driven simultaneously. During injection, this system allows mixing of both reservoir contents just before flowing in the needle. This formulation was previously used as embolic agent [23].

2.2.3 Organogel formulations

2.2.3.1 Preparation of single-solvent formulations

Polymers were dissolved in organic solvent under stirring at room temperature or at 50 °C, depending on solubility. Magnetic microparticles were incorporated using vigorous vortexing and sonication. The formulation was sterilized by autoclaving.

2.2.3.2 Preparation of cosolvent formulations

Cosolvents were added by diluting concentrated single-solvent formulations. The procedure was then identical.

Formulations were labeled H-xx, O-xx or CO-xx for hydrogels, organogels or cosolvents, respectively. An asterisk denotes incorporated magnetic microparticles.

2.3 Viscosimetry

A shear-stress controlled rheometer (Bohlin CVO 120, Malvern Instruments, Worcestershire, UK) was used, equipped with a 40-mm diameter cone-plate geometry, at a controlled temperature (± 0.1°C). We analyzed true molecular dispersions using a 1°-aperture angle for a 30 µm-gap, whereas the aperture angle was 4° for the 150 µm-gap when investigating dispersions carrying magnetic microparticles.

2.4 In vitro injections

For in vitro injection testing, we typically injected 0.1 to 0.5 mL of the formulation in a larger amount (more than 10 mL) of PBS pH = 7.4, at 35°C for thermo-sensitive systems and at room temperature for the other formulations. Syringeability itself was assessed with a needle adapted to the viscosity of formulation (from 24 G for lower viscosities to 14 G for higher viscosities). The formation process of the implant was carefully studied. We noted the characteristics of the forming implant growth during injection (more details were sometimes observed under stereomicroscope), as well as the overall time for complete implant formation and the mechanical characteristics of the resulting implant. In case of microstructural investigation, implants were cut (at least one hour after formation) in slices of 8 µm with a cryomicrotome at – 30°C. Observations were carried out directly in water, and samples were also mounted in Mowiol® for later observation using dark field microscopy.

2.5 In vivo testing of the tumor model

Female CB17 SCID mice (N = 5) were supplied by Hafran (Itingen, Switzerland). Female Swiss nude mice (N = 30) were supplied by Charles Rivers (Iffa Credo, Saint Germain sur l'Arbresle, France). Animal experiments were performed according to the ethical principles of laboratory animal care and

Swiss legislation. Experiments were specifically approved by the official committee of animal research surveillance of the local authority. Animals were maintained in SPF animal housing under a 12-h light and 12-h darkness cycle with normal diet, ad libitum, respecting a maximum of 5 animals per cage.

The human tumor cell line of the invasive breast ductal carcinoma with negative steroid receptor status, SK-BR-3 [24], was subcutaneously engrafted in SCID mice (N = 5). After intraperitoneal injection of anti-asialo GM1 antiserum (Wako, Neuss, Germany), $5 \cdot 10^6$ SK-BR-3 cells in 70 µL of culture medium were subcutaneously inoculated and allowed to form tumor grafts for 20 days before formulation injection. The SK-BR-3 cell line forms compact breast adenocarcinoma tumor xenografts. Four human tumor cell lines were subcutaneously engrafted in Swiss nude mice by a mince-trocar technique with an ovarian carcinoma cell line, SKOV-3 (N = 1), a glioblastoma cell line, LN229 (N = 3), and two colocarcinoma cell lines, T380 (N = 1) and Co112 (N = 25). An inoculum of about 15 mm^3 of excised and minced tumor was subcutaneously engrafted into the right flank of 5-week-old Swiss nude mice, and the nodule was allowed to grow for 4 to 6 weeks prior to formulation injection. SKOV-3 and LN229 led to dense ovarian carcinoma and glioblastoma tumors [25], respectively, and necrosis was indiscernible. In spite of large neovascularization at the margin, tumor tissue itself is only sparsely vascularized. T380 human colocarcinoma, which can only be maintained in vivo (absence of in vitro growth), has a strong intratumoral neovascularization derived from peripheral neoangiogenesis. T380 tumors remain mostly viable until exceeding 0.5 g (usually in 3 weeks of growth), following which the extent of necrosis can vary [26]. A necrotic tumor was defined as containing no more than 25% viable cells [27]. Tumors from the human colocarcinoma Co112 cell line showed large intratumoral vascularization through peripheral neoangiogenesis from the pseudocapsule composed of connective tissue [28]. Necrosis takes place early and is patchy at first and then confluences in the tumor center. This central necrosis is a common feature in Co112 tumors, and it is also observed in in vitro-grown multicellular spheroids and liver metastases [29]. Meanwhile, Baxter et al. [30] indicate that tumor vascular and interstitial spaces represent 7% and 38% of the tumor volume, respectively. For intratumoral injection, the same devices were used as those for in vitro testing. Avoiding anesthesia was particularly important for organogels because of the interaction of organic solvents with anesthetic agents.

2.6 Histology

The biopsies were fixed in 10% buffered formalin or Bouin's fixative. After 15 min pre-fixation, they were cut into slices of 5 mm. Tissue was then embedded in paraffin, and 8 µm-sections were cut by microtome. Manual section processing (deparaffinization, rehydration, H&E staining and dehydration) was in some cases preferred to the automatized one in order to prevent artifacts, such as implant detachment or solubilization by minimizing roughness and duration of the xylol bath. Finally, slices were mounted using Tissue Tek®.

3 Results and discussion

The formulation and the in vitro evaluation of syringeability as well as the implant characteristics are presented separately for hydrogels and organogels. We then discuss the in vivo evaluation of the most promising formulations.

3.1 Hydrogel formulations

We investigated three types of formulations based on (i) thermo-sensitive hydrocolloids, (ii) internal and (iii) external gelation of alginate relying on ionic crosslinking. Formulation types (i) and (ii) are syringeable in mono-injection, whereas formulation type (iii) requires dual syringe co-injection.

3.1.1 Thermosensitive formulations

The extemporaneously prepared, viscous thermosensitive 2% w/v chitosan formulation with 20% of magnetic microparticles was easily syringeable and underwent slow sol-gel transition within 5 minutes at 37°C. But after storage as short as one day, the formulation with magnetic microparticles was no

longer syringeable (even through a 14-G needle). This instability is also observed when adding the microparticles before – instead of after – adding HCl to solubilize the chitosan.

It is most likely that the silica interferes with the acido-basic equilibrium of chitosan, leading to pH-induced gelation. This precluded further in vivo testing. A 17% w/w aqueous poloxamer solution was able to accommodate a fraction of magnetic microparticles up to 20% w/v (formulation H-0*). This stable formulation had a low viscosity, and, after in vitro injection through a 22-G needle in 35 °C PBS, the formation of a soft plastic mass homogeneously entrapping the magnetic microparticles could be observed.

3.1.2 Alginate formulations based on internal gelification

Table 2.3 lists the various formulations based on the internal gelation of alginate that were tested in vitro. The gelation of aqueous 2 to 4% w/v alginate dispersions mixed with an aqueous dispersion containing 2 or 10% w/v of $CaSO_4$ powder (formulations H-1 and H-2) occurred in 1 to 2 min. We then investigated the association with the delaying gelation adjuvant Na_3PO_4 at 0.5% w/v (H-3 to H-6), as well as the influence of calcium sulfate particle size by using coarse or fine powders (H-5 and H-6). When adding 0.5% w/v Na_3PO_4 and10% w/v $CaSO_4$ coarse powder, gelation was very long (~ 60 min) (H-5), whereas it was too rapid (2 min) with the same proportion of fine powder (H-6). The resulting gels were flaccid and opaque. Thus, we could not exclude incomplete gelation, as part of the solid particles sedimented in the long term. The gelation time could not be optimized for suitable injection, nor could the gel properties be optimized for particle size. Again, the obtained gels were flaccid and opaque. Using 0.2 M K_2HPO_4 as an alternative delaying agent, added with 0.270 mM NaCl (H-7), led to very long gelation time (180 min) and flaccid gel characteristics. Therefore, we decided not to incorporate magnetic particles in these formulations. For pre-mixed injection, we studied an alternative system based on the proposal of Draget et al. [22] and Kuo and Ma.[21]. As a control, injection of CaCO3 alone, in any proportion, from 2 to 10% w/v, was not able to trigger the gelation of a 2% w/v sodium alginate aqueous solution (H-8 or H-9). When the alginate aqueous solution was

Table 2.3: Mono-injection of standard grade sodium alginate hydrogel formulations based on internal gelation.

Formulation composition										Type of mix	Implant characteristics and comments		
Code	Alginate (% w/v)	Calcium salt				Adjuvant			MagMP (% w/ v)		Gelation time (min)	Implant score	Macroscopic observations
		Type	Powder fineness	Concentration		Type	Concentration						
				mM	(% w/v)		mM	(% w/v)					
H-1	2	$CaSO_4$	Coarse	116	2	*no*	*no*	*no*	*no*	B	< 2	+	Elastic, opaque
H-2	2	$CaSO_4$	Coarse	580	10	*no*	*no*	*no*	*no*	B	< 1	+	Elastic, opaque
H-3	2	$CaSO_4$	Coarse	116	2	Na_3PO_4	3	0.5	*no*	B	60	-	Flaccid, opaque
H-4	4	$CaSO_4$	Coarse	580	10	Na_3PO_4	3	0.5	*no*	PMI	30	-	Flaccid, opaque
H-5	2	$CaSO_4$	Coarse	580	10	Na_3PO_4	3	0.5	*no*	B	60	-	Flaccid, opaque
H-6	2	$CaSO_4$	Fine	580	10	Na_3PO_4	3	0.5	*no*	B	2	-	Flaccid, opaque
H-7	2	$CaSO_4$	Coarse	1162	20	K_2HPO_4 / NaCl	100 / 135		*no*	B	180	-	Flaccid, opaque
H-8	2	$CaCO_3$	Coarse	200	2	*no*	*no*	*no*	*no*	PMI	*NA*	*NA*	*Control, no gelation*
H-9	2	$CaCO_3$	Coarse	1000	10	*no*	*no*	*no*	*no*		*NA*	*NA*	*Control, no gelation*
H-10	1.5	$CaCO_3$	Coarse	13.6	< 0.2	*GDL*	*27.3*	*0.49*	*no*	PMI	*10*	*++*	*Highly elastic, translucent*
H-11*	1	$CaCO_3$	Coarse	8.8	< 0.1	*GDL*	*22.5*		*10*	PMI	*10*	*+*	*Elastic*

Legend: Symbol * after formulation reference is a reminder that the formulation is loaded with magnetic microparticles. Concentration relates to the total volume of the formulation after mixing. MagMP refers to magnetic microparticles, and GDL refers to d-gluconolactone. Type of mix: (B) bulk in equal volumes; (PMI) Pre-mix and injection through a single syringe in equal volumes. Implant score: (–), (+), (++) stand for fluffy implant after incomplete gelation or no gelation, for cohesive and soft implant and for cohesive and strong implant, respectively.

extemporaneously mixed with a dispersion of $CaCO_3$ and the δ-gluconolactone in water, medium acidification was controlled by the rate of lactone hydrolysis, leading to a formulation (H-10) with a high syringeability and a suitable gelation time of 15 min. The formed gel was elastic, translucent and more homogeneous than the formulations with internal gelation based on $CaSO_4$. We then incorporated 20% w/v of magnetic particles in the alginate dispersion (i.e., 10% w/v in the final formulation), resulting in a viscosity below 1 Pa·s. A less homogeneous mixing was observed when magnetic microparticles where incorporated in the calcium salt compartment. Syringeability and gelation time were unchanged in the presence of magnetic microparticles, but the gel was slightly more prone to flow. The influence of the compartment volume ratio was also investigated. When half volumes of the $CaCO_3$ and δ-glucunolactone dispersion (but of double concentrations) were used, we obtained a less flowing gel. As observed by Kuo and Ma [21], other attempts based on mixing of $CaSO_4$, $CaCO_3$ (with various particle sizes) and δ-glucunolactone gelation were not successful. We finally opted for an in vivo evaluation of the formulation H-11*, i.e., the pre-mixed mono-injection of alginate 2% w/w aqueous that incorporates 20% w/v of microparticles in one compartment and an aqueous extemporaneous dispersion of $CaCO_3$ and δ-gluconolactone at a 1:2 molar ratio (40 mM and 80 mM, respectively) in the other compartment.

From these investigations, we confirmed observations that a large solid particle fraction could be responsible for weak mechanical characteristics, as reported by Draget et al. [22]. This is even more pronounced for our pre-mixed formulation because of high shearing during initial gelation and addition of magnetic microparticles.

3.1.3 Alginate formulations based on external gelation

We also tested dual-injection of formulations based on external gelation (Table 2.4). In the absence of magnetic microparticles, formulations based on 2% w/v of standard grade sodium alginate (SG-ALG) displayed an optimal syringeability when co-injected with an equal volume of $CaCl_2$ solution at a concentration ranging from 50 to 100 mM (formulation H-12 to H-22). The gels formed cohesive

Table 2.4. Co-injection of alginate formulations based on external gelation using a dual injection device, in the absence or presence (*) of 10% w/v magnetic microparticles.

Formulation composition				Syringe-ability score	Implant	
Code	Alginate		$CaCl_2$		Score	Macroscopic observations
	Type	% w/v	[mM]			
H-12	SG-ALG	4	200	+	++	Elastic, highly syneretic gel
H-13	SG-ALG	4	100	+	++	Elastic, highly syneretic gel
H-14	SG-ALG	4	50	+	++	Elastic, highly syneretic gel
H-15	MG-ALG	4	25	+	-	No gelation
H-16	SG-ALG	2	200	+	+	Syneresis
H-17	SG-ALG	2	150	+	+	Gelation in filaments
H-18	SG-ALG	2	100	++	+	Elastic bulk
H-19	SG-ALG	2	65	++	+	Elastic bulk
H-20	SG-ALG	2	50	++	+	Soft
H-21	SG-ALG	2	25	++	+	Soft
H-22	MG-ALG	2	25	++	+	Elastic bulk
H-23*	SG-ALG	2	10	++	-	No gelation
H-24*	SG-ALG	2	150	-	-	Gel fragmented
H-25*	SG-ALG	2	100	-	-	Gel fragmented
H-26*	SG-ALG	2	50	++	+	Cohesive gel
H-27*	SG-ALG	2	25	++	+	Cohesive gel
H-28*	MG-ALG	3	100	NA	NA	NA
H-29*	MG-ALG	3	75	+	-	Gel fragmented
H-30*	MG-ALG	3	50	+	+	Elastic bulk, slight syneresis
H-31*	MG-ALG	2	100	++	-	Gel fragmented
H-32*	MG-ALG	2	50	++	+	Elastic bulk, slight syneresis
H-33*	MG-ALG	2	25	++	+	Elastic bulk

Legend: Symbol * denotes formulations that contain 20% w/v of magnetic microparticles in the alginate solution, i.e., 10% in the implant after co-injection. Dual-injection was performed with equal compartment volumes. Syringeability score: (-) difficult, (+) acceptable, (++) easy. Implant score: (-) stands for fluffy or non- cohesive implant after incomplete gelation or no gelation, (+) stands for cohesive and soft implant and for cohesive, and (++) stands for strong implant. Remarks: in all cases magnetic microparticle loading could not be elevated above 20% w/v without inducing aggregation. Formulation H-28* could not be injected.

masses. Larger $CaCl_2$ concentrations led to gelation in filaments (H-17) and to syneresis, consisting of gel shrinkage with water expulsion (H-12, H-13, H-14 and H-16), while lower concentrations did not trigger gelation at all (H-15). In the range of 50 mM to 100 mM, syringeability was adequate for slow, continuous co-injection without plug formation. To ensure a homogeneous dispersion in the final gel, microparticles had to be incorporated in the alginate compartment. Incorporation in the $CaCl_2$ solution resulted in segregation from the gel formed by co-injection: rapid $CaCl_2$ diffusion triggered alginate cross-linking before microparticle mixing. Larger alginate concentrations were associated with higher gel cohesion and syneresis, albeit with an increased viscosity, thereby limiting syringeability and magnetic microparticle incorporation in the alginate compartment. Thus, the 2% w/v aqueous alginate dispersion could accommodate 20% w/v of magnetic microparticles (i.e., 10 % after injection). Such a concentration of magnetic microparticles would be suitable for tumor treatment through heating. Incorporating 20% w/v magnetic microparticles, the 2% w/v alginate solution required a lower $CaCl_2$ solution concentration (25 to a maximum 50 mM, H-26*, H-27*, H-32* and H-33*) for optimal syringeability and gelation time in co-injection. Higher $CaCl_2$ solution concentrations (100 to 150 mM) led to elastic gel fragments (H-24*, H-25*, and H-31*). For comparison, this was not observed in the absence of magnetic microparticles up to 200 mM of $CaCl_2$ (formulation H-12 to H-22). Micrometric microparticles act here as defects in the gel structure and lead to its fragmentation under the shear stress of injection.

Studies with medical grade alginate (MG-ALG) revealed similar optimum formulations, i.e., a 2% w/v alginate solution incorporating 20% w/v magnetic microparticles in co-injection with 25 to 50mM $CaCl_2$ solutions (H-33 and H-32). These formulations displayed excellent syringeability but, in comparison with standard grade sodium alginate, medical grade sodium alginate (MG-ALG) aqueous dispersions yielded more elastic gels able to withstand mechanical stress. This could be explained by a larger content of L-guluronic acid residues in MG-ALG. For in vivo investigations of alginate formulations based on external gelation, we opted for 2% w/v aqueous dispersions of both alginate types, incorporating 10% w/v magnetic microparticles (20% in alginate solution) in co-injection with 25 mM $CaCl_2$ aqueous solutions.

3.2 Organogel formulations

Formulations based on single organic solvents were first evaluated, with and without magnetic particles. Further experiments focused on additional formulations that incorporated a cosolvent to reduce side effects.

3.2.1 Single-solvent organogel formulations

In vitro performances of various polymer/solvent formulations without added magnetic particles are presented in Table 2.5. Generally, the maximum polymer concentrations investigated were 20% w/v, but the retained concentration for each solvent was that allowing for an easy syringeability, together with the ability to form a semisolid implant. A Newtonian behavior reflected the matching of polymer and solvent solubility parameters. Organogel formulations with lower polymer concentrations (<10% w/v) had excellent syringeability, superior to that of hydrogel formulations, and exhibited viscosities below 100 mPa·s. Macroscopically, in vitro injection testing revealed striking variations in the early formation of the first precipitated peripheral layer, the so-called skin, and in the overall gelation process leading to an implant. This in turn affects mechanical characteristics of the resulting implant. The delay in skin formation can be linked to the delay of demixing and precipitation, known in membrane science to be a determining factor for morphology [31]. In that work, van de Witte defines a rapid and delayed time for demixing and precipitation of a membrane as less than one second and on the order of seconds to minutes, respectively. At the microscopic level, a common feature of such large injected implants was the presence of large lacunae in the center, not observed for usual thicknesses of membranes. When considering peripheral layers, we observed the variety of microstructure described for wet-casted membranes [10,32].

We distinguished three types of implants formed (Fig. 2.1C). The first type, type I, was a sagging gelatinous mass formed within a short time, though with slow skin precipitation, in the order of 30 s. Examples of type I formulations include Tecogel at 8% w/v in DMI (O-2) and formulations based on cellulose acetate (CA) at 6 % w/v in DMSO or NMP (O-4 or O-5). Formulations comparable to O-4, but with 8.5% w/v CA solution in DMSO, centripetally formed an implant within 5 min [33]. Implants from formulations O-4 and O-5 revealed central lacunas and aggregates of spherical polymeric

Table 2.5. Single-solvent organogel formulations.

Formulation composition				Viscosity	Syringe-ability score	Implant characteristics and comments	
Code	Polymer		Solvent	(Pa.s)		Score	Macroscopic observations
	Name	(% w/v)					
O-1	Tecogel	10	DMSO	0.07	++	-	Fragments of translucent gel
O-2		8	DMI	0.13	++	+	Soft and plastic gel
O-3		15	NMP	0.25	+	-	Very soft gel with ball shape
O-4	CA320S	6	DMSO	0.05	++	-	Slow skin precipitation, aggregated microstructure. Implant soft and sagging, easily fragmented, 20% w max. magnetic microparticle incorporable
O-5		6	NMP	0.06	++	-	same as above
O-6	Tecothane	10	DMSO	0.47	-	+	White precipitate, slight supernatant turbidity
O-7		5	DMI	0.37	+/-	-	Soft translucent bulk precipitates
O-8		7.5	NMP	0.1	+	+	Rapid precipitation in highly porous implant. Thin sk (3 mm) upon sublayer (spherical macrovoids, 4 mm mean diameter), lacunas in the center.
O-9		7.5	Glycofurol	0.66	-	+	Tough implant with ball shape
O-10	MMA/EA	5	DMI	0.03	++	-	No implant, fluffy precipitation
O-11		15	DMI	0.19	++	++	Tough implant with ball shape (no macrovoid, semi-crytalline in surface). 20% w/v was maximum magnetic microparticle content incorporable
O-12		20	DMI	0.46	+/-	+	Hard wire friable. Rapid skin formation, but slow implant gelation
O-13		15	Glycofurol	0.54	+	+	Hard and slightly friable implant with ball shape, 20% w/v was maximum magnetic microparticle content incorporable (macrovoids)
O-14		10	NMP	0.02	++	+	Soft spherical implant (20% w/v is beyond maximur polymer concentration)
O-15	EVAL	8	DMSO	0.08	++	++	Spherical implant with cellular microstructure, resistant, tough, highly elastic and cohesive, 40% v maximum magnetic microparticle content incorporal (no macrovoids).
O-16		20	DMSO	0.3	++	++	Tougher EVAL implant, less elastic than O-15
O-17		4	NMP	0.02	++	NA	Precipitation ability insufficient
O-18		8	NMP	0.08	++	-	Leaky, supernatant opalescence, ball shaped impla too soft without resistance
O-19		20	NMP	1.64	+	+	Dense and tough implant.

Legend: the rheological behaviors were newtonian and viscosity values were obtained by fitting over the shear rate range 0.07–1000 s^{-1} (to 250 s^{-1} for MMA/EA formulations). Syringeability score: (+), (+/-), (+), (++) stand for difficult, acceptable, easy, and very easy, respectively. Implant score: (-) stands for fluffy or non cohesive implant or absence of precipitation, (+) stands for cohesive and soft implant, and (++) for cohesive and strong implant.

micelles. Microcrystalline domains are also likely, because cellulose acetate exhibits rapid crystallization [34]. A large peripheral rim of a dense polymer phase (ca. 50 and 30 μm thick for O-4 and O-5, respectively) was present, but skin or macrovoids as described previously [35] could not be observed. The second type of implant formation, type II, was observed for the more hydrophobic polyurethane, Tecothane, as 7.5% w/v solution in NMP (O-8), or for the acrylic Paraloïd at 15% w/v in DMI (O-11). Rapidly formed (less than 1 s), a hard but disrupting skin delayed the completion of implant formation, likely by limiting solvent diffusion. The resulting implant masses were highly rigid. Implants from the O-8 formulation showed large spherical voids in the center, a rim of dense polymer phase, spherical macrovoids (4 μm in diameter) in a peripheral sublayer and a solid polymer thin skin (less than 3 μm in thickness) [36]. This is consistent with the description of instantaneous nucleation and growth of the polymer lean phase as a mechanism of liquid-liquid demixing, with the subsequent glass transition of the polymer rich phase [37]. Formulation O-11 successively displayed a large surface skin layer (10 μm in thickness), supported by a layer with finger-like voids (37 ± 12 μm in length and 13 ± 5 μm in width), and an internal sub-layer containing numerous spherical and regular macrovoids (17 ± 7 μm as mean diameter). The solid polymer phase constituting the walls was also dense and continuous [38]. Type III implants, as exemplified by the 8% w/v EVAL solution in DMSO, were formed by rapid precipitation at the interface (skin formation in the order of 1 s), in agreement with the 3 or 1.3 s reported for similar EVAL in DMSO liquid embolic formulations by Taki et al. [39] or Yamashita et al. [40], respectively. After an intermediate delay necessary for completion of implant precipitation (ca. 30 s), the resulting elastic mass was highly cohesive and resistant. Similarly, Taki et al. reported an elastic and soft sponge-like consistency in 15 s [39]. This time was revealed to be dependent on EVAL concentration. At a microscopic level, this implant comported a thin skin (3 μm in thickness). This skin was supported by a sublayer including spherical macrovoids (8 ± 2 μm in diameter). Toward the center, macrovoids were larger (22 μm in diameter). In the center, lacunas were delimited by large solid polymer phase walls [39], which had a remarkable microcellular structure (as described in [38]), likely in relation with elasticity. Comparison of the two polyurethanes investigated revealed the role of polymer nature in implant formation. The amphiphilic Tecogel, due to its high swelling ratio (500%) in water, slowly precipitated and led to implant softness and plasticity, in contrast

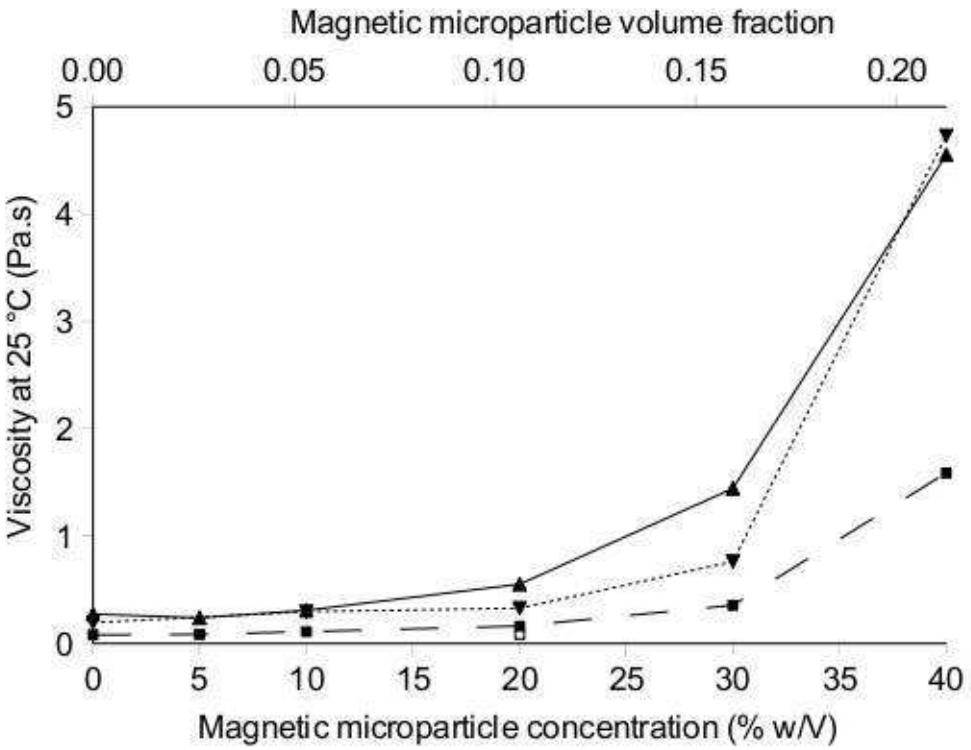

Figure 2.2: Influence of magnetic microparticle loading on formulation viscosity.

Alginate 2% w/v in water (▲), EVAL 8% w/v in DMSO (■), PMA 15% w/v in DMI (▼); (□) refers to a control consisting in 20% w/v magnetic microparticle suspended in DMSO.

with the hydrophobic Tecothane. Generally, during in vitro injection of various polymers, increasing the polymer concentration accelerated the interfacial precipitation, limiting solvent diffusion and thus increasing the time for complete implant formation.

For methacrylate copolymer formulations (O-10 to O-14), the maximum polymer concentration for suitable syringeability (20 % w/v) resulted in a dense, hard but slightly friable implant.

Selected organogels were loaded with magnetic microparticles. The highest dispersible solid fraction was 20% w/v for both 15% w/v MMA/EA formulations (O-11* with DMI and O-13* with GF), and 40% w/v for the EVAL formulation O-15* (with DMSO). The presence of magnetic microparticles resulted in a faster implant formation by reducing the polymer solution volume fraction. The

microstructure patterns described in the absence of microparticles were preserved, but the porosity (lacunas and macrovoids) was decreased with increasing magnetic microparticle fraction. At a microscopic level, the magnetic microparticles were invariably incorporated in the solid polymer phase, and no interface voids were observed. This is likely due to polymer filling of the silica matrix mesopores of the magnetic microparticles [41]. The initially formed precipitation layer was more frequently disrupted during injection of the formulation. This is due to reduced flexibility related to the microparticles, which concentrate through convection of polymer toward gelation front [41]. The effect of magnetic particle loading on the rheological properties is illustrated for EVAL and MMA/EA organogels in comparison with 2% w/v aqueous standard grade alginate solution (Figure 2.2). As the fraction of magnetic microparticles rose, the organogel formulations displayed increased viscosity, a yield stress and a shear-thinning behavior. It was decided to reduce the injection speed in order to favor syringeability. A slight friability was observed in the MMA/EA implants (O-11* or O-13*, for instance). In contrast, the formulation of EVAL 8% w/v in DMSO (O-15*), with up to 40% w/v of magnetic particles, was still easily syringeable and able to form a strong and elastic implant.

Incidentally, at higher injection speed (i.e., pressure), the measured implant mass was lower than expected from the injected volume. We could propose two hypotheses to explain the behavior of suspensions with such a high solid fraction. First, pressure can trigger partial aggregation of microparticles and cause phase segregation with filtration of the formulation through aggregated particles [42,43]. Through a statistical physics approach, the local network of these particles in dynamic interaction could allow storage of elastic energy. This could lead to overestimation of the injected volume when reading the syringe graduation [44].

Formulations without magnetic microparticles that represent the three implant types (O-2, Tecogel in DMSO, O-8, Tecothane in NMP, and O-15, EVAL in DMSO) were selected for in vivo experiments. Formulations with magnetic microparticles resulting in a wide range of implant mechanical characteristics were also investigated. For example, we evaluated rigid implants from O-11* (acrylic copolymer in DMI) and O-13* formulations (acrylic copolymer in glycofurol) versus elastic implants from the formulation O-15* (EVAL in DMSO)

Table 2.6: Cosolvent organogel formulations, precipitation and implant characteristics.

Formulation							Implant score
Code	Polymer		Solvent 1		Solvent 2		
	Abbr.	% w/v	Abbr.	% vol	Abbr.	% vol	
CO-1	EVAL	10	DMSO	70	PG	30	++
CO-2	MMA/EA	7	NMP	65	PG	35	NA
CO-3	Tecothane	9.5	DMSO	78	PG	22	NA
CO-4		5.4	NMP	50	PG	50	+
CO-5		3.6		34	PEG	66	+
CO-6		10		32		68	++
CO-7		3.6	NP	35	PEG	65	++
CO-8		5		30		70	++
CO-9		6.7		67	PG	33	-
CO-10	CA 398-3	2	DMSO	16.5	PEG	83.5	-
CO-11		4.2	DMSO	35	PG	65	-
CO-12		2.25	NMP	21	PEG	79	-
CO-13		10	NMP	40	PEG	60	-
CO-14		4.2	NMP	40	PG	60	+
CO-15		10	NMP	20	PG	80	
CO-16		5.8	NP	58	PG	42	NA
CO-17		3.4	NP	34	PEG	66	+
CO-18	CA 320-S	10	DMSO	50	PEG	50	-
CO-19		6		27	PG	73	+
CO-20		10	NMP	50	PEG	50	+
CO-21		6		30	PG	70	++
CO-22		12.5	NMP	50	HELA	50	++
CO-23	CAB 381-2	10	DMSO	50	PG	50	++
CO-24		10		50	PEG	50	+
CO-25		8.6	NMP	43	PG	57	++
CO-26		8.8		44	PEG	56	++

Legend: Implant quality score: (++), (+), (-) stand for elastic and cohesive, soft and cohesive, soft and plastic or fluffy, respectively. Polymer concentration is expressed as the final percent of the total volume of solvent and cosolvent (often, a concentrated polymer solution in solvent 1 was diluted by addition of a cosolvent).

3.2.2 Cosolvent organogel formulations

In order to circumvent potential deleterious effects of the solvent, we developed original organogel formulations based on polymer solutions in mixtures of two organic solvents, namely, the solvents used in single-solvent formulations, and more hydrophilic cosolvents, generally characterized by lower toxicity (Table 2.2). We selected the single-solvent formulations made of EVAL, Tecothane and an acrylic copolymer dissolved in DMSO or NMP as well as various cellulose esters (CA 320-S, CA 398-3 and CAB 381-2). The challenge to prepare these cosolvent formulations was to incorporate the hydrophilic cosolvent while preserving polymer solubilization. Unfavorable formulations led to a large rise in viscosity, sometimes associated with evidence of polymer desolvation, observed as inhomogeneities or cloudiness. This hindered the ability of these formulations to form implants. Adequate cosolvents were PG, PEG 200 and HELA for addition to solutions of EVAL, Tecothane or cellulose esters (CA-320S or CAB 381-2) in DMSO or NMP (Table 2.6). Formulation viscosity was generally higher, hence limiting syringeability, and skin formation was slower than that of single-solvent formulations. For EVAL and Tecothane cosolvent formulations, the implants appeared elastic and cohesive, just as they did for single-solvent formulations. In contrast with the single-solvent formulation, the implants formed by cosolvent formulations based on 5% w/v CA-320S were cohesive and demonstrated enhanced elasticity. Such formulations are promising for intratumoral injection. The best implants were obtained with formulations CO-1, CO-6, CO-7, CO-19, CO-21, CO-22, CO-23, CO-25 and CO-26 (see Table 2.6). The implant microstructure was studied for selected formulations. A Tecothane formulation in NMP-PEG (CO-6) resulted in an implant of similar morphology but that was less porous than the corresponding implant from the single-solvent formulation. In contrast to the corresponding single-solvent (in agreement with [45]) or Tecothane formulations, implants of the CA-320S formulation in DMSO or NMP with PG or PEG (CO-18, -19, -20 and -21) were composed of a continuous phase of densely packed polymer aggregates, displaying only fine pores and a few lacunas (type I). This can explain the increased toughness of the implant formed from the CA-320S in cosolvent formulation. With NMP and PEG (CO-20), we could also observe a skin layer and few macrovoids (type II-like).

The content of magnetic microparticles incorporable into the cosolvent formulations was generally limited to 10% w/v. Surprisingly, only the most viscous formulation (CO-22), with HELA as the cosolvent, could accommodate 20% w/v of magnetic microparticles. Since the incorporated particle fraction was generally low (10% instead of ≥ 20% w/v for single-solvent organogels), the interfacial precipitation and the implant formation, as tested in vitro, were not significantly different from those of the corresponding particle-free formulations. Similar to the single-solvent situation, magnetic microparticle incorporation led to reduced implant porosity, resulting in a particularly dense implant for the CA-320S cosolvent formulations. For in vivo testing, four formulations were selected among the suitable cosolvent formulations. Tecothane at 10% w/v in NMP/PEG200 32/68 with 10% of magnetic particles (CO-6) was chosen for the low toxicity of PEG. CA-320S at 6% w/v in NMP/PG 30/70 (CO-21) and DMSO/PG 27/73 with 10% w/v magnetic microparticles were chosen for the improved syringeability as well as the elasticity of the resulting implants, while CA-320S at 12.5% w/v in NMP/HELA 50/50 was chosen for the higher fraction of incorporable magnetic microparticles, namely, 20% w/v.

3.3 In vivo experiments

Selected hydrogel and organogel formulations were directly injected into solid tumors of human origin, with varying histo-morphologies, subcutaneously engrafted in immuno-deficient mice (Table 2.7).

Legend of table 2.7: Symbol * after formulation code is a reminder that the formulation is loaded with magnetic microparticles. Their concentration is expressed as a final percentage of the total volume of solvent and cosolvent. Tumor cell lines: Co112 (C), T380 (T), LN229 (L), SK-BR-3 (S). Systemic toxicity, Sys., was lethal (L), rapidly lethal (IL), transient, reversed in 24 hrs (T), or transient, reversed in few hours (t). Local toxicity: for all experiments we observed simple mechanical dilatation of the injected site (D), accompanied with transient edema of the tumor site after injection with limited intensity (e), transient edema of the tumoral site injected of larger magnitude (E). Implant distribution score: (-), (+/-), (+) and (++) stand for large leakages, intratumoral but leakages, intratumoral and intratumoral suitably in the tumor center and periphery, respectively. In situ implant characteristics score: (–), (+), (++) stand for fluffy or non-cohesive implants or the absence of precipitation, for cohesive and soft implants and for cohesive and strong implants, respectively.

Table 2.7: Performances of the formulations selected for *in vivo* experiments.

Formulation			*in vivo* test			Syringe-ability score	Toxicity		D_{diss}	Distribution of the implant *in situ*		Implant evaluation *in situ*	
Code	Components	[MagP] (% w/v)	n	Tumor	V_{inj} (ml)		Syst.	Local		Score	Detail of implant distribution	Score	Macroscopic observations
H-0*	poloxamer	20	2	C	0.5	+	no	D	0	-	No implant in tumor center, but within the pseudo-stromal capsule with leakage in the vicinity	-	Particles efficiently entrapped but implant soft and fluxing
H-8*	SG-ALG, $CaCO_3$	10	2	C	0.5	+	no	D	3	-	Distant leakage.	-	Fluffy, particles poorly entrapped
H-8*	SG-ALG, $CaCO_3$	10	2	C	0.5	+	no	D	7	-	No gel recovered	NA	NA
H-24*	SG-ALG, $CaCO_3$	10	2	C	0.5	+/-	no	D	0	+/-	Peripheral, frontward to axis of injection without needle displacement	+	Elastic and resistant.
H-18	SG-ALG, $CaCO_3$	0	1	C	0.5	+/-	no	D	7	+	Peripheral, homogeneous	+	Elastic and resistant. (cf J0)
H-24*	SG-ALG, $CaCO_3$	10	1	C	0.5	+/-	no	D	7	+	same as above	+	Elastic and resistant similar to H-18
H-19	SG-ALG, $CaCO_3$	0	2	C	0.5	+/-	no	D	7	+	same as above	+	Transluscent, elastic and resistant.
H30*	MG-ALG, $CaCl_2$	10	2	C	0.5	+/-	no	D	7	+	Seems less suitable than control, few leakages	+	Elastic and resistant.
O-2	Tecogel, DMI	0	1	S	0.5	++	RL	NA	1	-	Very little implant recovered from tumor site, potential dispersion of excess polymer	NA	NA
O-2	Tecogel, DMI	0	1	L	0.5	++	RL	NA	0	-	Little implant recovered from tumor site, potential dispersion of excess polymer	NA	NA
O-4	CA-320S, DMSO	0	1	S	0.5	++	L	NA	0	+/-	Little implant in tumor center (high tissue density), distant subcutaneous leakage	+	Fluxing
O-8	Tecothane, NMP	0	1	L	0.5	++	L	NA	0	+/-	suitable distribution in the tumor center, leakage (unfavorable tumor characteristics)	++	Hard and resistant.
O-11	MMA/EA, DMI	0	1	S	0.5	+	RL	NA	0	+/-	Little implant in tumor center (high tissue density), leakage in closed vicinity	++	Hard and tough.
O-13	MMA/EA, Glycofurol	0	1	S	0.5	+	RL	NA	0	+/-	Little implant in tumor center (high tissue density), leakage in vicinity	++	Hard but intermediate toughness
O-15	EVAL, DMSO	0	1	L	0.5	++	L	NA	0	+	Tumor center well implanted, leakage (unfavorable tumor characteristics)	++	Very elastic, resistant.
O-4*	CA-320S, DMSO	20	1	S	0.5	++	L	NA	0	+/-	Little implant in the tumor center, large subcutaneous leakage	+	Fluxing
O-11*	MMA/EA, DMI	20	1	C	0.5	+	L	NA	0	+/-	In the tumor center and retrogradely peripheral, leakage	+	Hard, intermediate toughness.
O-13*	MMA/EA, Glycofurol	20	1	T	0.5	+	L	NA	0	-	Little implant in tumor center, distant subcutaneous leakage	++	Intermediate hardness and toughness
O-15*	EVAL, DMSO	40	2	C	0.5	++	L	NA	0	++	Tumor center well implanted and interstitial extensions in periphery, leakage	++	Rugosity, very elastic, resistant.
O-15*	EVAL, DMSO	40	2	C	0.25	++	T	e	1	++	Tumor center well implanted and interstitial extensions in periphery	++	same as above
CO-6*	Tecothane, NMP+PEG	10	1	C	0.25	-	t	E	4	++	Confined to the tumor center, extensions in periphery closed to implant,no leakage.	++	Hard and resistant, alveole from air buble.
CO-19*	CA-320S, DMSO+PG	10	1	C	0.25	+/-	t	E	4	++	Tumor center partly implanted and interstitial extensions in periphery well confined	++	Elastic and tough.
CO-21*	CA-320S, NMP+PG	10	1	C	0.25	+/-	t	E	4	++	Tumor enter partly implanted and interstitial extensions in periphery few leakages	++	Elastic and tough.
CO-22*	CA-320S, NMP+HELA	20	3	C	0.25	-	t	E	2	++	Strictly confined to the tumor center, no diffusion in peripheral tumor tissue which are compacted	++	Highly homogeneous and dense, resistant with slight plasticity

3.3.1 Intratumoral injection of hydrogels

Intratumoral injection into Co112 xenograft of 0.5 mL of the thermosensitive formulation H-0* (17% w/v aqueous poloxamer solution incorporating 20% w/v of microparticles) was straightforward and well tolerated. The implant was distributed mostly within the tumor pseudocapsule and not in the tumor center itself, showing flaccidity that made it inadequate for tumor casting, probably due to a high interstitial pressure (Figure 2.3a). The implant periphery in contact with tumor fluids appeared spongy. The implant was partly resorbed at day 7.

Shortly after mixing, the alginate formulation based on internal gelation with 10% w/v magnetic microparticles (H-8*) led to an easy and well-tolerated injection into the Co112 tumor. After 3 days, only a small implant was localized in the tumor, while a significant subcutaneous leakage was observed (Figure 2.3b). In the case of injection in non-necrotic and compact ovarian carcinoma xenografts (SKOV-3), we observed large leakages and recovered even less of the implant following explantation (data not shown). The implant was fluffy and encapsulated in a hyaline membrane, and magnetic microparticles were not tightly entrapped. After 7 days, very few polymers or magnetic microparticles were recovered from the tumor site, except, marginally at locations distant from the leakage. Internal

Figure 2.3: Photomicrographs (left: 25X, right: 400X) of subcutaneous Co112 human colon carcinoma xenografts in Swiss nude mice after the direct injection of various hydrogel formulations.
Empty arrow heads (▲) indicate the injected material; t the tumor tissue; n the areas of necrosis; p the connective tissue pseudocapsule.
Row a shows the injected poloxamer-based formulation H-0*, incorporating 20% w/v magnetic microparticles (brown color), shortly after injection. The left panel shows a small amount of implant next to the tumor, mostly in the pseudocapsule and not in the area of necrosis. The right panel shows a higher magnification of the implant which displays a partially loose microstructure. **Row b** shows the injected alginate formulation based on internal gelation H-8*, with 10% w/v of magnetic microparticle, 3 days after injection. On the left, traces of the implant are found in an area of necrosis of the tumor. Note absence of an inflammatory response. The right panel shows the microstructure of the implant which is very loose, most probably due to insufficient internal gelation. **Row c** shows an implant from the alginate formulation based on external gelation H-24*, with 10% w/v magnetic microparticles, shortly after injection. The implant is confined to the necrotic center of the tumor and to peripheral areas of necrosis but is also found in the pseudocapsule. The right panel shows the microstructure of the implant, which is lamellar (black arrow).

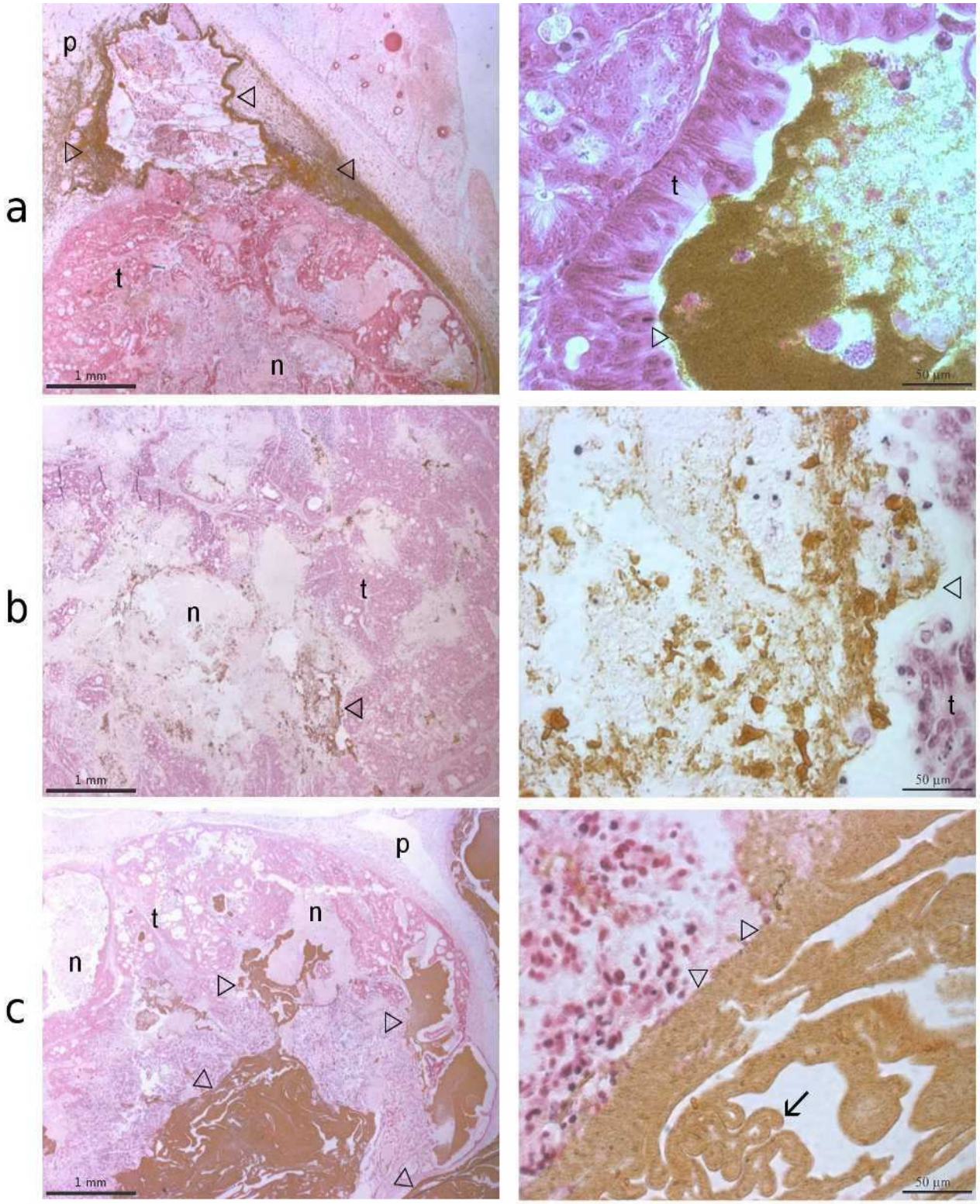

Figure 2.3

gelation seemed impeded in the tissue environment. The high fraction of magnetic particles, as well as the transient presence or the excess of calcium carbonate particles, could be responsible for decreased implant mechanical strength and the increased porosity and erodibility observed *in situ*.

Co-injection of formulations based on external gelation, both with (H-24* and H-30*) and without magnetic microparticles (H-18 and H-19), was more difficult due to the poor syringeability associated with the injection system itself (Duploject©). The partially lamellar implant (arrow, Figure 2.3c) was confined to the tumor, filling peripheral necrotic spaces, and was preferentially frontward in the axis of injection. Homogeneous implant distribution was achieved by distal insertion of the needle and slow withdrawal during injection. Magnetic microparticles were homogeneously entrapped, and the implant was both elastic and mechanically resistant. At day 0, we observed the gradual development of neutrophil granulocytes and macrophages in a thin rim of tissue surrounding the implant that formed in the space provided by central necrosis. Few inflammatory cells were found enclosed in the implant periphery. The reaction was comparable for implants containing magnetic microparticles and controls of the two alginate grades. In relation with the presence of inflammatory cells and/or incomplete alginate crosslinking, limited implant erosion was detected after 7 days of intratumoral implantation, similar to that described after rat intracardial injections [46], signifying an inflammatory response.

In spite of high implant biocompatibility, we estimated that the implantation patterns and the limited fraction of incorporable magnetic microparticles proved insufficient for further investigation of local hyperthermia treatment.

3.3.2 Intratumoral injection of organogels

As preliminary experiments, we injected 0.5 mL of formulations without magnetic microparticles into dense and poorly vascularized subcutaneous grafts from the ductal carcinoma SK-BR-3 and glioblastoma LN229 cell lines. Tecogel in DMI (O-2) did not form a firm implant in situ. Only a small amount of the easily injected polymer formulation was recovered from the tumor site. Its slow precipitation characteristics, which are potentially associated with instability in situ, could be

responsible for adverse migration of the polymer formulation in vivo. The formulation of cellulose acetate in DMSO (O-4) was highly syringeable, and the fluxing and leaky implant (type I) could be entirely recovered from the tumor and the stromal pseudocapsule vicinity. This implant distribution was also observed for type-II implant formulations, namely, Tecothane in NMP and MMA/EA in DMI or GF (O-11 and O-13). Although syringeability was more limited, hard implants were formed. It should be noted that their microstructures were superimposed with those observed in vitro. For the highly syringeable EVAL in DMSO formulation (O-15, Figure 2.4b), localization of the implant in the tumor center was improved before partial leaking occurred in close contact to the stromal pseudocapsule. Displaying type-III microstructure, the implant was elastic and resistant. Ductal carcinoma or glioblastoma xenografts, which formed compact tumor nodules, would thus require adaption of formulation work. When incorporating 20% w/v of magnetic microparticles, injection into ductal carcinoma grafts of formulation O-4* (CA-320S in DMSO) led to the same results as in the absence of microparticles (Figure 2.4a). Two acrylic formulations with high polymer concentration (O-11* and O-13* with 15% w/v MMA/EA in DMI or GF, respectively), incorporating 20% w/v of magnetic microparticles, were subsequently injected (0.5 mL) into subcutaneous tumor xenografts of the Co112 and T380 cell lines. Syringeability was acceptable, and the implant distribution of formulation O-11* in tumor tissue was mostly peripheral (Figure 2.4b). Little implant was recovered from the tumor center with the O-13* formulation, and most of the material leaked into the vicinity (Figure 2.4d). It is noteworthy that the implant microstructure corresponded to that determined in vitro and in vivo in the absence of magnetic microparticles. This indicates that organogel injection may be favored in cases of vascularized largely necrotizing tumors, such as Co112. The implant of EVAL formulation with a high fraction of magnetic microparticles (O-15*, with 40% w/v of magnetic microparticles) localized adequately in the tumor center. Implant extensions in the tumor reached the tissue periphery and could occasionally leak at the end into the stromal pseudocapsule (Figure 2.4c). Leakages were mostly avoided when only 0.25 mL of the O-15* formulation (EVAL in DMSO with 40% w/v microparticles) was injected. The shear-thinning behavior of formulations containing a large particle fraction could explain the high syringeability along with the tendency to diffuse into free spaces before precipitation takes place in situ. At a histological level, the implant appeared spongy but compact. We observed only

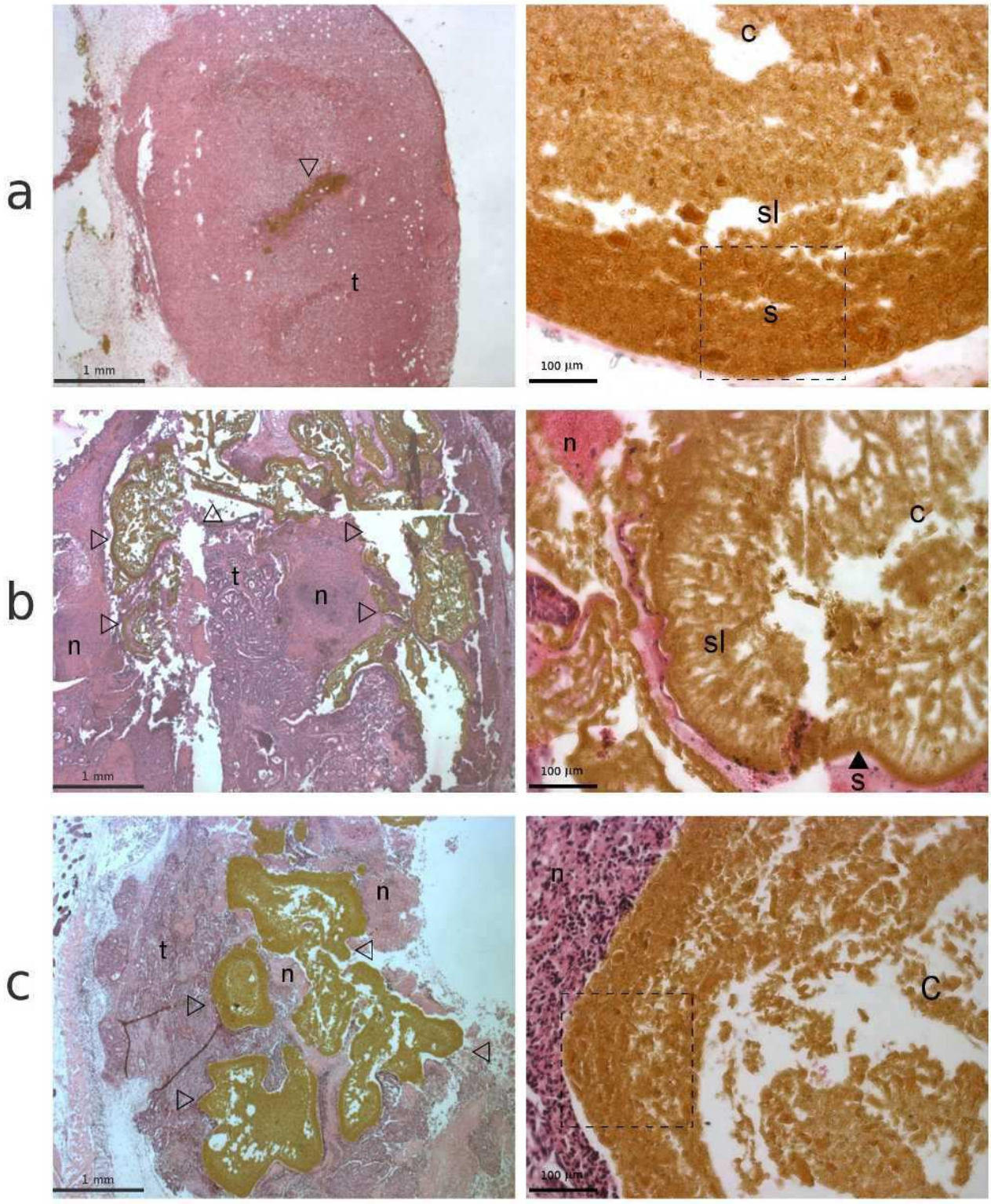

Figure 2.4

a few aggregates, as is commonly reported in embolization [14,39]. At day 1, we observed inflammatory cells in tumor tissue surrounding the implant corresponding to an acute inflammatory response. The implant itself was not infiltrated. The microstructure pattern found in vitro was confirmed and the implant was suitably elastic and resistant. The injection had to be slow, as determined in vitro. Histological changes following organogel formulation injection can be also attributed to the organic solvent itself [47,48].

During this preliminary investigation, 11 mice were injected with 0.5 mL of single-solvent organogel formulations. Organic solvent-induced acute toxicity, evidenced mainly by respiratory insufficiency, led to cachexia in the mice, requiring sacrifice. It is worth noting that the injected 0.5-mL volume in a 25 g mouse would correspond to 1.4 L in a 70 kg patient, representing an unrealistic injection volume per body weight. For the EVAL formulation in DMSO, which incorporated 40 % w/v of magnetic

Figure 2.4: Photomicrographs (right: 25X, left: 200X) of Swiss nude mice subcutaneous xenografts (SK-BR-3 or Co112) injected with single-solvent organogel formulations.
Empty arrow heads (▲) indicate the implant; T the tumor tissue; n the areas of necrosis; P the connective tissue pseudocapsule.
Row a, SK-BR-3 tumors injected with the cellulose acetate-based formulation O-4*, incorporating 20% w/v of magnetic microparticles. This tumor displays high tissue density and no necrosis area can be detected. Little implant localized to the tumor center and most of the implant was found flaccid in leakage. On the right, microstructure at 200X magnification shows a peripheral rim of dense polymer phase, the so-called skin, with magnetic microparticles embedded and a center with few voids, revealing a type I microstructure (see text and Fig. 1c). The initially precipitated peripheral layer, also called the "skin layer" (s, with indicative dashed lined box), is large and continuous (no voids). The microstructures of the internal sublayer (sl) and the implant center (c) display some continuity, the implant center being slightly less dense with sparse voids. **Row b**, Co112 tumor xenograft injected with the acrylic copolymer-based formulation O-11*, incorporating 20% w/v of magnetic microparticles. On the left, the implant mostly localized in the necrotic tumor periphery. On the right, the type II microstructure at 200X magnification. The initially precipitated skin layer (s, with indicative black arrow head) is thin and supported by a sublayer (sl) displaying macrovoids. The implant center shows larger voids. **Row c**, Co112 tumor xenograft injected with EVAL-based O-15* incorporating 40% w/v of magnetic microparticles. On the left, central distribution of the implant in the tumor with extensions toward its periphery. This high microparticles load masks some characteristics of type III microstructure in the large peripheral rim concentrating microparticles (dashed lined box), where implants devoid of microparticles show a remarkably thin initially precipitated skin layer and a porous sublayer. However, lacunas observed at low magnification in the center of implant (c) support type III microstructure.

Figure 2.5: Photomicrographs (right: 25X, left: 400X) of subcutaneous Co112 cell line xenografts in Swiss nude mice after direct injection of cosolvent organogel formulations.
Empty arrow heads (△) indicate the implant, t, the tumor tissue, n, the areas of necrosis, P, the stromal pseudocapsule.
Row a shows a xenograft 4 days after injection of the Tecothane-based formulation CO-6*, with 10% w/v of magnetic microparticles. On the left, the implant is localized to the tumor center and appears highly lacunate (more than corresponding single solvent formulation, in the absence of a hygroscopic cosolvent). On the right, a small extension displayed a type II microstructure (see text and Fig. 1c), composed of a thin skin that concentrates magnetic microparticles (dashed lined box), with the specificity of regular spherical macrovoids (v). **Row b** shows a xenograft 4 days after injection of cellulose acetate formulation CO-19*, with 10% w/v of magnetic microparticles. On the right, the implant partly localized to central tumor necrosis, and leaked in the stromal pseudocapsule. On the left, the implant appears as consisting of microparticle aggregates devoid of polymer partly due to polymer sensitivity to histological processing. Nevertheless, the homogeneous pattern argues for a type I microstructure. **Row c** displays a xenograft 2 days after difficult injection of the highly viscous cellulose acetate-based formulation CO-22*, with 20 % w/v of magnetic microparticles. On the right, the implant is exclusively localized to the tumor center. On the opposite side, a necrotic area appears somewhat bruised by the injection. Note that pleats in the tumor tissue (T) are artifacts. On the left, polymer sensitivity to the histological process, as previously, and a higher magnetic microparticle load make implant appear as packed aggregates consisting of the microparticles remaining after processing. A type I microstructure is likely here as well.

microparticles (O-15*), decreasing the injection volume to 0.25 mL reduced acute systemic toxicity to an acceptable level (transient abnormal gait and ocular irritation). We could then observe a transient local edema at the implant site, which developed in the first hours and was resorbed within one day. This could be linked to local toxicity due to the organic solvent, but it more likely originates from the embolization of tumor vessels. This formulation could be safely injected in 53 mice to demonstrate its antitumor activity following hyperthermia treatment under magnetic field exposure [49].

Therefore, in our investigation of cosolvent formulations, we opted for an injection volume of 0.25 mL. Following tumor injection of four cosolvent formulations incorporating magnetic microparticles, namely, CO-6,* CO-19*, CO-21* and CO-22* (Tecothane in DMSO+PEG, CA 320S in NMP+PEG, NMP+PG and NMP+HELA, respectively), we did not observe any manifestation of systemic toxicity. While the syringeability of CA formulations CO-19* and CO-21* was acceptable, formulation CO-22* could not be injected at all using manual syringes and standard needles. The use of a larger needle was

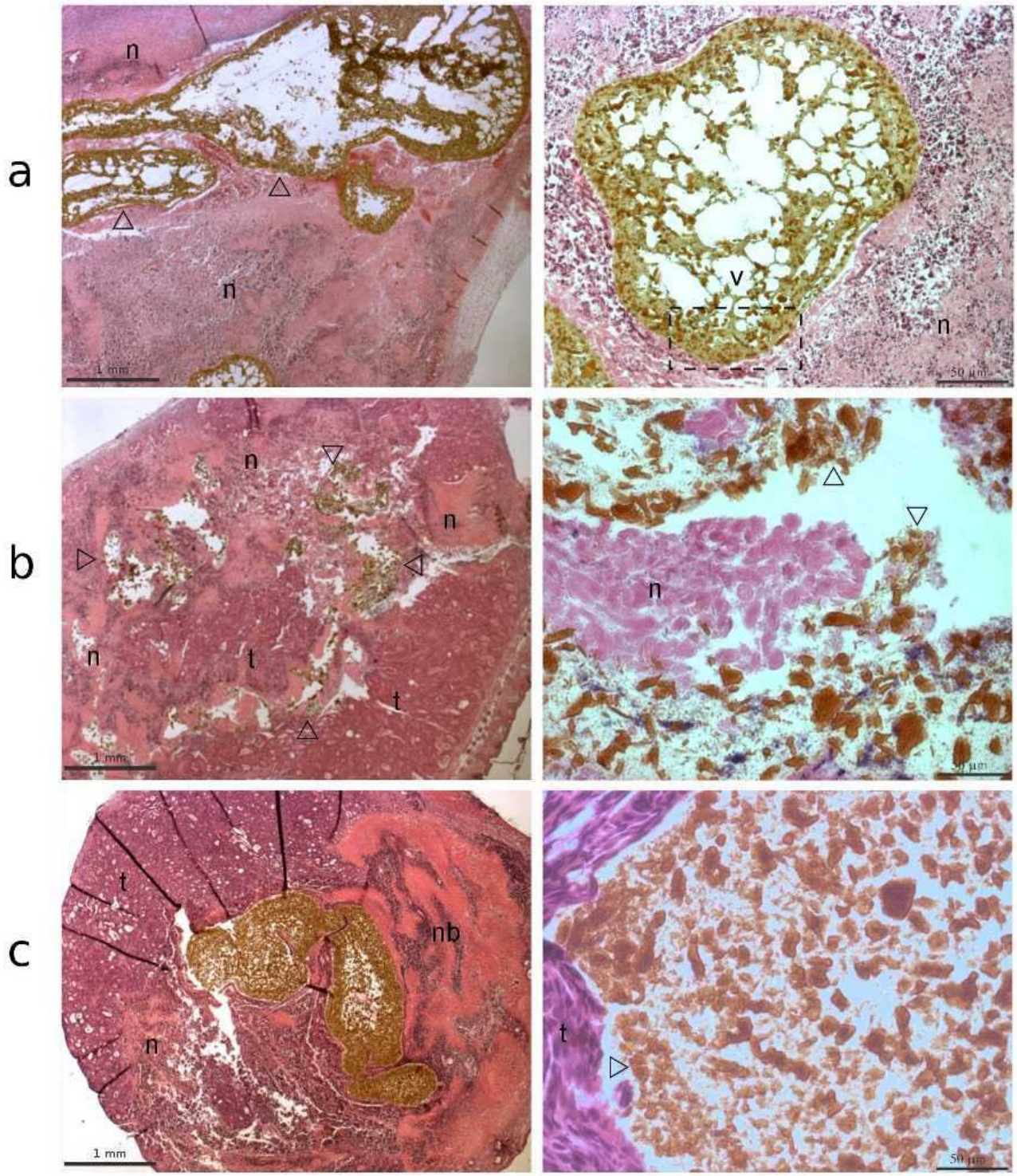

Figure 2.5

also required for the Tecothane-based formulation CO-6*. As compared with single-solvent formulations, edema formation was more important with the use of cosolvents, but it was equally reversible. The tumor edema formation is likely related to hygroscopically induced osmotic gradient from the solvent or cosolvent diffused into the interstitial spaces. In addition, at the cell wall level, solvents entail at least temporary breakdown of function leading to osmotic gradients with ensuing edema development. For the CO-19* (Figure 2.5b) and CO-21* cellulose acetate formulations with PG as the cosolvent, DMSO or NMP were equivalent as the solvent, without impacting on implant distribution. The implant localized satisfactorily in the tumor center and periphery. The highly viscous CO-6* and CO-22* formulations had a paste-like behavior during injection and resulted in an implant mass that was confined to the tumor center (Figure 2.5a and c). These formulations had no capacity to diffuse from the tumor center into more peripheral interstitial spaces. In the case of CO-22*, this was accompanied by signs of tumor bruising. Microscopically, the Tecothane implant formed from the CO-6* formulation exhibited numerous alveolar voids in the polymer matrix (Figure 2.5a), confirming the microstructure obtained in vitro and in vivo for the single-solvent formulation without magnetic microparticles. After four days, an inflammatory response was noted. At day 2, the CA-based implant from the CO-22* formulation (containing HELA) was accompanied by a significant inflammatory response in tumor tissue, but not the infiltrating the implant. The implant was compact and homogenous, displaying a type-I microstructure (Figure 2.5c). This argues in favor of a higher efficiency in tumor embolization. Formulations containing PG as the cosolvent (CO-19* and CO-21*) resulted in implants that satisfactorily localized in the tumor center and periphery. Similar to the in vitro experiments, these implants displayed a compact and homogeneous microstructure. After 4 days, a mild acute inflammatory response was noted, and implants were not infiltrated.

Depending on the viscosity and precipitation characteristics of the organogel formulation, two intratumoral injection scenarios should be considered: (i) The formulation is fluid, with a maximum viscosity of hundreds of mPa·s. This facilitates the diffusion into the tumor through the smallest free spaces, but with the tendency to reach the surrounding stromas by leaking. Then, the ability to cast these intratumoral free spaces with the forming implant is governed by the time to polymer precipitation. Rapid precipitation allows more implant to cast interstitial spaces of the tumor. (ii) The

formulation is viscous, with a viscosity of a few Pa·s. The diffusion into the tumor is limited to t

largest free spaces found in the center, and not to the smallest peripheral free spaces, thereby precluding leakage. In this case, the homogeneity in implant distribution within the tumor is mainly ruled by precipitation characteristics, with larger delays in precipitation favoring a homogeneous interstitial casting.

4 Conclusion and perspectives

From the in vivo experiments, we learned that vascularized and necrotizing tumors would be the most amenable to the administration of injectable vehicles forming in situ implants for magnetic particle-mediated local hyperthermia. Unfortunately, hydrogel formulations were insufficient for carrying out the proposed application. In our opinion, an important limitation in hydrogel formulation is the need for a high content of magnetic microparticles, which compromises sol-gel transition or mechanical strength of the gel, resulting in unstability of the implant. Despite their toxicity, organogel formulations appeared more suitable than hydrogels for intratumoral injection and implantation. Generally, adequate control of the implant distribution into the tumor center and periphery resulted from a trade-off between high formulation viscosity and rapidity of implant formation. High viscosity and rapid sol-gel transition tended to localize the implant into tumor center or vicinity. The formulation of EVAL 8 % w/v in DMSO with 40% w/v of magnetic microparticles appeared most favorable in view of magnetically induced local hyperthermia of the tumor. Importantly, the mechanical characteristics and microstructure of the implant can be tailored by choosing an appropriate polymer and solvent combination. Cosolvent formulations, despite their limited syringeability due to high viscosity, may offer a more acceptable safety profile than single-solvent formulations. Specific clinical applications, such as embolization of large abnormal vascular structures, may benefit from this approach, paving the way for expanded medical utility. We could also expect improvement in formulations from other

polymers, solvents or types of magnetic microparticles.

5 Acknowledgements

Grant support: Swiss National Science Foundation (grant 3200B0-104508), Switzerland. For sample preparation using a cryomicrotome, we are thankful to Ophélie Patthey-Vuadens (Laboratory of Pharmacology) and for cosolvent formulation work to Danielle Masuelle (Laboratory of Pharmaceutics and Biopharmaceutics), School of Pharmaceutical Sciences, University of Geneva, University of Lausanne, Geneva, Switzerland. For histology processing, we thank Susana Leuba, Department of Pathology, University Hospital of Lausanne, Lausanne, Switzerland.

6 References

[1] Laurent A. Materials and biomaterials for interventional radiology. Biomed Pharmacother 1998; 52(2):76-88.
[2] Jordan O, Doelker E, Rüfenacht D. Biomaterials Used in Injectable Implants (Liquid Embolics) for Percutaneous Filling of Vascular Spaces. Cardiovasc Intervent Radiol 2005; 28(5):561-569.
[3] Gutowska A, Jeong B, Jasionowski MU. Injectable gels for tissue engineering. Anat Rec 2001; 263(4):342-349.
[4] Hand JW, Streffer C, van Beuningen D, Vaupel P, Kallinowski F, Molls M et al. Hyperthermia and the Therapy of Malignant Tumors. Berlin: Springer-Verlag; 1987.
[5] Falk MH, Issels RD. Hyperthermia in oncology. Int J Hyperthermia 2001; 17(1):1-18.
[6] Wust P, Hildebrandt B, Sreenivasa G, Rau B, Gellermann J, Riess H et al. Hyperthermia in combined treatment of cancer. Lancet Oncol 2002; 3(8):487-497.
[7] Chenite A, Chaput C, Wang D, Combes C, Buschmann MD, Hoemann CD et al. Novel injectable neutral solutions of chitosan form biodegradable gels in situ. Biomaterials 2000; 21(21):2155-2161.
[8] Yu L, Ding JD. Injectable hydrogels as unique biomedical materials. Chem Soc Rev 2008; 37(8):1473-1481.
[9] Takao H, Murayama Y, Ebara M, Ishibashi T, Saguchi T, Irie K et al. New thermoreversible liquid embolic agent for embolotherapy: technical report. Neuroradiology 2009; 51(2):95-98.
[10] Matsuura T. Synthetic Membranes and Membrane Separation Processes. Boca Raton: CRC Press Inc; 1993.
[11] Wise DL. Encyclopedic Handbook of Biomaterials and Bioengineering. New York: M. Dekker; 1995.

[12] Terada T, Nakamura Y, Nakai K, Tsuura M, Nishiguchi T, Hayashi S et al. Embolization of arteriovenous malformations with peripheral aneurysms using ethylene vinyl alcohol copolymer. J Neurosurg 1991; 75(4):655-660.

[13] Jahan R, Murayama Y, Gobin YP, Duckwiler GR, Vinters HV, Vinuela F. Embolization of arteriovenous malformations with Onyx: Clinicopathological experience in 23 patients. Neurosurgery 2001; 48(5):984-995.

[14] Gobin YP, Murayama Y, Milanese K, Chow K, Gonzalez NR, Duckwiler GR et al. Head and neck hypervascular lesions: embolization with ethylene vinyl alcohol copolymer - laboratory evaluation in swine and clinical evaluation in humans. Radiology 2001; 221(2):309-317.

[15] Tokunaga K, Kinugasa K, Meguro T, Kawada S, Sugiu K, Nakashima H et al. Embolization of cerebral arteriovenous malformations with cellulose acetate polymer - Histological study of the resected specimens. Interv Neuroradiol 1998; 4(Suppl. 1):117-120.

[16] Tokunaga K, Kinugasa K, Kawada S, Nakashima H, Tamiya T, Hirotsune N et al. Embolization of cerebral arteriovenous malformations with cellulose acetate polymer: A clinical, radiological, and histological study. Neurosurgery 1999; 44(5):981-989.

[17] Tokunaga K, Kinugasa K, Meguro T, Sugiu K, Nakashima H, Mandai S et al. Curative treatment of cerebral arteriovenous malformations by embolisation using cellulose acetate polymer followed by surgical resection. J Clin Neurosci 2000; 7(Suppl. 1):1-5.

[18] Chastellain M, Petri A, Gupta A, Rao KV, Hofmann H. Superparamagnetic silica-iron oxide nanocomposites for application in hyperthermia. Adv Eng Mater 2004; 6(4):235-241.

[19] Chenite A, Buschmann M, Wang D, Chaput C, Kandani N. Rheological characterisation of thermogelling chitosan/glycerol-phosphate solutions. Carbohydr Polym 2001; 46(1):39-47.

[20] Jarry C, Chaput C, Chenite A, Renaud MA, Buschmann M, Leroux JC. Effects of steam sterilization on thermogelling chitosan-based gels. J Biomed Mater Res 2001; 58(1):127-135.

[21] Kuo CK, Ma PX. Ionically crosslinked alginate hydrogels as scaffolds for tissue engineering: Part 1. Structure, gelation rate and mechanical properties. Biomaterials 2001; 22(6):511-521.

[22] Draget KI, Ostgaard K, Smidsrod O. Homogeneous Alginate Gels - A Technical Approach. Carbohydr Polym 1990; 14(2):159-178.

[23] Raymond J, Metcalfe A, Desfaits AC, Ribourtout E, Salazkin I, Gilmartin K et al. Alginate for endovascular treatment of aneurysms and local growth factor delivery. AJNR Am J Neuroradiol 2003; 24(6):1214-1221.

[24] Lacroix M, Leclercq G. Relevance of breast cancer cell lines as models for breast tumours: an update. Breast Cancer Res Treat 2004; 83(3):249-289.

[25] Buchegger F, Adamer F, Schaffland AO, Kosinski M, Grannavel C, Dupertuis YM et al. Highly efficient DNA incorporation of intratumourally injected [I-125]iododeoxyuridine under thymidine synthesis blocking in human glioblastoma xenografts. Int J Cancer 2004; 110(1):145-149.

[26] Martin KW, Halpern SE. Carcinoembryonic Antigen Production, Secretion, and Kinetics in BALB/c Mice and a Nude Mouse-Human Tumor Model. Cancer Res 1984; 44(12):5475-5481.

[27] Halpern SE, Hagan PL, Garver PR, Koziol JA, Chen AWN, Frincke JM et al. Stability, Characterization, and Kinetics of 111In-labeled Monoclonal Antitumor Antibodies in Normal Animals and Nude Mouse-Human Tumor Models. Cancer Res 1983; 43(11):5347-5355.

[28] Povlsen CO, Rygaard J. Heterotransplantation of human adenocarcinomas of colon and rectum to mouse mutant nude. A study of 9 consecutive transplantations. Acta Pathol Microbiol Scand [A] 1971; 79(2):159-169.
[29] Sutherland R, Buchegger F, Schreyer M, Vacca A, Mach JP. Penetration and binding of radiolabeled anti-carcinoembryonic antigen monoclonal antibodies and their antigen binding fragments in human colon multicellular tumor spheroids. Cancer Res 1987; 47(6):1627-1633.
[30] Baxter LT, Zhu H, Mackensen DG, Jain RK. Physiologically based pharmacokinetic model for specific and nonspecific monoclonal antibodies and fragments in normal tissues and human tumor xenografts in nude mice. Cancer Res 1994; 54(6):1517-1528.
[31] de Witte P. Phase behavior of polylactides in solvent-nonsolvent mixtures. J Polym Sci Pt B-Polym Phys 1996; 34(15):2553-2568.
[32] Khulbe KC, Feng CY, Matsuura T. Synthetic Polymeric Membranes. Heidelberg: Springer-Verlag Berlin; 2008.
[33] Mandai S, Kinugasa K, Ohmoto T. Direct thrombosis of aneurysms with cellulose acetate polymer. Part I: Results of thrombosis in experimental aneurysms. J Neurosurg 1992; 77(4):497-500.
[34] Reuvers AJ, Altena FW, Smolders CA. Demixing and Gelation Behavior of Ternary Cellulose-Acetate Solutions. J Polym Sci Pt B-Polym Phys 1986; 24(4):793-804.
[35] Barton BF, Reeve JL, Mchugh AJ. Observations on the dynamics of nonsolvent-induced phase inversion. J Polym Sci Pt B-Polym Phys 1997; 35(4):569-585.
[36] Koenhen DM, Mulder MHV, Smolders CA. Phase separation phenomena during the formation of asymmetric membranes. J Appl polym Sci 1977; 21(1):199-215.
[37] Stropnik C, Musil V, Brumen M. Polymeric membrane formation by wet-phase separation; turbidity and shrinkage phenomena as evidence for the elementary processes. Polymer 2000; 41(26):9227-9237.
[38] Kaiser V, Stropnik C, Musil V, Brumen M. Morphology of solidified polysulfone structures obtained by wet phase separation. Eur Polym J 2007; 43(6):2515-2524.
[39] Taki W, Yonekawa Y, Iwata H, Uno A, Yamashita K, Amemiya H. A new liquid material for embolization of arteriovenous malformations. AJNR Am J Neuroradiol 1990; 11(1-2):163-168.
[40] Yamashita K, Taki W, Iwata H, Nakahara I, Nishi S, Sadato A et al. Characteristics of Ethylene-Vinyl Alcohol Copolymer (Eval) Mixtures. AJNR Am J Neuroradiol 1994; 15(6):1103-1105.
[41] Chung TS, Jiang LY, Li Y, Kulprathipanja S. Mixed matrix membranes (MMMs) comprising organic polymers with dispersed inorganic fillers for gas separation. Prog Polym Sci 2007; 32(4):483-507.
[42] Bohner M Theoretical considerations on the injectability of calcium phosphate cements, Proceedings of the 17th European Conference on Biomaterials, Barcelona, Spain, 2002. p.124.
[43] Bohner M, Baroud G. Injectability of calcium phosphate pastes. Biomaterials 2005; 26(13):1553-1563.
[44] Coussot P, Ancey C. Rhéophysique des pâtes et des suspensions. Les Ulis: EDP Sciences; 1999.
[45] Wang D, Li K, Teo WK. Relationship between mass ratio of nonsolvent-additive to solvent in membrane casting solution and its coagulation value. J Memb Sci 1995; 98(3):233-240.
[46] Landa N, Miller L, Feinberg MS, Holbova R, Shachar M, Freeman I et al. Effect of injectable

alginate implant on cardiac remodeling and function after recent and old infarcts in rat. Circulation 2008; 117(11):1388-1396.

[47] Sampei K, Hashimoto N, Tsukahara T, Kazekawa K, Iwata H, Takaichi S. Histological changes in brain tissue and vasculature after intracarotid infusion of organic solvents in rats. Neuroradiology 1996; 38:291-294.

[48] Dudeck O, Jordan O, Hoffmann KT, Okuducu AF, Tesmer K, Kreuzer-Nagy T et al. Organic solvents as vehicles for precipitating liquid embolics: a comparative angiotoxicity study with superselective injections of swine rete mirabile. AJNR Am J Neuroradiol 2006; 27(9):1900-1906.

[49] Le Renard PE, Buchegger F, Petri-Fink A, Bosman F, Rufenacht D, Hofmann H et al. Local moderate magnetically induced hyperthermia using an implant formed in situ in a mouse tumor model. Int J Hyperthermia 2009; 25(3):229-239.

Chapter 3

Magnetic and in vitro heating properties of implants formed in situ from injectable formulations and containing superparamagnetic iron oxide nanoparticles (SPIONs) embedded in silica microparticles for magnetically induced local hyperthermia .

published in Journal of Magnetism and Magnetic Materials, 323 (2011), 1054–1063

Pol-Edern Le Renard[1], Rolf Lortz[2], Carmine Senatore[3], Jean-Philippe Rapin[4], Franz Buchegger[5], Alke Petri-Fink[6], Heinrich Hofmann[7], Eric Doelker[1], Olivier Jordan[1].

[1]School of Pharmaceutical Sciences, University of Geneva, University of Lausanne, Geneva, Switzerland; [2]Departement of Physics, The Hong Kong University of Science & Technology , Clear Water Bay , Kowloon , Hong Kong; [3]Department of Condensed Matter Physics and MaNEP/NCCR, University of Geneva, Geneva, Switzerland; [4]Laboratory of Crystallography, University of Geneva, Geneva, Switzerland; [5]Service of Nuclear Medicine, University Hospital of Lausanne, Lausanne, University Hospital of Geneva, Geneva, Switzerland; [6]Department of Chemistry, University of Fribourg, Fribourg, Switzerland; [7]Laboratory for Powder Technology, Ecole Polytechnique Fédérale de Lausanne (EPFL), Lausanne, Switzerland.

Abstract

The biological and therapeutic responses to hyperthermia when it is envisaged as anti-tumor treatment modality are complex and variable. Heat delivery plays a critical role and is counteracted by more or less efficient body cooling, which is largely mediated by blood flow. In the case of magnetically mediated modality, the magnetic properties are also critically involved in the delivery of heat. We focus here on the magnetic characterization of two injectable formulations able to gel *in situ* to vehicle and entrap silica microparticles embedding SPIONs, whose syringeability and intratumoral distribution have previously revealed interesting *in vivo*. The first formulation is based on alginate, and the second on a poly(ethylene-co-vinyl alcohol) EVAL. Here we investigate the magnetic properties and heating capacities in an alternating magnetic field (141 kHz, 12 mT) for implants with increasing concentrations of magnetic microparticles. We found that the magnetic properties of the magnetic microparticles were preserved through the formulation and in the wet implant at 37°C, as *in vivo*. Using two orthogonal methods, a common SLP (20 $W.g^{-1}$) was found after weighting by magnetic microparticle fraction, suggesting that both formulations are able to properly bring the magnetic microparticles *in situ* while preserving their magnetic properties and heating capacities.

Keywords

Magnetically mediated hyperthermia; superparamagnetism; SPIONS; microparticles; composite magnetic microparticles; injectable formulations; in-situ forming implant; magnetic properties; SQUID; heating; AMF; specific power loss; calorimetry; pycnometry; laser diffraction; DFX; TEM; SEM

Chapter 3: Table of Contents

1 Introduction....177
2 Experimental details....179
2.1 Magnetic microparticles....179
2.2 Characterization methods....180
2.2.1 Pycnometry and size analysis by laser diffraction....180
2.2.2 X-ray diffraction: XRD....180
2.2.3 Transmission electronic microscopy: TEM....181
2.2.4 Scanning electron microscopy and energy-dispersive X-ray spectroscopy: SEM-EDX 181
2.3 Formulation preparation and in vitro implant formation....181
2.3.1 Liquid formulation preparations....181
2.3.1.1 Polymer solution preparations for the organogel formulation. 181
2.3.1.2 Polymer solution preparations for the hydrogel formulation....182
2.3.1.3 Magnetic microparticle incorporation....182
2.3.2 In situ formation of implants....182
2.4 Superconducting quantum interference device: SQUID....183
2.5 Heating capacities under an alternative magnetic field....183
2.5.1 Alternative magnetic field (AMF) generation and thermometry....183
2.5.2 Method A of SLP determination....185
2.5.3 Method B of SLP determination....186
3 Results and Discussion....188
3.1 Structural properties of the –SPION-silica composite microparticles....188
3.1.1 Size distribution analysis by laser diffraction....188
3.1.2 Particle analysis by TEM 189
3.1.3 Particle analysis by SEM-EDX 190
3.1.4 Crystalline structure by XRD 192
3.1.5 Magnetic properties by SQUID....194
3.2 Magnetic properties of implants (SQUID)....197
3.3 Heating capacities of implants under AMF 200
4 Conclusions....204
5 Acknowledgements....204
6 References....205

1 Introduction

Induced hyperthermia is a recent therapeutic approach in oncology protocols [1]. It consists of raising the temperature of a target tissue or body region affected by local tumor lesions or even heating the whole body in the case of extensively diffuse cancer lesions. These approaches are respectively called local, regional and whole-body hyperthermia [2]. Heat affects multiple and complex biological processes, possibly leading to therapeutic benefits. The direct cell killing effect of heat is observed *in vitro* for temperatures from 42°C, which corresponds to a threshold for cytotoxicity. Above 45°C, tissues directly coagulate. Nonetheless, in unfavorable metabolic microenvironments, such as those found in some tumor areas, the threshold can be observed at lower temperatures that are more easily achievable in clinical practice [3-6]. Heat also modulates tumor blood flow to varying extent and sequence, either positively and/or negatively. The vascular response of the tumor differs compared to basal blood flow and to the vascular response of normal tissue, leading to contrasting deleterious or beneficial therapeutic effects [6,7]. High tumor blood flow impedes heating through high convective heat dissipation. In contrast, low tumor blood flow can favor heat deposition and concentration due to low convection. This may lead to differential blood flow heat dissipation (decreased in tumors while increased in the surrounding tissues) and a resulting rather selective heat deposition in the tumor lesions [2]. The heat shock proteins, which are crucial to the heat shock response, also present ambivalent features [8]. On one hand, heat shock proteins may be associated with some form of thermotolerance [9-12]. On the other hand, heat shock proteins can also facilitate the unmasking of tumor antigens and their presentation, thereby favoring the immune response to cancer. These mechanisms induced by hyperthermia may thus indirectly lead to an increased anti-tumor response [2,13-17]. In clinical practice, hyperthermia is an accepted adjuvant to reference therapies, mainly chemo- and radio-therapies [18-20]. In these approaches, the physiological effects of heat such as the increased blood supply and oxygen levels are decisive [7,21]. To improve heating, numerous techniques have attempted to manipulate the tumor physiology, among which embolization has been revealed to be useful [4]. The technical limitations of the heat delivery and the poor control of the heat dose are also crucial and impede the effective distribution of cytotoxic temperatures and doses in the target volume.

Besides the various physical modalities of delivering heat to solid tumors (infrared, ultrasound, microwave and radio-frequency techniques), the magnetically induced hyperthermia modality is specifically based on heat dissipation through an interaction with the magnetic component of an alternative magnetic field [22,23]. This can be mediated by eddy currents, which dissipate heat in a metallic stent. However, the drawback is that this may lead to the adverse burning of the subcutaneous fat layer. Heating induction can be further mediated by the magnetic relaxations of so-called magnetic seeds [24]. Even at locations deep within the body, tissue areas enclosing magnetic seeds can be heated [25]. Two heating processes are possible. Large ferro- or ferri-magnetic particles dissipate heat through hysteresis effects in the form of domain wall motion, also called hysteresis losses [25-27]. Superparamagnetic nanoparticles allow heating through Brownian or Néel magnetic relaxation [28-32]. As for the latter, the negligible dipole-dipole magnetic interactions with coated particles (the coatings prevent surface interactions) allow for the safe injection in human bodies without the risk of adverse aggregation [33]. Regarding the biocompatibility, coated superparamagnetic iron oxide nanoparticles (SPIONs) are approved for human use [34]. Entrapping SPIONs in silica microparticles leads to superparamagnetic seeds with three advantages: i) inter-particle coupling through SPION-dipole interactions is avoided; ii) intrinsic superparamagnetism, i.e., Néel relaxation, is favored and iii) the rheological behavior of the microparticles incorporated into the liquid formulations allows for high syringeability. We previously developed formulations incorporating these (SPION)-silica composite microparticles on the basis of embolizing formulations. Although it is liquid before injection, the vehicle converts into a solid matrix in the injected tissue, forming a so-called implant that entraps the microparticles [35]. With this confined in the solid tumor, we can demonstrate the efficiency of heating in an animal model and the potential for local hyperthermia associated with such a formulation [36]. As for magnetically induced hyperthermia modalities, heating primarily relies on the magnetic properties of the injected materials. From a pharmaceutical standpoint, it is important to ensure the preservation of the magnetic properties in the final implant as well as the heating capacity under an alternating magnetic field. In the present work, we therefore characterized by means of a Superconducting Quantum Interference Device magnetometer (SQUID) the static magnetic properties of the SPION-silica composite microparticles and of the implants formed under conditions mimicking the in vivo

environment. Heating capacity was measured through power losses under alternating magnetic field., These characterizations were performed with increasing magnetic microparticle concentrations in the implants.

We focused these investigations on two formulations that had previously demonstrated high syringeability and proper intratumoral distribution, both essential criteria for therapeutic use [35]. One was based on alginate hydrogels that were cross-linked by co-injectable Ca^{2+}. The other formulation was based on a water insoluble polymer (poly(ethylene-co-vinyl alcohol), EVAL) organogel formed *in situ* through precipitation after organic solvent exchange with water.

2 Experimental details

2.1 Magnetic microparticles

Silica micron-sized particles embedding SPIONs were synthesized as previously described [37], noting that the batch used here differ from the batch used in chapter 2. Briefly, organic precursors of silica and iron chloride were mixed. The sol-gel precipitation of silica was triggered by soft heating. Then, iron oxide precipitation was carried out, and the sol-gel porosity helped the nucleation of iron oxide in the expected magnetite phase, which was black. Thereafter, a second heating at a higher critical temperature (800°C) ensured magnetite phase (black color bulk) oxidation to form the ferrimagnetic maghemite phase (tetragonal cell unit, red-brown color bulk), which could be considered as fully oxidized magnetite (c.a. $2Fe_3O_4 + 0.5O_2 \rightarrow 3\gamma Fe_2O_3$ [38]), while preserving maghemite from further transformation into hematite (αFe_2O_3, rhombohedral and canted ferromagnetic of red color bulk) [39]. The bulk maghemite-silica composite matrix resulting from this process was then grinded to form microparticles. A first coarse powder was obtained by ball milling. This coarse powder was then submitted to wet attrition to obtain a finer powder made of microparticles. A visual inspection of the resulting microparticles by eye and under microscope showed a reddish-brown color, more reddish than the bulk reference color, with respect to the color plates in Ref. [40]. With this reference, and further taking into account the variation of color with particle size, the slightly reddish-brown color of our

powder likely excludes the possibility of magnetite. In contrast, commercial samples made of a similar silica matrix containing nanoscaled crystallites of magnetite (as confirmed by X-ray) display a black color very close to the black color of bulk magnetite [40]. These organoleptic characteristics likely exclude the possibility that our microparticles contain nanoscaled magnetite crystallites. Finally, this magnetic seed powder contained 19.6 % iron oxide by mass, as determined by red-ox titration after silica matrix dissolution under acidic conditions.

2.2 Characterization methods

2.2.1 Pycnometry and size analysis by laser diffraction

We used a Helium pycnometer Accupyc 1330 (Micromeritics, Aachen, Germany) to determine the magnetic microparticle density and specific volume. Calibration and sample measurements were performed in a high accuracy mode. The size distribution of the microparticle powder sample dispersed in water was measured by laser diffraction with a Mastersizer apparatus (Malvern, Worcestershire, UK). We set the particle density to 2.39 (as previously determined by pycnometry determination). The microparticle refractive index (1.67) was calculated by the weight ponderation of the refractive index sol-gel silica microsphere (1.42; [41]) and maghemite (2.69) that compose the particle. An imaginary part (0.1) of the refractive index that corresponds to 10 % absorption was set according to instrument guidelines, given the opaque brown color of the raw powder sample by eye. The refractive index of the dispersion medium, i.e., water, was set at 1.33. The powder sample was added under stirring in the module dedicated to wet sample analysis, typically at 900 rpm, up to an opacity degree of about 20 % (corresponding volume concentration of 0.014 %).

2.2.2 X-ray diffraction: XRD

Samples were examined by XRD with a BRUKER D8 diffractometer using cupper $K_{\alpha 1}$ radiation (λ = 1.54056Å). Diffractograms were recorded in the range of $10<2\theta<100$ with a step of 0.014°, and the total data collection time was approximately 12 hours. Data were analyzed using the FullProf Suite [42].

2.2.3 Transmission electronic microscopy: TEM

Formvar-coated grids were made hydrophilic by residual gas ionization. Magnetic microparticles were suspended in water at 1% w/V and vigorously shaken, and 5 µL were allowed to deposit on the grid for 30 sec before removing the excess of suspension. The observations were performed using a Tecnai G2 TEM (FEI, The Netherlands), with a LaB_6 cathode, at 160 kV.

2.2.4 Scanning electron microscopy and energy-dispersive X-ray spectroscopy: SEM-EDX

Magnetic microparticles were coated by the sputter deposition of gold under 0.05 mbar of Argon for 5 min at a 10 mA current intensity. The SEM was a LEO 438 (Zeiss Carl, France). The module for EDX analysis was from Gloore Instrument AG (Switzerland).

2.3 Formulation preparation and *in vitro* implant formation.

2.3.1 Liquid formulation preparations

2.3.1.1 *Polymer solution preparations for the organogel formulation.*

A poly(ethylene-co-vinyl alcohol) (EVAL E-105 B Europe, Zwijndrecht, Belgium) with 44 mol % ethylene (ensuring flexibility) that is clinically used for embolization (Onyx®), was dissolved at 8 % w/V in dimethyl sulfoxide (DMSO, Acros Organics, Basel, Switzerland) at 50°C, as for formulation O-15 in chapter 2. The density was measured using a Mohr's balance, $d^{24\,°C}_{H_2O,\,0\,°C}$ = 1.11089. The magnetic composite silica microparticles were suspended using vigorous vortexing and sonication. Reminding that microparticle batch used here differs from particle batch used in chapter 2, the formulation incorporating 40% w/V of microparticles here, could be compared with formulation O-15* of chapter 2.

2.3.1.2 Polymer solution preparations for the hydrogel formulation

Low viscosity sodium alginate (Fluka, Buchs, Switzerland, 100 to 200 mPa.s for 1 % aq, 65-75 % glucuronic acid, corresponding to standar grade alginate described in chapter 2) was dissolved in ultrafiltrated water at 2 % w/V (as for formulations free of particles H-17 to 22, more precisely H-21 with regards to the $CaCl_2$ solution used for gelation: 25 mM, as described below). The density was measured using a Mohr's balance at 23°C, $d^{23\,°C}_{H_2O,0\,°C}$ = 1.01775. The magnetic composite silica microparticles were suspended using vigorous vortexing and sonication (reminding that particle batch and gelation's conditions slightly differ from those of chapter 2, the formulation incorporating 20 % w/V of microparticles here could be compared with formulation H-27* of chapter 2).

2.3.1.3 Magnetic microparticle incorporation

Hydrogel and organogel formulations were labeled as H-xx and O-xx, respectively, where the number xx refers to the mass percentage of the magnetic microparticles added to a given volume of liquid polymer solution, i.e., 5, 10 20, 40, 60, 80 and 100 % w/V. The mass fractions will constantly be restated for clarity, but attention should be paid to the system considered: liquid implant formulation before gelation or wet implant after gelation.

2.3.2 *In situ* formation of implants

All implants were prepared *in vitro*, mimicking the *in vivo* injection intended for the treatment of soft tissue solid tumors. The syringe and the receiving flask were weighted to quantify the experimental variation and allow for reliable composition determination. For full settling, we let the implant rest for 5 h in the flask after injection. The hydrogel formulation based on alginate was injected in a solution of $CaCl_2$ (Fluka, Buchs, Switzerland) at 25 mM in ultra-filtrated water. This acceptably mimics the *in vivo* co-injection, during which mixing with the ionic cross-linker (Ca^{2+}) solution occurs within the needle, not *in situ*. This allows for a more accurate determination of the injected masses. The organogel formulation was injected in water, allowing polymer precipitation and magnetic silica microparticle

entrapment to form *in situ* in the implant. A 27 G needle was used for microparticle concentrations below 40 % w/V, and a 19 G was used upon reaching this concentration. The uncertainty in the implant mass, measured by weight loss of the syringe, in parallel with the weight gain of the receiving flask, was below 0.8 % when comparing the mass of the harvested soaked implant. The resulting *in situ*-formed implants were harvested, excess liquid was drained while preserving the soaked state, and this was submitted for further magnetic characterization after weighing.

2.4 Superconducting quantum interference device: SQUID

Magnetic properties were characterized using a Superconducting Quantum Interference Device (SQUID), model MPMS2, Quantum Design, INC (San Diego CA, USA). We investigated the magnetic properties of the implants in a field and temperature range relevant for their clinical use, at 310 K (matching physiologic body temperature at 37°C), and between -39.8 to 39.8 $kA \cdot m^{-1}$ (-500 to 500 Oe), which may appear limited compared to other fundamental studies, but it more closely reflects the 0 – 9.55 $A \cdot m^{-1}$ (0 – 120 Oe) range that is acceptable for hyperthermia treatment. Soaked implants were sealed in a sample holding tube so that soaking was preserved. Control powder was sealed dry in a sample holding tube. The details of the sample compositions are shown in Table 3.1. The symmetry of the *M-H* loop was adjusted by subtracting Xoffset, corresponding to the remnant field from the magnetic field strength (*H*). The diamagnetic background was deduced by dividing the magnetization value (*M*) by the slope of the end region of the curve showing no hysteresis.

2.5 Heating capacities under an alternative magnetic field

2.5.1 Alternative magnetic field (AMF) generation and thermometry

The field generator (TIG 2.5, Hüttinger Elektronik GmbH, Freiburg, Germany) consisted of an alternating current generator feeding the coil inductor (the internal and external diameters and length of the horizontal coil were 54, 64 and 46 mm, respectively). With a small pick-up coil calibrated using a

Table 3.1: Sample details concerning the magnetic characterization by SQUID

Formulation	Constituting polymer in the mother solution	Polymer mass fraction in the mother solution	Polymer mass fraction in the liquid implant formulation	Magnetic microparticle mass fraction in the liquid implant formulation	Average mass of the liquid formulation injected for implantation (g)	Uncertainty in the average liquid formulation injected (mass %)	Weight of the wet implant sample introduced in SQUID (g)
O-05	EVAL	0.069	0.066	0.044	0.140	0.788	0.091
O-10	EVAL	0.069	0.063	0.083	0.156	0.383	0.105
O-20	EVAL	0.069	0.058	0.154	0.153	0.655	0.117
O-40	EVAL	0.069	0.050	0.265	0.159	0.880	0.134
O-60	EVAL	0.068	0.045	0.335	0.206	4.285	0.173
O-80	EVAL	0.068	0.042	0.379	0.256	0.063	0.219
O-100	EVAL	0.069	0.038	0.452	0.209	NA	0.201
H-05	Alginate Na	0.020	0.019	0.049	0.112	3.723	0.074
H-10	Alginate Na	0.020	0.018	0.088	0.125	5.101	0.100
H-20	Alginate Na	0.020	0.017	0.165	0.224	0.727	0.173
H-40	Alginate Na	0.020	0.014	0.281	0.155	1.540	0.148
H-60	Alginate Na	0.020	0.013	0.357	0.278	0.198	0.277
H-80	Alginate Na	0.020	0.011	0.451	0.232	4.731	0.245
H-100	Alginate Na	0.020	0.011	0.461	0.186	0.344	0.197
C	Weight of powder sample introduced in (g):						0.008

Legend: NA: not applicable

teslameter, we found a linear relationship between the magnetic field amplitude at 141 kHz and the generator peak-to-peak voltage. The current intensity was adjusted to impose the voltage corresponding to a 12-mT induction. The sample placed in a cylindrical plastic holder (0.4 cm in diameter and 3 cm in height) was isolated from the surroundings by a polystyrene foam chamber fitted within the coil. The surface temperature of the sample was monitored with a fluoroptic thermometer (Luxtron, Santa Clara CA, USA) using 200-µm diameter fiber optic probes. The device reported temperatures once every second with a 0.1-°C accuracy. A one-point calibration at 20.0 °C was performed. Data were acquired using Physitemp software (Luxtron, Santa Clara CA, USA). The implants were prepared as described in section 2.3.2. With this, we determined the specific loss power (SLP) by two methods: Method A and Method B.

2.5.2 Method A of SLP determination

The wet implant was placed in an insulated tube. The thermometric probe was inserted into the implant periphery. The tube was placed within the coil for magnetic induction by AMF. Experiments were performed in triplicate, except for H-40, for which only duplication was realized. We switched on the generator at t = 0 s. We recorded the temperature from t = 0 to at least t = 60 s. The derivative of the temperature by time (°C/s) was smoothed by the moving averaged widow method on five points. We then determined the maximum of this derivative occurring within the first 20 seconds. This maximum was considered to be the best approximation of the "adiabatic" specific heat losses of the boundary conditions. We then calculated the corresponding heat rate. For this, we neglected the polymer mass fraction within the wet sample (this is already low in the formulation, and it decreases with increasing magnetic microparticle fraction and after implant formation in water, with a mean polymer mass fraction in wet implants of 0.38 ± 0.36 %). We took into account the silica (SiO_2) mass present in the sample, as determined by injection weighing. Although negligible at low concentrations such as 5 % w/V, this fraction is of increasing importance in concentrated formulations. In the same way, we took into consideration the iron oxide (Fe_2O_3). Finally, the most important constituent to contribute to the heat capacity of the whole implant was the water (H_2O) mass present in the sample, which was

determined by desiccation. The standard (i.e., at 25°C) heat capacities in $J.K^{-1}.g^{-1}$ were 0.739, 0.651 and 4.18 for SiO_2 , Fe_2O_3 and H_2O, respectively. Method A thus allowed us to calculate the total heat production rate and the specific loss power (SLP) as normalized to the weight of the iron oxide, in W/g of iron oxide. For the method A, SLP was calculated according to equation 3.1.

$$SLP_{method\,A} = \frac{C_{SiO_2} \cdot m_{MP} \cdot (1 - x_{IO}) + C_{Fe_2O_3} \cdot m_{MP} \cdot x_{IO} + C_{H_2O} \cdot m_{WL}}{m_{MP} \cdot x_{IO}} \frac{n}{\sum_{i=1}^{i=n} \left[\frac{1}{\left(\frac{dT}{dt}\right)_s^*} \right]} \qquad \textit{Equation 3.1}$$

where:

- $SLP_{method\,A}$ is the specific loss power of implant (heat dissipated by the implant divided by iron oxide content) as determined by method A.
- T is the temperature
- t is the time
- C_{SiO_2} is the specific heat capacity of silica (0.739 $J \cdot K^{-1} \cdot g^{-1}$).
- m_{MP} is the exact mass of silica nanocomposite magnetic microparticles as calculated from Table 3.3 and 3.4.
- x_{IO} is the iron oxide fraction (0.196).
- $C_{Fe_2O_3}$ is the specific heat capacity of magnetite (0.651 $J \cdot K^{-1} \cdot g^{-1}$).
- C_{H_2O} is the specific heat capacity of water (4.18 $J \cdot K^{-1} \cdot g^{-1}$), that mainly compose the implant phase external to magnetic microparticles (heat capacity of the polymer has been neglected because of its small value and fraction).
- m_{WL} Is the mass of water in the implant determined by water loss calculated from Table 3.3.
- $\frac{n}{\sum_{i=1}^{i=n} \left[\frac{1}{\left(\frac{dT}{dt}\right)_s^*} \right]}$ is the mean initial implant heating rate (see Figure 3.6). It is the harmonic mean of maximum in the smoothed derivative of the temperature (T) as function of time (t) determined for n measurement (n = 3, except for H-40 for which n = 2; smoothing applied: 5 point moving average).

2.5.3 Method B of SLP determination

This method was adapted from Bretcanu et al [43]. It consisted of placing the wet implant, formed *in vitro* as previously described but with an adapted size, into an insulated vial in contact with 4 mL of additional water. This vial was then placed in the coil of the AMF inducer, to be submitted to a 2-min

AMF induction. The initial temperature was recorded. After the 2-min AMF induction, the final temperature was determined, with the vial rapidly shaken to ensure a homogeneous heat distribution. This allowed us to determine the ΔT of water during 2-min of heating by AMF induction, which is relevant for the *in vivo* conditions, where the solid tumor tissues can be approximated by certain water volumes. Here, because the major mass fraction in the system is water, which has the highest heat capacity, the other components of the implant can be neglected for calorimetric considerations. For the method B, SLP was calculated according to equation 3.2.

$$SLP_{method\ B} = \frac{C_{H_2O} \cdot (m_{WL} + m_{WA})}{m_{MP} \cdot x_{IO} \cdot t_{120}} \frac{n}{\sum_{i=1}^{i=n} \frac{1}{\Delta T}} \qquad \textit{Equation 3.2}$$

where:

- $SLP_{method\ B}$ is the specific loss power of implant (heat dissipated by the implant divided by iron oxide content) as determined by method B.
- C_{H_2O} is the specific heat capacity of water (4.18 $J \cdot K^{-1} \cdot g^{-1}$), in the phase external to magnetic microparticles, heat capacity of the polymer has been neglected because of its small value and fraction.
- m_{WL} is the mass of water in the implant determined by water loss calculated from Table 3.5.
- m_{WA} is the exact mass of water added with implant in the calorimeter (target mass 4 g, i.e. about 4 times implant weight).
- m_{MP} is the exact mass of silica nanocomposite magnetic microparticles as calculated from Table 3.3 and 3.5.
- x_{IO} is the iron oxide fraction (0.196).
- t_{120} is the time during which the system is warmed by magnetic induction and ΔT, the increase in temperature , is recorded, here 120 seconds.
- $\frac{n}{\sum_{i=1}^{i=n} \frac{1}{\Delta T}}$ is the harmonic mean of the increase in temperature *T*, for *n* = 3 measurements.

3 Results and Discussion

3.1 Structural properties of the SPION-silica composite microparticles

The densities of hematite, magnetite and maghemite are 5.26, 5.18 and 4.87 ($g.cm^{-3}$), respectively [39]. The density of the particles determined by pycnometry was 2.391 ± 0.001 $g.cm^{-3}$, i.e., a specific volume of 0.418 ± 0.002 $cm^3.g^{-1}$. The powder discharge density, i.e., the bulk powder specific volume, was roughly 0.3329 g/cm^3. This corresponds roughly to the intra- plus extragranular porosity of the discharged powder, i.e., the uncompressed powder, of 84 %.

3.1.1 Size distribution analysis by laser diffraction

The powder dispersion in the water analysis by laser diffraction revealed a mean diameter Dv(0,5) of 23.6 µm and a partially overlapping bimodal size distribution, as shown in Figure 3.1. The size distribution corresponding to the first mode, which can be considered as log-normal or normal, is characterized by a large span and is centered around a volume diameter of 10 µm. The size distribution corresponding to the second mode appears to be log-normal, sharper and centered on a volume diameter of 40 µm. Accurate measurement requires rapid stirring above 900 rpm, i.e., well above the 300-rpm threshold at which sedimentation hinders the 40-µm mode subpopulation. This bimodal distribution likely results from the two-step attrition processes of the bulk composite matrix leading to these microparticles. The first step, consisting of milling, leads to particles with diameters corresponding to the largest mode. The second step, a wet attrition, reduces the resulting coarse powder yield to the finest particles corresponding in diameter to the first observed mode.

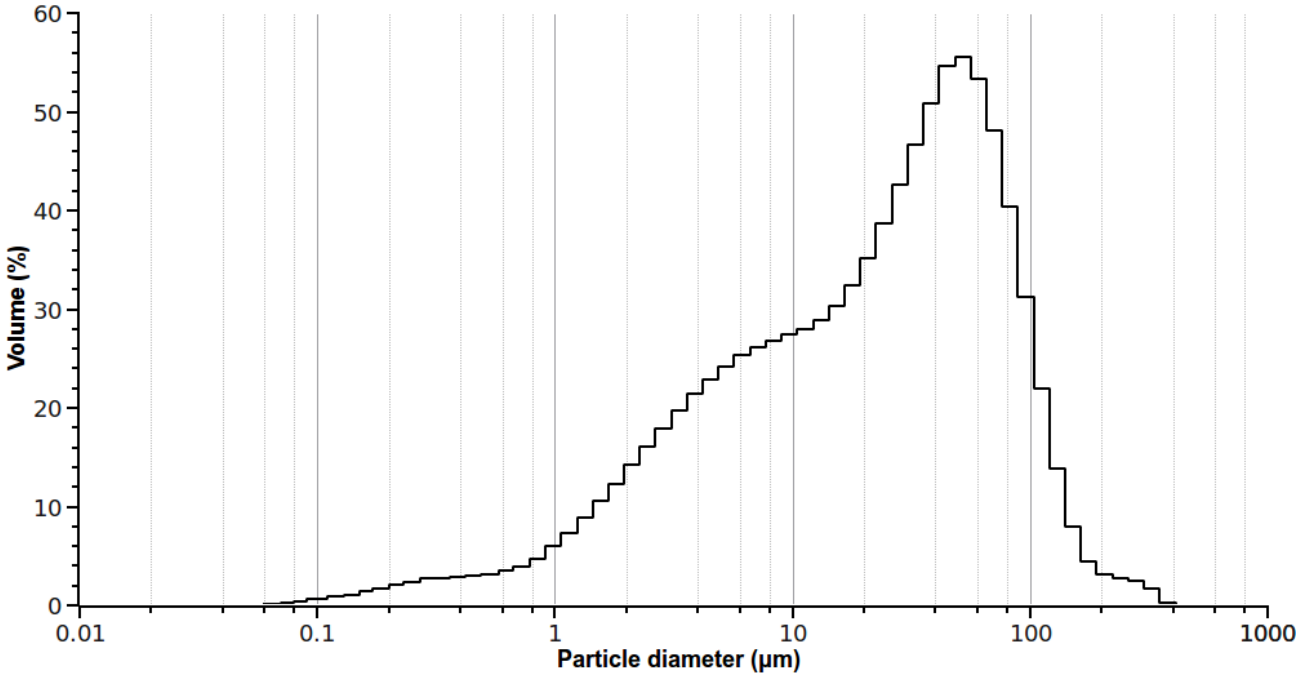

Figure 3.1: Size distribution of our particle powder sample by laser diffraction in a water dispersion. The stirring speed applied here was 960 rpm. A lower stirring speed may hinder the second-mode population (centered at 40 µm) by sedimentation of the largest particles.

3.1.2 Particle analysis by TEM

The observations of the magnetic microparticles by transmission electron microscopy are illustrated in Figure 3.2. The silica matrix is of intermediary electrodensity. The areas of lowest electrodensity correspond to voids, confirming the previously discussed porosity and suggesting the microporosity, and partially mesoporosity, well-known for the sol-gel preparation method. SPIONs of the highest electrodensity appear to be trapped in the mesopores. This confirms the role for mesopores in controlling nucleation and growth during subsequent thermal treatment

.

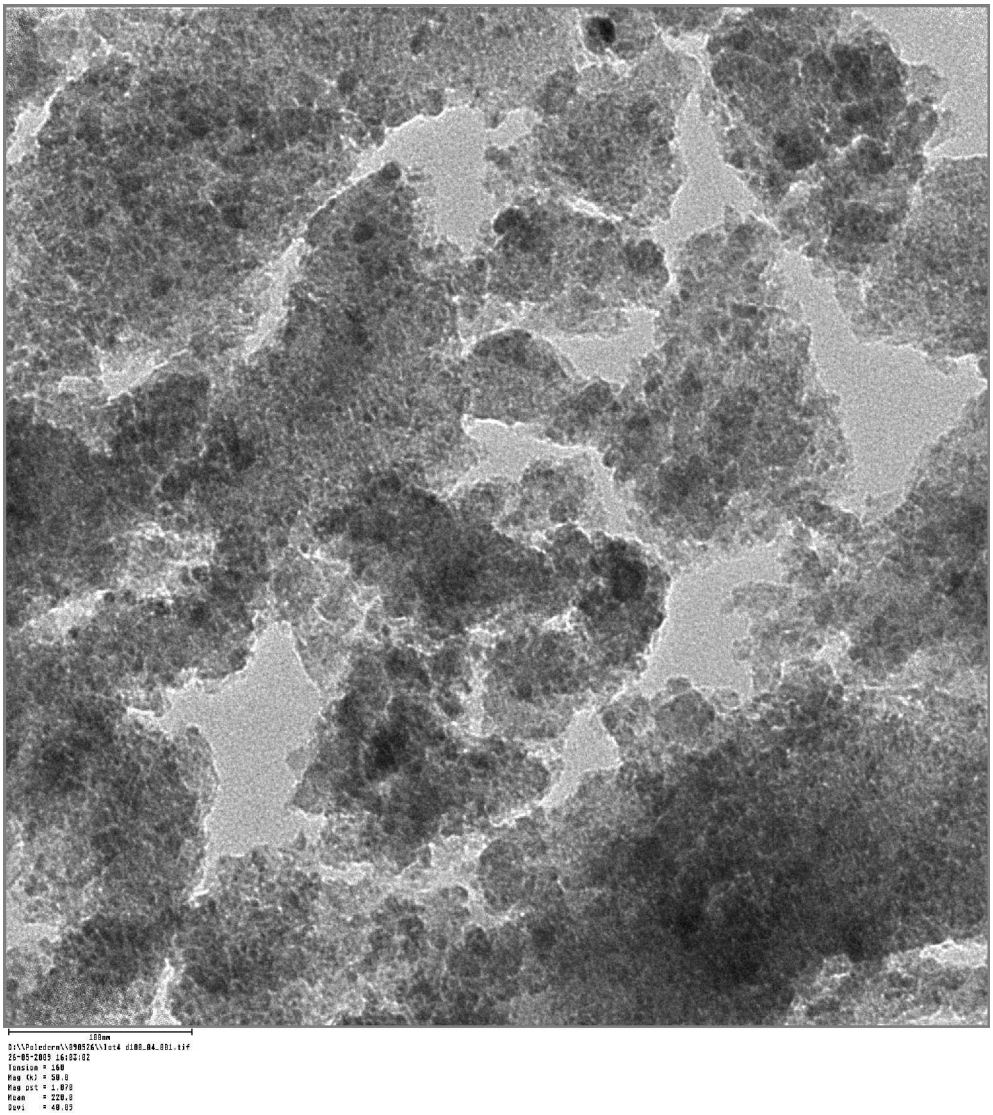

Figure 3.2: Transmission electron microphotograph of magnetic microparticles used as magnetic seeds for heating under AMF.
The microparticles consist of SPIONs of high electrodensity (dark spots) entrapped in a silica matrix of lower electrodensity (gray areas surrounding the dark spots). The lightest gray areas correspond to voids.

3.1.3 Particle analysis by SEM-EDX

High-magnification observations of a powder sample of magnetic microparticles by scanning electron microscopy are illustrated in Figure 3.3. One-micrometer microparticles can be discerned. These

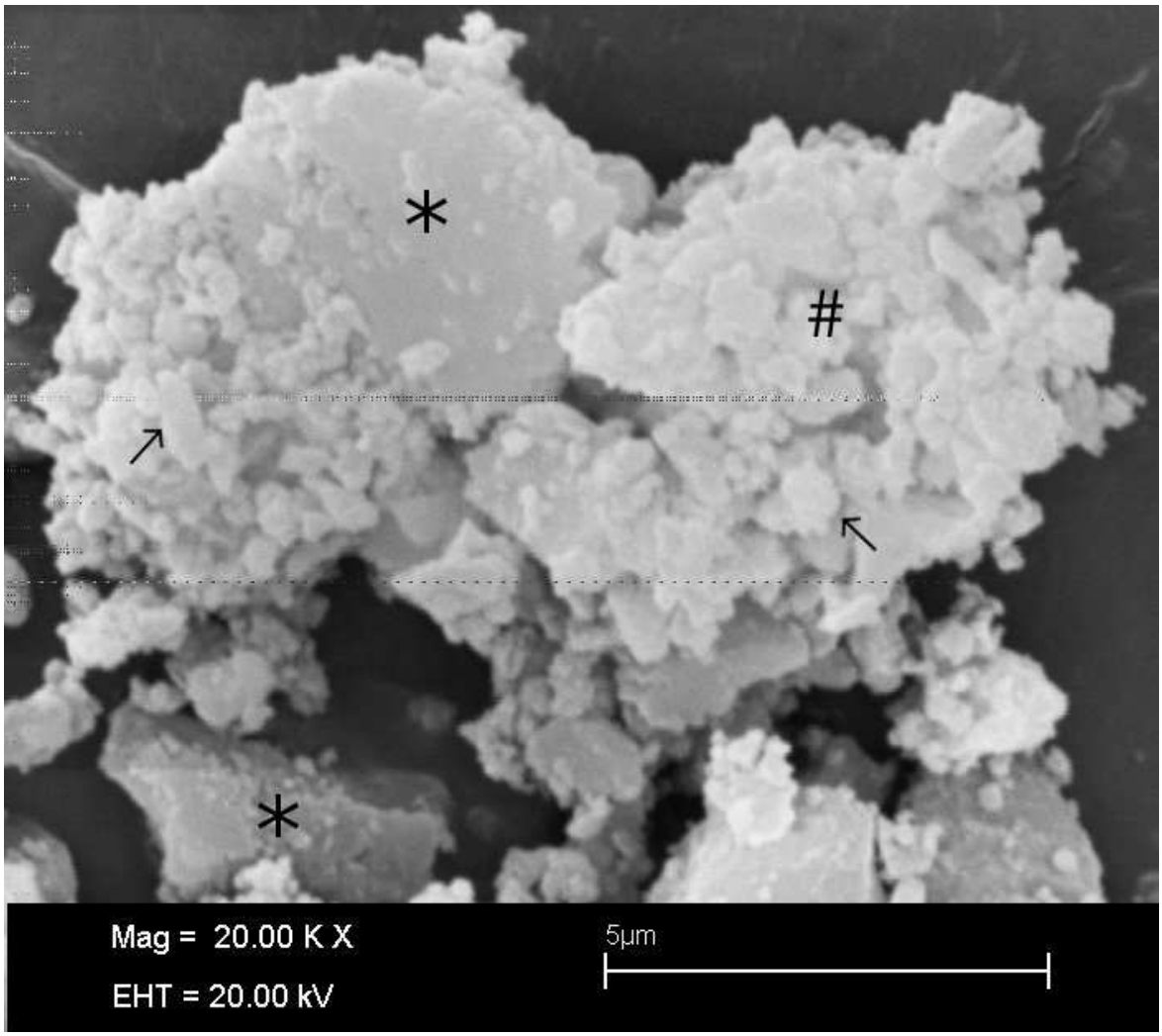

Figure 3.3: SEM image illustrating the characteristics of the magnetic seed powder samples prepared by milling bulk nancomposite and magnetic matrix followed by wet attrition.
The arrows indicate two particles of a numerous subpopulation with diameters in the range of 1 µm, as expected from the last step of wet attrition. These microparticles agglomerate into larger rough structures with sizes ranging from 5 to 10 µm (# mark). These aggregates are likely reversible and are not expected to be found upon dispersion in liquids, which notably contain polymers able to act as surfacting agents. The star marks indicate large structures with largest dimensions of 5 to 10 µm but with smooth facets and regular edges by contrast.

microparticles tend to aggregate in the dry powder sample. The larger rough structures, ca. 10 µm, are likely reversible aggregates of microparticles. These reversible aggregates could, to some extent, widen the volume diameter distribution of the first-mode particle subpopulation observed by laser diffraction

size analysis. In contrast, the smooth larger structures with regular edges (ca. 10 μm) could correspond to subsisting milled particles, as already evoked above. With regard to particle size, one should keep in mind that Energy-dispersive X-ray spectroscopy, EDX, allows for the analysis of the electronic transition occurring after incident electrons have interacted with the atoms of the sample (roughly one micrometer in depth from the sample surface) and caused an atom electron to be ejected. When an electron of the K-layer is ejected, an electron of the L-layer replaces this electron and produces a Kα-Xray that is specific to the atom. The calculation of the iron oxide content based on the hypothesis of sole Fe_2O_3 and SiO_2 compounds leads, for a representative point, to an iron oxide proportion of 23.7 +/- 0.1 %, close to that found by redox titration (19.6 %). Other points revealed highly oxidized compounds that could not be analyzed.

3.1.4 Crystalline structure by XRD

The X-ray powder diffractogram of magnetic microparticles is shown in Figure 3.4. The rise in intensity at small angle (from 2θ values of 10 to 25 °C) is typical of the amorphous silica phase. Analyzing the Bragg position of the reflexions, two structural models for Fe_xO_y could fit the obtained data: magnetite and maghemite. Because the crystallinity of the present sample does not reach the large levels of bulk samples, Rietveld refinement performed with both structural types cannot determine with certainty which model is the correct one, even if the maghemite one fits slightly better (Figure 3.4). Of note, the peak intensity is relatively low and appears limited compared to the background with respect to bulk maghemite. This could be ascribed to the nanometric scale of the maghemite crystallites within the silica matrix. This could also partly be explained by the presence of a fraction of amorphous iron oxide phase, which is probably limited to the surface layer at the boundary of the crystallite lattice.

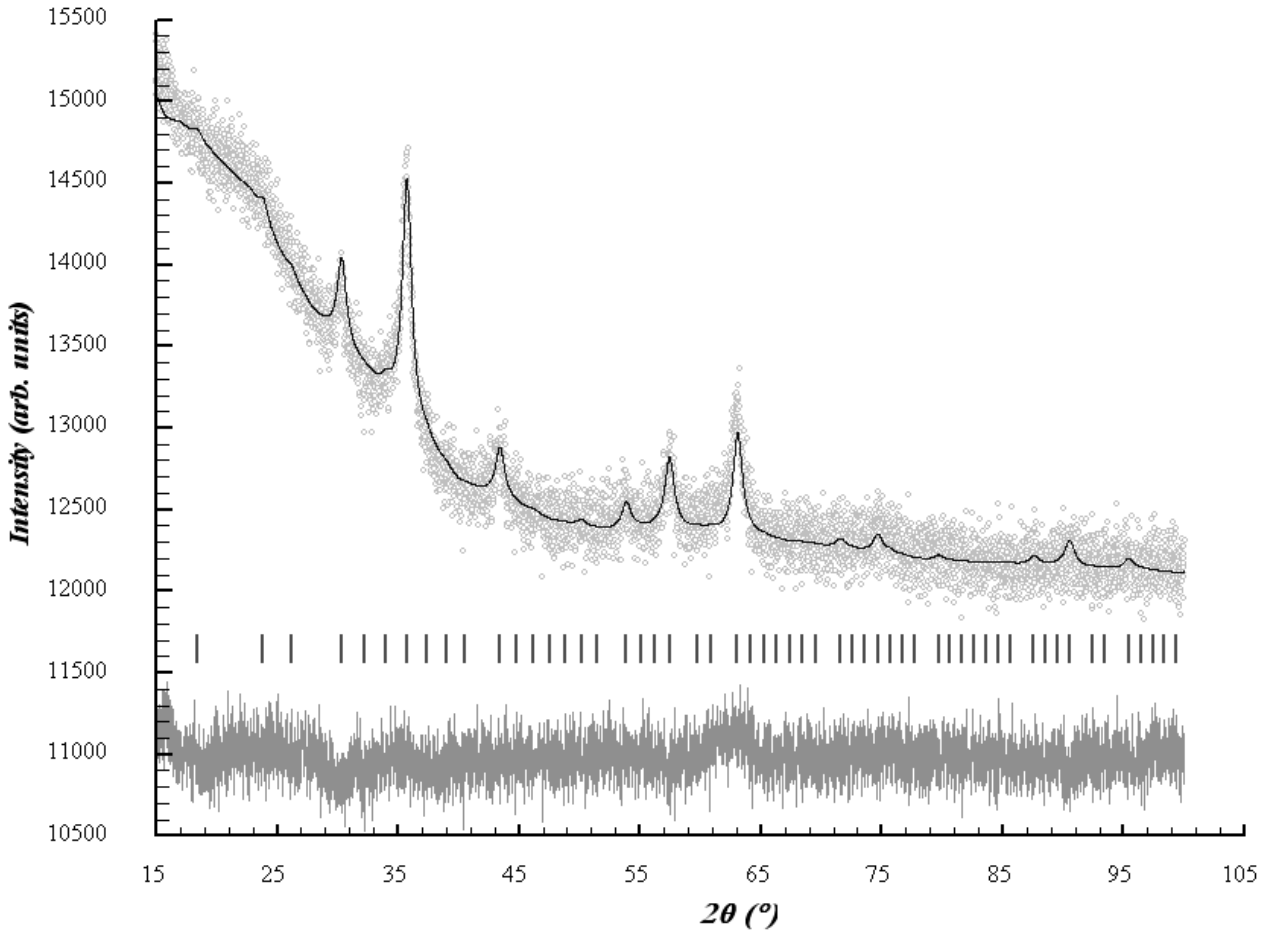

Figure 3.4: X-ray powder diffraction characterization. The observed intensity of diffraction by the magnetic microparticle powder is depicted by the open light gray circles (upper). The diffractogram calculated using Rietveld refinement for maghemite with Fullprof [42] is superimposed as the continuous black line. Reference 2θ values corresponding to Bragg diffraction rays for maghemite are displayed as dark gray vertical bars below (middle). The difference between the observed and calculated values of diffraction intensity is displayed below in the lighter gray line.

3.1.5 Magnetic properties by SQUID

The measurement of bulk magnetic microparticle powder samples gives the typical curve of a soft magnetic material displayed in Figure 3.5 [44], with low coercivity (H_C ~ 273.7 $A \cdot m^{-1}$, 3.44 Oe) and retentivity (B_R ~$1.2 \cdot 10^{-1}$ $A \cdot m^2 \cdot kg^{-1}$or emu per gram) of the magnetic seeds. Of note, in the case of soft magnetic materials, the difference between the intrinsic coercivity and the coercivity is negligible. Also, the gray dashed straight line in Figure 3.5 reflects the slope of the curve after hysteresis closure. This slope is classically described when saturation is reached during a hysteresis measurement, i.e., for a major hysteresis curve. For large magnetic fields, the hysteresis closes, and the magnetic induction, B, and the magnetization, M, are saturated (the saturation induction, B_S should be distinguished from saturation magnetization M_S). M is then constant. The linear increase in the induction, B, is then explained as the partial conversion of the magnetic field H into B. Nevertheless, because of the superparamagnetic behavior and with regards to the literature, it is worth pointing out the possibility that saturation is not effectively reached here and considering that such characteristics can be displayed by minor hysteresis curves in this specific case. Classically, the slope of $dB/dH = \mu_r \cdot \mu_0 = \mu$ tends beyond B_S toward μ_0 in SI units or 1 in cgs units, as the permeability μ(cgs) or μ_r(SI) approaches unity as H approaches infinity. However, the slope of the line beyond hysteresis closure does not normally appear to be unity because the B and H scales are quite different [38]. Permeability can be evaluated in our case to have a value of 0.32 per kg of magnetic seeds in the SI system or $3.87 \cdot 10^{-3}$ per gram of magneticseeds in the cgs system. Furthermore, in our case, a conjunction of the contributions of the diamagnetic silica matrix and the paramagnetic contributions of the iron oxide phase itself could enter the signal. We opted for the deduction of this permeability component to focus on the intrinsic induction (also called ferric induction) of the magnetic microparticles and to attain M. This results in the dashed hysteresis loop of Figure 3.5. This procedure does not change B_R (and M_R) and only raises the value of the still very low coercive field to $307 \cdot A \cdot m^{-1}$ (3.86 Oe). Within the model of fundamental studies but with respect to a much more limited field range, this hysteresis loop thus evidences a saturation of the ferrimagnetic phase, apparently at a field larger than 23.9 $kA \cdot m^{-1}$ (300 Oe). It is first important to note that saturation will thus never be reached in the clinical range of 0 – 9.5 $kA \cdot m^{-1}$ (0 –

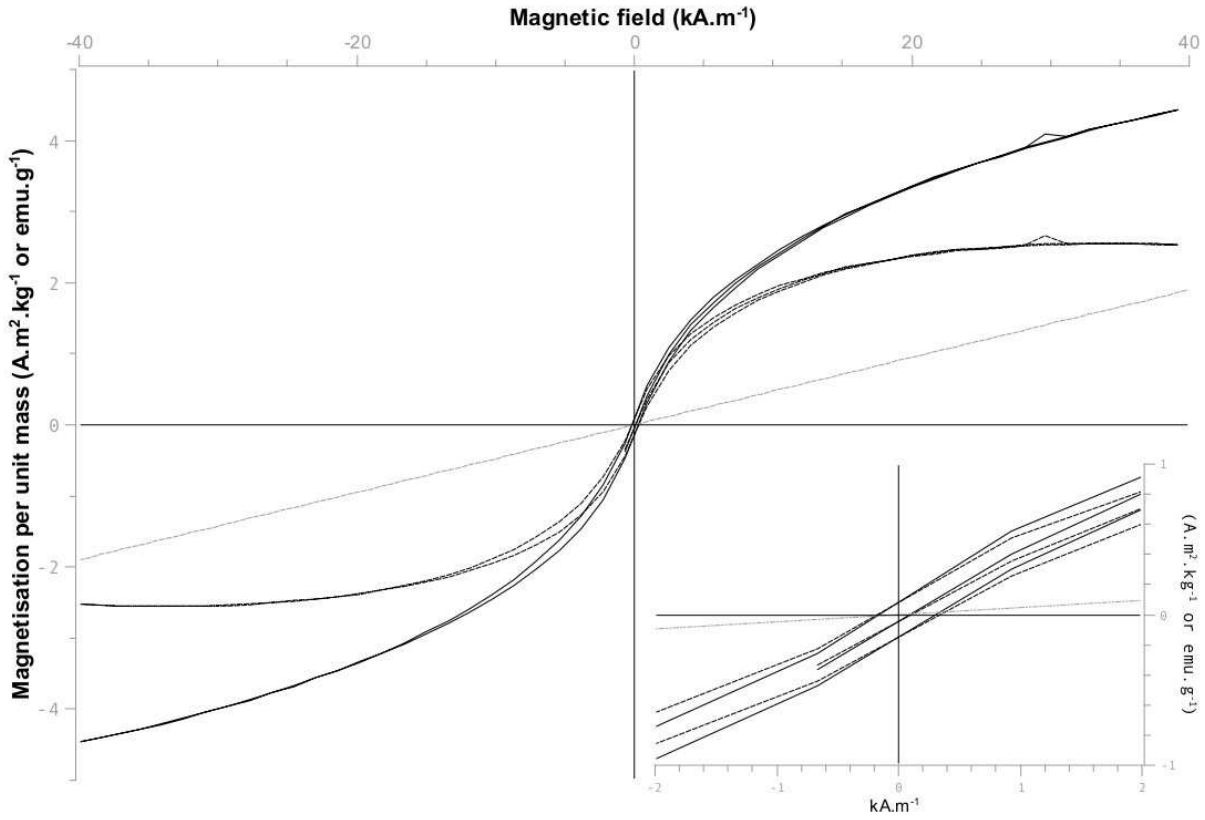

Figure 3.5: Magnetization curve of raw magnetic microparticles, control sample c, as determined by the SQUID loop measurement, characteristics of the superparamagnetic behavior (sample mass of 8 mg).
The directly obtained curve is depicted by a continuous black line. Shown by a straight dashed gray line are the paramagnetic contributions that were calculated. The dashed black line corresponds to the curve after the deduction of these paramagnetic contributions. The inset on the bottom right details these curves at small magnetic induction, as well as the offset applied to compensate for the small remnant field within this range. This reveals a very small hysteresis, characteristic of a largely superparamagnetic population of particles with a very low proportion of particles that are still blocked.

120 Oe) for the AMF induction of hyperthermia. The apparent saturation associates with a maximal intrinsic induction (corresponding to the so-called magnetization at saturation, σ_s, when the saturation is ascertained) of about 2.5 $A.m^2/kg$ of magnetic seeds (or 2.5 emu/g of magnetic seeds), which translates to 12.8 $A.m^2/kg$ of iron oxide. These values for materials with particular micro- and nano-

structures are classically compared with the reference experimental values for bulk materials to find a landmark (i.e., for maghemite: > 159 $kA \cdot m^{-1}$ (2000 Oe) for the saturation field, and $\sigma_S = 60 - 80$ $A.m^2/kg$ of bulk maghemite at 300 K, [40]). This comparison is only indicative and should be cautiously criticized in the case of complex microstructures. It is known that the saturation magnetization is highly dependent on magnetic particle interactions with the matrix in the case of composite materials and on magnetic particle concentrations within the matrix, which govern the interactions and coupling between particles [45,46]. In our case, the iron oxide concentration is relatively low and thus is not problematic. Also, the specific saturation magnetization decreases notably with increasing specific surface area [47] and is influenced by the particle morphology [48]. The saturation magnetization of maghemite nanoparticles embedded in a silica matrix was indeed demonstrated to decrease drastically when the temperature increased from 77 K to 300 K [49]. Although not clearly understood, this appears to be a consequence of the already-mentioned surface effects, prominent at the nanoscale, due to the paramagnetic external layer surrounding the ferrimagnetic core of the maghemite nanoparticles, resulting in a decreased magnetic diameter [50-52]. Because the magnetic moment is determined exclusively by the ferrimagnetic core where the spins are aligned as a result of the super-exchange interaction, the spontaneous magnetization consequently decreases [49]. In comparison, the variation of the saturation magnetization in bulk maghemite appears to be very limited, a seven-fold factor less over the same temperature range (the Curie point of maghemite, T_c ,can be interpolated on the order of 1123 K or 850 °C if it would not give prior temperature decomposition, [38]). It can thus be hypothesized that the magnetic diameter and saturation induction of the present nanocomposite magnetic seeds will be even lower at the investigated temperature of 310 K. This most likely explains why the reported saturation magnetization value of our maghemite nanocomposite particle is lower than the value for bulk maghemite. It is worth noting that the temperature used in our experiments, 310 K, matching the physiological body temperature (37°C), is relatively high and is rarely investigated. Regarding the susceptibility, attainable through the initial rising part of the curve, i.e., the virgin curve of our hysteresis loop measurement, we obtained a specific "intrinsic" mass susceptibility, $\chi_{im} = 3.8 \cdot 10^{-4}$ per kg of magnetic seeds (in the SI system, which in the cgs system gives $3.0 \cdot 10^{-2}$ per g of magnetic seeds in the implant by dividing by a conversion factor of

$4\pi \cdot 10^{-3}$), after the deduction of the paramagnetic contributions (which represent a mass "paramagnetic" susceptibility of $5 \cdot 10^{-5}$ per kg of magnetic seeds in SI, or $4 \cdot 10^{-3}$ per g magnetic seeds in cgs). As previously discussed, χ_{im} can be attributed to the iron oxide mass fraction, leading finally to a susceptibility of $1.9 \cdot 10^{-3}$ per kg of iron oxide in the SI system (i.e., 0.15 per g of iron oxide in the cgs system).

3.2 Magnetic properties of implants (SQUID)

The static magnetic properties of *in-situ*-formed implants based on the two formulations, hydrogel (Alginate 2 % w/V in water) or organogel (EVAL 8 % w/V in DMSO), with increasing magnetic microparticle concentrations (whose compositions are detailed in Table 3.1 with respect to the methodological approach detailed in section 2.3), appear to well correspond to the magnetic characteristics of the control magnetic particles. The hysteresis loops of all implants revealed similarities to that of the control sample (C), suggesting the preservation of the superparamagnetic behavior of microparticles in the implants formed *in situ*. It is important to note that the curves were even more similar when the magnetization values were weighted by the mass of constituting magnetic microparticles (or iron oxide content) determined on the basis of weighing the injections. This was not the case when the magnetization values were weighted by the masses of the wet implants introduced in the SQUID. The magnetic characteristics of the implants are summarized in Table 3.2, with respect to the magnetic characteristics of the control powder. As previously evaluated, the slope of dB/dH after hysteresis enclosure was deduced. The calculated contributions to permeability per gram of wet sample increased with the magnetic microparticle concentration, reaching, for the formulation with the largest concentration of magnetic microparticles (100 % w/v), half of the value measured for the control powder of magnetic microparticles. This deserves further comment. When looking at the weights of the injected formulations and of the wet implants introduced in the SQUID, we can exclude the effect of the alveolar water contained within the spongious microstructure of the implants (implant water contents ranged from 49 to 89 %, as also detailed in [35]). The magnetic effect of the polymer matrix should be

Table 3.2: Magnetic characteristics determined by SQUID

Formulation	Mass magnetic susceptibility by kg of sample as introduced in SQUID (SI unit systems, $m^3 \cdot kg^{-1}$)	Deduced contributions to permeability per kg of sample (SI unit systems, $m^3 \cdot kg^{-1}$)	Coercive field ($A.m^{-1}$)	Retentivity per unit mass of constituting magnetic seeds ($A \cdot m^2 \cdot kg^{-1}$ or $emu \cdot g^{-1}$)	Mass magnetic susceptibility per unit mass of constituting magnetic microparticles (SI unit systems, $m^3 \cdot kg^{-1}$)	Maximal magnetization per unit mass of constituting magnetic seeds ($A \cdot m^2 \cdot kg^{-1}$ or $emu \cdot g^{-1}$)	Hysteresis area per unit mass of constituting magnetic microparticles ($A \cdot m \cdot kg^{-1}$)
O-05	3.01E-5	3.91E-6	248.933	0.11390	3.82E-4	2.9233	3638
O-10	5.66E-5	7.40E-6	239.543	0.11393	3.95E-4	3.0210	3669
O-20	9.02E-5	1.15E-5	238.120	0.11171	3.91E-4	3.0038	3606
O-40	1.38E-4	1.75E-5	253.278	0.11556	3.81E-4	2.8844	3602
O-60	1.59E-4	2.11E-5	266.589	0.11633	3.48E-4	2.7495	3654
O-80	1.68E-4	2.14E-5	259.233	0.10823	3.31E-4	2.6760	3480
O-100	1.82E-4	2.36E-5	246.423	0.10155	3.37E-4	2.5969	3533
H-05	3.32E-5	4.31E-6	237.135	0.10942	3.89E-4	2.9489	3602
H-10	4.71E-5	6.12E-6	227.949	0.10152	3.71E-4	2.8437	3156
H-20	7.52E-5	1.01E-5	264.785	0.10128	3.05E-4	2.4570	3254
H-40	1.30E-4	1.46E-5	301.299	0.11868	3.92E-4	2.5771	4172
H-60	1.35E-4	1.71E-5	262.669	0.10916	3.29E-4	2.6575	3469
H-80	1.67E-4	2.21E-5	255.879	0.10914	3.38E-4	2.6562	3518
H-100	1.75E-4	2.30E-5	263.956	0.11505	3.50E-4	2.7822	3830
C	4.28E-4	4.86E-5	307.428	0.11745	3.80E-4	2.6581	3776

Legend: E-(x) stands for: $\cdot 10^{-(x)}$

considered, noting that the low polymer fraction decreases when the calculated contributions to permeability increase. It is likely that the matrix infiltrating micropores or the layer surrounding the particles, whose thickness decreases, would generate a permeability contribution opposed to the permeability contributions observed for the control. On the basis of an opposite contribution to permeability, one can also describe close associations of one constituent of the formulation or implant with the magnetic seeds of increasing mass fraction, likely involving the smallest porosities. We hypothesize that water, already present in the formulation for hydrogels or once precipitated in water for organogels, plays a prominent role in easily infiltrating the silica matrix and even the maghemite phase porosity. With a lower volume susceptibility, infiltrated water paramagnetism competes then with the silica diamagnetism. Regarding the coercivity, it should be restated that this parameter is only dependent on the microstructure and is related to the anisotropy. Similarly to an "intensive" magnetic property, coercivity is independent of the iron concentration [53]. In our case, the coercivity varied unpredictably for implants with increasing magnetic seed concentrations, but it remained constantly lower than or similar to the control powder. This indicates that there are no crucial anisotropy variations. Retentivity was also very comparable among the implants and control samples. The mass magnetic susceptibility and saturation magnetization of the implants were found here to be similar to those of control powder, and this was very concordant with the amount of magnetic seeds present in the implant. The hysteresis area (determined from the curves weighted by the amount of magnetic seeds constituting the implant) was reproducibly very constant. The small hysteresis area allows us to conclude that hysteresis losses would not significantly contribute to the heating in AMF. Therefore, in hydrogel and organogel formulations forming *in-situ* implants, the magnetic properties of nanocomposite iron oxide silica microparticles, on which magnetically mediated hyperthermia in AMF relies, are relatively preserved.

3.3 Heating capacities of implants under AMF

Wet implant preparation conditions for SLP determinations were comparable to the conditions of preparation used for the magnetic property characterizations, with both conditions similar to the *in vivo* conditions. SLP was determined at 141kHz and 12mT, per gram of iron oxide composing the implants by the two orthogonal methods: Methods A and B (see sections 2.5.2 and 2.5.3, respectively). Of note, the sample characteristics and experimental details for experimental Methods A and B can be found in Tables 3.3, 3.4 and 3.5. Results obtained by Methods A and B are gathered in Figure 3.6. Taking all these results together and taking variability in account, it appears that the intrinsic SLP associated with magnetic seeds is preserved in the various implants studied here, with the real intrinsic SLP value tending to be the SLP value determined for the control particles, c.a. 20 $W \cdot g^{-1}$ of iron oxide. From the pharmaceutical point of view, it should be mentioned that these formulations are also stable with regard to their magnetic properties and heating capacities over large periods of storage, and the limits of storage indeed rely on the loss of syringeability and implant formation capacity of the formulations (data not shown). With Method A, a short delay of a few seconds could be observed after switching on the AMF inducer before seeing a temperature increase. This delay could be attributed to the electromagnetic stabilization of the inducer. It could also result from the initial diffusion of heat in the implant (through thermal conductivity). The heat conduction through the silica matrix could be the limiting step in this case. Interestingly, when comparing both methods of SLP determination, it appears that Method A gives a poor precision for the implants containing low magnetic microparticle concentrations and likely associates with an overestimation of SLP. In contrast, Method B seems to be more precise at low magnetic microparticle fractions, but, regarding accuracy, the SLP seems underestimated in turn. For high magnetic microparticle concentrations, both methods appear to be relatively more accurate and precise, converging toward the SLP of c.a. 20 $W \cdot g^{-1}$ of iron oxide contained in the implant. This strongly supports the preservation of the intrinsic SLP of the magnetic microparticles within the implants formed by both formulation types, even if slight differences can be suggested when precisely considering the effect of the polymer matrix. It is worth noting that with

method B, the temperature elevation in water reported as the mean ΔT in Table 3.4 gives an idea of the tissue temperature that could be reached in the ideal situation where no heat dissipation by convection or conduction occurs. As mentioned in the introduction, the most important parameter of heat dissipation is the blood flow and its response to heat under the pathophysiological conditions considered, which can eventually lead to negligible tissue temperature elevation *in vivo*. In this regard, it should be noted that both formulations are also known to be embolizing agents capable of blocking blood flow in vascular or tumor lesions, mainly when injected through intravascular routes but also when injected in solid tumors. The embolizing characteristics could contribute to increase the heating efficiency *in situ* and thereby increase the therapeutic potential [36].

Table 3.3: Composition of the liquid formulation used to generate implants for heating capacities characterization by Method A or B of SLP determination

Formulation	Constituting polymer in the mother solution	Polymer mass fraction in the mother solution	Polymer mass fraction in the liquid implant formulation	Magnetic microparticle mass fraction in the liquid implant formulation
O-05	EVAL	0.07	0.066	0.038
O-10	EVAL	0.07	0.064	0.079
O-20	EVAL	0.07	0.059	0.143
O-40	EVAL	0.07	0.052	0.248
O-60	EVAL	0.07	0.046	0.329
O-80	EVAL	0.07	0.042	0.392
O-100	EVAL	0.07	0.037	0.460
H-05	Alginate Na	0.02	0.019	0.042
H-10	Alginate Na	0.02	0.018	0.091
H-20	Alginate Na	0.02	0.017	0.152
H-40	Alginate Na	0.02	0.015	0.262
H-60	Alginate Na	0.02	0.013	0.348
H-80	Alginate Na	0.02	0.012	0.417
H-100	Alginate Na	0.02	0.011	0.477

Table 3.4: Sample details concerning Method A of SLP determination

Formulation	Mean mass of the liquid formulation injected for implantation (g)	Variation between weightings in mass percentage	Weight of the wet implant (g)	Weight of the desiccated implant (g)	Mean initial implant heating rate (K/s)	Standard variation of the measured initial implant heating rate (K/s)
O-05	0.493	0.061	0.338	0.051	0.083	0.003
O-10	0.569	0.105	0.456	0.080	0.158	0.099
O-20	0.545	0.073	0.428	0.111	0.247	0.059
O-40	0.521	0.019	0.423	0.155	0.317	0.049
O-60	0.513	0.020	0.456	0.194	0.495	0.095
O-80	0.559	0.161	0.512	0.240	0.646	0.046
O-100	0.621	0.032	0.571	0.310	0.889	0.071
H-05	0.390	0.333	0.259	0.023	0.085	0.023
H-10	0.341	0.264	0.240	0.035	0.147	0.021
H-20	0.457	1.226	0.429	0.078	0.250	0.014
H-40	0.367	0.136	0.357	0.102	0.412	0.014
H-60	0.392	0.281	0.407	0.143	0.509	0.039
H-80	0.381	0.577	0.409	0.162	0.564	0.089
H-100	0.434	0.092	0.438	0.186	0.663	0.042

Table 3.5: Sample details concerning Method B of SLP determination

Formulation	Mean mass of the liquid formulation injected for implantation (g)	Variation between weightings in mass percentage	Weight of the wet implant (g)	Weight of the desiccated implant (g)	Mean ΔT during 2-min in AMF (K)	Standard variation of ΔT during 2-min in AMF (K)
O-05	1.012	0.040	0.714	0.104	0.678	0.203
O-10	1.041	0.019	0.753	0.140	1.350	0.346
O-20	1.121	0.036	0.896	0.227	3.827	0.808
O-40	1.237	0.016	1.083	0.370	5.956	0.501
O-60	1.328	0.038	1.166	0.508	10.782	1.514
O-80	0.635	0.063	0.579	0.276	6.249	1.323
O-100	1.090	0.073	1.034	0.366	10.119	0.561
H-05	0.950	0.105	0.722	0.058	0.761	0.351
H-10	1.037	0.617	0.902	0.105	1.322	0.153
H-20	0.553	0.887	0.504	0.095	1.142	0.602
H-40	0.746	0.496	0.740	0.206	4.529	0.237
H-60	1.211	0.025	1.331	0.427	8.215	0.462
H-80	1.048	0.114	1.147	0.435	9.639	0.964
H-100	0.796	0.000	0.870	0.538	10.430	1.408

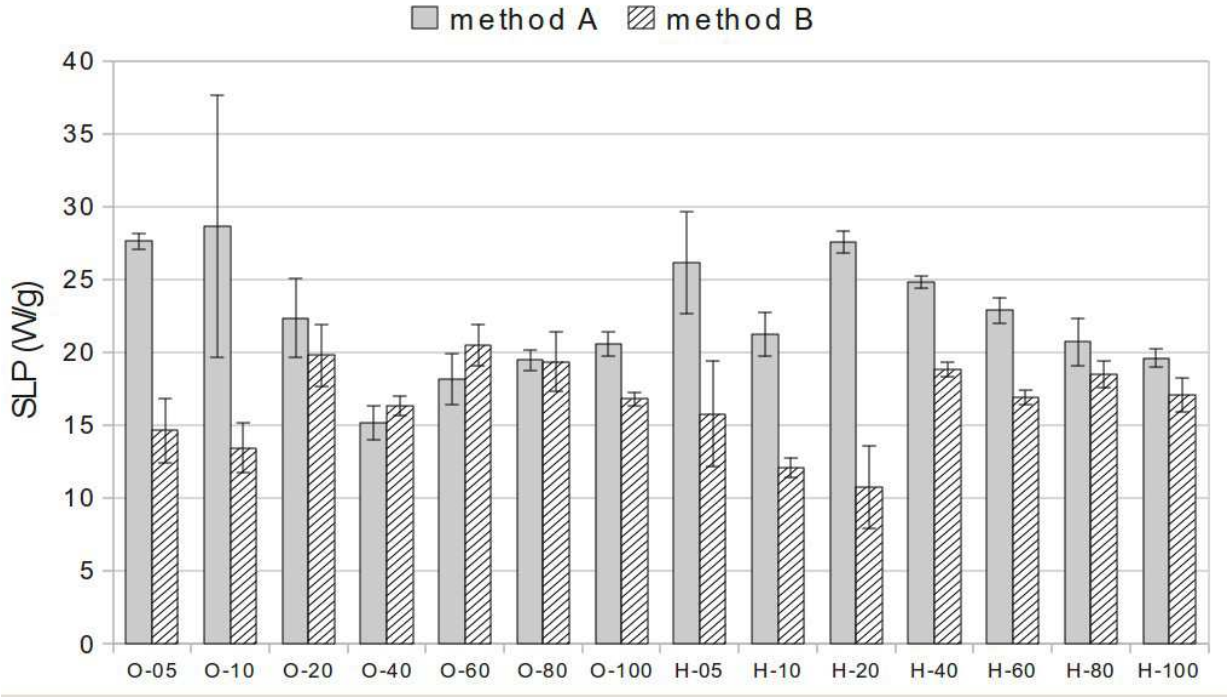

Figure 3.6: Specific Loss Power (SLP) in W/g of iron oxide contained in the wet implants formed from various formulations with increasing magnetic γFe_2O_3 nanocomposite silica microparticles when submitted to an alternating magnetic field (141 kHz, 12 mT) and as determined by the two methods as described in the section 2.5. Method A, gray bars, is based on the initial temperature increase of the implant; Method B, hatched bars, is based on the temperature elevation of c.a. 4 ml of water in contact with implant, as adapted from Bretcanu et al (*Acta Biomaterialia* 1 (2005) 421–429) [43]. Sample details can be found in Tables 3 and 4. The experiments were run in triplicate, excepting for H-40 with Method A (duplicate).

4 Conclusions

The superparamagnetic properties of magnetic silica composite microparticles embedding nanoscaled maghemite iron oxides are preserved in the injectable formulations for the whole range of concentrations that allow syringeability. These properties also remain preserved in the implants formed *in situ*.

The magnetic properties as well as the heating capacity, which is improved with increasing particle fraction can be extrapolated from the concentration of magnetic microparticles. With these AMF parameters, a straightforward determination of the dissipated heat is now possible. In association with previous *in vivo* studies, this further allows for the modeling of tissue heating *in vitro* and *in vivo*, and this improves our understanding of the heat delivery through formulations intended for magnetically mediated hyperthermia in the treatment of solid tumors.

5 Acknowledgements

Grant support: Swiss National Science Foundation (grant 3200B0-104508), Switzerland. For TEM analysis, we are thankful to Mr Bauer Cristoph, Department of Zoology and Animal Biology, University of Geneva, Geneva, Switzerland. For MEB and EDX analysis, we are thankful to Mrs Cravotto Geraldine, Department of Condensed Matter Physics, University of Geneva, Geneva, Switzerland.

6 References

[1] Baronzio GF, Hager ED. Hyperthermia in cancer treatment. Springer; 2006.

[2] Hildebrandt B, Wust P. The biologic rationale of hyperthermia. Cancer Treat. Res. 2007;134:171-184.

[3] Baronzio G, Fiorentini G, Cogle CR. Cancer Microenvironment and Therapeutic Implications: Tumor Pathophysiology Mechanisms and Therapeutic Strategies. Springer; 2009.

[4] Baronzio GF, Gramaglia A, Baronzio A, Freitas I. Influence of tumor microenvironment on thermoresponse: Biological and clinical implications. In: Hyperthermia in cancer treatment. Springer; 2006. p. 68-91.

[5] Vaupel PW, Kelleher DK. Metabolic status and reaction to heat of normal and tumor tissue. In: Thermoradiotherapy and thermochemotherapy - Volume 1: Biology, Physiology, and Physics. Springer; 1995. p. 159-176.

[6] Vaupel PW, Kelleher DK. Pathophysiological and vascular characteristics of tumours and their importance for hyperthermia: Heterogeneity is the key issue. Int J Hyperthermia. 2010 Mar 26;

[7] Kelleher DK, Vaupel PW. Vascular effects of localized hyperthermia. In: Hyperthermia in cancer treatment. Springer; 2006. p. 99-109.

[8] Latchman DS, editor. Stress Proteins. Berlin: Springer; 1999.

[9] Li GC, Calderwood SK. Hyperthermia classic article commentary: 'Re-induction of hsp70 synthesis: an assay for thermotolerance' by Gloria C. Li and Johnson Y. Mak, International Journal of Hyperthermia 1989;5:389-403. Int J Hyperthermia. 2009 Jun;25(4):258-261.

[10] Rylander MN, Feng Y, Bass J, Diller KR. Thermally Induced Injury and Heat-Shock Protein Expression in Cells and Tissues. Annals of the New York Academy of Sciences. 2006;1066(Cell Injury: Mechanisms, Responses, and Repair):222-242.

[11] Theodorakis NG, Drujan D, De Maio A. Thermotolerant cells show an attenuated expression of Hsp70 after heat shock. J. Biol. Chem. 1999 Apr 23;274(17):12081-12086.

[12] Coss RA, Sedar AW, Sistrun SS, Storck CW, Wang PH, Wachsberger PR. Hsp27 protects the cytoskeleton and nucleus from the effects of 42°C at pH 6.7 in CHO cells adapted to growth at pH 6.7. Int J Hyperthermia. 2002 1;18(3):216-232.

[13] Multhoff G. Heat shock proteins in immunity. Handb Exp Pharmacol. 2006;(172):279-304.

[14] Wells AD, Malkovsky M. Heat shock proteins, tumor immunogenicity and antigen presentation: an integrated view. Immunol. Today. 2000 Mar;21(3):129-132.

[15] Milani V, Noessner E. Effects of thermal stress on tumor antigenicity and recognition by immune effector cells. Cancer Immunol. Immunother. 2006 Mar;55(3):312-319.

[16] Manjili MH, Wang XY, Park J, Macdonald IJ, Li Y, Van Schie RCAA, et al. Cancer immunotherapy: stress proteins and hyperthermia. Int J Hyperthermia. 2002 Dec;18(6):506-520.

[17] Skitzki JJ, Repasky EA, Evans SS. Hyperthermia as an immunotherapy strategy for cancer. Curr Opin Investig Drugs. 2009 Jun;10(6):550-558.

[18] Hall EJ, Giaccia AJ. Hyperthermia. In: Radiobiology for the radiologist. Lippincott Williams & Wilkins; 2006. p. 469-490.

[19] Seegenschmiedt MH, Fessenden P, Vernon CC. Thermoradiotherapy and thermochemotherapy -

Volume 1: Biology, Physiology, and Physics. Springer; 1995.
[20] Seegenschmiedt MN, Fessenden P, Vernon CC. Thermoradiotherapy And Thermochemotherapy - Volume 2: Clinical Applications. Springer Verlag; 1996.
[21] Song CW. Effect of Local Hyperthermia on Blood Flow and Microenvironment: A Review. Cancer Res. 1984 Oct 1;44(10_Supplement):4721s-4730.
[22] Habash RWY, Bansal R, Krewski D, Alhafid HT. Thermal therapy, part 1: an introduction to thermal therapy. Crit Rev Biomed Eng. 2006;34(6):459-489.
[23] Habash RWY, Bansal R, Krewski D, Alhafid HT. Thermal therapy, part 2: hyperthermia techniques. Crit Rev Biomed Eng. 2006;34(6):491-542.
[24] Hergt R, Andrä W. Magnetic Hyperthermia and Thermoablation. In: Magnetism in Medicine: A Handbook. Weinheim: Wiley-VCH; 2007. p. 550.
[25] Andrä W, Häfeli UO, Hergt R, Misri R. Application of magnetic particles in medicine and biology. In: Kronmüller H, Parkin SSP, editors. Handbook of magnetism and advanced magnetic materials. John Wiley & Sons; 2007. p. 2460-2492.
[26] Dutz S, Hergt R, Mürbe J, Müller R, Zeisberger M, Andrä W, et al. Hysteresis losses of magnetic nanoparticle powders in the single domain size range. J Magn Magn Mater. 2007 Jan;308(2):305-312.
[27] Hergt R, Dutz S, Roder M. Effects of size distribution on hysteresis losses of magnetic nanoparticles for hyperthermia. J Phys Condens Matter. 2008;20(38):385214.
[28] Jordan A, Maier-Hauff K, Wust P, Johannsen M. Nanoparticles for Thermotherapy. In: Kumar CSSR, editor. Nanomaterials for Cancer Therapy. Weinheim: Wiley-VCH; 2006.
[29] Jordan A, Wust P, Fähling H, John W, Hinz A, Felix R. Inductive heating of ferrimagnetic particles and magnetic fluids: physical evaluation of their potential for hyperthermia. Int J Hyperthermia. 1993 Feb;9(1):51-68.
[30] Wust P, Gneveckow U, Johannsen M, Böhmer D, Henkel T, Kahmann F, et al. Magnetic nanoparticles for interstitial thermotherapy--feasibility, tolerance and achieved temperatures. Int J Hyperthermia. 2006 Dec;22(8):673-685.
[31] Hergt R, Andra W, d'Ambly C, Hilger I, Kaiser W, Richter U, et al. Physical limits of hyperthermia using magnetite fine particles. IEEE Trans. Magn. 1998 Sep;34(5):3745-3754.
[32] Hergt R, Dutz S. Magnetic particle hyperthermia - biophysical limitations of a visionary tumour therapy. J Magn Magn Mater. 2007 Apr;311(1):187-192.
[33] Thiesen B, Jordan A. Clinical applications of magnetic nanoparticles for hyperthermia. Int J Hyperthermia. 2008 Sep;24(6):467-474.
[34] Gupta AK, Naregalkar RR, Vaidya VD, Gupta M. Recent advances on surface engineering of magnetic iron oxide nanoparticles and their biomedical applications. Nanomedicine. 2007 2;2(1):23-39.
[35] Le Renard P, Jordan O, Faes A, Petri-Fink A, Hofmann H, Rüfenacht D, et al. The in vivo performance of magnetic particle-loaded injectable, in situ gelling, carriers for the delivery of local hyperthermia. Biomaterials. 2010 Feb;31(4):691-705.
[36] Le Renard P, Buchegger F, Petri-Fink A, Bosman F, Rüfenacht D, Hofmann H, et al. Local moderate magnetically induced hyperthermia using an implant formed in situ in a mouse tumor model. Int J Hyperthermia. 2009 May;25(3):229-239.

[37] Chastellain M, Petri A, Gupta A, Rao K, Hofmann H. Superparamagnetic silica-iron oxide nanocomposites for application in hyperthermia. Adv Eng Mater. 2004 Apr;6(4):235–241.
[38] Cullity BD, Graham CD. Introduction to Magnetic Materials. Wiley-IEEE; 2008.
[39] Schwertmann U. Iron Oxides in the Laboratory: Preparation and Characterization. 2nd ed. Weinheim: Wiley-VCH; 2000.
[40] Cornell RM. The Iron Oxides: Structure, Properties, Reactions, Occurrence and Uses. Weinheim [etc.]: VCH; 1996.
[41] Foladori P, Quaranta A, Ziglio G. Use of silica microspheres having refractive index similar to bacteria for conversion of flow cytometric forward light scatter into biovolume. Water Research. 2008 Aug;42(14):3757-3766.
[42] Rodriguez-Carjaval J. FullProf Suite [Internet]. 2009. Available from: http://www.ill.eu/sites/fullprof/index.html
[43] Bretcanu O, Spriano S, Verné E, Cöisson M, Tiberto P, Allia P. The influence of crystallised Fe3O4 on the magnetic properties of coprecipitation-derived ferrimagnetic glass-ceramics. Acta Biomater. 2005 Jul;1(4):421–429.
[44] Bretcanu O, Verné E, Cöisson M, Tiberto P, Allia P. Magnetic properties of the ferrimagnetic glass-ceramics for hyperthermia. J Magn Magn Mater. 2006 Oct;305(2):529–533.
[45] Kodama RH, Berkowitz AE, McNiff J, Foner S. Surface Spin Disorder in NiFe2O4 Nanoparticles. Physical Review Letters. 1996 Jul;77(2):394.
[46] Kodama RH. Magnetic nanoparticles. Journal of Magnetism and Magnetic Materials. 1999 Oct;200(1-3):359–372.
[47] Mollard P, Germi P, Rousset A. Surface effects on saturation magnetization of fine spinel ferrite particles. Physica B+C. 1977;86-88(Part 3):1393-1394.
[48] Batis-Landoulsi H, Vergnon P. Magnetic moment of γ-Fe2O3 microcrystals: morphological and size effect. Journal of Materials Science. 1983 Nov 1;18(11):3399-3403.
[49] Caizer C. Saturation magnetization of γ-Fe2O3 nanoparticles dispersed in a silica matrix. Physica B. 2003 Mar;327(1):27-33.
[50] Cannas C, Concas G, Musinu A, Piccaluga G, Spano G. Mössbauer spectroscopic studyof FE2O3 nanoparticles dispersed over a silica matrix. Z. Naturforsch. 1999;54 a:513-518.
[51] Cannas C, Concas G, Congiu F, Musinu A, Piccaluga G, Spano G. Mössbauer spectroscopic studyof FE2O3 nanoparticles dispersed over a silica matrix prepared by the sol-gel method. Z. Naturforsch. 2002;57 a:154-158.
[52] Tronc E, Fiorani D, Nogues M, Testa AM, Lucari F, D'Orazio F, et al. Surface effects in noninteracting and interacting gamma-Fe2O3 nanoparticles. J Magn Magn Mater. 2003 May;262(1):6–14.
[53] Wilson JL. Synthesis and magnetic properties of polymer nanocomposites with embedded iron nanoparticles. J. Appl. Phys. 2004;95(3):1439.

Chapter 4

Local moderate magnetically induced hyperthermia using an implant formed in situ in a mouse tumor model

published in International Journal of Hyperthermia,25 (2009):3,229 — 239

Pol-Edern Le Renard[1], Franz Buchegger[2], Alke Petri-Fink[3], Frederik Bosman[4], Daniel Rüfenacht[5], Heinrich Hofmann[3], Eric Doelker[1], and Olivier Jordan[1].

[1]School of Pharmaceutical Sciences, University of Geneva, University of Lausanne, Geneva, Switzerland; [2]Service of Nuclear Medicine, University Hospital of Lausanne, Lausanne, University Hospital of Geneva, Geneva, Switzerland; [3]Laboratory for Powder Technology, Ecole Polytechnique Fédérale de Lausanne (EPFL), Lausanne, Switzerland; [4]Department of Pathology, University Hospital of Lausanne, Lausanne, Switzerland; [5]Neurointerventional Service, University Hospital of Geneva, Geneva, Switzerland.

Abstract

Purpose: We investigate a new heat delivery technique for the local treatment of solid tumors. The technique involves injecting a formulation that solidifies to form an implant *in situ.* This implant entraps superparamagnetic iron oxide nanoparticles (SPIONs) embedded in silica microbeads for magnetically-induced moderate hyperthermia. Particle entrapment prevents phagocytosis and distant migration of SPIONs. The implant can be repeatedly heated by magnetic induction.

Methods: We evaluated heating and treatment efficacies by means of thermometry and survival studies in nude mice carrying subcutaneous human colocarcinomas. At day 1, we injected the formulation into the tumor. At day 2, single 20-min hyperthermia treatment was delivered by 141-kHz magnetic induction using field strengths of 9 to 12 mT under thermometry.

Results: SPIONs embedded in silica microbeads were effectively confined within the implant at the injection site. Heat-induced necro-apoptosis was assessed by histology at day 3. On average, 12 mT resulted in tumor temperature of 47.8°C, and over 70 % tumor necrosis that correlated to the heat dose (AUC = 282 °C·min). In contrast, a 9 mT-field strength induced tumoral temperature of 40.0 °C (AUC = 131 °C·min) without morphologically identifiable necrosis. Survival after treatment with 10.5 or 12 mT fields was significantly improved compared to non-implanted and implanted controls. Median survival times were 27 and 37 days vs. 12 and 21 days for 10.5-mT and 12-mT groups vs. non-implanted and implanted controls, respectively.

Conclusion: Five of eleven mice (45%) of the 12 mT group survived one year without any tumor recurrence, holding promise for tumor therapy using magnetically-induced moderate hyperthermia through injectable implants.

Keywords: Magnetic induced hyperthermia, superparamagnetic nanoparticles, implant, precipitating polymers, subcutaneous xenograft, necrotizing colocarcinoma, survival, thermometry

Chapter 4: Table of Contents

1 Introduction....211
2 Materials and Methods....212
2.1 Magnetics beads....212
2.2 Injectable formulation....213
2.3 Alternating magnetic field generator....213
2.4 Tumor model....214
2.5 Mice....214
2.6 Implantation....215
2.7 Thermometry....215
2.8 In vivo investigation protocols....215
2.9 Histology....216
2.10 Imaging....217
2.11 Statistics....217
3 Results....218
3.1 Precipitation of the injectable formulation fills the initially necrotic core and peripheral extensions of the tumor....218
3.2 The implant formed in situ can heat the tumor by magnetic induction at 141 kHz across the whole temperature range of moderate hyperthermia as a function of field strength....219
3.3 Above a threshold temperature, a larger delivered heat dose increases the extent of induced necro-apoptosis to whole tumor....221
3.4 Magnetically-induced heat delivery through an implant is highly efficient in treating solid tumor for a magnetic field strength of 12 mT....223
3.5 Computerized Tomography allows for precise implant imaging....224
4 Discussion....227
5 Acknowledgements....230
6 References....230

1 Introduction

Hyperthermia, the therapeutic application of heat, has revealed large benefits in oncology. Moderate hyperthermia (resulting in tissue temperatures of 40 to 46 °C) is associated with cytotoxic protein destabilization and denaturation. Cellular defense against heat consists in reactions favoring tolerance to heat stress, closely correlated with the induction of heat shock proteins. This tolerance is inhibited above the temperature threshold of about 42°C and the result is in a pronounced increase in cell death rate [1]. Moderate hyperthermia turns the vascular deficiency of a tumor to therapeutic gain by leveraging its relative enhanced sensitivity to heat damage. A variety of reference therapies in oncology – namely, radiotherapy, brachytherapy, chemotherapy or a combination thereof – have been synergistically combined with moderate hyperthermia [2,3].

The outcome of a hyperthermia treatment correlates to the heat dose administered [4], which, in turn, is dependent upon anatomical situation and heating modalities. Local hyperthermia aims to confine heat delivery to the lesion site. Despite steady improvements in heating localization of external or interstitial modalities based on standard heat application means (radiofrequencies, microwaves and ultrasounds), physical limitations still hinder the treatment of deep-seated lesions [5]. Power transmission in the case of acoustic or electromagnetic waves is limited by the reflection and absorption of power into tissue and interstitial liquid. In contrast, magnetic fields can cross the diamagnetic body of a patient without losses. Monodisperse superparamagnetic iron oxide nanoparticles (SPIONs) exposed to alternative magnetic fields (AMFs) convert the magnetization energy into heat. This scales as $P \propto \mathrm{H}^2 f^2$ where P is the power loss, H the AMF amplitude and f the frequency [6,7]. The rate of heat generation is larger than for metallic implant such as seed [8]. Magnetic fluid hyperthermia [9], i.e. heating interstitially injected SPIONs through alternating magnetic induction, has also shown promising clinical results [10-13]. One drawback of current administration techniques is that SPIONs fade ineluctably out from the injection site into the lymphatic and blood circulation or are sequestrated in macrophage, exposing patients to potentially toxic hazards [14].

We report here the feasibility of an original approach of magnetically induced local moderate

hyperthermia through an *in situ*-formed implant that traps SPIONs embedded in silica microbeads. After injection in aqueous environment and precipitation from their organic solvent formulation, water-insoluble polymer chains entangle and form a matrix holding the dispersed superparmagnetic microbeads. SPIONs are hence protected and durably confined at the injection site, avoiding their phagocytosis and distant migration. The opportunity to repeat implant heating in the long term as necessary could also offer therapeutic benefits. We performed thermometry and survival studies in a model of human colocarcinoma tumor that was subcutaneously engrafted in nude mice. Our goal was to assess heating efficiency and treatment potential of local moderate magnetically-induced hyperthermia delivered through the implant formed *in situ*.

2 Materials and Methods

2.1 Magnetics beads

We used silica particles containing 32% w/w of nanometric iron oxide particles of 10-nm mean diameter. The micron-sized particles had a density of 2.12 ± 0.02 g·cm^{-3} at 25°C. They were synthesized as described by Chastellain et al [15]. Briefly, tetramethoxysilane (45 ml) was added to a 2 M solution of $Fe(NO_3)_3 \cdot 9H_2O$ in ethanol (44.4 g iron salt in 55 ml ethanol). The mixture was stirred vigorously for 10 min, transferred to a sealed glass container and allowed to gel at 50 °C. The obtained brown gel was ground and separated by sieving. Particles smaller than 100 micrometers were thermally treated at 500 °C for 24 hrs, followed by high-energy attrition milling for 1 hr. Measurements using a Superconducting QUantum Interference Device (SQUID) confirmed superparamagnetic properties. The Specific Absorption Ratio (SAR), which reflects the heating capacities, is conventionally defined as the slope of the initial temperature rise multiplied by the specific heat capacity. In our case, this was in the order of 18 W/g iron oxide for a 12-mT magnetic field. The volume median diameter of the silica beads containing the iron oxide was determined on a Malvern Mastersizer as (D(v,0.5)) = 0.9 µm. The sizes of the magnetic iron oxide nanoparticles as established by transmission electron microscopy

(TEM), X-ray diffraction (XRD), and zero-field cooled magnetic measurements were 9 ± 1 nm, 11.3 ± 1nm and 15.5 ± 1.3 nm, respectively.

2.2 Injectable formulation

The ethylene vinyl alcohol copolymer EVAL™ 105-B (EVAL Europe, Zwijndrecht, Belgium) was dissolved at 8 % (w/v) in pharmaceutical grade dimethyl sulfoxide (DMSO) (Gaylord Chemical Corp., Los Angeles, USA). Using ultrasound and vigorous mechanical stirring, the beads were suspended at 40 % (w/v) in the resulting polymer solution. The preparation was finally sterilized by 15 min steam autoclaving at 121°C. As flocculated sedimentation occurred during storage, energetic shaking restored suspension homogeneity before use. Based on pycnometric measurements and calculations, the resulting density of the formulation was in the order of 1.26 $g \cdot cm^{-3}$.

2.3 Alternating magnetic field generator

The field generator used (TIG 2.5, Hüttinger Elektronik GmbH, Freiburg, Germany) consisted of an alternating current generator feeding the coil inductor (internal, external diameters and length of the horizontal coil were 54, 64 and 46 mm respectively). A conical tube mouse restrainer was introduced within the coil so that the implanted tumor was positioned at the center. With a small pick-up coil calibrated using a teslameter, we found a linear relationship between the magnetic field amplitude at 141 kHz and the generator peak-to-peak voltage. Current intensity was adjusted to impose the voltage corresponding to the chosen field strength.

2.4 Tumor model

Tumors generated by subcutaneous injection of the human Co112 colon carcinoma cells were maintained by serial subcutaneous transplantation in Swiss nude mice [16]. About 15 mm^3 of excised and minced tumor was subcutaneously engrafted into the right flank of 5-week old Swiss nude mice and the nodule was allowed to grow for 4 to 6 weeks. We determined the volume of the tumor (V_{tum}) by measuring with caliper three tumor dimensions: length (l), width (w) and thickness (t) and using the following formula: $V_{tum}=0.5(lwt)$ [17], with an uncertainty of ±15 %. Care was taken to implant the tumor above hind leg musculature in order to avoid detrimental heat exposure of intestinal tissues. The obtained tumor showed peripheral angiogenesis, necrosis in the tumor center core and a pseudocapsule composed of connective tissue. Central necrosis is a common feature in Co112 tumors, also observed in *in vitro*-grown multicellular spheroids and liver metastases [18].

2.5 Mice

One-month old female Swiss nude mice were supplied by Charles Rivers (Iffa Credo, Saint Germain sur l'Arbresle, France). Animal experiments were performed according to the ethical principles of laboratory animal care and Swiss legislation. Experiments were specifically approved by the official committee of animal research surveillance of the local authority. Animals were maintained in SPF animal house under a 12 hrs light and 12 hrs darkness cycle with normal diet, *ad libitum*, respecting a maximum of five animals per cage. Animals were euthanized by asphyxia under CO_2 saturated atmosphere.

2.6 Implantation

We set the injection volume to 0.25 ml (i.e., 84.1 mg of magnetic microparticles or 26.9 mg of iron oxide) to ensure that the intra-tumoral implant mass would be sufficiently large to heat the entire tumor. This injection volume was as large as or slightly larger than the tumor volume. The DMSO dose injected was below the mouse intraperitoneal LD_{50} (13 g/kg [19]). The formulation was slowly injected over a 1-2 minute period into the tumor through a 22G needle. Systemic and local toxicities were limited. Thanks to the brownish color and stiffness of the implant, we could manage and verify correct implant distribution by observing tissue darkening and induration. The implant first entered into the necrotic core and then extended towards the surrounding pseudocapsule to reach the peripheral border of the tumor. To avoid distant leakage, we paid special attention to needle positioning, in order to distribute the implant uniformly without accumulation in a part of the nodule. The procedure gave rise only to transient perinodular edema, which was spontaneously resorbed by the time we proceeded to alternating magnetic field stimulation.

2.7 Thermometry

We monitored temperature with a fluoroptic thermometer (Luxtron, Santa Clara CA, USA) using three fiber optic probes of 200 μm diameter. The device reported temperatures once a second with 0.1 °C accuracy. A one-point calibration at 20.0 °C was performed before each experiment. Data were acquired using Physitemp software (Luxtron, Santa Clara CA, USA).

2.8 In vivo investigation protocols

1) Thermometry studies: 0.25 ml of the 8 % (w/v) EVAL solution in DMSO containing 40 % (w/v) microbeads was injected into each mouse tumor (Day 1). After 24 hrs, the animal was exposed to a 20-min alternating magnetic field (141 kHz), under halothane-induced general anesthesia (Day 2). We investigated five magnetic field strengths: 9, 10, 10.5, 11 and 12 mT with respectively n = 5, 3, 6, 3 and 5 animals per group. Temperatures were monitored in the tumor, on the skin over the tumor, and in the hollow of the brachial plexus. The animals were sacrificed 24 hrs later (Day 3) for standard histology. Tumor size in the animals used for thermometry studies was in the range of 0.1 to 0.3 cm^3.

2) Survival studies: For the survival investigation protocol, we injected 0.25 ml of 8% (w/v) EVAL solution in DMSO containing 40 % (w/v) beads (Day 1). After 24 hrs, animals were exposed to an alternating magnetic field (141 kHz) for 20 min (Day 2). Two thermometry probes were affixed to the skin over the tumor, and one was fixed over the brachial plexus. Animals were sacrificed when the tumor volume reached ten times the initial volume. We investigated four groups: control with neither implant nor magnetic field (n = 6), implanted control (no magnetic field) (n = 7), 10.5 mT treated (n = 7), and 12 mT treated (n = 11). Animals were assigned to different treatment and control groups in order to ensure similar mean tumor sizes: the respective mean initial tumor sizes and standard deviations were 59 (± 54) mm^3 for the control group, 52 (± 44) mm^3 for the implanted control group, 53 (± 33) mm^3 for the 10.5-mT treated group and 64 (± 42) mm^3 for the 12-mT treated group. In a multigroup comparison, tumor size in the different groups was indeed shown to be very similar (Friedman test: $p > 0.8$).

2.9 Histology

The tumors and part of the surrounding tissues (overlying skin and adjacent muscle fascia or peritoneum) were fixed in buffered neutral formalin (1:10). Three-millimeter thick slices were

embedded in paraffin (through alcohol dehydration and xylol clearing), and 5 μm thick sections were stained with hematoxylin and eosin. The ratio of necrotic tumor to whole tumor volume was semi-quantitatively scored from 0 to 100 %. Microphotography was performed with a Nikon eclipse E800 microscope (Olympus Corp., Center Valley, USA) and histomorphometry using ImageJ 1.38x software (National Institutes of Health).

2.10 Imaging

For magnetic resonance imaging, we used a MRI scanner (Achieva 1.5T, Philips, Eidhoven, The Netherlands). For micro-computerized tomography, we used a Micro-CT scanner (Skyscan 1076, Kontich, Belgium)

2.11 Statistics

StatView version 5.0 (SAS Institute Inc.©) software was used for statistical analysis. Statistical significance was considered at $p < 0.05$. For the thermometry study, we used the Kruskall-Wallis test, the Mann-Whitney U test and the Spearman correlation test. For the survival studies, we employed the Friedman test and Kaplan Meyer analysis.

3 Results

3.1 Precipitation of the injectable formulation fills the initially necrotic core and peripheral extensions of the tumor

Injection of the formulation was accompanied by mild acute toxicity [20,21]. The injected 0.25-ml volume in a 25 g mouse would translate to 700 ml in a 70 kg patient, representing indeed a large injection volume per body weight. Systemic manifestations, most probably due to DMSO, consisted of transient fatigue and ocular irritation with eyelid ptosis. Locally, we observed edematous dilatation of the tumor site. Edema was rapidly reversed along with solvent clearance. Afterwards, the implanted tumor when recovered was shown to have dimensions larger than the initial tumor.

As previously observed in other experiments, Co122 tumors showed extensive central necrosis (up to 50%) [22]. Similar necrotic centers have been observed in Co112 multicellular spheroids grown in vitro [23]. Under electron microscopy, the Co112 tumor spheroids developed junctional complexes and desmosomes, while oxygen measurements had shown severe central hypoxia [24]. Histology confirmed that the implant was invariably present in the necrotic tumor core and extended towards the viable peripheral rim of cells. We observe basal inflammatory response in either the control or the implanted control groups, sacrificed one day after injection (Figure 4.2A). Occasionally, an implant extension had leaked into peritumoral loose connective tissue, mostly in the case of small and vital tumors. To assess implant distribution, we quantified the percentage of the implant that was in contact with stromal tissue (Table 4.1) and found correlation only with the initial tumor volume (Spearman $\rho = 0.645$; $p = 0.0412$), not with thermometry parameters.

Entrapment of microbeads within the implant polymer network was confirmed through use of the Prussian Blue stain, which identified iron oxide nanoparticles. *In vitro,* bare SPIONs of nanoscale size

were also efficiently trapped by this network. A preliminary formulation study with a batch of finer sub-micrometer beads confirmed entrapment efficiency but resulted in poor syringeability and an inadequate implant distribution pattern.

Table 4.1: Summary of parameters (mean ± SD) calculated for each group of the thermometry study for 5 magnetic field strengths.

Field strength (mT)	9 (n = 5)	10 (n = 4)	10.5 (n = 5)	11 (n = 3)	12 (n =5)
Initial tumor volume (mm^3)	217 ± 254	110 ± 40	129 ± 88	279 ± 60	220 ± 104
Tumor ET (°C)	40.0 * ± 3.1	42.7 † ± 3.0	42.8 § ± 2.6	43.5 ‖ ± 1.6	47.8 *†§‖ ± 2.2
Tumor AUC (°C·min)	131.1 * ± 44.3	180.1 † ± 45.1	177.3 § ± 40.1	183.8 ‖ ± 34.0	282.5 *†§‖ ± 40.0
Skin ET (°C)	38.6 *‡ ± 3.0	42.0 † ± 3.4	42.2 §‡ ± 2.2	43.5 ‖ ± 2.0	48.4 *† §‖ ± 2.0
Tumor necrosis (%)	67 ± 25	65 ± 21	54 ± 23	52 ± 13	78 ± 6

The U Mann-Withney test was used to evaluate statistical significance between the groups of mice. *§$P < 0.001$, †‖‡$P < 0.05$.

3.2 The implant formed in situ can heat the tumor by magnetic induction at 141 kHz across the whole temperature range of moderate hyperthermia as a function of field strength

Thermograms consistently exhibited a similar shape (Figure 4.1A). After a steep increase during the first 5 min, temperatures reached a plateau corresponding to an equilibrium between implant heat production and dissipation through diffusion and convection. The observed plateau temperature was not due to a diminishing response capacity of the superparamagnetic beads, since stepwise field increase in a separate experiment had produced stepwise increasing temperatures throughout the 25-min exposure period (Figure 4.1B). To obtain a parametric value of this equilibrium, we defined the Equilibrium

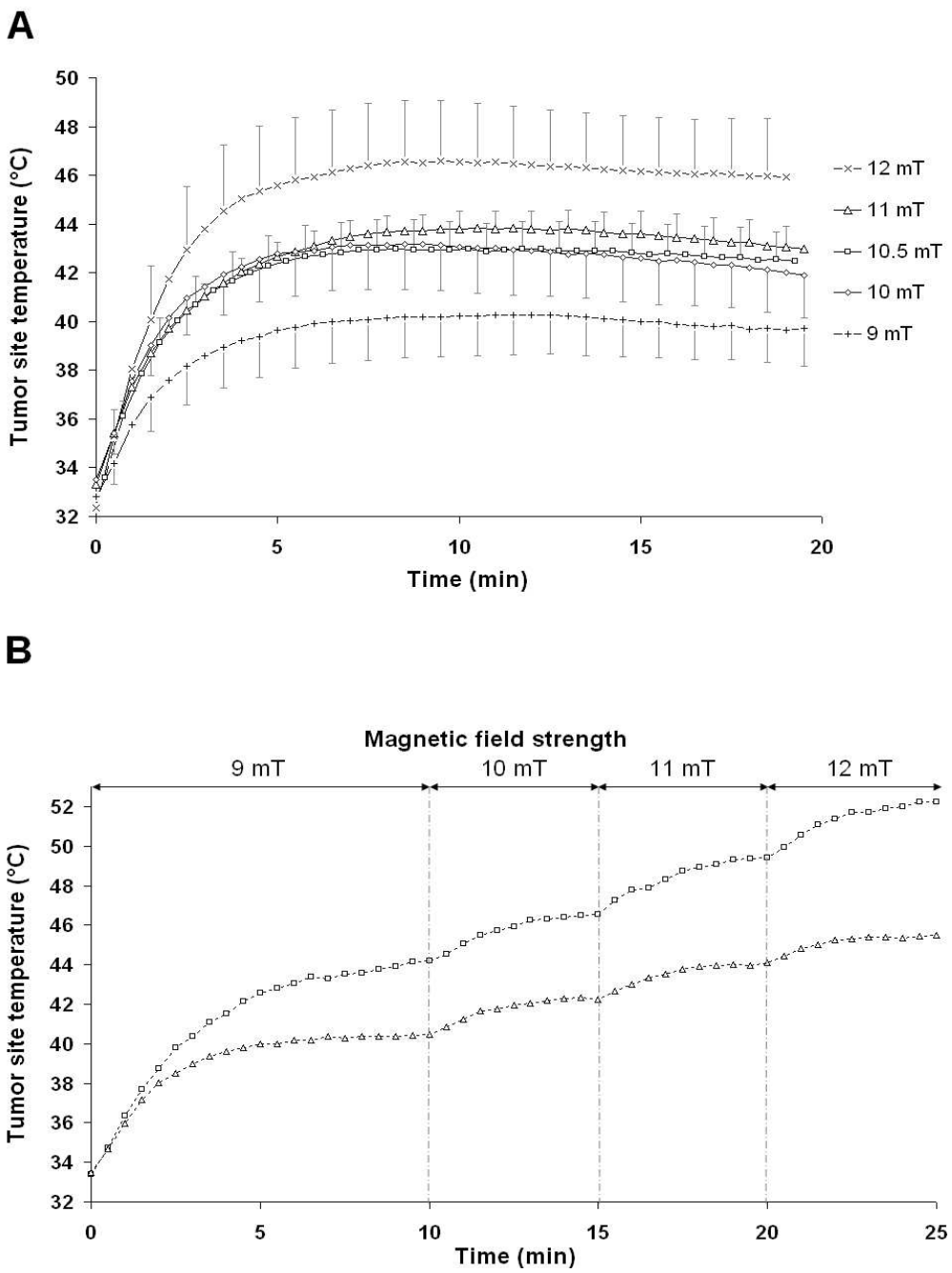

Figure 4.1. Thermograms representing tumor temperature as a function of time.

A. During single 20-min treatments in a 141 KHz alternating magnetic field, for magnetic field strengths of 9 mT (n = 5), 10 mT (n = 4), 10.5 mT (n = 5), 11 mT (n = 3), 12 mT (n = 5). B. During two stepwise 25-min treatments in an 141-KHz alternating magnetic field. Magnetic field strength was 9 mT from 0 to 10 min, 10 mT from 10 to 15 min, 11 mT from 15 to 20 min, 12 mT from 20 to 25 min.

Temperature (E.T.) as the averaged temperature over the final 15 min of magnetic field application. Table 4.1 shows that the mean tumor site E.T. increased with magnetic field strength (Spearman $\rho = 0.724$; $p < 0.001$). We observed the lowest mean tumor site E.T. (40.0 °C) for the group treated with the lowest magnetic field strength, i.e. 9 mT (Table 4.1). Treatments with intermediate magnetic field strengths of 10 to 11 mT led to intermediate mean values of tumor site E.T. between 42.5 to 43.5 °C that were not statistically different. For the group treated with 12-mT magnetic field, the mean tumor site E.T. of 47.8°C was significantly larger than for all other magnetic field strengths.

The area under the curve (AUC) of temperature as a function of time is a parameter related to the heat dose delivered during a given treatment [25,26]. For the group treated with the highest magnetic field strength (12 mT), we recorded a more than two-fold increase in mean AUC (282.5 °C·min) as compared to the group treated with 9 mT (131.1 °C·min). Mean AUC for intermediate magnetic field strengths of 10 to 11 mT were again intermediate (Table 4.1). When considering the entire range of investigated magnetic field strengths, AUC was positively correlated with the 5 different magnetic field strengths applied (Spearman $\rho = 0.739$; $p < 0.001$).

3.3 *Above a threshold temperature, a larger delivered heat dose increases the extent of induced necro-apoptosis to whole tumor*

The necrosis to tissue ratio, as quantified using histology, was not significantly different between injected and non-injected controls, suggesting that the implant itself does not induce necrosis. We assessed the heating efficiency microscopically in terms of coagulation necrosis of vital tumor and adjacent tissues. In the case of low heat delivery, the extent of spontaneous and heat-induced necrosis overlapped. However, the extent of the necrosis was quite different between moderately and intensively heated tumors. Figure 4.2B shows heat-induced damage patterns for three tumors treated at magnetic field strengths of 10, 10.5 and 12 mT, respectively. For treatments associated with temperature higher than 44 °C, we observed extensive tumor necrosis and coagulation necrosis. In the vicinity of the

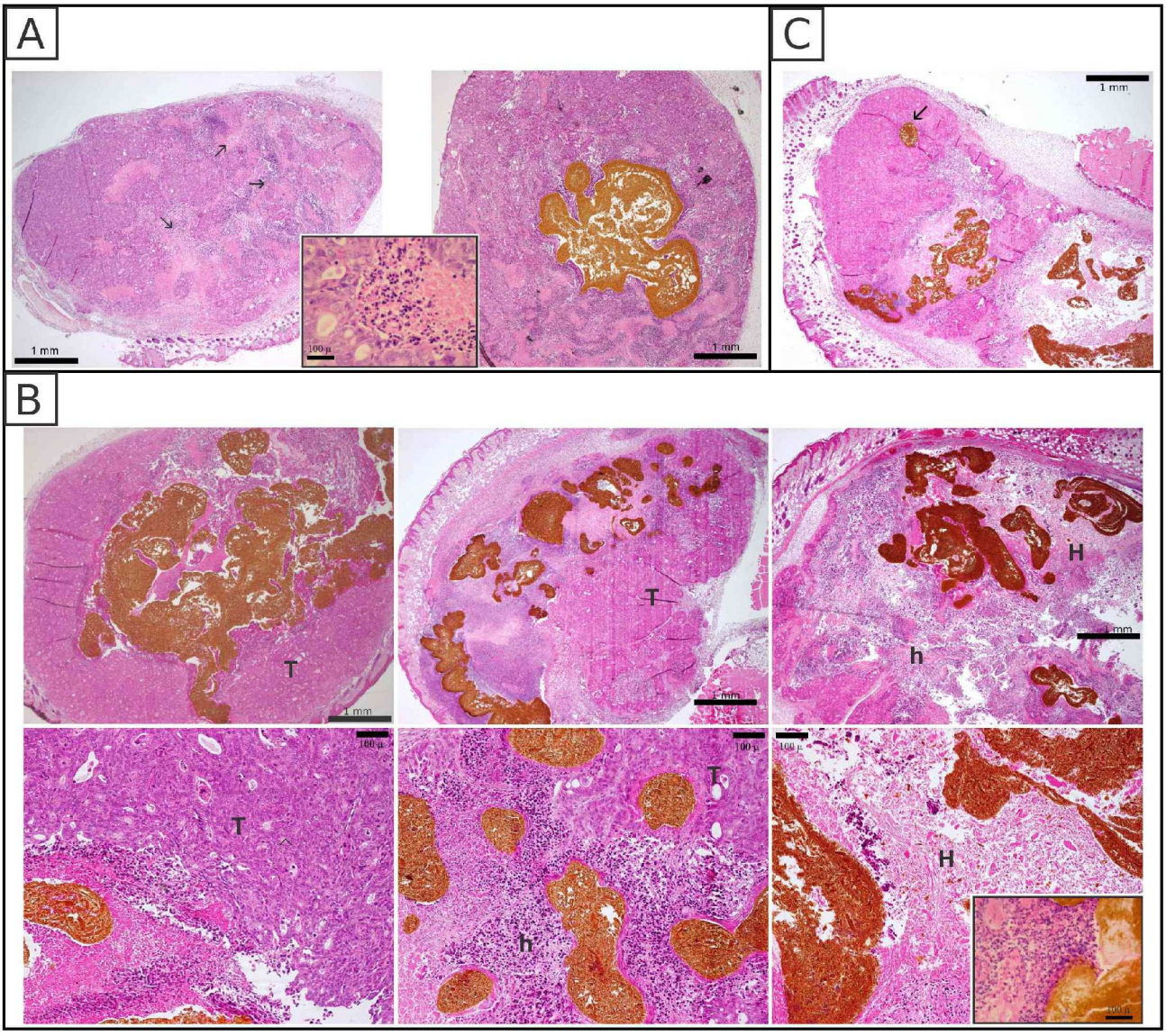

Figure 4.2. Microphotographs at D2 (with or without implant injection at D0 and hyperthermic treatment at D1).

Panel A shows at left the control Co112 tumor, with non-induced necrosis (arrow) that typically did not exhibit an inflammatory reaction (insert), and at right the control with the nonheated implant shown in brown. Panel B displays three treated tumors at low magnification in the upper row and at higher magnification in the lower row. On the left, a tumor treated with a magnetic field strength of 10 mT (MET = 39.5 °C, AUC = 152.8 °C1min) leaving most of viable tumor tissue (T) without any heat-induced necrosis. In the middle, a tumor treated with a magnetic field strength of 10.5 mT (MET = 44.0 °C, AUC = 211.8 °C1min) shows clear heat-induced necrosis (h) around the implant, but more distant tumor tissue remains viable. On the right, a tumor treated with a magnetic field strength of 12 mT (MET = 46.2 °C, AUC = 284.3 °C1min) illustrates heat induced necrosis (h) covering most of the tumor and effecting intense thermal damage (H) in the vicinity of implant, accompanied by an inflammatory reaction (neutrophils and macrophages, see insert). Panel C illustrates the topographic association between implant and heat-induced necrosis. A small isolated extension of the implant (arrow) did not trigger heat damage, in contrast to the more voluminous main body of the implant.

implant, we observed an inflammatory infiltrate of neutrophils and macrophages as part of non-specific immune response to necrosis. Focal necrosis of the immediately adjacent connective and muscle tissues can be attributed to heat, since this was absent in mice injected with implant alone or at lower heating levels. Likewise, the skin, especially over the implanted tumor, showed heat-induced necrosis. In some animals, muscle tissue at the peritoneal side of the tumor showed signs of thermal damage. For treatments reaching less than 42 °C, no significant heat-induced necrosis was observed. Notably, heat-induced necrosis was not observed in implanted mice exposed to the magnetic field strength of 9 mT and was only occasionally found in mice exposed to 10 or 10.5 mT, clearly depending on heating intensity. It was found that AUC was well correlated with heating efficiency at the tissue level, quantified in terms of the percentage of tumor necrosis (Spearman $\rho = 0.468$; $p < 0.05$).

3.4 *Magnetically-induced heat delivery through an implant is highly efficient in treating solid tumor for a magnetic field strength of 12 mT*

In groups of animals matched for tumor size, magnetically induced heating of the implant prolonged survival time as defined by growing to 10 times the initial tumor size. After a single 20-min treatment, a median survival time of 27 days was observed for the group treated with a magnetic field strength of 10.5 mT (Figure 4.3). Median survival time increased further to 37 days for mice treated with 12 mT, as compared with 12 days for non-implanted controls and 21 days for implanted controls. Finally, only one complete response was observed in the 10.5 mT group, while 5 of 11 animals (45 %) treated with 12 mT exhibited complete responses that persisted until the one-year mark, when mice were sacrificed. Kaplan-Meyer analysis revealed significant differences between the 10.5-mT treated group and the non-implanted control group ($p < 0.05$), while the 12-mT treated group was significantly different when compared to the implanted and non-implanted controls ($p<0.05$ and $p<0.01$, respectively).

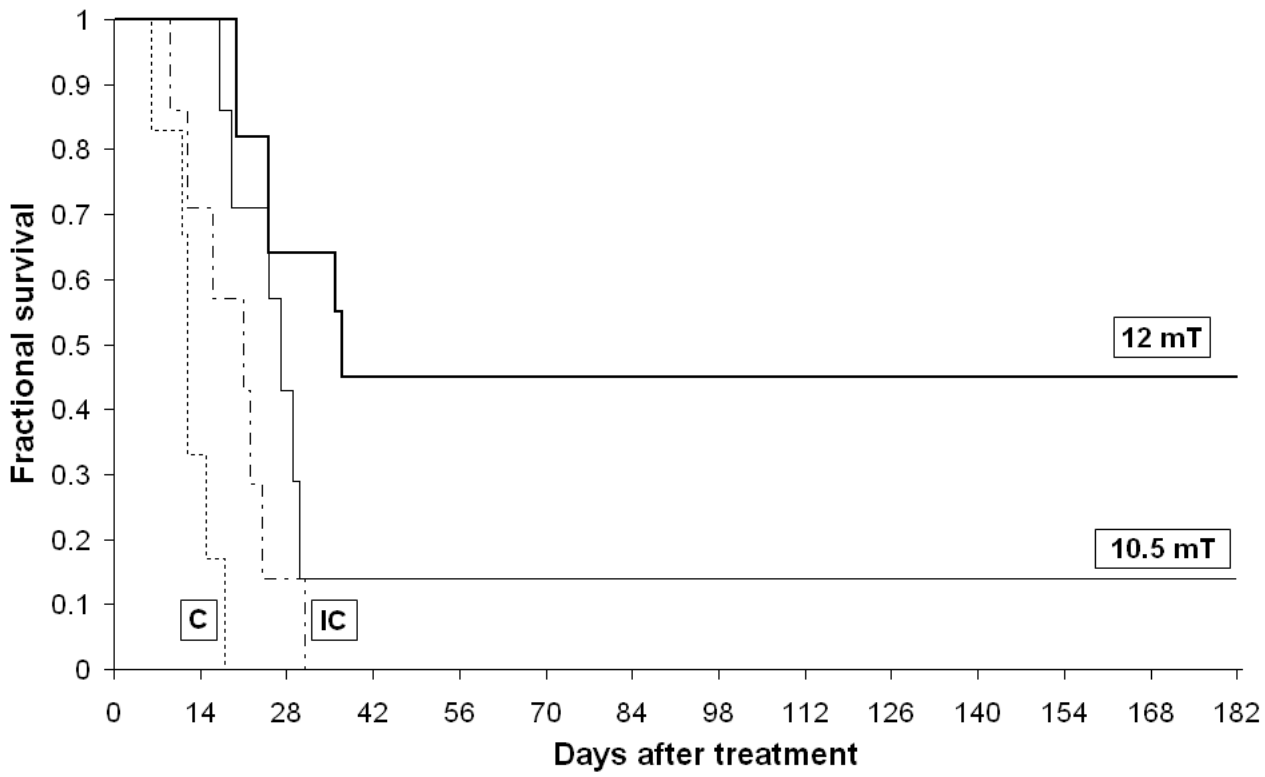

Figure 4.3: Survival curves.
Dotted line: control group (C), n = 6; dashed line: implanted control group (IC), n = 7; normal line: 10.5-mT treated group, n = 7; bold line 12-mT treated group, n = 11. Note that in the group treated with a 12-mT alternating magnetic field, 5 of 11 mice survived 12 months after treatment without tumor relapse.

3.5 Computerized Tomography allows for precise implant imaging

We studied implant precipitation pattern *in vivo* using Magnetic Resonance Imaging (MRI) and Computerized Tomography (CT) of two implanted and non-treated mice. In MRI, silica-embedded SPIONS led to a susceptibility artifact, partially masking the implanted tumor (Figure 4.4). We confirmed entrapment of the beads at the injection site through the absence of distant artifacts. In contrast, micro-computerized tomography allowed detailed imaging of the implant, confirming intra-tumor precipitation pattern of the implant (Figure 4.5). Image contrast was set in the bone density range

to ensure proper imaging of the high-density implant, albeit masking soft tissues. Randomly distributed density measurements (n=100) recorded in the implant volume suggested a relatively homogeneous iron distribution, with a variation coefficient of 10 % over the whole implant.

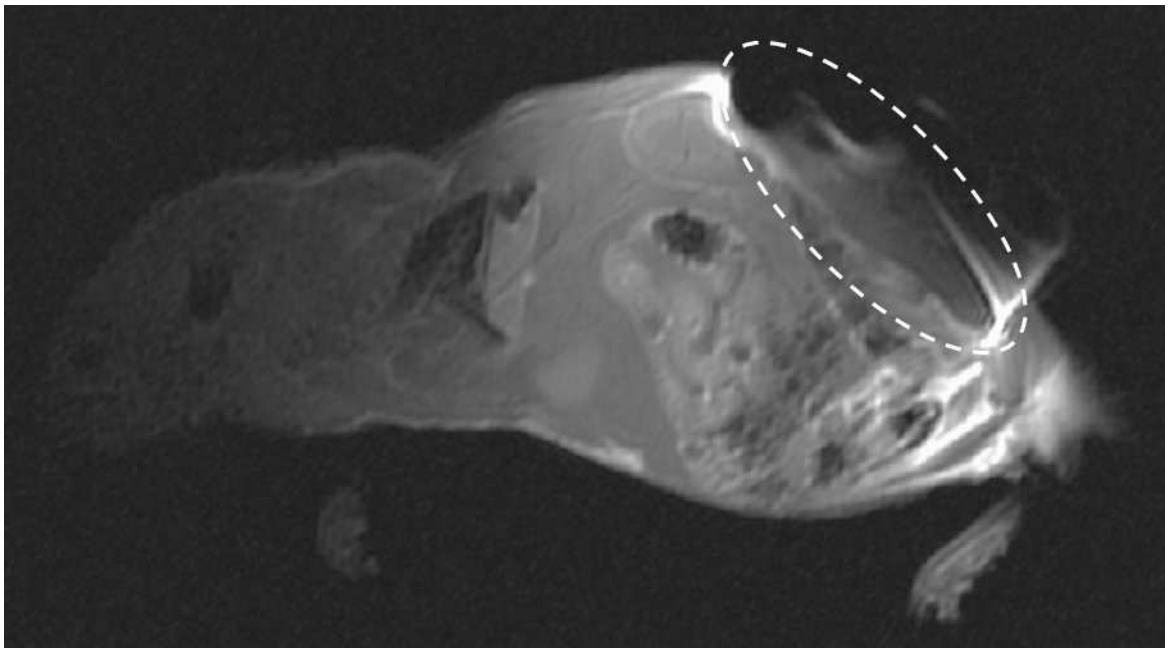

Figure 4.4. Implant imaging by MRI.
MRI imaging of a Swiss nude mouse bearing a subcutaneous tumor injected with 0.25 ml of the implant formulation, with a T1 weighted sequence. The tumor zone is enclosed in the dotted white circle, highlighting the susceptibility artifact caused by SPION entrapped in the implant.

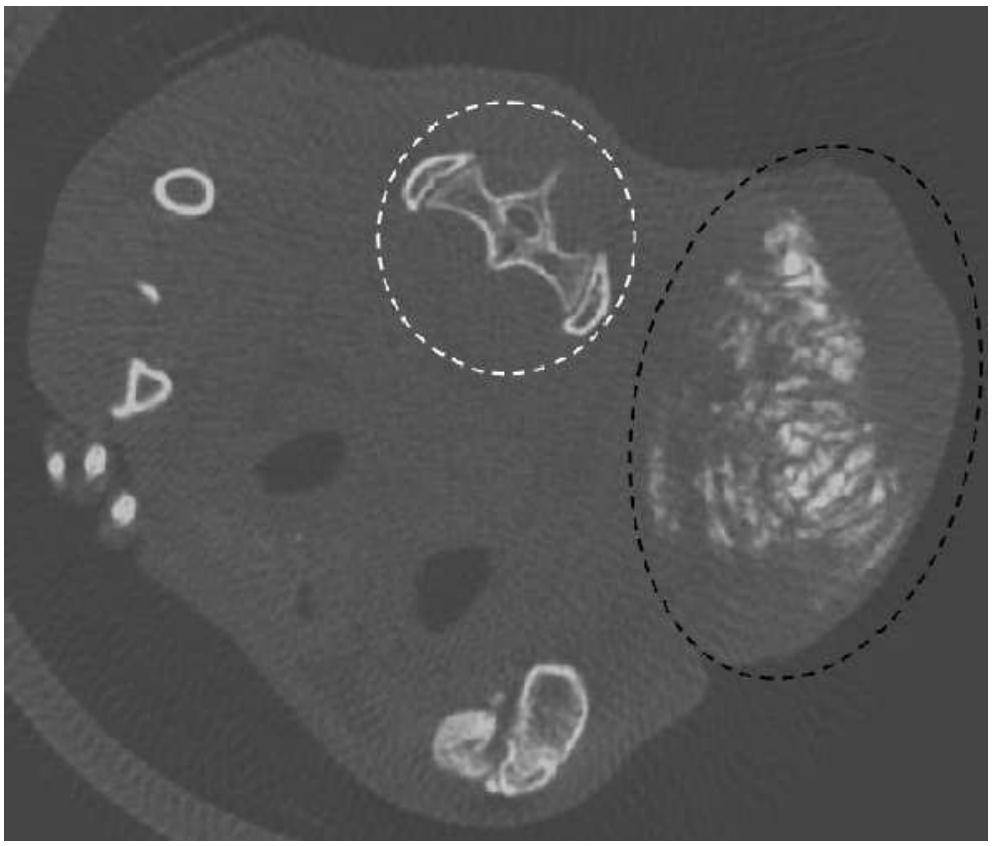

Figure 4.5. Implant imaging by micro-computerized tomography (CT)
CT of a Swiss nude mouse bearing a subcutaneous tumor punctured with 0.25 ml of the implant formulation. As presented in this transversal section, we can precisely localize the implant (in white) and the tumor that is enclosed within the dotted black circle. The SPIONs entrapped in the implant allowed for X-ray absorption with an absorption density close to that of bone (see, for instance, the spinal vertebrae and iliac wing highlighted by the dotted white circle). Note that the window is adjusted for bone density without further soft tissue contrast refinements or the use of contrast agent.

4 Discussion

Our results show the feasibility of implant-mediated hyperthermia using an injected formulation of superparamagnetic beads that solidifies upon contact with interstitial fluid.

A gradual injection gave sufficient time for the formulation to spread into the tumor before subsequent precipitation and solid implant formation in situ. The tumor necrotic center was initially filled, and the precipitation subsequently extended towards the peripheral tumor spaces. Although attractive, the concept of an implant layer in contact with the outer tumor rim, where vital cancer cells are found, seems impractical due to the dense heterogeneous tissue surrounding the tumor core. In the absence of image guidance, tumor core injection lead to a more controlled implantation. This last step was critical with regard to eventual occurrence of leakage. The implant volume was constrained *in situ* to match the tumor volume. The injection volume of 0.25 ml was acceptable even if it was larger than initial tumor volume. This is partly explained by implant mass loss following diffusion and exchange of DMSO with water (~ 16 %), and partly by tumor distension following implantation and edema resorption. Similar formulations without magnetic particle have shown in preliminary *ex vivo* experiments [27], that implant volume was constant in situ and that the DMSO solvent most likely induced tissue swelling. Noteworthy, the resulting viscoelasticity of such formulation, as in the case of bone cements, can lead to overestimation of the injected volume due to contraction. This can also be associated with needle withdrawal before complete flow arrests, as well as with compositional variations following filtration through reversible particle aggregates [28,29]. The implant was localized at the center of the tumor but it did extend into peripheral layers. This was particularly appropriate for magnetically-induced delivery of heat produced by the entrapped superparamagnetic micron-sized particles. This entrapment was very efficacious and we never observed particles outside the tumor volume under multiple orthogonal techniques (histology, CT and MRI). We also attempted to use smaller particles, including sub-micrometer silica beads and 20-nm bare SPIONs. We observed efficient entrapment in the precipitated polymer network, but, with these smaller beads, the preparation resulted in rheological behavior that was prone to leakage.

In a clinical scenario, the application of AMF could lead to safety concerns. The side effects of AMF can include nonspecific heating outside the target volume due to the magnetic induction of current density called eddy currents (EC) [30]. More problematic is the case of radiofrequencies [31], for which adverse excitation of neurons can be easily triggered by induced electric fields. Heat produced by EC, scaled as: $SAR_{EC} \propto (H \cdot f)^2 r^2$, where SAR is the specific absorption rate (W/g tissue), and r is the radius of exposed region [32], can lead to distant painful hot spots that would limit the values of f and H , and thus the heating possibilities. The AMF used here is associated with $(H \cdot f)$ values ranging from $10 \cdot 10^8$ to $13.5 \cdot 10^8$ A/(m·s) for 9 mT (7.2 kA/m) and 12 mT (9.6 kA/m), at 141 kHz. Theses fields did not induce any directly measurable effect in control mice that had not received any implant. Accordingly, we believe that this approach would be entirely appropriate for human [33]. In the case of AMF treatment of prostate cancer, the pelvic skin fold is at particular risk of hot spot triggered by EC. However values of $(H \cdot f)$ values up to $5 \cdot 10^8$A/(m·s) were safe for 100% of the patients [34,35]. As for AMF treatment of glioblastomas, no side effects were reported during skull exposition for $(H \cdot f)$ values up to $13.5 \cdot 10^8$ A/(m·s) [36]. $(H \cdot f)$ values higher than $20 \cdot 10^8$A/m/s have been used *in* and *ex vivo* [37,38]. Pulses of very high amplitude have been experimentally used in mice[32].

The investigated 9- to 12-mT field strengths induced a tissue temperature rise from mild hyperthermia in the range of 39 – 42 °C extending to cytotoxic moderate hyperthermia in the range of 42 – 48°C. Treatments at higher temperatures were associated with extensive tumor necrosis and collateral damage mainly to adjacent skin. It is worth mentioning that the tissue origin is of importance: mouse tissues are more sensitive to heat than the human tissues used here in form of the human tumor transplant.

Under alternating magnetic field induction, the measured skin temperatures were generally less than intra-tumor temperatures, so long as heating remained at non-toxic levels. However, on reaching toxic heat levels, the skin temperature rose to intra-tumoral levels (see Table 4.1). These observations underline the importance of cooling by tissue perfusion [39,40]. When skin blood perfusion breaks down as a consequence of heat damage to the vasculature, the cooling effect of blood perfusion stops and skin temperature raises to a value close to the tumor temperature.

The extent of heat-induced necrosis seemed to be related to the manner of implant distribution *in situ*. Thus, around extensions that were confluent or of large cross-section, necrosis was wider than around

thin implant extensions (Figure 4.2C). It is likely that the latter delivered less heat to surrounding tissues [41]. Certainly, this could result from a combination of different factors: first, a threshold mass for dissipating significant heat [42] from the implant center to distant tissue areas, and, secondly, a differential effectiveness in vascular cooling [43]. Indeed, since cooling efficiency is directly related to the contact area between implant and tissue, whereas heating power is proportional to implant mass, small implants that present a higher surface/mass ratio will be more efficiently cooled. Measurement of the necrosis rim width in biologically relevant implants as well as *in vitro* or *in vivo* thermal mapping studies indicated a necrosis extent on the order of 2-3 mm, compatible with previously published observations [44].

Our survival study revealed an important therapeutic potential for a single 20-min treatment based on the sole cytotoxicity of hyperthermia. We observed a minor growth delay in the group that received the implant but was not submitted to magnetically induced heating. Although we cannot fully exclude local toxicity of DMSO, this growth delay is more likely due to implant precipitation in capillaries and secondary hemostasis, leading to antineoplastic effects through hypoxia. Magnetically induced hyperthermia treatment, however, did increase significantly the median survival time. A number of definitive complete responses were observed at a rate that depended on the magnetic field amplitude. It is well known that temperature distribution in tumor is essential to assessing treatment responses [45]. This distribution is directly related to magnetic field strength and implant localization, and its control depends on thermometry data. The suboptimal heating of peripheral tumor cells allows for a tumor relapse when tissue escapes the cytotoxic area of the temperature gradient. In comparison to the 10.5-mT single 20-min treatment, these considerations suggest that one might achieve a better outcome by increasing the magnetic field strength to 12 mT.

A survival study using imaging techniques could adress the important issue of implant distribution. It would allow controlled injection of the implant and, if necessary, exact localization of thermometry probes. Clinically, imaging could allow a control of the correct implant size and localization to further improve or predict heat delivery. While MRI appeared most sensitive to the presence of the superparamagnetic beads, leading locally to some artifacts, CT was most appropriate for implant imaging without any obvious artifacts in its vicinity. Furthermore, soft tissue contrast agent would

allow studies of intratumoral implant distribution.

Regarding the implant durability, we retrieved intact implants as expected at D14, but we observed partial degradation at D48 in two treated mice. No implant or tumor was macroscopically observable after the one year survival period. These sparse data points suggest that unexpected degradation occurs after a few months. The high solid fraction may account for loss of implant strength, and the heating process may accelerate focal inflammatory events. These observations warrant further investigations into the distribution and metabolism pathways of iron in the implants, compared to SPIONs, free or embedded in silica beads.

In conclusion, these results demonstrate the efficacy of superparamagnetic particles embedded in an *in situ* formed implant to deliver thermal energy in a therapeutically relevant range [46]. Sustained moderate hyperthermia at clinically relevant field strengths were produced in a necrotizing tumor model, holding promise for implant-mediated local hyperthermia therapy.

5 Acknowledgements

Grant support: Swiss National Science Foundation (grant 3200B0-104508), Switzerland. For histology processing, we are thankful to Susana Leuba, Department of Pathology, Hospital University of Lausanne, Switzerland. We also thank Xavier Montet of the Radio-diagnostic Service, University Hospital of Geneva, Switzerland for MRI and micro-computerized tomography imaging support. We wish to thank Frances Godson of the Radio-oncology Service, University Hospital of Lausanne, Switzerland for manuscript proof reading.

6 References

[1] Hildebrandt B, Wust P, Ahlers O, Dieing A, Sreenivasa G, Kerner T, Felix R, Riess H. The cellular and molecular basis of hyperthermia. Crit Rev Oncol Hematol 2002; 43(1):33-56.

[2] Hand JW, Streffer C, van Beuningen D, Vaupel P, Kallinowski F, Molls M, Scherer E, Engelhardt

R. Hyperthermia and the Therapy of Malignant Tumors. Berlin: Springer-Verlag, 1987.
[3] Falk MH, Issels RD. Hyperthermia in oncology. Int J Hyperthermia 2001; 17(1):1-18.
[4] Dewhirst MW, Viglianti BL, Lora-Michiels M, Hanson M, Hoopes PJ. Basic principles of thermal dosimetry and thermal thresholds for tissue damage form hyperthermia. Int J Hyperthermia 2003; 19(3):267-294.
[5] Sapozink MD, Corry PM, Kapp DS, Myerson RJ, Dewhirst MW, Emami B, Herman T, Prionas S, Ryan T, Samulski T, Sapareto S, Shrivastava P, Stauffer P, Waterman F. RTOG Quality assurance guidelines for clinical trials using hyperthermia for deep-seated malignancy. Int J Radiat Oncol Biol Phys 1991; 20(5):1109-1115.
[6] Rosensweig RE. Heating magnetic fluid with alternating magnetic field. J Magn Magn Mater 2002; 252:370-374.
[7] Wang XM, Gu HC, Yang ZQ. The heating effect of magnetic fluids in an alternating magnetic field. J Magn Magn Mater 2005; 293(1):334-340.
[8] Jordan A, Wust P, Fahling H, John W, Hinz A, Felix R. Inductive heating of ferrimagnetic particles and magnetic fluids - Physical evaluation of their potential for hyperthermia. Int J Hyperthermia 1993; 9(1):51-68.
[9] Jordan A, Scholz R, Wust P, Fahling H, Felix R. Magnetic fluid hyperthermia. In: Hafeli U, Schütt W, Teller J, Zborowski M, eds. Scientific and Clinical Applications of Magnetic Carriers. New York: Plenum Press, 1997, pp. 569-595.
[10] Johannsen M, Gneveckow U, Thiesen B, Taymoorian K, Cho CH, Waldofner N, Scholz R, Jordan A, Loening SA, Wust P. Thermotherapy of prostate cancer using magnetic nanoparticles: Feasibility, imaging, and three-dimensional temperature distribution. Eur Urol 2006; 52(6):1653-1662.
[11] Wust P, Gneveckow U, Johannsen M, Bohmer D, Henkel T, Kahmann F, Sehouli J, Felix R, Ricke J, Jordan A. Magnetic nanoparticles for interstitial thermotherapy – feasibility, tolerance and achieved temperatures. Int J Hyperthermia 2006; 22(8):673-685.
[12] Johannsen M, Gneveckow U, Taymoorian K, Thiesen B, Waldofner N, Scholz R, Jung K, Jordan A, Wust P, Loening SA. Morbidity and quality of life during thermotherapy using magnetic nanoparticles in locally recurrent prostate cancer: Results of a prospective phase I trial. Int J Hyperthermia 2007; 23(3):315-323.
[13] Maier-Hauff K, Rothe R, Scholz R, Gneveckow U, Wust P, Thiesen B, Feussner A, von Deimling A, Waldoefner N, Felix R, Jordan A. Intracranial thermotherapy using magnetic nanoparticles combined with external beam radiotherapy: Results of a feasibility study on patients with glioblastoma multiforme. J Neurooncol 2007; 81(1):53-60.
[14] Moghimi SM, Hunter AC, Murray JC. Nanomedicine: current status and future prospects. FASEB Journal 2005; 19(3):311-330.
[15] Chastellain M, Petri A, Gupta A, Rao KV, Hofmann H. Superparamagnetic silica-iron oxide nanocomposites for application in hyperthermia. Adv Eng Mater 2004; 6(4):235-241.
[16] Povlsen CO, Rygaard J. Heterotransplantation of human adenocarcinomas of colon and rectum to mouse mutant nude. A study of 9 consecutive transplantations. Acta Pathol Microbiol Scand [A] 1971; 79(2):159-169.
[17] Sun LQ, Vogel CA, Mirimanoff RO, Coucke P, Slosman DO, Mach JP, Buchegger F. Timing

effects of combined radioimmunotherapy and radiotherapy on a human solid tumor in nude mice. Cancer Res 1997; 57(7):1312-1319.

[18] Sutherland R, Buchegger F, Schreyer M, Vacca A, Mach JP. Penetration and binding of radiolabeled anti-carcinoembryonic antigen monoclonal antibodies and their antigen binding fragments in human colon multicellular tumor spheroids. Cancer Res 1987; 47(6):1627-1633.

[19] Budden R, Kuhl UG, Buschmann G. Studies on pharmacodynamic activity of several drug solvents .1. Diethyleneglycolmonoethylether, N,N-Diethylacetamide, Dimethylsulfoxide. Arzneimittelforschung 1978; 28(9):1571-1579.

[20] Mottu F, Laurent A, Rüfenacht DA, Doelker E. Organic solvents for pharmaceutical parenterals and embolic liquids. A review of toxicity data. PDA J Pharm Sci Technol 2000; 54(6):456-469.

[21] Mottu F, Stelling MJ, Rüfenacht DA, Doelker E. Comparative hemolytic activity of undiluted organic water-miscible solvents for intravenous and intra-arterial injection. PDA J Pharm Sci Technol 2001; 55(1):16-23.

[22] Buchegger F, Haskell CM, Schreyer M, Scazziga BR, Randin S, Carrel S, Mach JP. Radiolabeled fragments of monoclonal antibodies against carcinoembryonic antigen for localization of human colon carcinoma grafted into nude mice. J Exp Med 1983; 158(2):413-427.

[23] Sutherland RM, Buchegger F, Schreyer M, Vacca A, Mach JP. Penetration and binding of radiolabeled anti-carcinoembryonic antigen monoclonal antibodies and their antigen binding fragments in human colon multicellular tumor spheroids. Cancer Res 1987; 47(6):1627-1633.

[24] Sutherland RM, Sordat B, Bamat J, Gabbert H, Bourrat B, Mueller-Klieser W. Oxygenation and differentiation in multicellular spheroids of human colon carcinoma. Cancer Res 1986; 46(10):5320-5329.

[25] Sapareto SA, Dewey WC. Thermal dose determination in cancer therapy. Int J Radiat Oncol Biol Phys 1984; 10(6):787-800.

[26] Lepock JR. Cellular effects of hyperthermia: Relevance to the minimum dose for thermal damage. Int J Hyperthermia 2003; 19(3):252-266.

[27] Jordan O, Doelker E, Defabiani N, Caviezel A, Iselin C. Novel injectable urethral bulking agents for the treatment of urinary incontinence. J Mater Sci Mater Med 2004; 15(4):519-522.

[28] Bohner M. Theoretical considerations on the injectability of calcium phosphate cements. Proceedings of the 17th European Society for Biomaterials Conference, Barcelona, Spain, September 2002

[29] Bohner M, Baroud G. Injectability of calcium phosphate pastes. Biomaterials 2005; 26(13):1553-1563.

[30] Bernhardt JH, Brix G. Safety aspects of magnetic fields. In: Andra W, Nowak H, eds. Magnetism in Medicine. Weinheim: Wiley-CH, 2007, pp. 76-95.

[31] Gellermann J, Wust P, Stalling D, Seebass M, Nadobny J, Beck R, Hege HC, Deuflhard P, Felix R. Clinical evaluation and verification of the hyperthermia treatment planning system HyperPlan. Int J Radiat Oncol Biol Phys 2000; 47(4):1145-1156.

[32] Ivkov R, DeNardo SJ, Daum W, Foreman AR, Goldstein RC, Nemkov VS, DeNardo GL. Application of high amplitude alternating magnetic fields for heat induction of nanoparticles localized in cancer. Clin Cancer Res 2005; 11(19 Pt 2):7093s-7103s.

[33] Wust P, Gneveckow U, Johannsen M, Bohmer D, Henkel T, Kahmann F, Sehouli J, Felix R,

Ricke J, Jordan A. Magnetic nanoparticles for interstitial thermotherapy--feasibility, tolerance and achieved temperatures. Int J Hyperthermia 2006; 22(8):673-685.

[34] Johannsen M, Gneveckow U, Thiesen B, Taymoorian K, Cho CH, Waldofner N, Scholz R, Jordan A, Loening SA, Wust P. Thermotherapy of prostate cancer using magnetic nanoparticles: Feasibility, imaging, and three-dimensional temperature distribution. Eur Urol 2006; 52(6):1653-1662.

[35] Johannsen M, Gneveckow U, Taymoorian K, Thiesen B, Waldofner N, Scholz R, Jung K, Jordan A, Wust P, Loening SA. Morbidity and quality of life during thermotherapy using magnetic nanoparticles in locally recurrent prostate cancer: Results of a prospective phase I trial. Int J Hyperthermia 2007; 23(3):315-323.

[36] Maier-Hauff K, Rothe R, Scholz R, Gneveckow U, Wust P, Thiesen B, Feussner A, von Deimling A, Waldoefner N, Felix R, Jordan A. Intracranial thermotherapy using magnetic nanoparticles combined with external beam radiotherapy: Results of a feasibility study on patients with glioblastoma multiforme. J Neurooncol 2007; 81(1):53-60.

[37] Hilger I, Andra W, Hergt R, Hiergeist R, Schubert H, Kaiser WA. Electromagnetic heating of breast tumors in interventional radiology: In vitro and in vivo studies in human cadavers and mice. Radiology 2001; 218(2):570-575.

[38] Hilger I, Hiergeist R, Hergt R, Winnefeld K, Schubert H, Kaiser WA. Thermal ablation of tumors using magnetic nanoparticles - An in vivo feasibility study. Invest Radiol 2002; 37(10):580-586.

[39] Lyng H, Rofstad EK. Thermal dose and secondary tumour cell death. Int J Hyperthermia 1993; 9(5):755-61.

[40] Moroz P, Jones SK, Gray BN. The effect of tumour size on ferromagnetic embolization hyperthermia in a rabbit liver tumour model. Int J Hyperthermia 2002; 18(2):129-40.

[41] Andra W, d'Ambly CG, Hergt R, Hilger I, Kaiser WA. Temperature distribution as function of time around a small spherical heat source of local magnetic hyperthermia. J Magn Magn Mater 1999; 194(1-3):197-203.

[42] Rabin Y. Is intracellular hyperthermia superior to extracellular hyperthermia in the thermal sense? Int J Hyperthermia 2002; 18(3):194-202.

[43] Kolios MC, Worthington AE, Holdsworth DW, Sherar MD, Hunt JW. An investigation of the flow dependence of temperature gradients near large vessels during steady state and transient tissue heating. Phys Med Biol 1999; 44(6):1479-1497.

[44] Hergt R, Andra W. Magnetic hyperthermia and thermoablation. In: Andra W, Nowak H, eds. Magnetism in Medicine. Weinheim: Wiley-CH, 2007, pp. 551-570.

[45] Dewhirst MW, Sneed PK. Those in gene therapy should pay closer attention to lessons from hyperthermia. Int J Radiat Oncol Biol Phys 2003; 57(2):597-599.

[46] Hergt R, Andra W, d'Ambly CG, Hilger I, Kaiser WA, Richter U, Schmidt HG. Physical limits of hyperthermia using magnetite fine particles. IEEE Trans Magn 1998; 34(5):3745-3754.

Summary and conclusions

In this work, we address originally the pharmaceutical formulation of injectable implants that are capable of solidifying *in situ* to be used as a vehicle for magnetic microparticles that are entrapped in the implant formed to perform a local moderate hyperthermia treatment of solid tumors in a mouse model. Microparticles that are made of superparamagnetic iron oxide nanoparticles (SPIONs) embedded in a silica matrix were found to be highly suitable for this purpose.

The developed injectable formulations could prove helpful in numerous-specific *in vivo* applications of magnetically induced hyperthermia by injectable implantation. Moreover, in the search for a better understanding of this type of injectable formulation, we have identified the main parameters at the macroscopic and microscopic levels that are necessary for the adaptation of various formulations when envisaged as vehicle for microparticles. A crucial influence of the incorporated microparticles on the rheological behavior appeared to consist in a general lowering of mechanical strengths. On the one hand, this effect is undoubtedly advantageous in the viscous state, i.e., the liquid formulation state, to favor viscous flow and improve syringeability. Some formulations that are difficult to inject could be more easily injected when incorporating microparticles. On the other hand, for the purpose of efficiently entrapping the microparticles in an implant, this rheological influence becomes more of a drawback in the solid state, i.e., the implant formed *in situ*, by lowering the durability of the implant and raising its friability and sensitivity to erosion. Both aspects had to be balanced to obtain a successful formulation.

Among the investigated hydrogel formulations, we did not succeed in incorporating the microparticles into chitosan-based formulations due to the probable incompatibility of the silica matrix with this positively charged polymer. This phenomenon may be remedied with other more sophisticated embedding matrices or through a formulation adaptation that we did not implement. We could not obtain suitable hydrogel formulations when they were based on the gelation of poloxamer or internal gelation of alginate. With these formulations, which already lead to implants with lower durability, even in the absence of microparticles, a poor entrapment of microparticles, if any, was observed.

Only hydrogel formulations based on the external gelation of an aqueous dispersion of 2% w/v of

sodium alginate appeared to be suitable, with a maximum incorporable fraction of microparticles of 20% w/v, with regard to heating capacities. It should be noted that the syringeability could probably benefit from the use of more-suitable devices in place of the one used in our work.

Organogel formulations could be straightforwardly injected through a syringe that is compatible with the use of organic solvents, but the use of solvents raises toxicity concerns. In comparison with the hydrogel formulation, single-solvent organogel formulations were prone to incorporate a large fraction of microparticles that were efficiently entrapped *in situ*. The formulation of poly(ethylene-*co*-vinyl alcohol) (EVAL) 8 % w/v in DMSO demonstrated the best performance in terms of particle incorporation capacities, syringeability and mechanical implant characteristics, in particular after intratumoral *in vivo* injection. The less toxic co-solvent formulations showed interesting syringeability and implant characteristics for a more limited incorporable fraction of microparticles. This is related to the fact that the polymer is in a lower state of solvation when dispersed in a mixture of hydrophobic (yet water miscible) solvent with more hydrophilic organic solvents, compared with the single organic solvent dispersion. This led to an increase in viscosity and thus a decrease in syringeability. More viscous formulations required a lower injection rate than the single-organogel formulations. In particular, during the injection of the more viscous co-solvent formulations (it is noteworthy that these were also the most viscous hydrogel formulations), the tip of the needle had to be shifted within the tumor along a trajectory that was adapted to obtain a homogeneous distribution of the implant, as was reported for the intratumoral injection of magnetic liposome.

On the model of fundamental works in membrane technology, the systematic study of the formulations based on injectable precipitating organogels led us to lay the basis of a microstructural classification that could be helpful for further work in the present field. Thanks to the examination of the precipitation kinetics of the injectable formulations at the microscopic level and to observations of the formed implants, we could understand how crucial the rheological influence of the microparticles and the co-solvents are on the precipitation kinetics, (particularly) at the precipitation interface. Consequently, the rheological behavior and co-solvent nature governed the bulk precipitation and, ultimately, the mechanical and microstructure characteristics of the final implant.

Thanks to the *in vivo* testing, we learned that the injection rates used to inject small drug solutions are not suitable and favor leakage. A slightly slower and more gradual injection rate, with short breaks, is

preferred because it allows the implant to diffuse in interstitial spaces before the desolvatation and precipitation take place in these spaces. Because the injectable formulations forming an implant *in situ* have relatively high viscosity, a high injection rate seemed to be associated with a higher interstitial pressure augmentation that could cause vascular and interstitial spaces to collapse. This characteristic was basically a distinctive feature of *in vivo* injections, compared with *in vitro* test injections in water during preformulation.

For one selected formulation of both the hydrogel and organogel type, i.e., alginate 2% w/v in an aqueous dispersion incorporating 20 % w/v of magnetic microparticles and EVAL 8 % w/v in DMSO incorporating 40 % w/v of magnetic microparticles, we observed that the static magnetic properties of the microparticles were preserved once they were entrapped in the solid implant formed from the hydrogel and organogel formulations. We also found that the magnetic properties of the implants and their heating capacities are both related to the concentration of microparticles. The fact that the intrinsic magnetic properties remained constant for the implants with maximal microparticle concentrations suggests that the silica matrix efficaciously prevents unwanted magnetic interactions, which could affect the heating properties. This point would benefit from further magnetic characterization under dynamic conditions, with hysteresometry, for instance. Because the specific power loss (SPL) is measured with several different methods in the literature, which makes SPL values difficult to compare, we used two orthogonal methods to identify the true value of the SPL. This resulted in a SPL value of about 20 W per gram of iron oxide, which accounted for 19.6 % w/v of the microparticles.

With this information, we could validate the feasibility of such an approach directly *in vivo*, in a tumor model relevant for oncology: a human colocarcinoma engrafted in Swiss nude mice, using the formulation of EVAL 8% w/v in dimethylsulfoxide incorporating 40% w/v of magnetic microparticles. According to the thermometry investigations and the biological responses to the moderate hyperthermia revealed in our study, a value of 12 mT was observed to be the optimal magnetic amplitude of the alternating magnetic field generated in our set-up for the fixed and theoretically optimized frequency of 141 kHz. In comparison, 11 mT could lead to the temperature range corresponding to mild hyperthermia. Regarding the SPL, the *in vivo* calculated values agreed well with the *in vitro* values

despite slight inter-batch variations in the microparticles used for some *in vitro* investigations and for the *in vivo* investigation. We could thus demonstrate that the implant formed *in situ* could cast and heat the subcutaneous Co112 tumor. Once implanted, there was no apparent modification of the solid implant upon heating compared with nonheated controls. The survival studies revealed that the hyperthermia treatment mediated by the magnetically induction of implant heating was able to significantly delay the median tumor growth time, with an effect that was positively related to the magnetic field amplitude. Additionally, the survival rate increased from 10 to 45 % with increasing magnetic field from 10.5 to 12 mT, respectively. This suggests a substantial potential in terms of tumor response and survival that could be of therapeutic interest.

Considered altogether, our results explain the basic and critical parameters for the proper development of injectable formulations to form an implant *in situ*. The characteristics of the polymer solution, essentially its viscosity, together with the necessary particles fraction for convenient heating, are undoubtedly the limiting factors for injectability. These formulation parameters influence the characteristics of the implant in other ways once the implant has been formed, and they should be considered more carefully in future investigations or developments of such formulations. When a solid implant of high mechanical strength is required, such as in vertebroplasty in place of polymerizing cement, the formulation forming an implant *in situ* can be oriented toward concentrated polymer solutions, which are highly viscous and can support a high magnetic particle fraction. The detrimental effect on syringeability would reserve their injection to the large cannulas and devices in use for this technique but would supply a large heating capacity. Applications to vertebroplasty are among the most promising for the studied formulations.

The implants with intermediary mechanical characteristics *in situ* , i.e., of lower polymer concentration together with the adapted magnetic particle concentration, would be suitable for use as bulking agent in lesioned bladders or prostates, similar to the soft materials already indicated. The corollary medium injectability characteristics would only be applicable for the relatively invasive injection technique that these anatomic indications allow. This would ultimately permit a local moderate hyperthermia treatment of a possibly cancerous lesion. As is the case for vertebroplasty, prostate cancer treatment is a field with a high demand for novel approaches, for which the present findings would be of particular

relevance.

Finally, such an injectable formulation, loaded with active principle, whose composition would permit a syringeability that is applicable for minimally invasive injections, i.e., low content in polymer or magnetic particles, would also form *in situ* an implant of limited mechanical strength. This would be useful in situations such as those for which pharmaceutical depots are needed. The heating capacities with available inductors for most of the presently developed magnetic particles are also limited. As such, this technique could only be used for mild hyperthermia or for heat-triggered drug release as well as for the heat-targeted accumulation of systemically administrated drugs or to locally increase the therapeutic index. This technique also has the potential for important additive or synergistic effects. Here, the improvement of magnetic particles and the scrupulous screening of the formulation parameters raised in our work would be crucial to obtain the maximal heating capacity, heating localization and conditions of maximal additive or synergistic effects in combination with other therapeutic approaches.

Résumé

Dans ce travail, nous envisageons une approche galénique originale basée sur la formulation de préparations injectables capables de se solidifier *in situ*, servant de véhicule de microparticules magnétiques qui seront piégées dans l'implant formé en vue de permettre un traitement de tumeurs solides modèles chez la souris par hyperthermie locale modérée. Les particules magnétiques consistent en une matrice de silice poreuse qui renferme des nanoparticules d'oxyde de fer superparamagnétiques (SPIONs). Ces nanoparticules, en permettant l'interaction avec un champ magnétique alternatif de source externe, génèrent la chaleur que l'implant délivre ainsi à la tumeur. Leur potentiel pour l'hyperthermie magnétiquement induite a déjà été démontré en clinique après leur injection intratumoral sous forme de suspension, selon la technique dite hyperthermie *fluide magnétique (Magnetic Fluid Hyperthermia*), que nous ne traiterons pas directement ici, mais dont nous évoquerons certains aspects incontournables. Dans notre cas, le champ magnétique alternatif provient d'un générateur couplé à une bobine cylindrique permettant d'y placer une souris porteuse de la tumeur implantée à traiter, à la fréquence théoriquement prédéterminée de 141 kHz.

Nous avons tout d'abord tenté, au travers d'un travail bibliographique de large portée et de réflexions approfondies, de définir la place de notre approche en regard des particularités techniques, biologiques et surtout physiopathologiques de l'hyperthermie, en se concentrant sur ses modalités locales pour le traitement de tumeurs solides et ce en regard des biomatériaux variés qui peuvent être indiqués pour l'induction magnétique de l'hyperthermie locale.

Nous avons ensuite abordé notre travail de formulation pharmaceutique dans l'optique de cerner la fraction maximale de microparticules magnétiques qui puisse être véhiculée, au travers d'études *in vitro* complétées *in vivo* le cas échéant. D'un côté, nous avons étudié des formulations aqueuses à base d'hydrogels qui forment un implant après injection selon des mécanismes variés: par thermoréversion pour le chitosan et les poloxamères - formulations qui se sont révélées infructueuses - et par pontage ionique, ici de l'alginate par l'ion calcium. Deux alternatives en relation avec l'injectabilité ont été envisagées. La première a trait à un dispositif bi-compartimental de co-injection avec dans un compartiment la dispersion aqueuse d'alginate de sodium, à laquelle il convient absolument d'ajouter les microparticules magnétiques que l'on souhaite incorporer (20 % m/V maximum), et dans l'autre une

solution de chlorure de calcium. Lors du mélange qui se réalise à l'entrée de l'aiguille, les ions calcium diffusent rapidement et interagissent avec les unités guluroniques de l'alginate, déclenchant la formation du gel qui constituera l'implant, processus que l'on qualifie de *gélification externe*. Bien que peu pratique, ceci a conduit à des implants de bonne qualité, caractérisés par une distribution intratumorale acceptable bien qu'ayant tendance à l'inhomogénéité. Un mécanisme alternatif de gélification retardée, dite *gélification interne*, basé sur le mélange de la dispersion d'alginate (à laquelle il convient préférentiellement d'incorporer les microparticules magnétiques) avec une suspension de sel de calcium peu soluble (carbonate, phosphate ou sulfate) permet une injectabilité standard pendant une fenêtre de temps acceptable, celle de la dissolution du sel de calcium. Malheureusement, la qualité des implants ainsi formés ne s'est pas révélée adéquate.

D'un autre côté, nous avons développé une large gamme de formulations à base d'organogel capables de former par précipitation un implant *in situ* lors de l'échange avec l'eau tissulaire du solvant organique de la solution de polymère. Une variété d'associations de polymères et de solvants organiques a été étudiée. Concernant les polymères, nous nous sommes intéressés à un poly(éthylène-*co*-alcool vinylique) (EVAL®), à des polyuréthanes à dominante de monomères aromatiques ou aliphatiques (Tecothane® et Tecogel®, respectivement), à un copolymère acrylique, le poly(méthacrylate de méthyle-*co*-acrylate d'éthyle) (Paraloid A12®), à deux acétates de cellulose, l'un de bas poids moléculaire (CA-320S®), l'autre de plus haut poids moléculaire (CA-398-3®) et finalement à un acéto-butyrate de cellulose (CAB-381-2®). Nous avons aussi examiné différents solvants candidats à la formulation d'injectables: le diméthylsulfoxyde, la N-méthylpyrrolidone, le glycofurol, le diméthyl-isosorbide et la 2-pyrrolidone. L'injectabilité et la qualité des implants formés par les formulations à base d'organogels se sont souvent montrées supérieures à celle des formulations à base d'hydrogels. Ces formulations montrent cependant une certaine toxicité due au solvant organique, dont la part systémique, qui est apparue exacerbée du fait du modèle animal, apparaît indésirable. Nous avons alors développé des formulations basées sur l'incorporation d'un « co-solvant » plus hydrophile et moins toxique, en remplacement d'une partie du solvant organique de base qui constitue les formulations précédentes, dites « en solvant simple ». Pour ce faire, nous sommes plus particulièrement intéressés au propylène glycol, au polyéthylène glycol 200 et au N-(2-hydroxyéthyl)lactamide. Ces formulations, dites en « co-solvant », ont démontré un moindre pouvoir d'incorporation des microparticules magnétiques, à une concentration finalement comparable en efficacité à celle observée pour les

formulations à base d'hydrogels. Ceci est à relier avec l'augmentation de viscosité associée à l'incorporation de solvants plus hydrophiles, dénotant une diminution de la capacité de ces mélanges de solvants à solubiliser les polymères, ceci au détriment de l'injectabilité. Nous avons en revanche noté une bonne distribution de l'implant dans la tumeur. À noter que l'influence du co-solvant, tout comme celle des microparticules sur le front de précipitation, est apparue cruciale pour comprendre les caractéristiques mécaniques de l'implant formé dans son état final. Les études microscopiques poussées nous ont amenés à proposer une classification des implants fondée sur leur microstructure en lien avec la cinétique de précipitation, classification d'intérêt très général pour les futurs travaux de formulation de tels implants.

Nous avons par ailleurs conduit une étude des caractéristiques magnétiques, ainsi que des capacités de chauffage qui leur sont associées, et vérifié que celles-ci soient préservées au sein des implants de deux formulations représentatives des hydrogels et des organogels, à savoir une dispersion aqueuse alginate de sodium à 2% m/V et une dispersion d'EVAL à 8% m/V dans le diméthylsulfoxyde, incorporant respectivement 20 et 40 % m/V de microparticles magnétiques.

Pour la validation de la faisabilité technique de cette modalité d'hyperthermie *in vivo*, nous avons sélectionné en première intention la formulation d'EVAL à 8% m/v dans le diméthylsulfoxyde incorporant 40 % m/V de microparticules. L'injection intratumorale, a été suivie, le lendemain, d'une séance de 20 minutes d'induction magnétique de l'hyperthermie. Les études thermométriques lors de cette expérience d'hyperthermie nous ont permis de déterminer l'amplitude de champ magnétique optimale, 12 mT, afin d'obtenir les températures de l'ordre de 43 à 45°C qui relèvent de l'hyperthermie dite modérée (les amplitudes inférieures conduisant à des températures de 40 à 43°C qui caractérisent l'hyperthermie dite douce). Avec ce même schéma de traitement hyperthermique, les études de survie après traitement ont confirmé le potentiel antitumoral d'un tel traitement par hyperthermie seule. Pour une amplitude de 12 mT, nous avons observé un taux de survie des animaux à 1 an d'environ 45 %, alors qu'il n'a été que de 10 % pour l'amplitude de 10,5 mT et nul pour les témoins. Ceci suggère finalement un potentiel thérapeutique qui pourrait intéresser l'oncologie clinique, qui fait avec succès de plus en plus appel à l'hyperthermie douce, voire, si possible modérée, comme traitement adjuvant pour améliorer le contrôle de l'évolution de la tumeur.

Les facteurs dénotés dans ce travail influencent par ailleurs les caractéristiques de l'implant, et seront amenés pour les prochains développements de telles formulations à prendre une importance notable. Si

un implant résistant est souhaitable, comme ce serait le cas pour la vertébroplastie en alternative aux ciments traditionnellement utilisés, le travail de formulation peut être orienté vers des solutions concentrées de polymères de viscosité élevée. Ceci en limitera l'injectabilité et restreindra leur injection aux dispositifs et canules d'usage en vertébroplastie mais offrira une large capacité de chauffage. Les applications en vertébroplastie sont parmi les plus prometteuses pour les formulations étudiées.

Un implant de caractéristiques mécaniques intermédiaires formé à partir de solution de polymère de concentration intermédiaire incorporant une fraction de microparticules adaptée serait indiqués pour un usage en tant qu'agent de remplissage sur le modèle de ceux utilisés en cas de pathologie vésicale ou prostatique par exemple, mais qui dans le cas présent seraient cancéreuses. Ceci a pour corollaire une injectabilité intermédiaire qui conviendrait aux dispositifs encore relativement invasifs permis pour cet usage. Ceci ouvre la possibilité d'un traitement de la lésion cancéreuse par hyperthermie locale modérée, particulièrement prometteuse dans l'indication de tumeurs primaires de la prostate.

Finalement, une formulation injectable formant un implant *in situ* dont la composition serait ajustée pour une injectabilité par des dispositifs très peu invasifs, soit de faible teneur en polymère ou particules, formeront des implants de caractéristiques mécaniques *a fortiori* plus limitées, pour lesquels, concernant les indications, on peut faire un parallèle avec les formulations pharmaceutiques formant un dépôt pour la libération prolongée de principes actifs. Les capacités de chauffage en regard des capacités techniques actuelles en clinique seraient plus restreintes. Ainsi, on peut les envisager pour l'hyperthermie douce ou pour déclencher la libération de principes actifs comme pour cibler par la chaleur, c'est-à-dire l'accumulation d'un principe actif administré par voir systémique ou l'augmentation des effets d'une thérapeutique sous l'influence de la chaleur. Cela est relation avec des effets additifs et synergistiques très sophistiqués et d'importance. Ici les améliorations apportées aux particules magnétiques ainsi que la prise en compte des paramètres de formulations que nous avons étudiés permettrait d'atteindre des capacités optimales de chauffage plus élevées, une localisation du chauffage plus précise et également d'obtenir des effets additifs ou synergiques avec d'autres thérapies. Concernant les applications à envisager le plus directement pour les formulations développées au cours ce travail, nous recommandons tout particulièrement l'application à la vertébroplastie et au traitement du cancer de la prostate, deux domaines où de nouvelles approches sont souhaitables.

Abbreviations

A: Ampere (SI unit)
Å: Angstrom
acetyl CoA: acetyl co-enzyme A
ADCC: antibody-dependent cellular cytotoxicity
AEH: arterial embolization hyperthermia
AMF: Alternative magnetic field (without more precision includes rotating and alternating magnetic fields)
ATBE: active thermal bystander effect
ATP : Adenosine triphosphate
ATPase: enzyme catalyzing ATP hydrolysis
AUC: the area under thermogram curve
B: magnetic induction field
°C: Celsius grade, unit for temperature (*T*)
CA: carbonic anhydrase
CA9: carbonic anhydrase IX (or hMN)
CD: cluster of differentiation (CD-3,-4, -8....)
cDNA: *cf.* DNA
CEM: cumulative equivalent heating at 43°C
CML: cationic magnetoliposomes
DC: dendritic cells
DIH: direct injection hyperthermia
DNA: deoxyribonucleic acid
cDNA: circular deoxyribonucleic acid
DMPG: dimyristoyl-phosphatidylglycerol
DMSO: dimethylsulfoxide
DOTAP: N-(2,3-Dioleoyloxy-1-propyl)trimethylammonium methylsulfate
DPPG: dipalmitoyl-phosphatidylglycerol
DTA : differential thermal analysis
E: energy of activation in the Arrhenius equation
EGFR: epidermal growth factor receptor
EM43:equivalent heating minutes at index temperature of 43°C
EMF: Electromagnetic field
emu: electromagnetic units
ET: equilibrium temperature (plateau temperature)
f: frequency
FACS analysis: analysis by means of a fluorescent-activated cell sorter
FAD: flavin adenin dinucleotide (oxidized state)
$FADH_2$: reduced flavin adenin dinucleotide
Fc: fragment constant of the antibody
FDA : Food and Drug Administration, USA
g: gram
GHz: gigahertz
GTP : Guanosine triphosphate
H magnetic field strength (magnetic excitation vector)
H_c: coercivity
HER2: the human epidermal growth factor tyrosine kinase receptor 2 (*cf*. EGFR)
HIF1: hypoxia-inducible factor 1 (heterodimer of HIF1A and HIF1B)
HLA: Human leukocyte antigen involved in human histocompatibility system
hMN: human MN antigen (or CA9)
HMOX: heme oxygenases (HMOX1 or HSP32 and HMOX2
HSE: heat shock element DNA sequence
HSF: Heat shock transcription factor (in mammals three homologs: HSF1, 2 and 4)
Hz: Hertz, SI unit for frequency (*f*)
IGF-IR: insulin growth factor-I receptor
IL: interleukine (IL-1, IL-6, IL-8...)
INF-γ: Interferon gamma
k: the (in)activation rate (*cf* Arrhenius equation)
K: Kelvin grades, SI unit for temperature (*T*)
kcal: kilocalorie, cgs unit for energy
kg: kilogram (SI unit)
kHz: kilohertz
kOe: kilo-oersted
µ: micrometer
m: meter(SI unit)
mg: milligram
MHC-I: major histocompatibility complex class I, (equivalent in animal to HLA in human)
MHz: megaHertz
ml: milliliter
ML: magnetoliposomes
mm: millimiter
mol: mole
mPa·s: millipascal-second (viscosity)
MRI: Magnetic resonance imaging
mRNA: messenger ribonucleic acid
M_s: saturation magnetization
mT: millittesla
NAD^+: nicotinamide adenine dinucleotide (oxidized state)
$NADH+H^+$: reduced nicotinamide adenine dinucleotide
NF-κB: nuclear factor κB, latent gene regulatory proteins (e.g. transcription factor), central in most inflammatory responses
NK cell: natural killer cell
nm: nanometer
NML: neutral magnetoliposomes

NRG: neuregulin (NRG1, the malignant EGF-like growth factor or Heregulin β1)
Oe: Oerstedt (cgs unit for B)
p53 protein: product of 53 kDa of a very important tumor suppressor gene thus named protein p53.
PAI-I : Plasminogen Inhibitor Activator I (serpin peptidase inhibitor 1, SERPINE1)
PCNA: proliferating cell nuclear antigen
pH_e: extracellular pH
pH_i : intracellular pH
pg: picogram
PMMA: polymethyl methacrylate
pO2: partial pressure in molecular oxygen
ρ: density
R: the gas constant (*cf.* Arrhenius equation)
RANK: receptor activator of NF-kB
RNA: ribonucleic acid
rRNA : ribosomal ribonucleic acid
ROS: reactive oxygen species
rRNA: *cf.* RNA
s: second, SI unit for time (*t*)
SAR: specific absorption rate (less appropriate than specific loss power, *cf.* SLP)
SBF: simulated body fluid
SEM: scanning electron microscopy
SERPINE1: *cf.* PAI-I
SLP: specific loss power (more appropriate denomination than specific absorption rate, *cf.* SAR)
SOD: superoxide dismutase
SOD1: Cu, Zn-SOD superoxide dismutase
SPION: superparamagnetic iron oxides nanoparticles (mono-domain magnetic particles)
STAT: signal transducer and activator of transcription (STAT-1, STAT-3...)
T: Tesla (SI unit for B)
***T*:** temperature (in Celsius grade: °C: or Kelvin grade, SI: K)
t: time (in second: s, minutes: min, days: d)
TATA: tumor-associated transplantation antigens
TBF: tumor blood flow
TEM: transmission electron microscopy
TID: thermal isoeffect dose
TNF-α: tumor necrosis factor alpha (pro-inflammatory cytokine, with IL-1)
TRAP: tartrate-resistant acid phosphatase
TUNEL: TdT-mediated dUTP nick end-labeling (specific of apoptosis)
US: ultrasounds
VEGF: vascular endothelial growth factor
W: Watt, SI unit for power
WBH: whole body hyperthermia
XDH: xanthine dehydrogenase
XO: xanthine oxidase,
XRD: X-ray diffraction